University of Alberta

Self-Assembling Nanotubes Based on Guanine-Cytosine Module: Synthesis, Assembly and Structure Studies

by

Grigory Alexandrovich Tikhomirov

A thesis submitted to the Faculty of Graduate Studies and Research
in partial fulfillment of the requirements for the degree of

Doctor of Philosophy

Department of Chemistry

Edmonton, Alberta
Fall 2008

Library and Archives Canada

Published Heritage Branch

395 Wellington Street
Ottawa ON K1A 0N4
Canada

Bibliothèque et Archives Canada

Direction du Patrimoine de l'édition

395, rue Wellington
Ottawa ON K1A 0N4
Canada

Your file Votre référence
ISBN: 978-0-494-46437-3
Our file Notre référence
ISBN: 978-0-494-46437-3

NOTICE:
The author has granted a non-exclusive license allowing Library and Archives Canada to reproduce, publish, archive, preserve, conserve, communicate to the public by telecommunication or on the Internet, loan, distribute and sell theses worldwide, for commercial or non-commercial purposes, in microform, paper, electronic and/or any other formats.

The author retains copyright ownership and moral rights in this thesis. Neither the thesis nor substantial extracts from it may be printed or otherwise reproduced without the author's permission.

AVIS:
L'auteur a accordé une licence non exclusive permettant à la Bibliothèque et Archives Canada de reproduire, publier, archiver, sauvegarder, conserver, transmettre au public par télécommunication ou par l'Internet, prêter, distribuer et vendre des thèses partout dans le monde, à des fins commerciales ou autres, sur support microforme, papier, électronique et/ou autres formats.

L'auteur conserve la propriété du droit d'auteur et des droits moraux qui protège cette thèse. Ni la thèse ni des extraits substantiels de celle-ci ne doivent être imprimés ou autrement reproduits sans son autorisation.

In compliance with the Canadian Privacy Act some supporting forms may have been removed from this thesis.

While these forms may be included in the document page count, their removal does not represent any loss of content from the thesis.

Conformément à la loi canadienne sur la protection de la vie privée, quelques formulaires secondaires ont été enlevés de cette thèse.

Bien que ces formulaires aient inclus dans la pagination, il n'y aura aucun contenu manquant.

Canada

ABSTRACT

Nanoscale tubular architectures have attracted significant attention in recent years because of their promise for construction of electronic devices, sensor, storage and transport systems, and stimuli responsive materials. Rosette Nanotubes (RNTs) are biologically-inspired organic nanotubes that can be assembled from a small molecule that combines Guanine and Cytosine's hydrogen bond arrays. The ability to control dimensions with atomic precision, versatile outer surface functionalization procedures developed, tunable chirooptical properties and stability, along with biocompatibility make the RNTs a very attractive platform for construction of functional nanoscale materials. To assemble functional materials from the RNTs several current challenges have to be resolved. Possible solutions for three major challenges – understanding RNTs supramolecular structure, control of the aggregation and shape of their hierarchical assemblies, and making them conductive – are addressed in the respective chapters 2, 3, and 4 of this work.

In Chapter 1 the field of the self-assembled nanotubes is reviewed. The nanotubes are classified based on the type of the modules they are assembled from. Assembly of the nanotubes from hydrogen-bonded rosettes is reviewed in details. Challenges for the class of assembled organic nanotubes and for RNTs specifically are outlined and their possible solutions are discussed.

In Chapter 2 the structure of the G^C module was established in solution and in the solid state based on a number of 1D and 2D NMR spectroscopy at different field strengths. It was found that only protonated G^C modules, but not the rosettes, are

observed by solution NMR. In the solid state, deprotonated G^C module was shown to have hydrogen bonding patterns consistent with rosette nanotube structure.

In Chapter 3 a number of hydrophobic Guanine-Cytosine derivatives were synthesized. The possibility of controlling the aggregation of the nanotubes into discrete hierarchical structure is demonstrated by SEM, TEM, AFM, DLS, XRD, and SAED on various surfaces and in solution.

In Chapter 4 helical RNT bundles were assembled and coated with silver. It was shown that the resulting Ag-RNT composites were conductive and SERS-active.

AKNOWLEDGEMENTS

I would like to thank Professor Hicham Fenniri for his guidance throughout my graduate school and for tremendous personal development opportunities in multidisciplinary nanoscience he has created in Supramolecular Nanoscale Assembly Group (SNAG). I would like to thank my mother Tat'yana Tikhomirova for developing my curiosity and love for knowledge. I would like to thank my high school chemistry teacher Antonina Alexandrovna for initiating my journey of learning in chemistry and science in general. I am very grateful to my undergraduate (Drs. Igor Morozov, Sergei Troyanov, Marina Nemilova, Piotr Zorky, Tamara Kuznetsova) and graduate (Professors Nikolay Zefirov, Eugeniy Babaev) supervisors, as well undergraduate, graduate students, instructors and professors who were my mentors at Moscow State University.

I would like to thank my supervisory committee members Professors Richard McCreery, Christopher Cairo, David Perrin, Michael Doschak, Todd Lowary, Dennis Hall, and Rik Tykwinski for taking time to serve on my committee. I would like to thank my great teachers at the University of Alberta Professors Dennis Hall, Rik Tykwinski, Jonathan Veinot, Chris Backhouse, Al Meldrum, and Frederick West. I am very grateful to people who taught me the essential instrumental skills necessary to carry out my research: Mark Miskolzie, Glen Bigam, Drs. Ryan McKay, James Wigginton (solution NMR), Daniel Salamon (SEM, EDX), Greg Popovich, Al Meldrum, Julie Qian (TEM), Stephanie Bozic, Ken Bosnick (Microfabrication), Aktary Mirwais (E-beam lithography), Steve Launchpach (AFM, XRD), Mike Xia (LC MS, IR, Raman, UV, CD).

Some of the work described in this thesis was done in collaboration with a number of experts whose great help is acknowledged: Jae-Young Cho (some TEM, AFM, and

XRD), Mark Miskolzie, Ryan McKay (solution NMR), Devin Sears, Darren Brouwer (solid state NMR), Lei Fan, Souhaila Bouatra (^{15}N labeled intermediate synthesis), Ramon Alvarez-Puebla (SERS of silver coated helical bundles), Ken Bosnick (microfabrication, conductivity measurements), Shihong Xu (XPS), modeling studies (Takeshi Yamazaki), IR and elemental analysis (Wayne Moffat), HRMS (Angela Morales).

Many thanks to Dr. Andrew Myles, Dr. Rachel Beingessner, Dr. Ramon Alvarez-Puebla, Dr. Juan-Pablo Bravo-Vasques, Dr. Christophe Danumah, Dr. Darren Makeiff, Dr. Sandipta Acharya, Dr. Souhaila Bouatra, Dr. Baker Jawabrah Al-Hourani, Dr. Jae-Young Cho, Dr. Savariraj Kingsley, Dr. Azizul Haque, Mr. Ross Johnson, Dr. Jesus Moralez, Mr. Martins Oderinde, Mr. Gabor Borzsonyi, Ms. Usha Hemraz, Mr. Mustapha St. Jules, and other Supramolecular Nanoscale Assembly Group members for their many scientific discussions and suggestions.

Graduate assistantships and scholarships from University of Alberta and National Science and Engineering Research Council Nano Innovation Platform as well as research funding from National Research Council's National Institute for Nanotechnology are greatly acknowledged.

TABLE OF CONTENTS

page

CHAPTER 1. A review of Assembled Organic Nanotubes.....1

1.1. Nanotubes assembled from amphiphilic molecules.....2

1.2. Nanotubes assembled from linear molecules via helical folding.....8

1.3. Nanotubes assembled from macrocycles.....11

1.4. Nanotubes assembled from hydrogen bonded rosettes.....16

(1) Rosettes stabilization approaches.....18

(A) Metal coordination 18

(B) "Peripheral crowding".....20

(C) Covalent linking.....22

(D) Directed hydrogen bonding.....22

(E) Other approaches.....23

(2) Stacking stabilization approaches.....24

(A) Metal coordination.....24

(B) Covalent linking.....25

(C) Using polar solvents.....27

1.5. Nanotubes assembled from DNA tiles.....29

1.6. Comparison of different classes of nanotubes.....30

1.7. Conclusion, outlook and statement of goals.....34

(1) Achieving understanding of RNTs structure.....35

(2) Assembly of large hierarchical structures from RNTs.....36

(3) Making RNTs conductive.....38

CHAPTER 2. NMR Studies of G^C Modules Assemblies 40

2.1. Objectives.....40

2.2. Overview of NMR studies in G^C system.....40

2.3. Solution NMR studies.....42

2.4. Solid state NMR studies.....56

(A) Peak assignments.....56

(B) Evidence for RNT hydrogen bonding.....61

2.5. X-ray diffraction studies.....65
2.6. Conclusions.....67
2.7. Experimental part 69

CHAPTER 3. Assembly of Hydrophobic Organic Nanotubes 104
3.1. Objectives.....104
3.2. Overview of known nanotubes assemblies.....105
3.3. Design.....105
3.4. Synthesis.....107
3.5. Self-assembly studies.....111
(A) Self-assembly studies in hexane.....112
(B) Self-assembly studies in chloroform.....116
(C) Self-assembly studies in decanol.....133
(D) Self-assembly studies in heptanol.....136
(E) Self-assembly studies in butanol.....139
(F) Self-assembly studies in nitromethane.....142
(G) Self-assembly studies in DMF.....146
(H) Self-assembly studies in DMSO.....162
3.7. Conclusions.....165
3.8. Experimental part 168

CHAPTER 4. Helical Nanotube Bundles and Their Metallization.....201
4.1. Objectives.....201
4.2. Making organic nanostructures conductive: a brief review.....201
4.3. Assembly of helical nanotube bundles 203
4.4. Electroless silver deposition on RNTs helical bundles.....221
4.5. Conductivity measurements 231
4.6. Optical enhancing properties of silver coated RNTs bundles.....234
4.7. Conclusions.....237
4.8. Experimental part 239
References.....243
APPENDIX.....256

LIST OF TABLES

Page

3.1. Ratio major/minor found from the integration of well resolved proton signals of major and minor species....45

3.2. Chemical shifts and correlations for two tautomers based on ^{1}H, ^{13}C, ^{15}N NMR, ^{1}H-^{13}C HMQC, ^{1}H-^{13}C HMBC, ^{1}H-^{15}N HSQC, ^{1}H-^{15}N HMQC, *^{1}H-^{15}N gHMBC*, and NOESY....49

3.3. ^{15}N chemical shift tensors determined from spinning sideband profiles in slow CP MAS spectra at 4.7 T....58

3.4. Solid-state ^{1}H and ^{15}N isotropic chemical shifts and observed correlations for G^C samples....60

4.1. Concentration of the G^C aldehyde (columns) and ratios of aldehyde/$AgNO_3$ used for silver deposition studies....221

4.2. Selected area electron diffraction data assignment for silver coated RNTs. Literature data are for silver metal with f.c.c. crystal structure and lattice parameter a0 = 4.0862 Å....226

LIST OF FIGURES

Page

1.1. Lipid nanotube (LNT) (left) and the first amphiphilic molecule reported to self-assemble into LNTs (m=8, n=9) (right).....3

1.2. Example of bolaamphiphilic molecule self-assembling into nanotube.....4

1.3. Schematic illustration of amphiphile self-assembly into nanotubes in both polar (water) and nonpolar (toluene) solvents.....4

1.4. Structures of nanotube forming rod-coil and coil-coil copolymers (left). The scheme of nanotube formation from triblock copolymer and TEM image of the corresponding nanotubes.....6

1.5. Schematic illustration for the various templating features of LNTs: (1) surface modification; (2) organic–inorganic hybrids; (3) crystallization and/or deposition in bilayer membrane walls; (4) helical organization; (5) confinement. 8

1.6. Peptide β-helix structure and proton channel assembled from Gramicidin A dimer in lipid membrane – a biologically important nanotube.....9

1.7. Oligophenylacetylene folding equilibrium between the open state and the helical folded structure (space-filling representation). The ester substituents on each phenyl ring have been omitted in the space-filling model for clarity.....10

1.8. Oligo(pyridine-alt-pyridazine) and its model (N-atoms are black, C-atoms are gray, S-atoms are light, H-atoms and side chains are omitted for clarity). Freeze-fracture electron micrographs of 12 in CH_2Cl_2 (a) and pyridine (b) showing fiber network formation with helical textures.....11

1.9. Schematic diagram of nanotube self-assembly from cyclic D, L-peptides.....12

1.10. Formation of a cyclodextrin nanotube by covalent capture of a polyrotaxane precursor.....13

1.11. Several members of Moore's shape-persistent phenylene ethynylene macrocycles family.....14

1.12. Höger's coil-ring-coil block copolymers forming long aggregates of stacked rings surrounded by a polystyrene sheath. AFM image of 0.15 wt% 56 in cyclohexane on mica.....14

Page

1.13. Strategy for the synthesis of cyclic comb-like copolymers and their self-assembly....15

1.14. The scheme illustrating two step assembly of Rosette Nanotube (RNT) via rosette....16

1.15. G-quartet formed from guanine derivatives, its self-assembly into G-quadruplex and a an example of crystal structure of Na^+ form of the parallel-stranded G-quadruplex $[d(TGGGGT)]_4$....17

1.16. Guanine's hydrogen bonding array and two examples of non-rosette organization. Arrows in the tapes show dipole moment directions....18

1.17. Self-assembly/self-organization of lipophilic folate derivatives. Ion-responsive self-assembled liquid crystals are formed on reaction with ions. The ribbon structures of a folic acid derivative undergo an ion-templated transformation to discotic tetramers....19

1.18. The conformationally constrained guanosine forms a G-quartet exclusively....20

1.19. Schematic representation of the aggregation between M2 and B2 when the two azobenzene moieties of M2 take (a) E- or (b) Z-conformations. For M2, the E- and Z-conformations of the azobenzene moieties are shown by folding their arms....21

1.20. Cyanuric scid – melamine lattice and possible (top). Whitesides' "hub" approach to pre-organization of three melamines to stabilize the rosette motif....22

1.21. The directed self-assembly of rosettes using DDA·AAD array....23

1.22. Secondary interactions in DAA-ADD and ADA-DAD hydrogen bonded arrays....23

1.23. Zimmerman's pyrido[4,3-g]-quinoline system....24

1.24. The cation-templated self-assembly of 16 equivalents of 5-silyl-2,3-O-isopropylidene guanosine (2) gives a lipophilic G-quadruplex $[2]_{16}3K^+/Cs^+4pic^-$ in the solid state and in solution. This G-quadruplex, with four stacked G-quartets, is prepared quantitatively by extracting salts from water with a solution of 2 in $CHCl_3$....25

Page

1.25. Whitesides' and Reinhoudt's approaches to stacked rosettes based on the melaminecyanuric acid cyclic H-bonding array. Tong-shaped building blocks Ar1 and Ar2 co-assemble into cage-like substructures forming tubular stacks (Ar1, Ar2=benzene, furane, naphthalene, calix[4]arene). TEM image of bundled aggregates formed from tubular assemblies. Bottom: examples of Reinhoudt's and Whitesides' molecules.....28

1.26. Fenniri's multichannel RNTs with crown ether function (top) and amino acid containing "double decker" with a covalent link between two G^Cs for improved stability. Stained TEM (A, C) on carbon film and TM–AFM images on mica of compound 3 assembled in water.....28

1.27. Design and modelling of DNA nanotubes.....30

1.28. Approaches to tubular assembly: A) lipid nanotubes, B) nanotubes assembled from linear molecules via helical folding, C) nanotubes assembled from macrocycles, D) nanotubes assembled from hydrogen bonded rosettes, E) nanotubes assembled from DNA tiles.....31

2.1. ^{1}H NMR spectrum of **2-1** (previously proposed structure) using water saturation pulse sequence in 10% D_2O–H_2O at 27°C (500 MHz). The appearance of the satellites for NH signals upon cooling to 2°C. H(g) is said to be obscured by water peak.....42

2.2. The low field part of ^{1}H NMR spectrum of **2-1** in DMF-d_7 at -60°C. Major correlations observed in series of 1D difference NOE experiments in the same conditions are also shown. Assignments are made also based on HMBC, NOE and COSY experiments.....43

2.3. ^{1}H NMR spectrum of **2-4** in 3:1 (v/v) $CDCl_3$–DMSO-d_6 at 5°C (800 MHz).....45

2.4. VT NMR of **2-2** in 1:1 (v/v) $CDCl_3$–DMSO-d_6 at 5 – 80°C (400 MHz).....47

2.5. Compounds synthesized for NMR studies. Counter ion for protonated forms is either Cl^- or CF_3COO^-.....48

2.6. Major resonance structures of **2-2**.....50

2.7. H, C, N resonances assignments and major correlations in NOE, HMBC, and ^{15}N NMR spectra.....51

2.8. Dilution (DMSO) and variable temperature (1:1 (v/v) $CDCl_3$–DMSO-d_6) NMR studies summary for **2-2**.....52

Page

2.9. Deprotonated G^C (**2-5**) and protonated G^C (**2-4**) self-assembling modules. The nitrogens in bold-face type have been ^{15}N-labeled.....56

2.10. Solid-state NMR spectra of **2-5** (*top*) and **2-4** (*bottom*): (a) ^{1}H MAS NMR spectra obtained with 60 kHz MAS at 21.1 T, (b) ^{15}N CP MAS NMR spectra obtained at 4.7 T, (c) ^{13}C CP MAS NMR spectra obtained at 4.7 T.....57

2.11. Experimental (*top*) and calculated (*bottom*) ^{15}N CP MAS NMR spectra obtained at 4.7 T of (a) **2-5** at 1.4 kHz MAS frequency and (b) **2-4** at 1.2 kHz MAS frequency.....58

2.12. Two-dimensional correlation spectra for (*a-c*) **2-5** and (*d-f*) 4: (*a,d*) ^{1}H-^{15}N CP-HETCOR obtained at 21.1 T with 60 kHz MAS frequency; (*b,e*) ^{15}N-^{15}N $SR26_4$[11] dipolar DQ correlation obtained at 4.7 T with 4 kHz MAS frequency; (*c,f*) ^{1}H-^{1}H BABA dipolar DQ correlation obtained at 21.1 T with 60 kHz MAS frequency.....59

2.13. Hydrogen bonding in **2-5** between adjacent deprotonated G^C molecules in rosette nanotubes.....63

2.14. ^{15}N-^{15}N refocused INADQUATE spectra of (a) **2-5** and (b) **2-4** obtained at 4.7 T. The strongest correlation for 5 arises from the intermolecular hydrogen bond mediated J-coupling between N3 and N6.....63

2.15. Small angles powder XRD pattern obtained for (a) **2-4** indexed according to hexagonal packing model (b, c). (d) The powder of the G^C hydrochloride salt **2-5** (top) compared to free G^C base **2-4** (bottom).....66

2.1. Two possible nanotube structures: (left) rosette nanotube and (right) helical tape.....68

2. 2. ^{1}H NMR spectra of **2-2** in (A) DMF-d_7 (-60°C, 400 MHz), (B) 1:1 (v/v) $CDCl_3$–DMSO-d_6 (-40°C, 500 MHz), (C) 1:1 (v/v) $CDCl_3$–DMSO-d_6 (0°C, 400 MHz), (D) DMSO-d_6 (27°C, 800 MHz). Note sharpening of the NH signals as polarity of the solvent and temperature decrease. Protons c and d appear at the same chemical shift in DMF (~9.5 ppm).....71

2. 3. ^{1}H NMR spectra of **2-2** mixed with a standard p-chloro-bromobenzene (resonances marked by a star) in DMSO-d_6 (27°C, 600 MHz, acquisition time is 56 hours).....72

2. 4. Key NOEs observed for **2-2** in DMF-d_7 (-60°C, 400 MHz).....72

Page

2.5. ^{1}H NMR spectra of **2-3** in (a) DMF-d_7 (-60°C, 500 MHz), (b) 1:1 (v/v) $CDCl_3$–DMSO-d_6 (5°C, 800 MHz), (c) DMSO-d_6 (27°C, 800 MHz).....73

2. 6. Low field portion of ^{13}C NMR spectra of **2-3** in DMSO-d_6 (27°C, 800 MHz) (a) fully H decoupled, (b) selective decoupling of half of Ha nuclei (presaturation of low field signal of NH doublet).....74

2.22. ^{15}N NMR spectra of **2-3** in (A) DMSO-d_6 (27°C, 800 MHz, 1 hour) and (B) DMF-d_7 (-60°C, 500 MHz, 14 hours).....74

2.23. ^{1}H-^{15}N HSQC spectrum of **2-3** in DMF-d_7 (-60°C, 500 MHz).....75

2.24. ^{1}H-^{15}N HMQC spectrum of **2-3** in DMF-d_7 (-60°C, 500 MHz) J_{xh} = 10 Hz.....75

2.25. ^{1}H-^{15}N HMQC spectrum of **2-3** in DMF-d_7 (-60°C, 500 MHz) J_{xh} = 5 Hz.....76

2.26. ^{1}H-^{15}N HMBC spectrum of **2-3** in DMF-d_7 (-60°C, 400 MHz) J_{xh} = 7 Hz.....76

2.27. ^{1}H NMR spectra of **2-4** in (A) DMF-d_7 (-50°C, 500 MHz), (B) DMF-d_7 (27°C, 500 MHz), (C) 1:1 (v/v) $CDCl_3$–DMSO-d_6 (5°C, 800 MHz).....86

2.28. ^{15}N NMR spectra of **2-4** in (A) DMF-d_7 (27°C, 400 MHz, 10 hours, with NOEs) and (B) DMF-d_7 (27°C, 500 MHz, 10 hours, no NOEs), 1:1 (v/v) $CDCl_3$–DMSO-d_6 (25°C, 800 MHz) (27°C, 500 MHz, 10 hours, no NOEs, coupled to H).....87

2.29. ^{1}H-^{15}N HMQC spectrum of **2-4** in DMF-d_7 (-60°C, 400 MHz) J_{xh} = 10 Hz.....87

2.30. ^{1}H-^{15}N HMQC spectrum of **2-4** in DMF-d_7 (-60°C, 400 MHz) J_{1xh} = 90 Hz.....88

2.31. ^{1}H-^{15}N HMBC spectrum of **2-4** in DMF-d_7 (-60°C, 400 MHz) J_1 = 90 Hz, J_n = 10 Hz.....88

2.32. SEM images of **2-5** (<0.1 mg/ml, MeOH, carbon film).....89

2.33. ^{1}H NMR spectra of **2-7** in (A) DMF-d_7 (-60°C, 400 MHz), (B) 1:1 (v/v) CD_2Cl_2–DMSO-d_6 (27°C, 400 MHz), (C) DMSO-d_6 (27°C, 400 MHz), (D) CD_3OH (27°C, 400 MHz, presaturation).....96

2.34. Effect of methanol hydroxyl saturation at rt on appearance of ^{1}H NMR spectra of **2-7** in CD_3OH.....96

Page

2.35. Effect of temperature on appearance of low field portion of ^{1}H NMR spectra of **2-7** in CD_3OH (no presaturation used).....97

2.36. Key NOEs observed for **2-7** in DMF-d_7 (-50°C, 400 MHz).....97

2.37. SEM images of **2-2** (7 mg/ml, DMSO, carbon film).....97

2.38. SEM images of **2-2** (4 mg/ml, 1:1 (v/v) $CDCl_3$–DMSO-d_6, carbon film).....98

2.39. SEM images of **2-2** (3 mg/ml, 3:1 (v/v) $CDCl_3$–DMSO-d_6, carbon film).....98

2.40. SEM images of **2-2** (2.4 mg/ml, CD_3OH, carbon film).....99

2.41. SEM images of **2-2** (4.3 mg/ml, DMF-d_7, carbon film).....99

2.42. Key NOEs observed for **2-1** in DMF-d_7 (-60°C, 400 MHz).....100

2.43. COSY spectrum of **2-1** in in DMF-d_7 (-60°C, 400 MHz).....100

3.1. Examples of Percec's amines.....107

3.3. Schematic representation of the assembly of a RNT from G^C module functionalized with dendritic amines.....107

3.3. Attempts to functionalize G^C module via Heck reaction.....108

3.4. Synthetic scheme used to synthesize G^C derivatives **1a-f**.....109

3.5. Summary of the morphologies obtained from **1a–f** in the indicated solvents (0.25 g/L).....111

3.6. SEM images of **1a** cast on carbon film (0.25 g/L, hexane).....113

3.7. Height and amplitude (right) AFM images of **1a** cast on carbon film (0.25 g/L, hexane).....113

3. 1. Dynamic light scattering (DLS) regularization diagram showing the hydrodynamic diameter (DH) for compound **1a** (0.25 g/L) versus scattering intensity in hexane (A) methanol (B), and chloroform (C).....113

3.9. SEM images of **1b** cast on carbon film (0.25 g/L, hexane).....114

3.10. SEM images of **1c** cast on carbon film (0.25 g/L, hexane).....114

Page

3.11. SEM images of **1d** cast on carbon film (0.25 g/L, hexane)..... 115

3.12. SEM images of **1e** cast on carbon film (0.25 g/L, hexane)..... 115

3.13. SEM images of **1f** cast on carbon film (0.25 g/L, hexane).....115

3.14. SEM images of **1a** cast on carbon film (0.25 g/L, $CHCl_3$)..... 117

3.15. Energy filtered (zero loss) TEM images of **1a** (0.25 g/L in $CHCl_3$) on carbon-coated grid showing the lamellar organization of the spheroids. Scale bars = 100 nm..... 117

3.16. TM-AFM amplitude images of compound **1a** (0.25 g/L) cast from $CHCl_3$ on mica showing background material surrounding nanospheroids..... 118

3.17. SAED of an individual nanospheroid assembled from **1a**. Two visible reflections on the left image correspond to 4.5 (d_1) and 3.2 (d_2) nm. Additional weak reflections corresponding to 0.70 (d_3), 0.41 (d_4) and 0.28 (d_5) nm were revealed by adjusting the contrast (right image).....119

3.18. XRD spectrum of nanospheroids prepared according to Method 1 (left) and Method 2 (right) described in section 4 (above).....119

3. 2. SEM micrograph (A), TM-AFM height image (B) and height profile (C) of compound **1a** (0.25 g/L) cast from methanol on HOPG (A) and mica (B). The (x,y) scale in C is in nm.....120

3. 3. Hierarchical self-assembly of organic nanospheroids.....121

3. 4. Solvent promoted transition between three levels of hierarchical self-assembly for **1a**.....121

3.22. SEM images of 1b cast on carbon film (0.25 g/L, $CHCl_3$).....123

3.23. SEM and S(T)EM (right) images of **1b** cast on carbon film (0.25 g/L, $CHCl_3$).123

3.24. SEM images of **1c** cast on carbon film (0.25 g/L, $CHCl_3$).....124

3.25. SEM images of **1d** cast on carbon film (0.25 g/L, $CHCl_3$).....124

3.26. SEM and STEM (right) images of **1d** cast on carbon film (0.25 g/L, $CHCl_3$)....124

3.27. TM-AFM amplitude images of compound **1d** on mica (0.25g/L, $CHCl_3$).....125

Page

3.28. SEM images of **1e** cast on carbon film (0.25 g/L, $CHCl_3$)....125

3.29. SEM images of **1f** cast on carbon film (0.25 g/L, $CHCl_3$)....126

3.30. Concentration dependence of **1a** morphology (time = 1 hour)....126

3.31. Time dependence of **1a** morphology (0.05 g/L)....127

3.32. Time dependence of **1a** morphology (0.10 g/L)....127

3.33. Time dependence of **1a** morphology (0.25 g/L)....127

3.34. Time dependence of **1a** morphology (3.0 g/L)....127

3.35. SEM images of the bow ties assembled from **1a** with instrument's stage tilted 30°....128

3.36. TEM images of unstained "bow ties" assembled from 1a....129

3.37. TEM images of "bow ties" assembled from **1a** and stained with uranyl acetate....129

3.38. TM-AFM images of bow ties assembled from **1a** in cast on carbon film (0.1 g/L, $CHCl_3$)....130

3.39. Schematic illustration of crystal splitting (A) and examples of different forms of splitting in minerals (B-E), inorganic nanostructures (F-I), and synthesized in this work RNTs bow-ties (J-N)....132

3.40. SEM images of **1a** cast on carbon film (0.25 g/L, decanol)....134

3.41. TEM images **1b** cast on carbon film stained with uranyl acetate (0.25 g/L, decanol). Measured nanotubes diameter is 4.6 ± 0.5 nm....134

3.42. SEM images of **1b** cast on carbon film (0.25 g/L, decanol)....134

3.43. SEM images of **1c** cast on carbon film (0.25 g/L, decanol)....135

3.44. SEM images of **1d** cast on carbon film (0.25 g/L, decanol)....135

3.45. SEM images of 1e cast on carbon film (0.25 g/L, decanol)....135

3.46. SEM images of **1f** cast on carbon film (0.25 g/L, decanol)....136

3.47. SEM images of **1a** cast on carbon film (0.25 g/L, heptanol)....137

Page

3.48. TEM images **1a** cast on carbon film stained with uranyl acetate (0.25 g/L, heptanol). Measured nanotubes diameter is 4.5 ± 0.5 nm.....137

3.49. SEM images of **1b** cast on carbon film (0.25 g/L, heptanol).....137

3.50. SEM images of **1c** cast on carbon film (0.25 g/L, heptanol).....138

3.51. SEM images of **1d** cast on carbon film (0.25 g/L, heptanol).....138

3.52. SEM images of **1e** cast on carbon film (0.25 g/L, heptanol).....138

3.53. SEM images of **1f** cast on carbon film (0.25 g/L, heptanol).....139

3.54. SEM images of **1a** cast on carbon film (0.25 g/L, butanol).....139

3.55. SEM images of **1b** cast on carbon film (0.25 g/L, butanol).....140

3.56. TEM images **1a** cast on carbon film stained with uranyl acetate (0.25 g/L, butanol). Measured nanotubes diameter is 4.7 ± 0.6 nm.....140

3.57. SEM images of **1c** cast on carbon film (0.25 g/L, butanol).....140

3.58. SEM images of **1d** cast on carbon film (0.25 g/L, butanol).....141

3.59. SEM images of **1e** cast on carbon film (0.25 g/L, butanol).....141

3.60. SEM images of **1f** cast on carbon film (0.25 g/L, butanol).....141

3.61. SEM images of **1a** cast on carbon film (0.25 g/L, nitromethane).....142

3.62. Cryo-TEM images **1a** cast on carbon film stained with uranyl acetate (0.25 g/L, nitromethane). Measured nanotubes diameter is 4.7 ± 0.3 nm.....143

3.63. SEM images of **1a** cast on carbon film (0.25 g/L, nitromethane).....143

3.64. SEM images of **1b** cast on carbon film (0.25 g/L, nitromethane).....144

3.65. SEM images of **1c** cast on carbon film (0.25 g/L, nitromethane).....145

3.66. SEM images of **1d** cast on carbon film (0.25 g/L, nitromethane).....145

3.67. SEM images of **1e** cast on carbon film (0.25 g/L, nitromethane).....145

3.68. SEM images of **1f** cast on carbon film (0.25 g/L, nitromethane).....146

Page

3.69. SEM images of **1a** cast on carbon film (0.25 g/L, DMF).....147

3.70. TEM images **1a** cast on carbon film stained with uranyl acetate (0.25 g/L, DMF). Measured nanotubes diameter is 4.4 ± 0.5 nm.....147

3.71. TEM images **1a** cast on carbon film stained with uranyl acetate (0.25 g/L, DMF).....148

3.72. AFM images **1a** cast on HOPG (0.25 g/L, DMF). Measured nanotubes diameter is 4.7 ± 0.3 nm.....148

3.73. SEM images **1b** cast on carbon film (0.25 g/L, DMF).....149

3.74. SEM images **1c** cast on carbon film (0.25 g/L, DMF).....149

3.75. SEM images **1d** cast on carbon film (0.25 g/L, DMF).....150

3.76. SEM images **1e** cast on carbon film (0.25 g/L, DMF).....150

3.77. SEM images **1f** cast on carbon film (0.25 g/L, DMF).....150

3.78. SEM images of **1a** donuts at 30 kV (left) and 1 kV electron beam accelerating voltages.....151

3.79. SEM images of **1a** donuts on tilted stage.....151

3.80. SEM images of **1a** assembled at different concentrations.....152

3.81. Time dependence of **1a** sonicated for 10 sec at 0°C and assembled at 0°C (0.25 mg/ml).....152

3.82. Time dependence of **1a** sonicated for 10 sec at 25°C and assembled at 25°C (0.25 mg/ml).....153

3.83. SEM of **1a** boiled for 10 seconds cast on carbon film (0.25 mg/ml, DMF).....153

3.84. Examples of nanorings obtained by drying effect from (A) CNT bundles, (B) metal nanoparticles, (C) porphyrin derivative. SEM images (left) and corresponding scheme (right).....154

3.85. An example of CNTs covalently closed into rings. (A) Scheme of the process. (B) AFM image of the nanorings on mica.....155

Page

3.86. Representative SEM images illustrating "loop templating rings" mechanism of the donuts formation....157

3.87. Representative SEM images illustrating "loop templating rings" mechanism of the donuts formation (A-I). Energy filtered TEM images of unstained donuts showing layered structure of donuts (J, K, M, N). AFM amplitude image of nanodonuts(L, O)....158

3.88. Representative SEM images illustrating concentric rolling ribbons mechanism....159

3.89. SEM images illustrating helical twist along the some donuts' perimeter....161

3.90. SEM images illustrating "thick bundle ends' fusion" mechanism....161

3.91. SEM images illustrating "budding" mechanism....161

3.92. SEM images **1a** cast on carbon film (0.25 g/L, DMSO)....163

3.93. TEM images **1a** cast on carbon film stained with uranyl acetate (0.25 g/L, DMSO). Measured nanotubes diameter is 4.4 ± 0.5 nm....163

3.94. SEM images **1b** cast on carbon film (0.25 g/L, DMSO)....164

3.95. SEM images **1c** cast on carbon film (0.25 g/L, DMSO)....164

3.96. SEM images **1d** cast on carbon film (0.25 g/L, DMSO)....164

3.97. SEM images **1e** cast on carbon film (0.25 g/L, DMSO)....165

3.98. SEM images **1f** cast on carbon film (0.25 g/L, DMSO)....165

3. 99. Various morphologies generated from the same molecule (**1a**) in different solvents....166

4.1. Scheme illustrating the assembly of aldehyde functionalized RNT and its coating with silver....203

4.2. SEM images of helical RNT bundles assembled from G^C aldehyde in water (carbon grid, 1 g/L)and (bottom two images) S(T)EM of stained with uranyl acetate helical bundles....204

Page

4.3. TEM images of unstained (left) and stained with uranyl acetate (right) helical bundles assembled in water (carbon grid, 1 g/L). White scale bars are 20 nm....205

4.4. TM-AFM height (A, C, E), amplitude (B, D, F), and phase (G) images of helical bundles assembled in water (carbon grid, 1 g/L) using ultra-high resolution tips. Inset is the height profile of the double helix shown on panels E, F, and G....206

4.5. TM-AFM height images of helical bundles assembled in water (carbon grid, 1 g/L) using regular AFM tips....207

4.6. Representative SEM images illustrating time dependence of G^C aldehyde in water (boiled, 0.1 g/L, carbon film)....207

4.7. Representative SEM images illustrating time dependence of G^C aldehyde in water (boiled, 0.25 g/L, carbon film)....208

4.8. Representative SEM images illustrating time dependence of G^C aldehyde in water (boiled, 1.0 g/L, carbon film)....209

4.9. TM-AFM height images of helical bundles assembled in water (2 days, mica, 0.25 g/L) using regular AFM tips....210

4.10. Examples of achiral molecules assembling into helical fibers. Molecules on the left and EM pictures on the right....212

4.11. Assembly of the rosette and its stacking at 15° turn relative to the other rosette....214

4.12. Two types of helices observed for G^C aldehyde assemblies in water (0.25 g/L, carbon film). 215

4.13. SEM images of various aggregates formed from helical bundles (0.25 g/L, carbon film)....217

4.14. SEM (A–D), TEM (E, F) images of platelets formed from G^C aldehyde (0.25 g/L, carbon film, two weeks) and SAED of individual platelet (G)....218

4.15. Powder XRD and corresponding SEM images of G^C aldehyde before (A) and after (B) self-assembly....219

4.16. Crystals grown from 2-2 in concentrated aqueous HCl....220

Page

4.17. Representative SEM images of nanotube bundles coated with silver.....222

4.18. Representative SEM images of nanotube bundles coated with silver.....223

4.19. Representative SEM images of nanotube bundles coating with silver experiments.....224

4.20. TEM images of nanotube bundles coating with silver experiments (M12 conditions).....224

4.21. Representative SEM images of nanotube bundles coating with silver experiments (M33) using three weeks aging time (A, B), four weeks aging time (C, D), using TBAF (E, F).....225

4.22. SAED pattern obtained for silver coated RNTs bundles (M12).....226

4.23. EDX (A) and XPS (B) of silver coated RNTs obtained in conditions M12. Copper peak in EDX comes from the TEM grid that was used as a substrate. Potassium comes from contamination present in the instrument.....227

4.24. Nanoparticles distribution along silver coated DNA (A), and platinum coated porphyrin nanotubes (B).....228

4.25. Silver nanowires obtained at M41 conditions after two months.....230

4.26. Schematic representation of the interdigitated electrodes coated with nanowires and SEM images of actual device fabricated.....232

4.27. SEM images of four devices based on individual electrodes design.....233

4.28. (A) Electronic spectroscopy of HRN and Ag-HRN (RNTs coated with silver). Inset shows the deconvolution result for longitudinal and transversal plasmons. (B) Raman and SERS (obtained on silver colloids) spectra of HRN and the SERS spectrum of the silver coated RNTs (λ_{ex}: 785 nm). (C) SERS and SERRS spectra of MB, 2NAT and R6G (10^{-7} M) on Ag-RNTs.....234

LIST OF ABBREVIATIONS

AFM	Atomic force microscopy
aq	Aqueous
BABA	Back-to-back
Boc	*t*-Butyloxy carbonyl
$(Boc)_2O$	Di-*t*-Butyl dicarbonate
br	Broad
C	Carbon or Celsius
calcd	calculated
$CHCl_3$	Chloroform
CH_2Cl_2	Methylene chloride
CH_3CN	Acetonitrile
CH_3NO_2	nitromethane
CNT	carbon nanotube
COSY	Correlation spectroscopy
CP	Cross polarization
d	Doublet
DCE	1,2-Dichloroethane
DCM	Dichloromethane
dH_2O	Deionized water
DIPEA	Diisopropylethylamine
DLS	Dynamic light scattering
DMAP	4-N,N-Dimethylaminepyridine

DMF	Dimethyl formamide
DMSO	Dimethylsulfoxide
DNA	Deoxyribonucleic acid
DOSY	Diffusion ordered spectroscopy
DQ	Double quantum
EA	Ethyl acetate
EDX	Energy dispersive X-ray analysis
EM	Electron microscopy
ESI	Electrospray ionization
Et_3N	Triethylamine
FG	Functional group
G^C	Guanine-Cytosine
H	Hydrogen
H-bond	Hydrogen bond
h	Hour
HCl	Hydrochloric acid
Hex	Hexane
HETCOR	Heteronuclear correlation
HMBC	Heteronuclear multiple bond correlation
HMQC	Heteronuclear multiple quantum coherence
HOPG	Highly ordered pyrolytic graphite
HR	High resolution
HSQC	Heteronuclear single quantum coherence

INADEQUATE	Incredible Natural Abundance Double Quantum Transfer Experiment
IR	Infra red
K_2CO_3	Potassium carbonate
LNT	Lipid nanotube
m	Multiplet
MAS	Magic angle spinning
MeOH	Methanol
mp	Melting point
MS	Mass spectrometry
$NaHCO_3$	Sodium bicarbonate
Na_2SO_4	Sodium sulfate
NH_4Cl	Ammonium chloride
$NH_2OH{\cdot}HCl$	Hydroxylamine hydrochloride
NMR	Nuclear magnetic resonance
NOESY	Nuclear Overhauser Enhancement Spectroscopy
NP	Nanoparticle
NT	nanotube
PDI	Polydispersity index
$POCl_3$	Phosphorous oxychloride
ppm	Part per million
R_f	Retention factor
RNT	Rosette nanotubes

rt	Room temperature
s	Singlet
SAED	Selected area electron diffraction
SEM	Scanning electron microscopy
S/N	Signal to noise ratio
S_NAr	Nucleophilic aromatic substitution
S(T)EM	Transmission mode of scanning electron microscopy
STM	Scanning tunneling microscopy
t	Triplet
TBAF	Tetrabutylammonium fluoride
TCT	2,4,6-Trichloro-[1,3,5]triazine
TEA	Triethylamine
TEM	Transmission electron microscopy
TFA	Trifluoroacetic acid
TFAA	Trifluoroacetic anhydride
THF	Tetrahydrofuran
TLC	Thin layer chromatography
TM-AFM	Tapping mode atomic force microscopy
UV	Ultra violet
XPS	X-ray photoelectron spectroscopy
XRD	X-ray diffraction
2D	Two-dimensional

1. A review of Assembled Organic Nanotubes

Since the award of the Nobel Prize in Chemistry to Jean-Marie Lehn, Donald Cram, and Charles Pedersen for their pioneering work in supramolecular chemistry in 1987, the field has evolved into a powerful tool of materials chemistry and nanotechnology.[1] The supramolecular approach has become complementary to covalent synthesis, and this is frequently the only way to access various complex functional materials.[2, 3]

Among supramolecular assemblies, hollow tubular structures of molecular dimensions have shown promise to become the next generation of functional materials with a wide range of applications from drug delivery vehicles[4] to light emitters for photonics[5] and nanowires.[6] Tubular architectures have also been used for sensing, transport, catalysis, storage, and other applications.[7] They can serve as scaffolds for confining materials in a quasi-one-dimensional system which may lead to novel properties. Tubes with at least one dimension lying within 1 – 1000 nanometers scale, or "nanotubes", have been known for a long time as an integral part of biological systems (some biological nanotube structures are sometimes referred to as "microtubules"). Examples of their biological significance in nature include scaffolding and packaging roles played by cytoskeletal microtubules and viral coat proteins, respectively, as well as the chemical transport and screening activities of membrane channels[8]. Biological systems make extensive use of self-assembling supramolecular strategies in the preparation of such tubular assemblies. Several approaches that mimic biological strategies of self-organization as well as original, non-natural self-assembly schemes have been proposed to assemble synthetic nanotubes. These synthetic strategies are reviewed here, and classified based on the nature of building blocks and self-assembly

forces involved. It is worth mentioning that the most widely known class of nanotubes – graphitic carbon nanotubes (CNTs)[9] – are out of the scope of the present review, since their syntheses are not based on the self-assembly paradigm. This review also excludes numerous nanotubes that were found in crystal structures of small molecules where no evidence was provided that the nanotubes exist on their own either in solution or on a substrate.[10, 11] Cylindrical pores found in crystal X-ray analysis gave many authors the reason to call the structures "nanotubes", however many of these tubular structures are not thermodynamically stable in solution. Only the tubular structures that have been proven either by electron or atomic force microscopies as independent self-sustained structures (on a substrate) are reviewed in the following sections.

This review is not intended to cover all of the possible ways to assemble nanotubular structures, but rather to outline major concepts of nanotube assembly, so that researchers in the nanotube field can orient themselves in the system to better understand the importance of their research.

1.1. Nanotubes assembled from amphiphilic molecules

Amphiphilic molecules, of which detergent surfactants are typical examples, possess antagonistic hydrophilic and hydrophobic moieties in the same molecule. Carbohydrate amphiphiles, commonly referred to as glycolipids, greatly contribute to the structural stability and the function of biomembranes in living systems.[12] Lipid nanotubes (LNTs) are one of numerous classes of morphologies that have been assembled from amphiphilic molecules (Figure 1.1). The assembly mode of amphiphiles depends on the molecular shape and solution conditions such as lipid concentration, electrolyte concentration, pH, and temperature.[13] The latter parameters can be used to control their

self-assembly. Lipid bilayers are the most common aggregates formed by amphiphilic molecules. The hydrophobic effect causes aggregation and holds the bilayer together. Repulsive hydration and steric forces, on the other hand, prevent the formation of large, three-dimensional crystals. The bilayers can further evolve into infinite planar bilayers, spherical or tubular vesicles, and micelles.

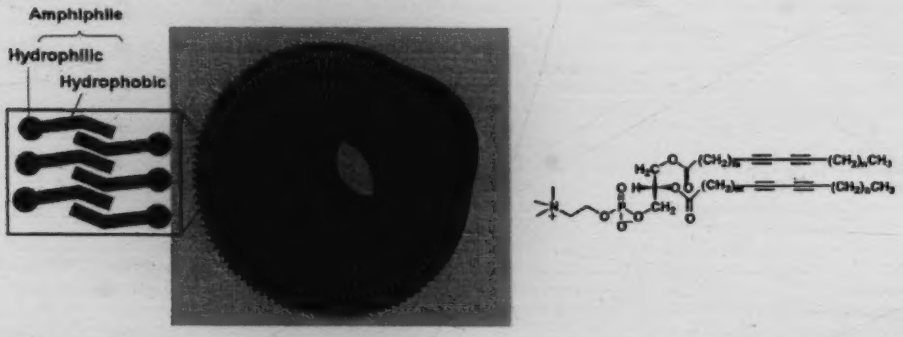

Figure 1. 1. Lipid nanotube (LNT) (left) and the first amphiphilic molecule reported to self-assemble into LNTs (m=8, n=9) (right). Reproduced in part with permission from ref 7. Copyright 2005 American Chemical Society.

Even though no universal strategy to self-assemble LNTs from lipid bilayers has been developed so far, a number of structural correlations between amphiphile and resulting bilayer architecture have been revealed.[14] Interestingly the first synthetic LNT[15] was obtained in 1984 – years before widely publicized carbon nanotubes were discovered by Iijima[9] in 1991.

Bolaamphiphilic molecules having two polar groups separated by a hydrophobic linker can also self-assemble to form nanotubes. Symmetric and asymmetric bolaamphiphiles can be used to assemble nanotubes with desired dimensions and inner and outer tube surface chemistry.[16, 17] An example of a helical nanotube was reported for the assembly of N,N-eicosanedioyl-di-L-glutamic acid[18] (Figure 1.2) in alcohol-water mixtures. Hydrogen bonds between amide fragments of the molecules are proposed to be responsible for maintaining the helical structure.

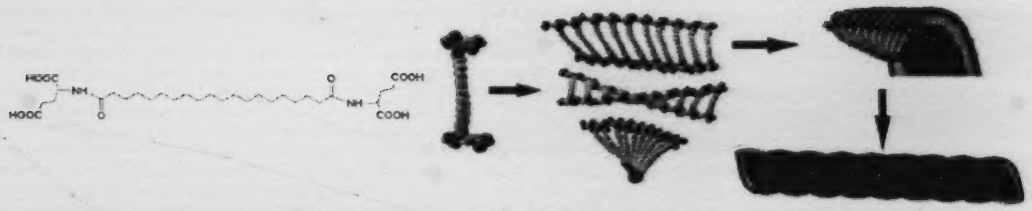

Figure 1. 2. Example of bolaamphiphilic molecule self-assembling into nanotube. Reproduced with permission from ref 18. Copyright 2005 Royal Society of Chemistry.

A large variety of hydrophilic and hydrophobic groups can be used in the construction of amphiphilic and bolaamphiphilic molecules for nanotube self-assembly. Phosphorylated glycerin, saccharides, aminoacids, and oligopeptides as a hydrophilic moiety coupled with long alkyl chains, benzene, heterocycles, cholesteric systems as their hydrophobic counterpart are among most popular fragments used to tailor nanotube-forming amphiphiles.[7]

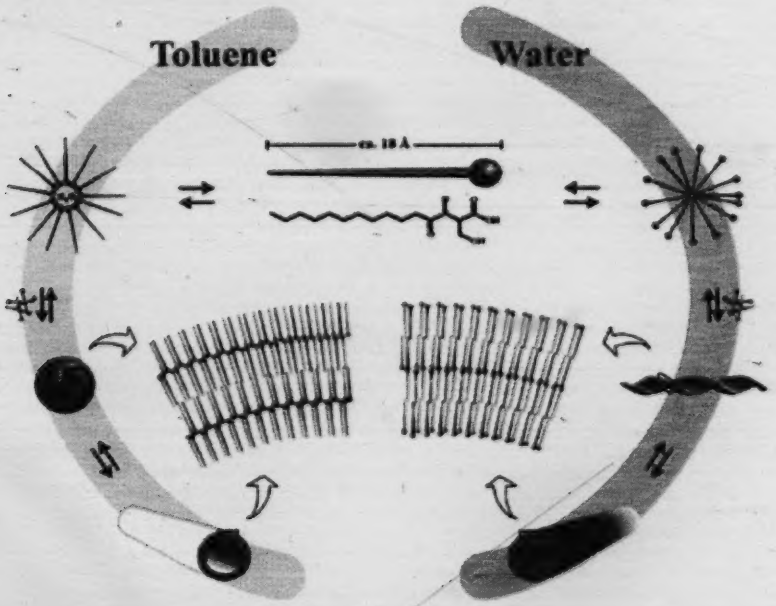

Figure 1. 3. Schematic illustration of amphiphile self-assembly into nanotubes in both polar (water) and nonpolar (toluene) solvents. Reproduced with permission from ref 19. Copyright 2001 American Chemical Society.

The vast majority of low molecular weight amphiphiles form nanotubes only in highly polar solvents – most frequently water. A polar solvent is normally required to stabilize a structure with polar surfaces, thus minimizing the interfacial energy (Figure 1.1). The only example of head-to-head packing of low molecular weight amphiphiles has been reported by Boettcher et al, who, by using cryo-electron microscopy, detailed the molecular packing features and aggregation pathways of tubular structures in organic solvents. Hot solutions (>80 °C) of N-dodecanoyl (D or L-) serine in toluene (Figure 1.3) were cooled to room temperature to produce gels consisting of LNTs and vesicles. Comparative cryo-transmission electron microscopy permitted the first direct comparison of the molecular tubular structures (diameters, 80-130 nm) obtained from the amino acid amphiphile under normal and reversed polarity conditions. All supramolecular assemblies had similar multilayers with a measured periodicity of 3.30 ± 0.01 nm both in water and in toluene, giving normal bilayers with the hydrophilic headgroups oriented toward the aqueous environment and "inverse" bilayers with the alkyl chains oriented toward the hydrophobic toluene phase, respectively (Figure 1.3).

Polymers, unlike low molecular weight amphiphiles, can be designed to self-assemble into nanotube architectures in solvents covering the polarity range from hexane to water. Two polymer types that are particularly prone to form nanotubes are rod-coil block copolymers and coil-coil block copolymers. Rod-coil block copolymers have a rigid (rod) block that tends to form a highly crystalline domain, providing anisotropic intermolecular interactions. Poly(phenylquinoline)-block-polystyrene (PPQ-b-PS) self-assembles to form spheres, lamellae, microtubes, or vesicles in mixtures of trifluoroacetic acid (TFA) and dichloromethane (Figure 1.4).[20] The main determinants of the

morphologies are the initial solvent composition and the evaporation rate of the solvent. Microtubes with 1-3 μm outer diameters become the major morphology when the TFA composition is high. The shorter rigid block results in smaller assemblies. Since the length of the blocks can be controlled with high precision, the dimensions of the resulting nanotubes can be controlled (Figure 1.4). Redox-active organometallic nanotubes with widths of 29-40 nm can be obtained from the self-assembly of the rod-coil block copolymer poly(ferrocenyldimethylsilane)-block-poly(dimethylsiloxane) (PFS-b-PDMS) (Figure 1.4).[21] The PDMS/PFS block length ratio of the copolymer affects the final morphology. If the PDMS/PFS ratio is between 1:12 and 1:18, long hollow nanotubes form, whereas a block ratio of 1:6 results in the formation of cylindrical micelles. Addition of water to the self-assembly solvent (hexane) induces the conversion of discrete nanotubes into bundles.

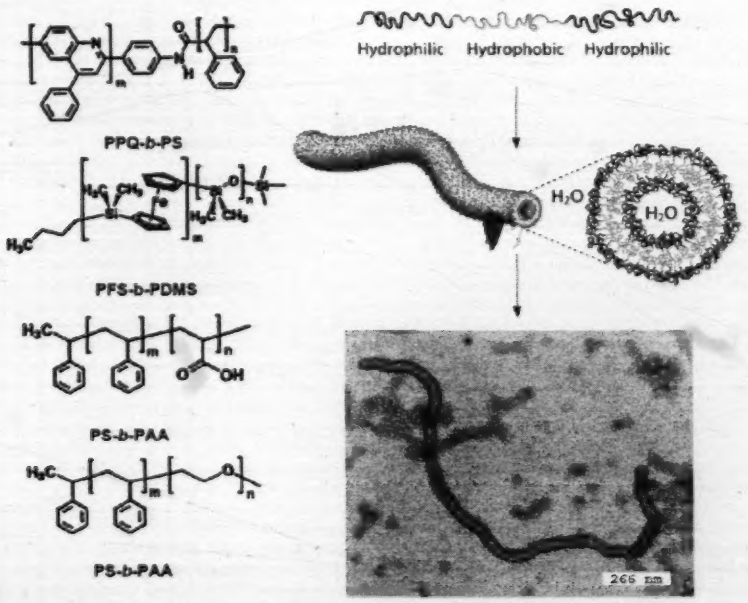

Figure 1. 4. Structures of nanotube forming rod-coil and coil-coil copolymers (left).The scheme of nanotube formation from triblock copolymer and TEM image of the corresponding nanotubes.[22] Reproduced with permission from ref 22. Copyright 2004 Royal Society of Chemistry.

Polystyrene-block-poly(acrylic acid) (PS-b-PAA) and polystyreneblock-poly(ethylene oxide) (PS-b-PEO) (Figure 1.4) aggregate into various morphologies such as spheres, rods, vesicles, lamellae, nanotubes, and large compound micelles.[23] In these so-called crew-cut aggregates, the corona-forming block is much shorter than the core-forming block. The aggregate morphology of these kinetically trapped self-assemblies is affected by many factors. The ratio between the two blocks is especially important for controlling their morphologies, which is also the case for the rod-coil block copolymers described above. The assemblies are prepared by dropwise addition of water, a poor solvent for the hydrophobic block, into a polymer solution in DMF, followed by dialysis to remove the residual DMF completely.

For nonionizable PS-b-PEO block copolymers, the PS/PEO block ratios are critical determinants of the resulting morphologies. Copolymers with 240/15 to 240/45 ratios often produce tubular morphologies.[24] As the PEO block is made longer, the resulting morphologies progress from lamellar tape and lamellar rods to spherical micelles. The wall thicknesses of the nanotubes are typically ca. 20 nm, and their outer diameters are ca. 100 nm. The lengths can reach hundreds of micrometers. The formation mechanism of these nanotubes is unclear, although adhesive contact and fusion of vesicles are involved.[24]

Nanotubes assembled from amphiphilic molecules have been shown to have potential applications (Figure 1.5) in the field of biomedicine for drug storage and delivery.[25, 26] The hollow cylinders of the LNT can modulate the nucleation, growth, and deposition of inorganic substances on their external and internal surfaces, in the hollow cylinder, and in the bilayer membrane wall. Templating the LNTs enables one to produce

diverse 1-D nanostructures, such as nanotubes, concentric tubular hybrids, complex helical architectures, and 1-D arrays of quantum dots.[27]

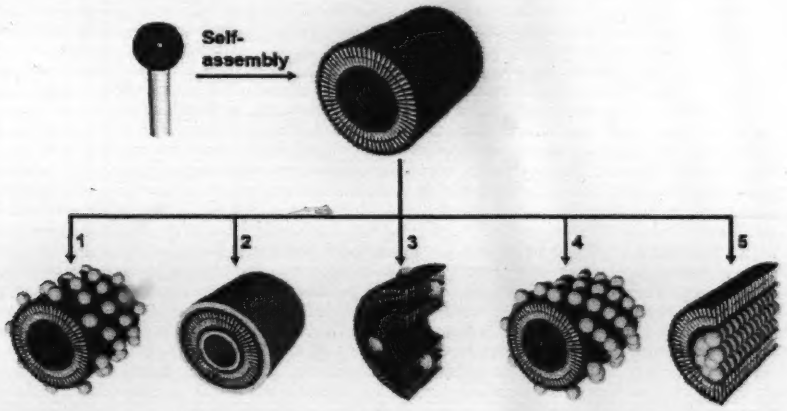

Figure 1. 5. Schematic illustration for the various templating features of LNTs: (1) surface modification; (2) organic–inorganic hybrids; (3) crystallization and/or deposition in bilayer membrane walls; (4) helical organization; (5) confinement. Reproduced with permission from ref 27. Copyright 2001 American Chemical Society.

LNTs can also be converted into nanowires without metallization. Aida et al reported that an amphiphilic derivative of hexa-peri-benzocoronene assembles into LNTs that can be made conductive by oxidizing them with NO^+.[6]

1.2. Nanotubes assembled from linear molecules via helical folding

Helical folding of peptides or proteins aggregates is the dominant mode of tubular assembly used by Nature. β-Helices are peptide secondary structural motifs in which the backbone folds into a helical conformation stabilized by β-sheet-type hydrogen bonding (Figure 1.6). Amino acid side chains protrude outward, leaving an unoccupied central pore running the length of the helix axis. The average radius of the β-helix pore depends upon the helix periodicity, or number of residues per turn, with larger periodicities giving rise to larger pores. In principle, helix periodicity can be controlled by varying the

backbone hydrogen-bonding register, making helices potentially attractive scaffolds for preparation of tubular structures with tailored internal dimensions.

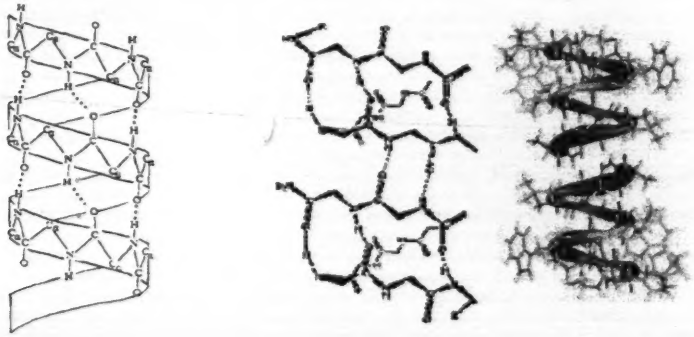

Figure 1. 6. Peptide β-helix structure and proton channel assembled from Gramicidin A dimer in lipid membrane – a biologically important nanotube. Reproduced in part with permission from ref 28. Copyright 1974 American Chemical Society.

Helical folding of nonbiological molecules into nanotubes has been described by Moore et al.[29] The design takes advantage of Moore's "shape-persistent" approach to nanoscale architectures in which rigid phenylacetylene subunits are coupled together with a meta relationship (Figure 1.7), and thus nucleate helix-turn conformations within the resulting oligomer. A helical conformer could be stabilized by solvophobically-driven packing between backbone phenyl rings. Moore reasoned that these interactions would favor self-organization of linear oligomers into folded helical conformations. The relatively wide angle of the turn (approximately 120°) prevents a close packed core, resulting in a hollow coil reminiscent of peptide β-helices. The spontaneous folding of this linear synthetic polymer into a compact, defined shape places oligophenylacetylenes into the growing family of molecules known as "foldamers".[30]

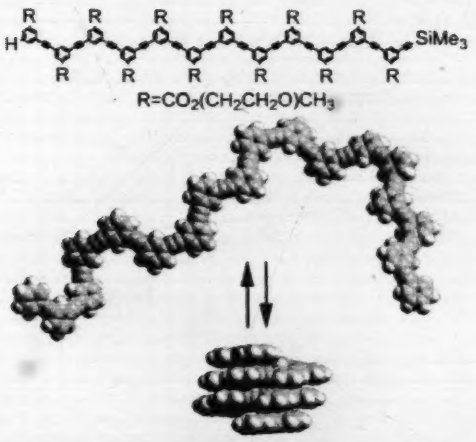

Figure 1. 7. Oligophenylacetylene folding equilibrium between the open state and the helical folded structure (space-filling representation). The ester substituents on each phenyl ring have been omitted in the space-filling model for clarity. Reproduced with permission from ref 30. Copyright 2001 American Chemical Society.

A rare example of nanotubes obtained via helical folding characterized by electron microscopy was reported by Lehn.[31] The oligo(pyridine-alt-pyridazine)s (Figure 1.8) adopt a helical conformation with 12 heterocyclic units per turn, having a central cavity measuring ~8–9 Å in diameter. In solution, up-field-shifted NMR signals due to off-set stacking of aromatic rings indicate formation of the helical conformation. Interestingly, the aromatic signals are further shifted with increasing concentration pointing to aggregation of the helices. Vapor-pressure osmometry (VPO) confirms formation of higher aggregates, namely duplexes, in a variety of solvents. Freeze-fracture electron microscopy shows an extensive network of linear and intertwined chiral fibers of high aspect ratio, i.e., micrometer length and ~80 Å diameter. The fibers are composed of coiled-coil bundles of two or three individual supramolecular helices. The self-aggregation to supramolecular stacks and superhelices is based on intra- and intermolecular π–π stacking interactions between overlapping and neighboring aromatic helix turns.

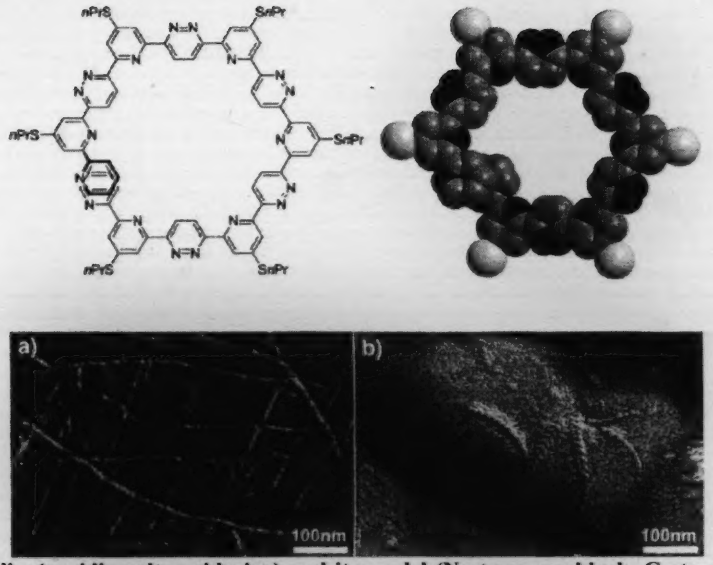

Figure 1. 8. Oligo(pyridine-alt-pyridazine) and its model (N-atoms are black, C-atoms are gray, S-atoms are light, H-atoms and side chains are omitted for clarity). Freeze-fracture electron micrographs in CH_2Cl_2 (a) and pyridine (b) showing fiber network formation with helical textures. Reproduced with permission from ref 30. Copyright 2001 American Chemical Society.

1.3. Nanotubes assembled from macrocycles

A novel class of self-assembling nanotubes has been introduced by Ghadiri and co-workers.[32] These are based on cyclic peptide molecules consisting of even numbered alternating D- and L-amino acids. They have shown that these molecules self-assemble via hydrogen bonding into nanotubes (Figure 1.9). The resulting nanotubes can be inserted into lipid membranes and act as channels.[33] This feature is important for such nanotubes' pharmacological applications development.

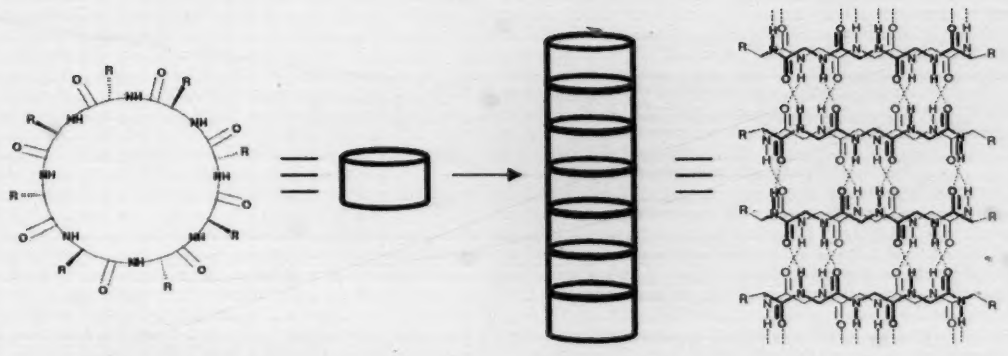

Figure 1. 9. Schematic diagram of nanotube self-assembly from cyclic D, L-peptides.

An interesting feature of this peptide nanotube is the ease with which the external surface properties and the internal diameter of the tube may be altered by changing the appropriate amino acid side chains and the size of the peptide ring, respectively. For example, it was shown that with appropriate hydrophobic side chains, these cyclic peptides partition into nonpolar lipid bilayers and self-assemble to form artificial transmembrane ion channels. Similar systems have also been utilized as biosensors for detection of ions and small organic molecules.

An interesting approach to organization of macrocycles into nanotubes was described by Harada et al.[34] A tubular cyclodextrin polyrotaxane was assembled by threading a single polyethylene glycol bisamine molecule. Furthermore, the cyclodextrin rings can be covalently linked and the thread removed, resulting in nanotubes that were studied by NMR, IR, UV and gel filtration.

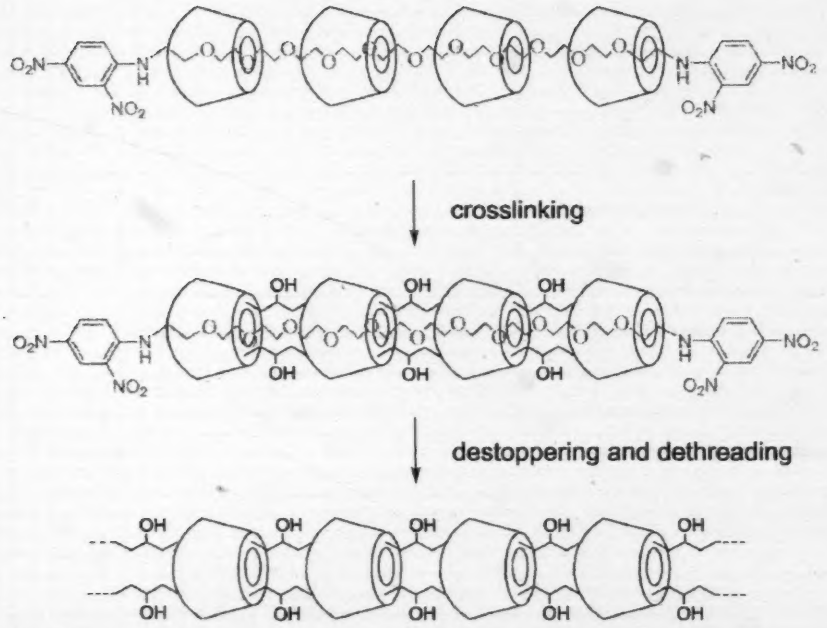

Figure 1. 10. Formation of a cyclodextrin nanotube by covalent capture of a polyrotaxane precursor. Reproduced with permission from ref 30. Copyright 2001 American Chemical Society.

Zhang and Moore have developed macrocycles with the ability to self-aggregate in solution at high concentrations (Figure 1.11 $R_1 = R_2 = OH$).[35] NMR titration experiments monitoring the upfield shift of aromatic protons with increasing concentration indicate cooperative π–π stacking interactions between the aggregating macrocycles. Since then, a number of other macrocycles have been studied and it was found that their self-association behavior varies with the structure of the backbone as well as the side chains. In agreement with Hunter and Sanders,[36] electron-poor aromatic systems such as benzoates in macrocycles shown on Figure 1.11 favor aggregation, while in the case of electron rich moieties such as phenolates, phenyl ethers, and benzyl ethers, no self-association was found.[35] The association constants were deduced from NMR and vapor-pressure osmometry studies, which confirmed that no aggregates larger than dimers were

formed in chloroform. Later on, the same group introduced an additional solvophobic driving force by substitution with polar triglyme side chains and as a result, higher association constants leading to formation of larger (than dimeric) aggregates were obtained

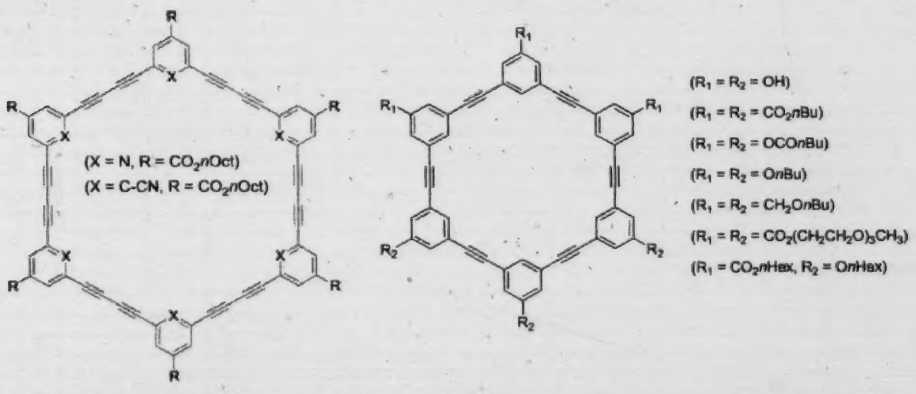
(X = N, R = CO2nOct)
(X = C-CN, R = CO2nOct)
(R1 = R2 = OH)
(R1 = R2 = CO2nBu)
(R1 = R2 = OCOnBu)
(R1 = R2 = OnBu)
(R1 = R2 = CH2OnBu)
(R1 = R2 = CO2(CH2CH2O)3CH3)
(R1 = CO2nHex, R2 = OnHex)

Figure 1. 11. Several members of Moore's shape-persistent phenylene ethynylene macrocycle family

An interesting study by Höger and coworkers describes the self-assembly of coil-ring-coil block copolymers (Figure 1.12), in which the macrocycle is linked between two narrowly dispersed polystyrene blocks of various lengths.[37]

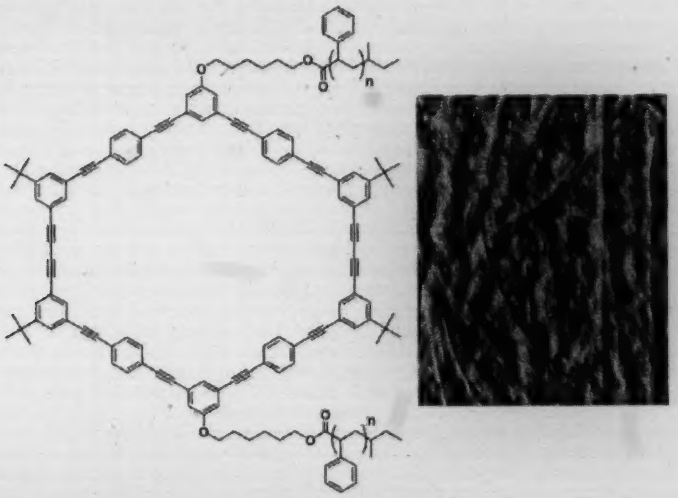

Figure 1. 12. Höger's coil-ring-coil block copolymers forming long aggregates of stacked rings surrounded by a polystyrene sheath. AFM image of 0.15 wt% in cyclohexane on mica. Reproduced with permission from ref 37. Copyright 2001 Wiley Interscience.

Upon cooling in cyclohexane, the stacking of the cyclic moieties driven by the amphiphilic structure results in formation of hollow cylinders with an average length of ~500 nm. A combination of DLS, X-ray scattering, TEM, and AFM experiments confirms the existence of such long cylindrical aggregates. The high persistence length of this supramolecular polymer of ~100 nm indicates the surprisingly high rigidity of the structure.

The only reported example of using polymer macrocycles to assemble nanotubes has been recently reported by Schappacher and Deffieux.[38] Their strategy is based on the synthesis of a triblock copolymer ABC, in which the long central block B is extended by two short A and C sequences bearing reactive antagonist functions. When reacted under highly dilute conditions, this precursor produces the corresponding macrocycle by intramolecular coupling of the A and C blocks. Chloroethyl vinyl ether was selected as the monomer for the central block B, because it can be readily derivatized into brushlike polymers by a grafting process. The corresponding macrocyclic brushes were decorated with polystyrene or randomLy distributed polystyrene/polyisoprene branches. In a selective solvent for the polyisoprene branches, the macrocyclic brushes self-assemble into cylindrical tubes of up to 700 nanometers in length (Figure 1.13).

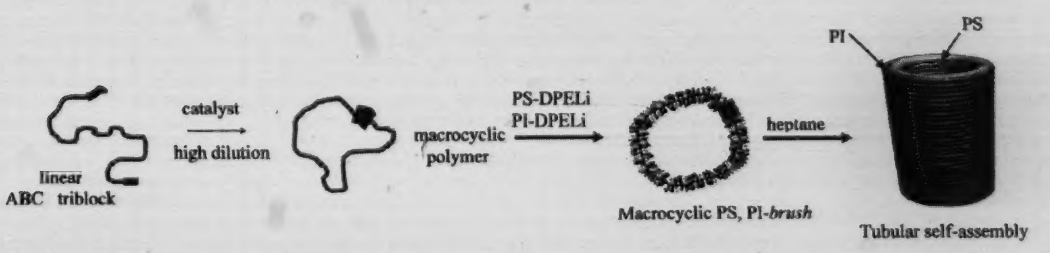

Figure 1. 13. Strategy for the synthesis of cyclic comb-like copolymers and their self-assembly. Adapted with permission from ref 38. Copyright 2008 American Association for the Advancement of Science.

1.4. Nanotubes assembled from hydrogen bonded rosettes

The two previous sections 1.2. and 1.3. have detailed ways in which macrocycles and coiled molecules can self-organize into tubular materials by virtue of their well-defined shape. In those examples, cylindrical shape is immediately apparent from the monomeric species; pore size is defined by the degree of coiling or the ring size. A more complex approach to tubular constructs relies on the two step hierarchichal noncovalent assembly of Rosette Nanotubes (RNTs). In the first step, a rosette is formed via hydrogen bonding between several molecules that become the segments of a disc with a hole in its centre. In the second step the supramolecular rosettes stack to form a column via π–π stacking interactions and/or solvophobic interactions where the individual holes arrange into a channel running the length of the structure. Conceptually, such an approach is similar to the stacking of molecular discs; however, this strategy demands higher order self-assembly as the discs are now separated into many sections.

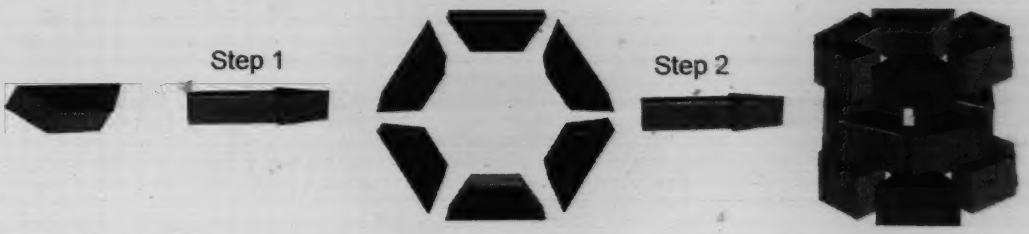

Figure 1. 14. The scheme illustrating two step assembly of Rosette Nanotube (RNT) via rosette.

This assembly motif has been demonstrated in Whitesides and co-workers' exploration of mesoscale assemblies, as well as their earlier studies on the construction of melamine:cyanuric acid molecular rosettes.[39] The assembly of individual molecules into rosettes as the target architectureis interesting on its own and has frequently been the ultimate goal of many reports. As a result, the organization of rosettes into nanotubes has

frequently not been explored. In cases where the nanotubes' formation is investigated, the experimental proof for their existence as independent architectures is insufficient. This review will focus mainly on the rosette nanotubes whose existence as independent architectures has been convincingly demonstrated. Even though the structures of some rosette nanotubes were conclusively established in solid state by single crystal X-ray analysis, these examples were not included in this review if no evidence for the nanotube formation in solution or on a substrate by electron or scanning probe microscopies was provided.

Biological inspiration.

Nature has been a source of inspiration for the design of hydrogen bonded rosette-based nanotubes. The guanine tetrameric rosette (G-quartet) was identified by Gellert et al[40] in gels formed by guanylic acid in 1962. It has later been shown that G-quartets are the core of so called G-quadruplexes that have a number of important biological functions.[41] G-quadruplexes are formed by vertical stacking of multiple G-quartets (Figure 1.15).

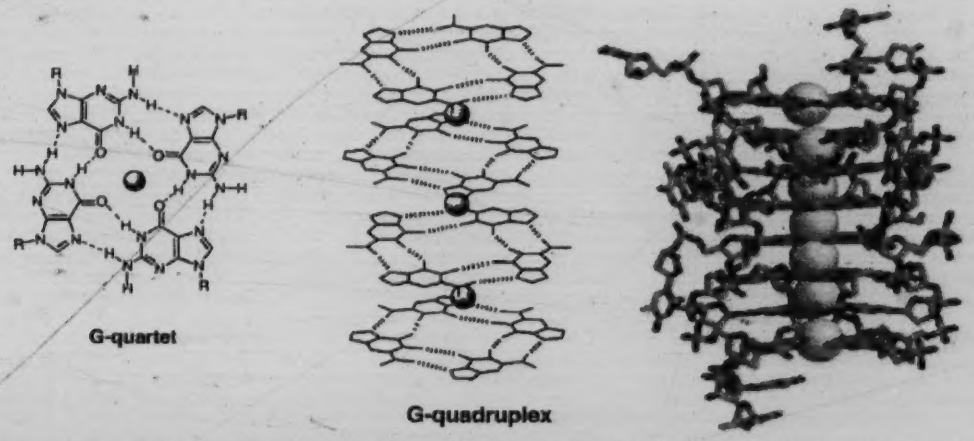

Figure 1. 15. G-quartet formed from guanine derivatives, its self-assembly into G-quadruplex and an example of crystal structure of Na^+ form of the parallel-stranded G-quadruplex $[d(TGGGGT)]_4$. Adapted with permission from ref 42. Copyright 2004 Wiley Interscience.

A guanine molecule can organize into various non-rosette motifs using its three hydrogen bond donor and four hydrogen bond acceptor sites (Figure 1.16).

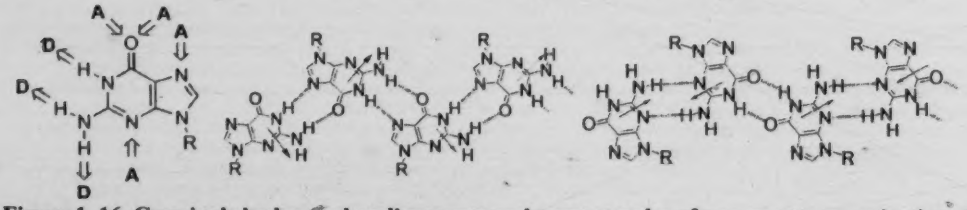

Figure 1. 16. Guanine's hydrogen bonding array and two examples of non-rosette organization. Arrows in the tapes show dipole moment directions.

Hydrogen bonding and π-π stacking are weak interactions that can therefore be influenced by minor changes in environment (e.g. solvent) and assembling module structure. The relative weakness of the interactions also means that self-assembly is a dynamic and thermodynamically controlled process. That is, the assembly outcome is determined by the free energy change between resulting architecture and starting components rather than by the activation energies of the assembly processes.

To assemble nanotubes exclusively from individual modules under thermodynamic control, one has to ensure that (1) the *rosette* structure has the lowest energy of all possible hydrogen bonded motifs (Figure 1.14, Step 1) and (2) the *rosette nanotube* energy is lowest relative to other assemblies (Figure 1.14, Step 2). The next section is an outline of the approaches used to achieve preferential rosette (1) and rosette nanotubes (2) assembly.

(1) Rosette stabilization approaches

(A) Metal coordination for rosette stabilization.

Organization of molecules into rosettes is common in naturally-occurring biological systems and commonly involves metal coordination. The G-quartet structure in a G-quadruplex is stabilized over various ribbon motifs via guanine's carbonyl oxygen

interaction with cations. Alkaline and alkaline-earth cations were found to provide rosette dominance as studied by single crystal X-ray analysis[43] and NMR.[44] This property was used by Kato and co-workers[45] to prepare synthetic dynamic materials based on a pterin motif. They found that temperature and cations induce a phase change in folate-derived liquid crystals. X-ray diffraction and IR spectroscopy studies indicated that lipophilic folates with 2-(3,4-dialkoxyphenyl)ethyl substituents formed thermotropic liquid crystals (Figure 1.17). Two liquid-crystal phases are formed depending on the conditions: a smectic and a columnar discotic phase. The pterin rings of the folate hydrogen bond to give a self-associated ribbon structure, which is the basis for the smectic phase. Alternatively, the folate ring forms a cyclic tetramer in the presence of a cation, which leads to a columnar discotic liquid crystal. The smectic phase was transformed into the hexagonal discotic phase upon addition of alkali-metal salts. The finding that cations can trigger rearrangement from an H-bonded ribbon to cyclic tetramer indicates that folate-derived liquid crystals are dynamic materials, which are able to change their structure and properties in response to an external stimulus.

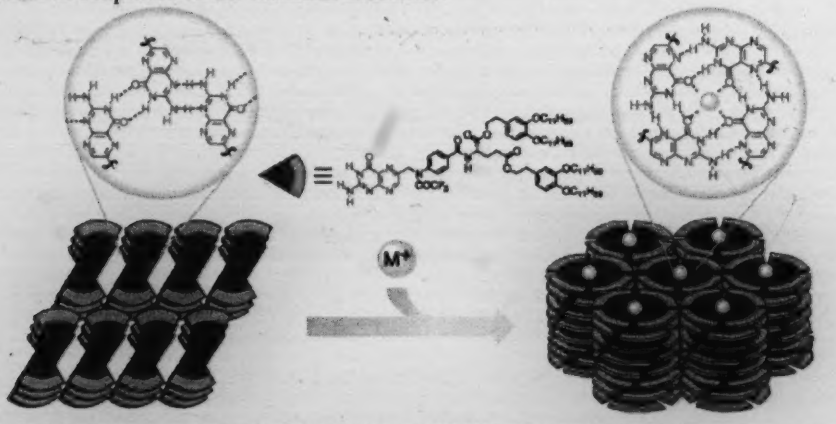

Figure 1. 17. Self-assembly/self-organization of lipophilic folate derivatives. Ion-responsive self-assembled liquid crystals are formed on reaction with ions. The ribbon structures of a folic acid derivative undergo an ion-templated transformation to discotic tetramers. Adapted with permission from ref 42. Copyright 2004 Wiley Interscience.

(B) "Peripheral crowding" for rosettes stabilization

Another way to coax modules to assemble into rosettes is known as "peripheral crowding". Sessler et al.[46] have shown that a guanine modified with a large substituent, revealed a hydrogen-bonded G-quartet without need for cation by single crystal X-ray analysis. Solution NMR spectroscopy in CD_2Cl_2 also showed characteristic signals for a stable G-quartet. The critical feature needed to obtain an empty G-quartet is a conformationally-constrained monomer (Figure 1.18). In the absence of a cation, unconstrained guanosine derivatives self-associate to give ribbon structures by using the N3 position as a hydrogen-bond acceptor. The dimethylaniline substituent forces the nucleoside into a syn conformation, where the sugar blocks the adjacent nitrogen lone pair, thus preventing ribbon formation.

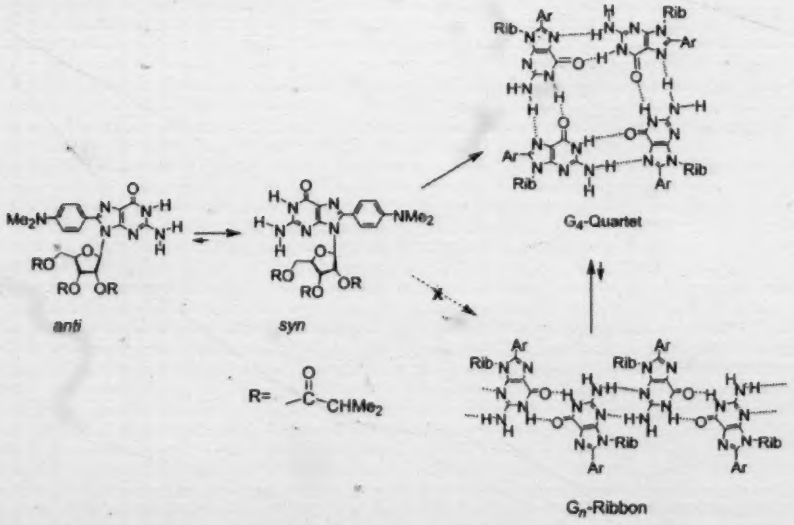

Figure 1. 18. The conformationally constrained guanosine forms a G-quartet exclusively. Adapted with permission from ref 42. Copyright 2004 Wiley Interscience.

An interesting application of the "peripheral crowding" concept was found by Yagai et al. (Figure 1.19).[47] They prepared azobenzene-appended melamine M2 and

barbiturate B2, both possessing bulky tridodecyloxyphenyl (TDP) wedge(s). The geometrical isomer EE-M2 bearing two E-azobenzene moieties readily complexed with B2, affording a remarkably stable cyclic hexamer EE-$M2_3 \cdot B2_3$ (rosette) in chloroform, toluene, and methylcyclohexane, as confirmed by size exclusion chromatography, dynamic light scattering, ^{1}H NMR, and UV-vis studies. The E→Z photoisomerization of the azobenzene moieties upon irradiation with UV light was significantly suppressed in the rosette because of the steric crowding of the TDP wedges (total of nine TDP wedges in a rosette), whereas irradiation of the monomeric EE-M2 resulted in facile transformation into ZZ-M2 bearing two Z-azobenzene moieties. ^{1}H NMR studies of the complexation of the initially photogenerated ZZ-M2 with B2 revealed that it is hard for ZZ-M2 to form a rosette with B2 because of the intermolecular steric interaction between the TDP wedges.

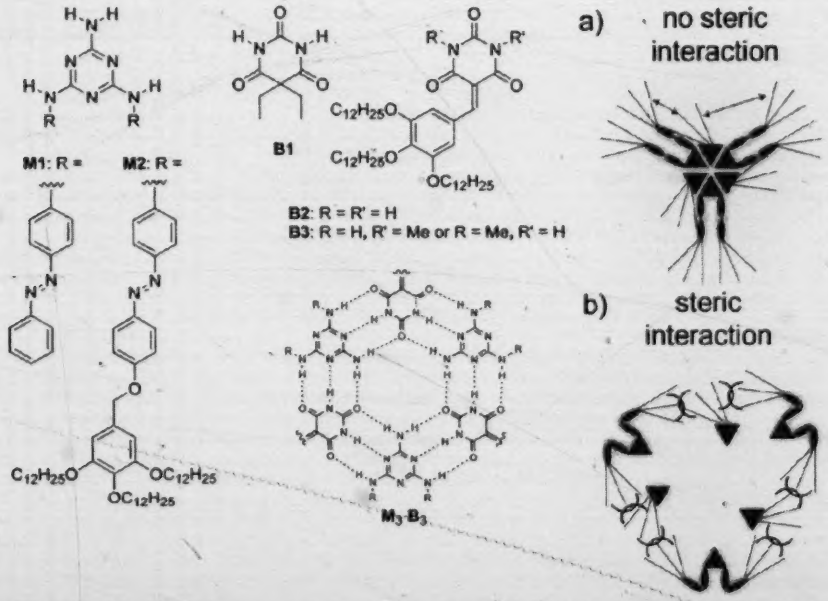

Figure 1. 19. Schematic representation of the aggregation between M2 and B2 when the two azobenzene moieties of M2 take (a) E- or (b) Z-conformations. For M2, the E- and Z-conformations of the azobenzene moieties are shown by folding their arms. Reproduced with permission from ref 47. Copyright 2004 American Chemical Society.

(C) Pre-organization of rosettes via covalent linking

To favor the rosette formation over linear and crinkled tape motifs in cyanuric acid – melamine assemblies, Whitesides and coworkers[48] have attached three melamine units (M) to a "central hub" in order to pre-organize the module for the rosette assembly (Figure 1.20). This approach, however, prevents rosette organization into longer than two-stack nanotubes and blocks the channel.

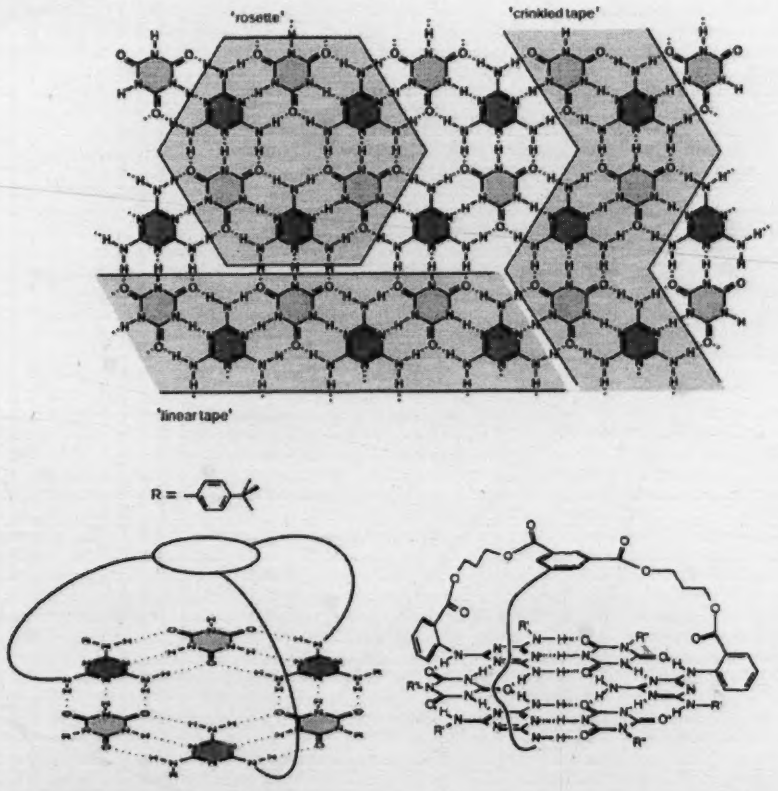

Figure 1. 20. Cyanuric acid – melamine lattice (top). Whitesides' "hub" approach to pre-organization of three melamines to stabilize the rosette motif. Reproduced with permission from ref 48. Copyright 2004 American Chemical Society.

(D) Rosette stabilization through directed hydrogen bonding

Using donor – donor – acceptor · acceptor – acceptor – donor triple hydrogen (DDA·AAD) bonding array to direct module assembly into rosettes was suggested by

Lehn[49] for binary systems, and by Lehn,[50] Mascal[51] and Zimmerman[52] for single component (self-complementary) systems (Figure 1.21). It should be noted that hydrogen bonding is significantly stronger in DDA·AAD motifs compared to DAD·ADA motifs with the same number of hydrogen bonds due to the presence of fewer unfavorable secondary interactions (Figure 1.22).

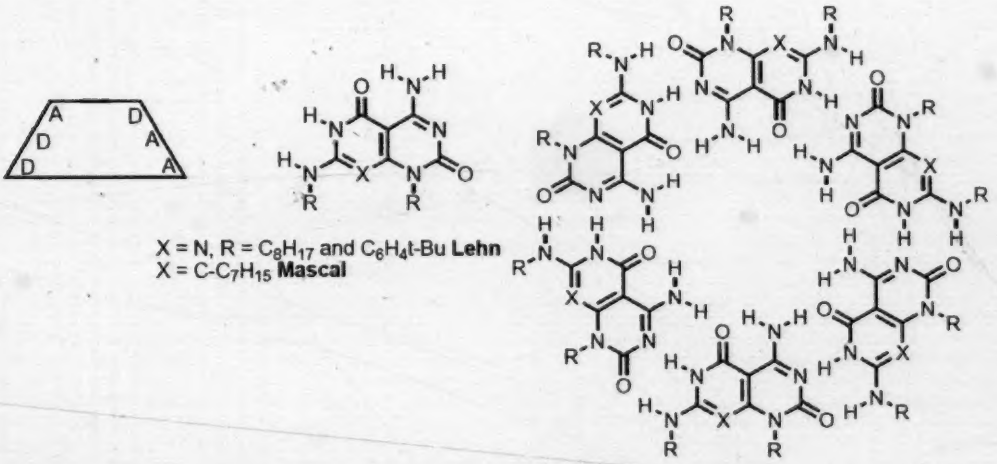

Figure 1. 21. The directed self-assembly of rosettes using a DDA·AAD array

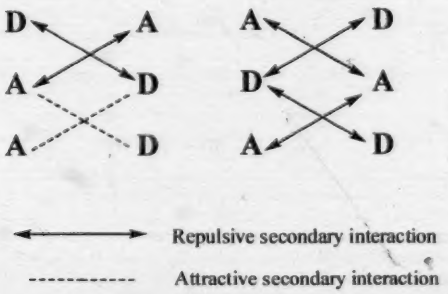

Figure 1. 22. Secondary interactions in DAA-ADD and ADA-DAD hydrogen-bonded arrays.

(E) Other approaches to rosette stabilization

In some cases, rosettes were found to be dominant species while none of the factors (A – D) were apparently contributing.[53-55] Zimmerman[53] explained this fact for his

pyrido[4,3-g]-quinoline rosette based on simple thermodynamic considerations. Compound **1**, a pyrido[4,3-g]-quinoline that was designed to form cyclic trimer $\mathbf{1}_3$ or linear aggregates (e.g., $\mathbf{1}_n$) of any length, including dimers (Figure 1.23). According to Zimmerman even though $\mathbf{1}_3$ and $\mathbf{1}_n$ contain similar contacts, $\mathbf{1}_3$ should be of greater stability because it contains two hydrogen bonds per molecule of **1**, while $\mathbf{1}_n$ contains only $(2n + 2)/(n + 2)$ hydrogen bonds per **1**. Zimmerman's explanation seems to be reasonable, however it should work only for small n, which should be more important during the early stages of self-assembly. If a cyclic aggregate contains n subunits, its advantage over the analogous linear aggregate will vanish as n becomes large. Therefore it's unclear how valid the explanation is for $n = 6$ and 12.[54]

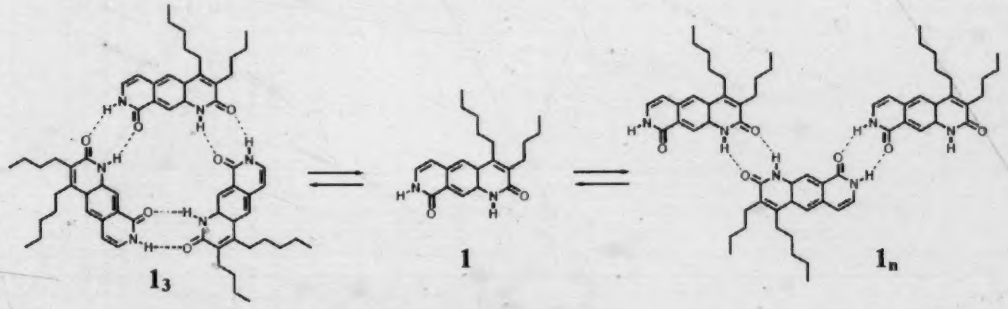

Figure 1. 23. Zimmerman's pyrido[4,3-g]-quinoline system.[53]

(2) Stacking stabilization approaches

(A) Metal coordination for stacking stabilization

A metal cation in a G-quadruplex is responsible for stabilizing not only the rosette, but also the stack. It was shown[56] by single crystal X-ray analysis that each potassium ion in quadruplex $\mathbf{2}_{16}$ has four closest contacts with eight oxygen atoms of two adjacent stacks (Figure 1.24). Since there are no G-quartet stacks known that exist without a cation

or covalent link between the stacks (see next section), just the π–π stacking interaction alone might not be enough to maintain the columnar stack. Metal ions are thus essential for both the rosette's and the stack's stabilization.

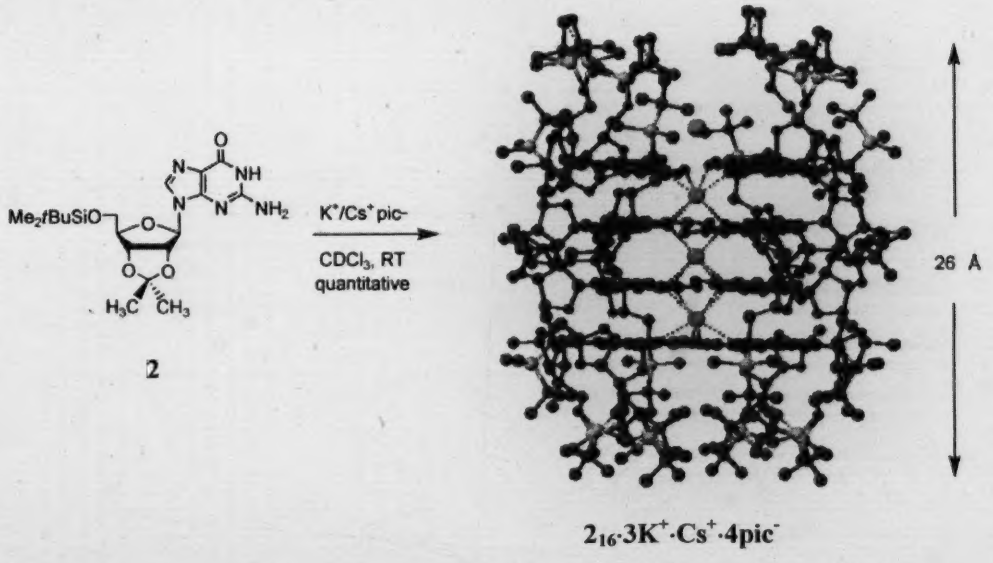

2

$2_{16}{\cdot}3K^{+}{\cdot}Cs^{+}{\cdot}4pic^{-}$

Figure 1. 24. The cation-templated self-assembly of 16 equivalents of 5-silyl-2,3-O-isopropylidene guanosine (2) gives a lipophilic G-quadruplex $|2|_{16}3K^{+}/Cs^{+}4pic^{-}$ in the solid state and in solution. This G-quadruplex, with four stacked G-quartets, is prepared quantitatively by extracting salts from water with a solution of 2 in $CHCl_3$. Adapted with permission from ref 42. Copyright 2004 Wiley Interscience.

(B) Covalent linking of rosettes for stacking stabilization

Covalent linking of two or more modules to stabilize stacking was suggested by Whitesides[57, 58] and Reinhoudt[59] for BA–M system (Figure 1.25). Certain rosettes do not stack at all unless linked. For example, linked aminapyrazole rosette stacks were reported recently,[60] while aminapyrazole itself does not stack,[61] even in the solid state, probably due to low energy of π–π stacking interactions for such a small heterocycle.

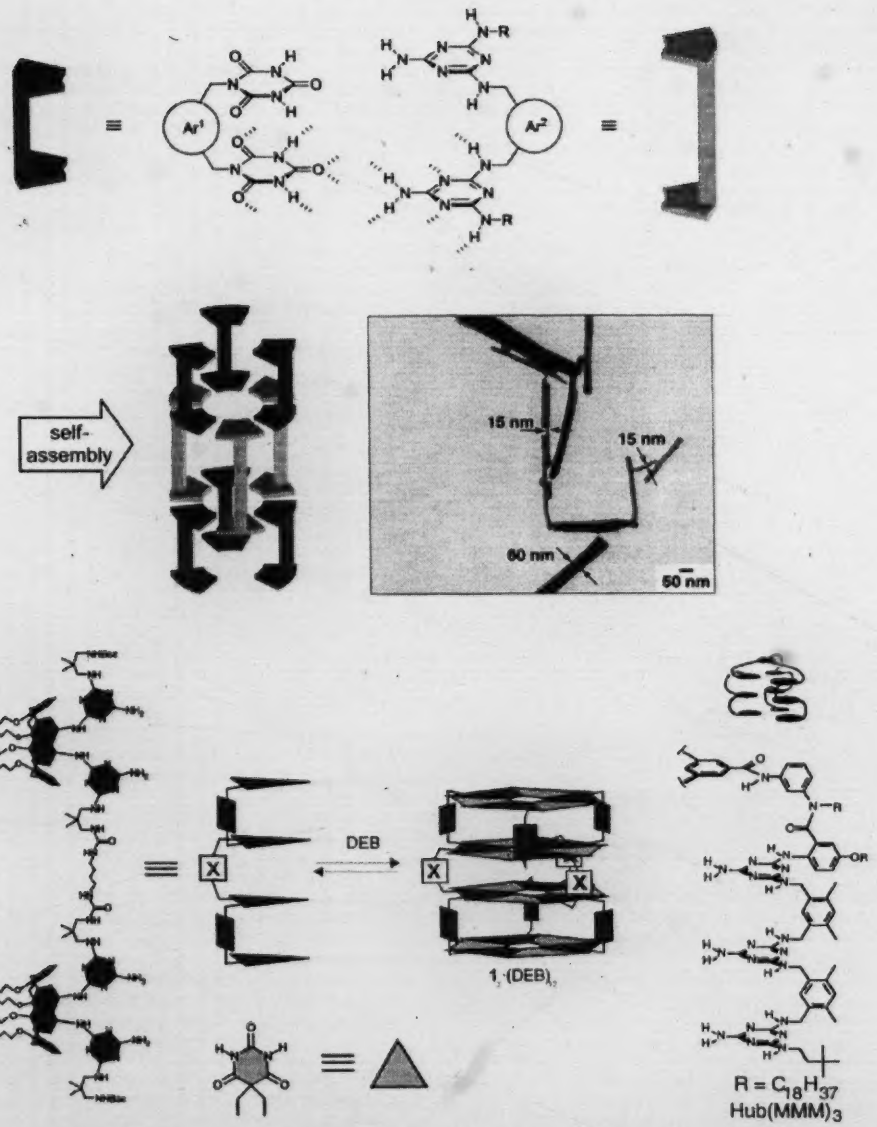

Figure 1. 25. Whitesides' and Reinhoudt's approaches to stacked rosettes based on the melaminecyanuric acid cyclic H-bonding array. Tong-shaped building blocks Ar1 and Ar2 co-assemble into cage-like substructures forming tubular stacks (Ar^1, Ar^2=benzene, furane, naphthalene, calix[4]arene). TEM image of bundled aggregates formed from tubular assemblies. Bottom: examples of Reinhoudt's and Whitesides' molecules. Reproduced with permission from ref 57. Copyright 1995 American Chemical Society.

(C) Stacking stabilization by using polar solvents

Our research group has shown that stacking of rosettes assembled from self-complementary guanine-cytosine (G^C) can be enhanced by using highly polar solvents like water and methanol.[62-67] In polar solvent, essentially solvophobic stacking between rosettes becomes more favorable compared to nonpolar solvents. Development of a versatile functionalization approach has allowed attachment of diverse functionalities to G^C that are expressed on the outer-tube surface after self-assembly (Figure 1.26). The G^C based RNTs have shown promise as functional materials, with a growing number of applications from chiroptical materials to bone implant coatings. Dynamic light scattering (DLS), transmission electron microscopy (TEM), scanning electron microscopy (SEM), atomic force microscopy (AFM), nuclear magnetic resonance (NMR), electron spectroscopy (UV-vis), circular dichroism (CD), and high resolution mass-spectroscopy (MS), and computer modeling were used to study their assembly.[62-67]

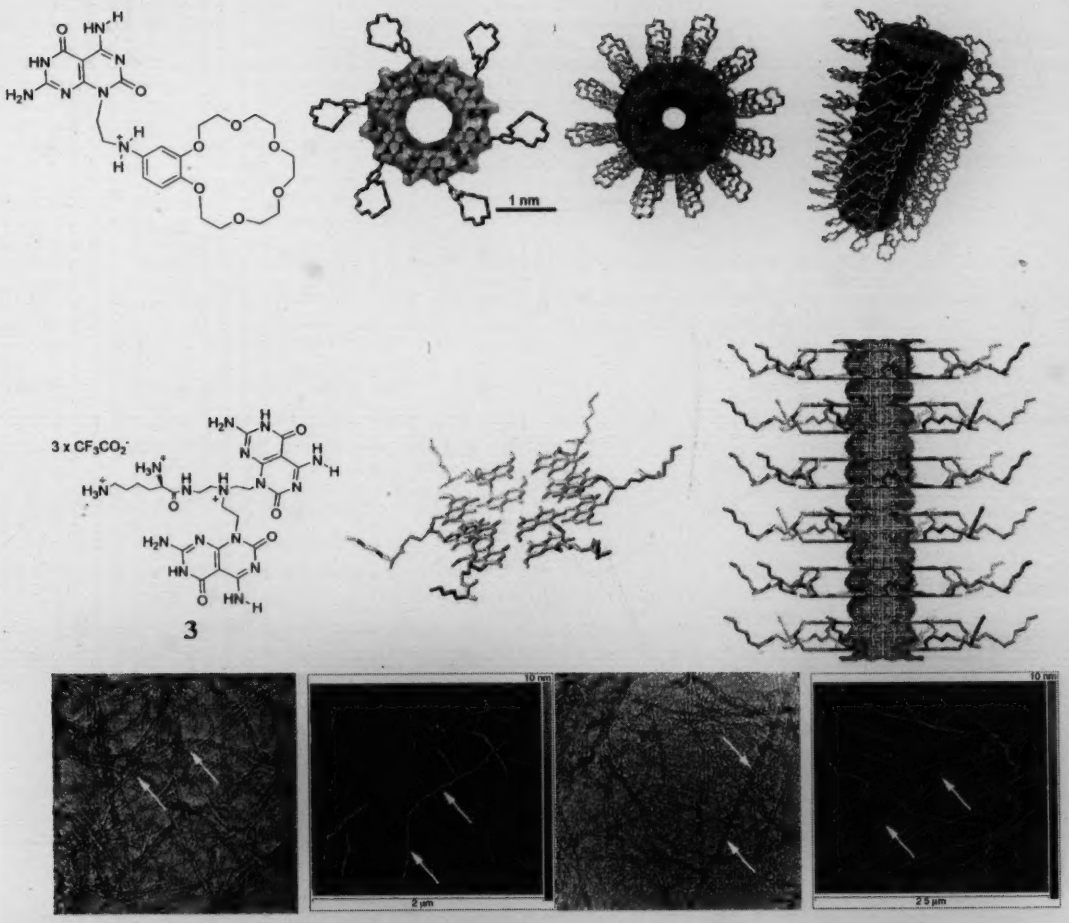

Figure 1. 26. Fenniri's multichannel RNTs with crown ether function (top) and amino acid containing "double decker" with a covalent link between two G^Cs for improved stability. Stained TEM (A, C) on carbon film and TM–AFM images on mica of compound 3 assembled in water. Reproduced with permission from refs 62 and 64. Copyright 2002 and 2005 American Chemical Society.

1.5. Nanotubes assembled from DNA tiles

Nucleic acids provide a unique paradigm for constructing molecular devices.[68] They support a diversity of structural and functional motifs governed by predictable properties of the double helix, such as base pairing, stacking, and energetics. These properties allow the design of DNA complexes analogous to the abstract tiles of mathematical tilings. Such DNA tiles can be programmed to self-assemble into a variety of two-dimensional (2D) arrays. Some early designs of 2D arrays accidentally formed tubes.[69] Since then several general approaches to design tiles that reliably form nanotubes have been developed.[11, 69, 70] A typical design for a DNA nanotube is shown below (Figure 1.27). DNA assembly offers unprecedented versatility for programmable design of functional nanotube architectures. Inner and outer surfaces of a nanotube can be functionalized with desired functionality placed exactly where it is needed. DNA nanotubes represent a potential breakthrough in the self-assembly of nanometer-scale circuits for electronics because they can be targeted to connect at specific locations on larger-scale structures and can subsequently be metallized to form nanometer scale wires.[71] Other potential uses of DNA nanotubes are inspired by analogy with the roles of nanotubes and nanofilaments in living cells: as structural supports for the cytoskeleton (e.g., actin filaments), as tracks for the transport of microscopic cargo (e.g., microtubules conveying vesicles), and as moving parts for cellular motility (e.g., flagella). DNA nanotubes may eventually be engineered to mimic all of these functions.

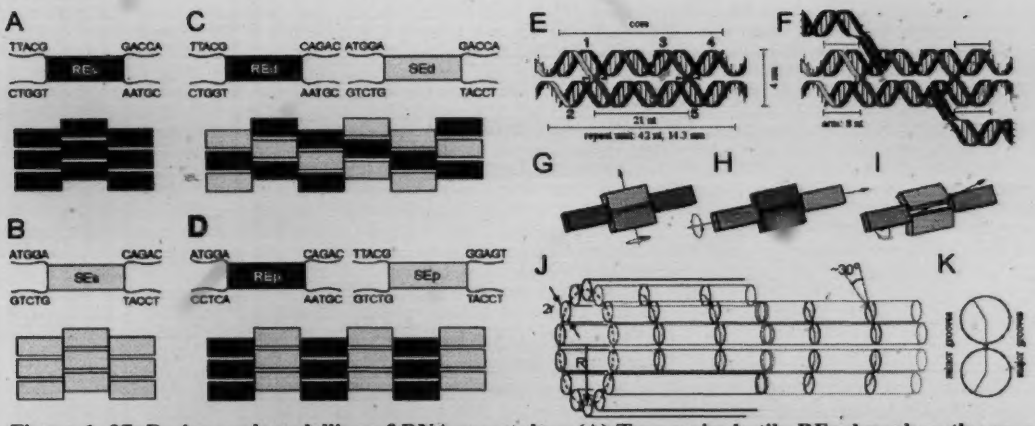

Figure 1. 27. Design and modelling of DNA nanotubes. (A) Top: a single tile REs, based on the core RE, bears 4 sticky ends. Bottom: Complementarity between sticky ends directs the tiles to form a regular lattice. (B) A single tile SEs, based on a difference core SE, and its lattice. (C) Two tiles, REd and SEd, can assemble into a lattice with diagonal stripes; alone each tile could assemble into a linear strip. (D) Another pair of tiles, REp and SEp, cannot assemble independently but together can form a lattice with stripes perpendicular to the long axis of the tiles. (E) Structure of a DAE-E molecule. Each tile is assembled from five single strands: two of 37 nucleotides (nt) (top and bottom, no. 1 and no. 5), two of 26 nt (left and right, no. 2 and no. 4) and one of 42 nt (central, no. 3). Triangles mark two crossover points, separated by two helical turns (21 nt). Arrowheads point from 5' to 3'. Sticky ends (5 nt) are at the ends of the no. 2 and no. 4 strands. (F) Tile structure with hairpins (8 nt stem, 4 nt loop) on the no. 1 and no. 5 strands between the 14th and 15th nt from their 5' ends. Molecular models suggest that these hairpins attach underneath the molecule, as depicted here; in a tube they would be on the outside. (G and H) Two in-plane rotational symmetries that, if satisfied by a patch of tiles, encourage molecular strain to balance, resulting in a flat sheet. (I) A rotational symmetry, satisfied by DAE-E molecules, that permits curvature. (J) Heptagonal tube of radius R. In each tile, two cylinders of radius r represent the double-helices. Black circles mark crossover points defines the minor groove. Tiles from (A), (B), or (D) may form tubes of any number of tiles in circumference; tiles from (C) only tubes of an even number. (K) Cross-section of the tile from (J) at a crossover point. Reproduced with permission from ref 10. Copyright 2004 American Chemical Society.

1.6. Comparison of different classes of nanotubes

The five classes of organic nanotubes reviewed – nanotubes assembled from amphiphiles, from linear molecules via helical folding, from macrocycles, from hydrogen bonded rosettes, and from DNA tiles – cover most of the known strategies of artificial tubular assembly (Figure 1.28). Biological assembly of microtubules follows helical folding of 1D array of tubulin[72] and similar organizations have been proposed for some of the hydrogen bonded structures; however, no experimental evidence supporting the

proposed structure was provided for the latter.[54, 55] There are also "barrel" approaches[73] to nanotubular assembly mimicking naturally occurring protein based ion channels and Fujita's metal coordination approach;[74] however, they lack generality and are limited to a few examples.

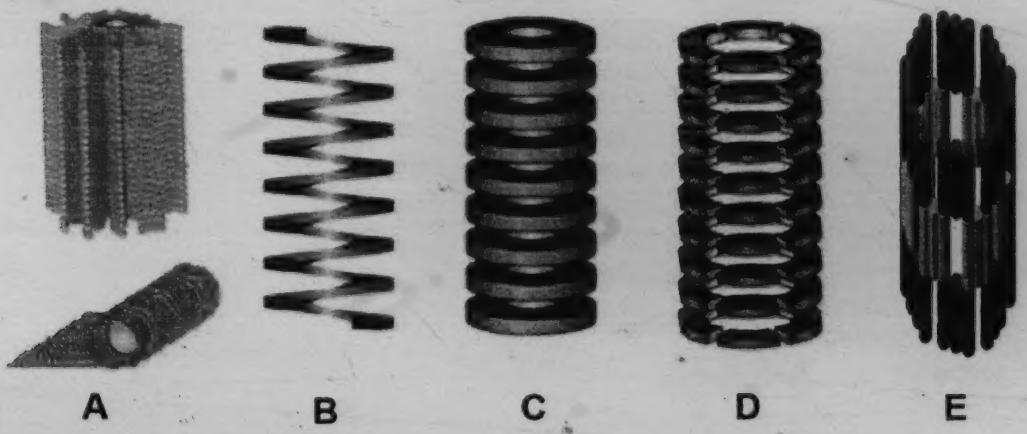

Figure 1. 28. Approaches to tubular assembly: A) lipid nanotubes, B) nanotubes assembled from linear molecules via helical folding, C) nanotubes assembled from macrocycles, D) nanotubes assembled from hydrogen bonded rosettes, E) nanotubes assembled from DNA tiles. Adapted with permission from ref 13. Copyright 2005 American Chemical Society.

As shown in Figure 1.28 major classes of nanotubes LNT can be seen as rolled sheets of lipid bilayers (A), helical folding of a linear molecule affords nanotubes (B), stacking of macrocycles results in nanotubes (C), such stacking following the macrocycles assembly via hydrogen bonding leads to nanotubes (D), and programmed DNA tile assembly yields the most sophisticated DNA nanotubes (E). This classification, however, does not reflect the mechanism of the respective nanotubes assembly. For instance, the assembly of LNTs can proceed through various complex architectures such as vesicles and helical ribbons before evolving into the nanotube.

To understand the potential of these alternative approaches to nanotube construction it is useful to compare their synthetic accessibility, functionalization versatility, dimensions, and the possibility of integration into functional devices.

LNTs (A) are by far the cheapest nanotubes. Most of the surfactants used for LNT assembly can be synthesized in one step or even obtained as byproducts from natural sources.[75, 76] However, the critical association concentrations necessary to achieve self-assembly of LNTs are generally higher than the ones for others tubes. Solid-phase methods for oligophenylacetylene and oligopeptide synthesis have been developed making some of the helically folded nanotubes (B) readily available. Nanotubes (C) and (D) can be quite affordable. Even though they could expensive, DNA tiles can be prepared using automatic DNA synthesizers with less human effort than that required for preparation of nanotubes (C) and (D).

The self-assembly outcome of an amphiphile is very dependent on its structure. Often even minor changes in the amphiphile structure can result in the destabilization of tubular morphology and the domination of other assemblies e.g. spherical vesicles.[77] Dimensions of the tubes (A) – inner diameter, thickness of the wall, and length – are also highly dependent on the amphiphile structure. Even though LNTs with wide range of dimensions can be prepared (e.g. thickness can be varied from 10 to 100 nm), the fine tuning of their dimensions and surface chemistry has not been achieved.

The nanotubes obtained by helical folding (B) can be obtained with a limited selection of inner pore sizes (normally under 1.0 nm), but with a more tuneable wall thickness. Chemistry of the pore therefore cannot be varied significantly, but the tubes' outside surface can be appended with a wide range of functional groups. The length can

be controlled if the length of the linear precursor can be controlled (which is usually the case in olygopeptides automated synthesis). Solvent selection is also limited mostly to polar ones, since the assembly is mainly driven by hydrophobic interactions.

The inner channel diameter and wall thickness for tubes (C) and (D) can be fine-tuned by the macrocycle design (C) and size and/or number of modules that assemble into the hydrogen bonded rosette (D). That is normally achieved synthetically. The inner and outer surface chemistry as well as functional group density can be manipulated with high precision as well. However functional groups cannot be placed in defined spots on the pattern, like, for example, decorations on the Christmas tree. Using the latter analogy, placing a candy on one branch will result in each branch of the tree having exactly the same candy. At this stage there is no way to control the length of (C) and (D). The average length can to a very limited degree be controlled kinetically by limiting the assembly time (e.g. by casting on substrate and removing the solvent) or thermodynamically (e.g. by varying the assembly temperature and thus varying contribution of entropy component of the assembly process).[78] In both of these cases, polydispersed nanotube populations are obtained. When the stacking interactions are too weak to maintain tube growth, the length can be controlled by varying the length of the covalent linker and the number of modules attached to the linker.[57]

Nanotubes constructed from DNA tiles (E) are probably the most versatile NTs when it comes to control of dimensions and surface chemistry. Here, functional groups can very often be placed at pre-defined locations in the inner and outer surfaces. The nanotubes can also be designed to branch out. DNA nanotubes also have the highest potential to be integrated into functional devices.

1.7. Conclusion, outlook and statement of goals:

RNTs challenges and possible solutions

Significant progress in the area of organic nanotubes in last decade has been possible due to the highly developed toolkit available for covalent synthesis and recent advances in non-covalent synthesis (self-assembly). Advances in the synthesis of oligomers and polymers with controlled lengths and sequences, including those on the solid support and on automated synthesizers, have allowed for structure – activity relationships to be established, as well as molecular level design principles essential for successful supramolecular tubular construction, in particular for block copolymers and olygopetide nanotubes, to be understood. On the other hand, supramolecular science has evolved and grasped a much deeper understanding of the fundamental principles of self-assembly. The advent of dynamic covalent chemistry and combining them with combinatorial methodology exemplifies perhaps the most powerful recent development. Last but not least, the development of sophisticated analytical tools, most notably scanning probe techniques, electron microscopies, and nuclear magnetic resonance, has had a significant impact on the field.

However, past accomplishments do not completely solve the many problems that exist in the field of supramolecular organic nanotubes. Solving these problems is necessary to construct functional materials based on rosette nanotubes. The work presented in this thesis is focused on three specific challenges. These challenges and their possible solution are introduced below:

1) Achieving understanding of RNTs structure

2) Assembly of large hierarchical structures from RNTs

3) Making RNTs conductive

1) Achieving understanding of RNTs structure

A thorough understanding of the RNTs structure is essential for developing the structure – activity/function relationship necessary to construct functional materials based on RNTs. It is also important to understand the factors that contribute to RNT stability. In spite of the fact that RNTs are probably the most well studied organic nanotubes, many questions about their structure remain unanswered: (a) the exact structure of the G^C base in RNTs is not known, (b) exact orientation of rosettes and interrosette distances are not known, (c) the mechanism of nanotube formation is not fully understood, and (d) the rate of assembly and disassembly are not known. Some insights have been obtained using computer modeling, however direct experimental proofs are needed. These can be obtained using X-ray diffraction, solid state and dynamic liquid phase Nuclear Magnetic Resonance techniques, ultra-high resolution Transmission Electron Microscopy (TEM) and TEM based holography, and Scanning Tunneling Microscopy. In this work, a combination of solution NMR, solid state NMR, electron microscopy and X-ray diffraction has been used to answer these questions. NMR is a useful technique in that it can provide intermolecular NOE correlations necessary to elucidate hydrogen bonding in the rosette. Electron microscopy and X-ray diffraction provide nanoscale dimension that can be related to the molecular model of rosette nanotubes. This work is presented in chapter 2.

2) Assembly of large hierarchical structures from RNTs

Assembly of mesoscale (100 nm – 100 μm) structures from nanotubes is necessary to bridge the gap between nano- and macro-scale worlds. Nano-scale features will be thus combined with better processability of mesostructures. To assemble nanotubes into meso-scale architectures, organization of nanotubes into more complex highly hierarchical structures should be studied. Almost all of the published reports on nanotubes investigate the assembly of the molecules *into* nanotubes. In this work, assembly structures *from* nanotubes has been studied. A great challenge here is developing a way to create nano- and meso-scale structures with a variety of shapes from the same building block. Assembly of the rosette nanotubes relies on weak interactions and therefore greatly depends on the properties of the medium in which assembly is carried out. The strength of the interactions between nanotubes is expected to depend on the chemical functionality expressed on the outside walls and the nature of the solvent. So far, only RNTs with polar substituents soluble in water and methanol have been synthesized.[62-64, 67, 78] In the current work rosette nanotubes with a number of hydrophobic substituents have been synthesized. Hydrophobic substituents are expected to make RNTs soluble in solvents with low polarity, thereby allowing for the intertubular interactions in the assembly of RNT-based mesoscale architectures to be fine-tuned depending on the particular organic solvent chosen. In addition the effect of temperature and assembly time on the morphology has been studied. HRSEM was chosen as a morphology screening tool, due to its simplicity and speed in generating high quality topographical information. Detailed insight into molecular organization of nanotubes in the aggregates has been obtained using high resolution TEM and AFM which provided qualitative information on

nanostructure dimensions with subnanometer resolution. This work is described in Chapter 3.

3) Making RNTs conductive

The miniaturization of electronic devices driven by recent advances in nanotechnology demands increasingly smaller nanostructures that are capable of electron transport. A number of high aspect ratio conductive nanostructures have been prepared,[79] but smaller and more reliable nanowires with various electrical properties are required. Several ways to prepare RNT-based nanowires are suggested below.

a) Making RNTs conductive via exploiting their *core electron transfer capabilities*. It is well know that guanine in DNA can be a transporter for electron holes.[80] To generate a hole in a G^C module, an electron has to be removed by an oxidizing agent. Therefore the electrochemical nature of individual G^C bases and their assemblies has to be studied in detail. However, making a conductive RNT is not enough. It has to be integrated into conductive circuits in order to be studied. One way to assemble a conductive circuit is by covalently linking a single G^C module to the tip of a CNT and then constructing a RNT in a gap between two functionalized CNTs. CNTs, in turn, can be integrated into a circuit easily. A similar approach was recently demonstrated for measuring DNA conductivity.[81]

b) Making RNTs conductive via *attachment of organic groups that can be converted into nanowires*. This can be achieved by appending a diacetylene group to the G^C followed by its polymerization into conjugated wire after self-assembly.[82] An

aniline moiety can also be attached and polymerized to form conductive polyaniline wires.

c) Making RNTs conductive via *deposition of conductive inorganic substance*. This can be achieved by appending functional groups to RNTs that have affinity for metal ions and then reducing the metal ions. Most literature reports that use one dimensional organic nanostructures as a template assembly of metallic nanowires are carried out in two steps: a) addition of metal ions that adhere to the organic nanostructure and b) addition of the reducing agent to reduce metal ions adsorbed on the template. The performance of the nanowires obtained in this approach is often very poor, because metal nanoparticle arrays are not continuous, and the minimum thickness of these nanowires is rarely less than 100 nm.[83-85] In the current work, an improved strategy for RNT templated nanowire fabrication has been investigated. Attachment of a functional group that has both affinity for metal ions and ability to reduce them eliminates the necessity to add an external reducing agent. This is expected to create smother and smaller nanowires. G^C modules with formyl function have been synthesized and assembled into nanotubes. Silver ions then have been absorbed and reduced on the outside walls of the RNTs to create a continuous array of the silver nanoparticles. This work is described in Chapter 4.

A number of other important challenges in RNT field are currently under investigations in our research group, including: developing universal strategies to control the dimensions and chemistry of RNTs, improving RNT's mechanical strength, RNT placement control, and making stimuli responsive RNTs. Due to the importance and breadth of this field, I was attracted to the three diverse challenges discussed above. I decided to tackle these challenges in this thesis work in order to achieve a better

understanding of RNTs structure (Chapter 2), assembly of large hierarchical structures from RNTs (Chapter 3), and the synthesis of conductive RNTs (Chapter 4).

2. NMR Studies of G^C Module Assemblies

2.1. Objectives

An in depth understanding of the RNTs structure at the atomic level is essential for the rational design and construction of RNT-based functional materials. It is also important to understand the factors that contribute to RNT stability. In spite of the fact that RNTs have been quite extensively studied by NMR and electron and atomic force microscopies for almost a decade,[50, 62-64, 67, 78] many questions about their structure remain unanswered. For instance, the exact structure of the G^C base within RNTs is still unknown, and there is no direct experimental proof for the existence of the rosette structure proposed by Lehn[50] (Figure 1.21). Since numerous attempts to grow crystals suitable for single crystal X-ray diffraction have not been successful, NMR appears to be the best tool for the characterization of the RNTs' 3D structure. The objective of the work reported in this chapter is to elucidate the atomic structure of RNTs in solution and in the solid state. A number of 1D NMR (^{1}H, ^{13}C, ^{15}N, difference NOE), 2D NMR (COSY, HMQC, HMBC, ^{1}H–^{15}N J_1 HSQC, ^{1}H–^{15}N J_n HMQC, ^{1}H–^{15}N HMBC, NOESY, tROESY, HNN COSY, DOSY), and solid state NMR (^{1}H, ^{13}C and ^{15}N MAS, 2D ^{15}N-^{15}N DQ, ^{1}H-^{15}N CP-HETCOR, ^{15}N-^{15}N refocused INADEQUATE) experiments at different field strengths (200 – 900 MHz) were used to characterize assemblies formed from protonated and deprotonated G^C modules.

2.2. Overview of NMR studies in G^C system

Increased interest in supramolecular materials and recent advances in NMR spectroscopy (new pulse sequences for dynamic experiments, multinuclei NMR, high

field instruments, new solid state NMR approaches) have resulted in a substantial increase in the power of NMR as a reliable tool for structural analysis of complex self-assembling systems. NMR has been successfully used to study self-assembling oligomers and polymers.[86-88] There are three important pieces of information that can be obtained from solution NMR techniques: a) the structure of the self-assembling modules, b) the structure of supramolecular assembly, c) thermodynamic and kinetic parameters of the assembly process. In general, depending on the nature of the assembly, only a part of this information can be obtained.

Incorporation of guanine and cytosine nucleobases with complementary acceptor–acceptor–donor (AAD) and donor–donor–acceptor (DDA) hydrogen bonding patterns into a single molecule (G^C) was first reported by Lehn[50] and Mascal[51] and was found to assemble into hexameric rosette structures. Only ^{1}H NMR resonances in chloroform were provided, and variable temperature ^{1}H NMR in toluene was mentioned in the papers. Although the molecular weight was estimated by vapour pressure osmometry and gel permeation chromatography indicating G^C hexamer formation, it is not clear if the individual modules, rosettes or tubes were observed by NMR.

A G^C analog was reported by Mascal and coworkers.[51, 89] They were able to obtain crystals suitable for synchrotron single crystal X-ray diffraction analysis and solved the structure. Crystals grown from DMSO showed the presence of hexameric rosettes. This is the best-known experimental evidence of rosette formation by a G^C derivative. Only 1D ^{1}H and ^{13}C NMR were reported for this compound. Attempts to crystallize G^C modules synthesized by our group have been unsuccessful. Formation of nanotubes with high polydispersity is probably the major obstacle for crystallization.

Mascal's success in growing the crystals is possibly due to relatively weak π–π stacking for his G^C analog thus preventing nanotube formation in DMSO.

2.3. Solution NMR studies

The structure of G^C heterobicycle for a series of water-soluble derivatives (e.g., **2-1**) was previously proposed to be as shown in Figure 2.1 partially based on NMR experiments.[62, 63, 78]

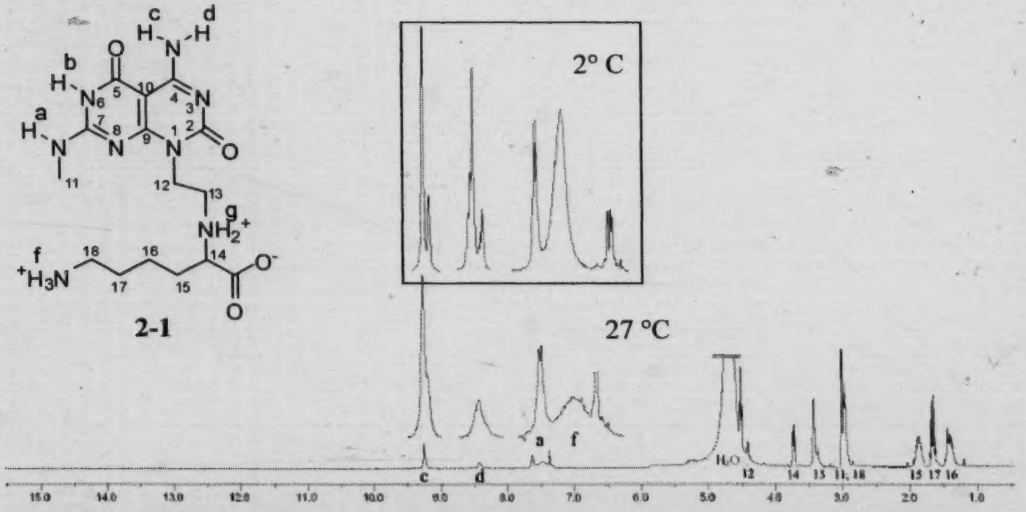

Figure 2. 1. ^{1}H NMR spectrum of 2-1 (previously proposed structure) using water saturation pulse sequence in 10% D_2O–H_2O at 27 °C (500 MHz). The appearance of the satellites for NH signals upon cooling to 2 °C. H(g) is said to be obscured by water peak.

The ^{1}H NMR spectrum recorded at room temperature in water was missing some expected signals at lower fields (e.g. H*b*). It should also be noted that integral values for the exchangeable protons H*c* and H*d* are lower than expected. This was thought to be due to fast exchange with the solvent (H_2O).

When a COSY experiment was performed in water, no correlation between H*c* and H*d* was observed. This is most likely due to fast exchange of NH protons in water at

room temperature, which should be slower in aprotic solvent at lower temperatures. It is expected that H*c* and H*d* will have different chemical shifts since the rotation of NH_2 group should be slow on NMR time scale due to an intramolecular hydrogen bond between carbonyl and H*c*, as well as the conjugation of the nitrogen lone pair with the G^C module π electrons. The difference in integral values measured from the spectrum recorded in water arises from the different exchange rates with the solvent. H(d), which is not intramolecularly bonded, exchanges much faster than H(c). Using a water presaturation pulse sequence or D_2O as a co-solvent reduces integral values even more. To slow down H exchange with the solvent, the spectrum of **2-1** was recorded in DMF (aprotic) at – 60 °C (Figure 2.2).

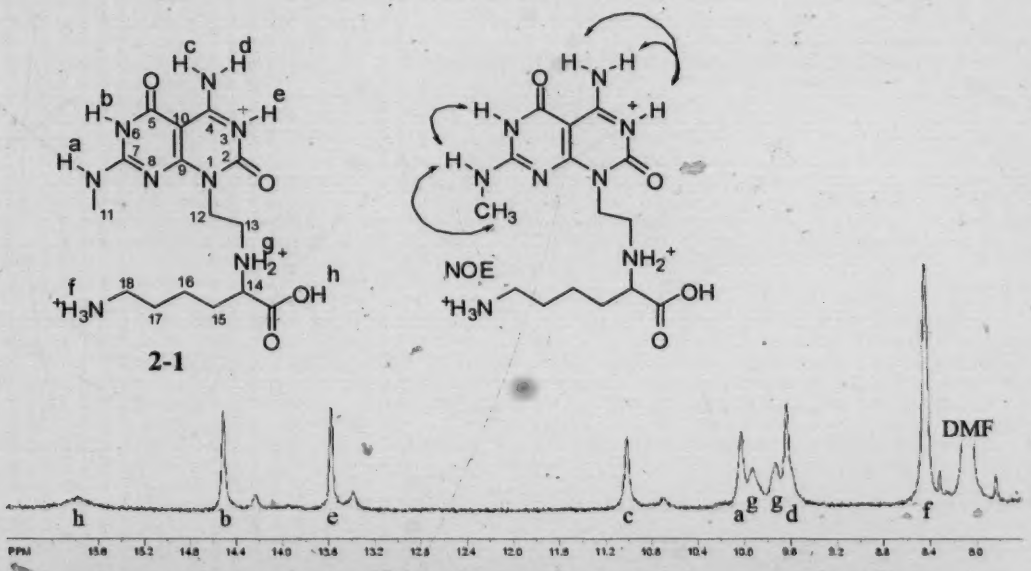

2-1

Figure 2. 2. The low field part of ^{1}H NMR spectrum of 2-1 in DMF-d_7 at -60 °C. Major correlations observed in series of 1D difference NOE experiments in the same conditions are also shown. Assignments are made also based on HMBC, NOE and COSY experiments (see experimental part for details). Two H*g* signals are due to one of Hgs bonding to adjacent carbonyl of cytosine.

Recording the NMR spectrum in DMF revealed three additional resonances at low field that were not observed in water. A different structure consistent with a number

of NMR experiments was proposed (Figure 2.2). Signals at *c* and *d* showed correlation in the COSY spectrum in DMF at -60°C, indicating that they are part of the NH_2 group rather than *b* and *d* respectively as was reported before.[63, 64, 67, 78]

It is expected that all basic sites would be protonated at the pH at which the spectra were recorded in water (pH = 2.4), since trifluoroacetic acid was used in the final deprotection step leading to compound **2-1**. The structure most consistent with NMR experiments is shown on Figure 2.2. and is based in part on a series of 1D NOE experiments at –60 °C. Assignments were also corroborated by COSY, NOESY and HMBC experiments (see spectra in experimental sections). Elemental analysis was consistent with three molecules of an acid bound to each molecule of **2-1** and is therefore in agreement with the number of proton signals observed by ^{1}H NMR.

Satellite signals were observed for a number of G^C derivatives, but they were difficult to distinguish at room temperature and on instruments with field strength less then 11.7 Tesla (500 MHz). Overlapping of broadened major and minor signals because of exchange with solvent was the main difficulty. To investigate the nature of the species that give rise to the major and minor peaks, model compound **2-2** (Figure 2.3) was synthesized, and extensively studied in several solvents. It was found that each proton has a minor satellite signal and their ratio was constant for all of the protons in a given solvent. ^{13}C NMR revealed the presence of satellites for every carbon resonance as well, with the same major/minor ratio obtained from ^{1}H NMR. These results indicate that there are two species giving rise to two sets of signals. In agreement with these observations, the ratio of major/minor was found to generally decrease as polarity increased (Table 2.1).

Table 2.1. Ratio major/minor* found from the integration of well resolved proton signals of major and minor species. The ratio for water soluble G^C derivative is given for a water soluble G^C derivative, since 2-2 is practically insoluble in water.

Solvent system	major/minor
DMSO-$CDCl_3$ 1:3	12.9
DMSO-CD_3CN 1:1	9.4
DMSO-DMF 1:1	7.8
DMF	7.2
DMSO-CD_3NO_2 1:1	6.5
DMSO-$CDCl_3$ 1:1	6.2
MeOH	4.8
DMSO	4.2
DMSO-H_2O 5:2	3.8
H_2O[78]	3.0

* major/minor ratio was obtained as a ratio of integral values of major and minor peaks

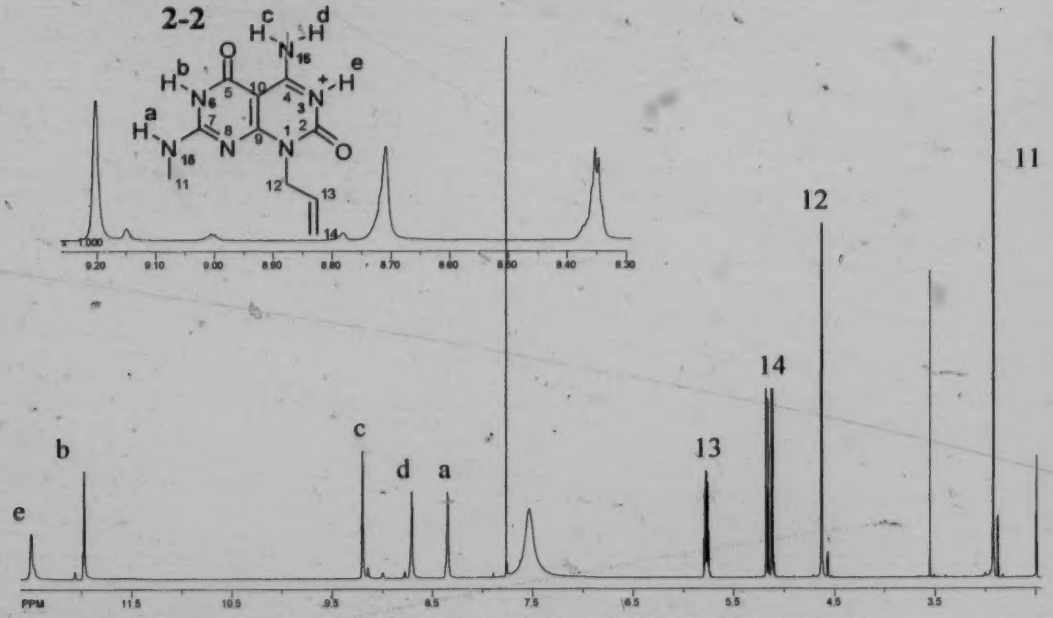

Figure 2. 3. ^{1}H NMR spectrum of 2-2 in 3:1 (v/v) $CDCl_3$–DMSO-d_6 at 5 °C (800 MHz).

There could be several reasons for the satellite peak's presence: (A) impurities, (B) proton transfer equilibria, (C) G^C oligomer formation, (D) side chain rotamers, and (E) tautomerism. The following discusses each possibility:

(A) Impurities cannot be the source of the minor set of signals, since **2-2** was found pure by elemental analysis and high resolution mass spectrometry. Also, similar satellite peaks were observed for other G^C bases prepared by different methods. Furthermore, minor and major peak coalescence was observed by ^{1}H NMR spectroscopy above 65 °C with complete restoration of the spectrum upon cooling (Figure 2.4). Also, the same batch of compound gave different major/minor ratio (Table 2.1) when dissolved in different solvents.

(B) According to elemental analysis there is one HCl molecule per molecule of **2-2**. The possibility for the satellite signals originating from protonated and deprotonated species can be ruled out since the number of protons observed by NMR is the same for the major and minor species.

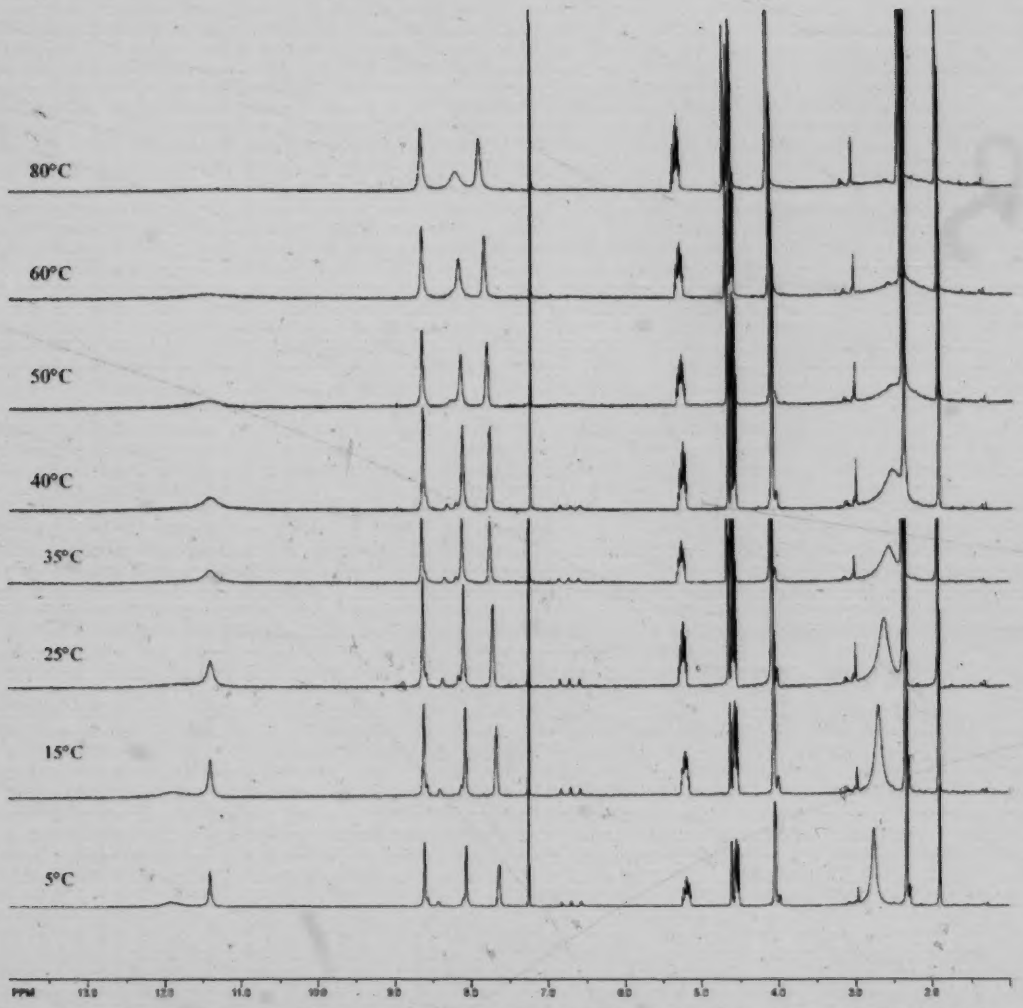

Figure 2. 4. Variable temperature NMR of 2-2 in 1:1 (v/v) $CDCl_3$–DMSO-d_6 at 5 – 80 °C (400 MHz).

(C) To see if the minor peaks arise from dimers or higher order aggregates, a dilution experiment was carried out. The ratio major/minor was found to be independent of the concentration of **2-2** (within experimental error). A DOSY experiment gave the same diffusion coefficient, suggesting similar molecular weight for both sets of signals. Moreover, peak width, expected to be larger for higher order aggregates, was found to be

constant for both major and minor species. Therefore the satellite peaks are not due to different association motifs of the same molecule.

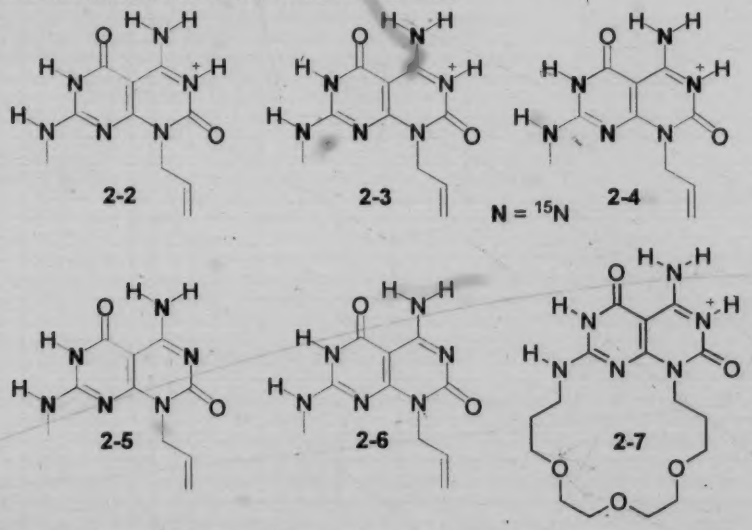

Figure 2. 5. Compounds synthesized for NMR studies. Counter-ion for protonated forms is either Cl^- or CF_3COO^-.

(D) Existence of two side chain rotamers interconverting slowly on the NMR time scale is not consistent with several important observations. Firstly, satellites were found for all protons and carbons of G^C derivatives. Side chain rotation should noticeably affect only the side chain. Secondly, the satellite peaks for the side chains were observed only for H*11*, *12*, and *13* – the closest to G^C – while for the rest of the side chain there was only one set of peaks, indicating that the phenomenon originates in the G^C fragment rather than the side chain. Thirdly, the rotation of the allyl side chain of compound **2-2** is very unlikely to be hindered, yet the satellites for H*12* and H*13* were observed, with the expected greater chemical shift difference for H*12* and C*12*. The 13C and 1H chemical shift difference is practically undistinguishable for *14*. Finally, for compound **2-7** where rotation around C*7*–N*15* bond is locked by the introduction of a linker connecting C*7* and N*1*, the satellite peaks were still observed by ^{1}H NMR.

All of the above mentioned observations indicate that tautomerism is responsible for the satellite peaks. Below is the proposed structure of the major species (T1) based on detailed NMR studies. At this stage the data is insufficient to unambiguously establish the structure of minor species (T2).

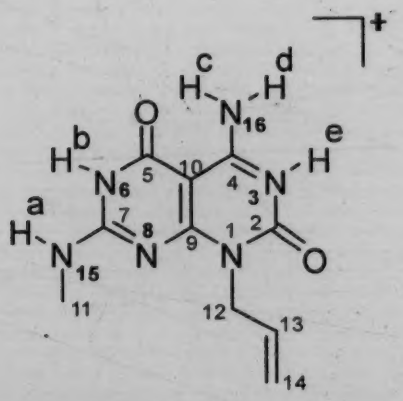

Table 2.2*. Chemical shifts and correlations for two tautomers of 2-4 based on ^{1}H, ^{13}C, ^{15}N NMR, ^{1}H-^{13}C HMQC, ^{1}H-^{13}C HMBC, ^{1}H-^{15}N HSQC, ^{1}H-^{15}N HMQC, *^{1}H-^{15}N gHMBC*, and NOESY (see experimental part for details).

C/N	δ, ppm		Correlation to H(#)		proton	δ, ppm		NOE to H(#)
	T1	T2	T1	T2		T1	T2	T1
C(2)	147.99	147.89	12,13,14, c	12	H(b)	12.07	11.98	a
C(4)	156.51	156.27	c, d		H(c)	9.20	9.15	d, e
N(16)	99.08	98.88	c, d, c, d, *c, d*	c, d, c, d, *c, d*	H(d)	8.71	8.78	c, e
C(5)	161.33	162.48	c	a				
N(8)	180.65	136.64	a, *a*	*a*				
C(7)	155.92	156.62	a, 11	a, 11				
N(15)	92.24	95.46	a, a, 11, e, *11, a*	a, 11, *11*	H(a)	8.35	9.00	11, b
C(11)	28.00	28.56	a, 11	a, 11	H(11)	2.92	2.88	a, b, 12
N(6)	148.32	142.46	b, b, *b, a*	*a*	H(e)	12.50	12.38	c, d
C(9)	160.00	159.32	12,13,14, a, d	12				
C(10)	83.01	82.18	b, c, d, e	c, d				
C(12)	44.72	44.11	13, 14, 12	13, 14, 12	H(12)	4.63	4.57	11, 13, 14
C(13)	132.36	132.20	12, 14, 13	12, 14, 13	H(13)	5.78	5.77	12, 14
C(14)	118.18	117.79	12, 13, 14	12, 13, 14	H(14)	5.14	5.12	12, 13
N(3)	137.31	182.39	e, e					

* Listed for each experiment values were recorded in the solvent and at the temperature where minimum overlapping of the resonances occurs. ^{1}H, ^{1}H-^{13}C HMQC, ^{1}H-^{13}C HMBC, ^{1}H-^{15}N HSQC, ^{1}H-^{15}N HMQC, *^{1}H-^{15}N gHMBC*, and NOESY were recorded in 1:1 (v/v) $CDCl_3$–DMSO-d_6 at – 40 °C. ^{13}C, ^{15}N NMR were recorded in DMSO-d_6 at + 27 °C. NOESY was also recorded in DMF-d_6 at – 60 °C.

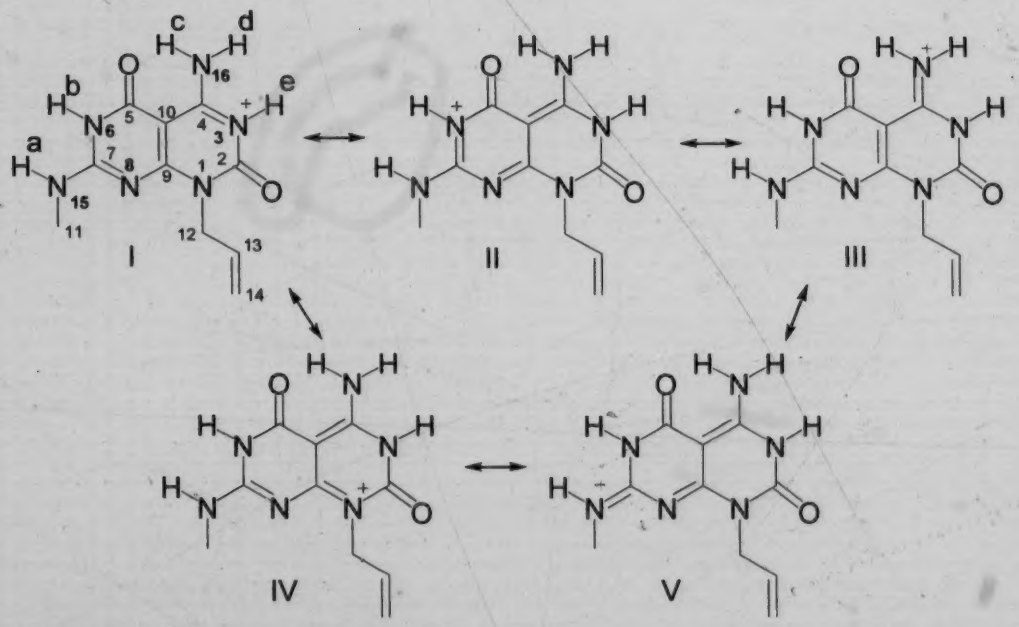

Figure 2. 6. Major resonance structures of 2-2.

Placing a positive charge on N*3* is arbitrary, since the charge in the actual structure is distributed over the conjugated bicyclic system. Resonance structure I is probably the best canonical representation, because H*e* resonates at the lowest field indicating the lowest electron density around it. The difference in chemical shift between H*b* and H*e* is small ~0.5 ppm, indicating that structures I and II contribute almost equally, perhaps with a higher positive charge on H*e*. The latter possibility is supported by the fact that N*3* appears at higher field than N*6* in the ^{15}N NMR spectrum. It should be noted that chemical shift is a tensor and cannot always be correlated with electron density on the corresponding nucleus. N*3* is the most basic ($pK_a \sim 4.5$) nitrogen (pK_a of N*8* is ~ 1.1)[90] so it is expected that **2-2** would be protonated when excess TFA ($pK_a = 0.30$) or HCl (pK_a = -7) is used for protecting group removal in the final synthetic step leading to compound **2-2.**

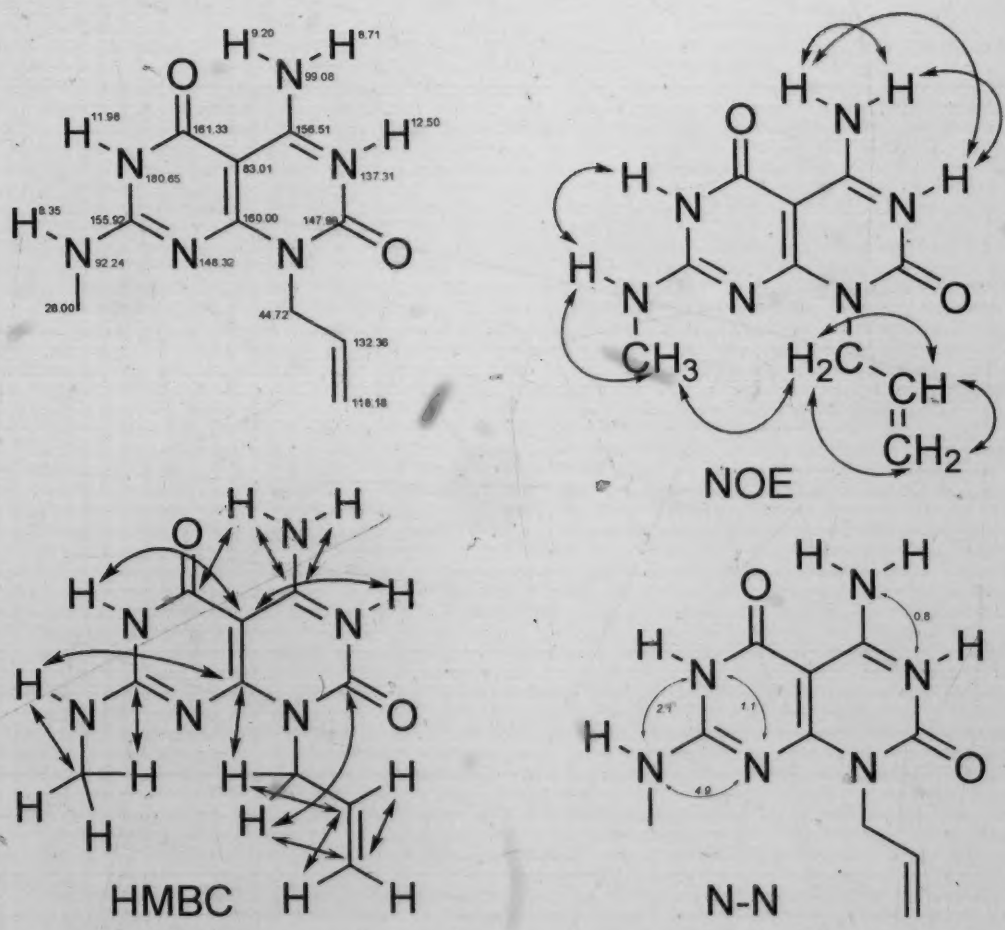

Figure 2. 7. H, C, N resonances assignments and major correlations for 2-4 in NOE, HMBC, and ^{15}N NMR spectra in solution.

It should be noted that it takes a very high number of scans to detect some of ^{1}H-^{13}C multiple bond correlations. HMBC experiment carried out for 52 h (number of collected transients is 112) on an 800MHz instrument was still missing some of the expected correlations for NH protons, probably due to small coupling constants and reduced correlation time caused by exchange with solvent. Several ^{1}H-^{13}C HMBC experiments were run with coupling constant J_{nxh} = 2, 5, 7, 10, 12, 15, 18 Hz to ensure that all the correlations are revealed. To ensure the collection of weak correlations of exchangeable

protons, low temperature experiments were performed. ^{1}H-^{15}N HSQC was carried out for J = 2, 5, 10 Hz. The solvent systems were selected that allow for maximum sharpness of the NH protons. All H–N scalar coupling constants were found to be ~ 90 Hz, which is a typical value. Determination of all C–N coupling constants was impossible due to the complicated splitting patterns.

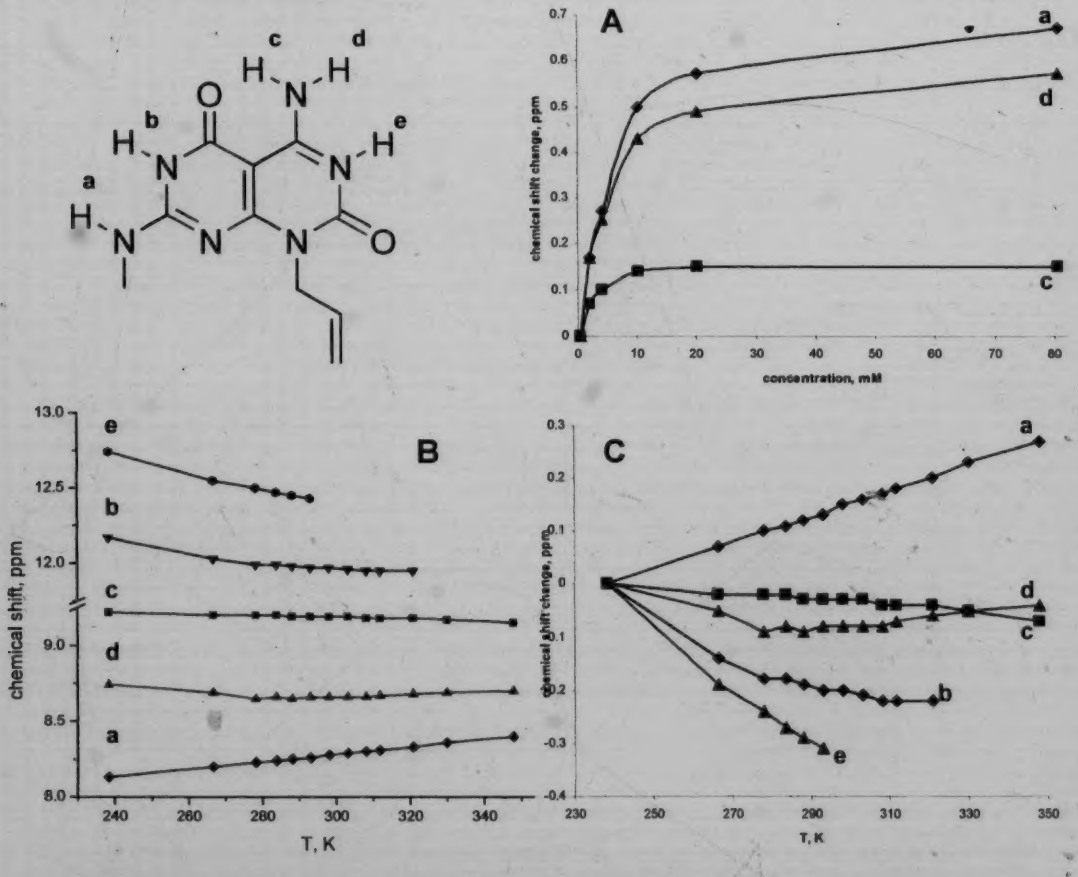

Figure 2. 8. (A) Dilution in DMSO and (B, C) variable temperature (1:1 (v/v) $CDCl_3$–DMSO-d_6) NMR studies summary for 2-2. H*b* and H*c* are not visible in DMSO. Carrying out dilution studies in $CDCl_3$–DMSO mixture is impractical due to low solubility of 2-2.

As can be seen from dilution NMR studies (Figure 2.8A) intramolecularly bonded H*c* shows a smaller change in chemical shift upon dilution compared to H*a* and H*d*. This can

be explained by a high exchange rate on the NMR time scale. The chemical shift changes observed are probably due to a change in compound/water molar ratio rather than equilibrium between associated and monomeric molecule. This is in agreement with the fact that chemical shifts do not depend on concentration of **2-1** in water. Furthermore, H-bonded aggregates should give broader signals since they have higher molecular weights. The peak widths do not change with concentration in all solvent systems studied. Temperature dependence (Figure 2.8B, C) of chemical shifts is too small to draw any conclusions.

To determine the association state of **2-2** in solution, a DOSY experiment was performed in DMSO. Using the Stokes-Einstein equation,[91] the size and molecular weight derived from the diffusion coefficients were found to be 1.2 nm and 250 g/mol, respectively, and are consistent with the size (0.9 – 1.2 nm) and molecular weight (249 g/mol) of **2-2** for both major and minor species. This result suggests that G^C modules are in a monomeric state in solution.

Interestingly, DLS of the same solution that was used for NMR showed the presence of large (100 – 1000 nm) aggregates. Drop casting the solution on a carbon film or mica substrate revealed the presence of high aspect ratio nanostructures, whose diameters obtained by TEM and AFM images are in agreement with the values obtained from computer modelling of RNTs. There are at least two possible explanations for the presence of aggregates: (1) the aggregates are RNTs formed from deprotonated G^C module that is present in equilibrium concentration in solution and (2) the aggregates are formed from the protonated G^C base.

Protonation of **2-2** was established in aprotic solvents solvent where it is possible to see the highly acidic protons (DMSO, chloroform – DMSO mixtures, DMF). In water – a protic solvent – it is not possible to see H*b* and H*e* (see Figure 2.1). However, the concentration of protonated species can be estimated from pK_a of N*3* = 4.5, and initial concentration of **2-2** (2.5 mg/mL, 10 mM) leading to a pH = 3.25 in water. At this pH, ~ 5% (0.5 mM) of the compound will be deprotonated. 100-fold dillution (0.1 mM, 0.025 mg/mL) is calculated to increase the population of deprotonated species to 50% if no buffers are used to maintain a constant pH. It should be noted that for compound **2-1**, the amount of deprotonated species is even lower than for **2-2**, due to additional protons present from two moles of acid that protonate basic nitrogens of the side chain. It was found by elemental analysis that each molecule of **2-1** bound to three molecules of acid (HCl or TFA). Based on this observation, it is likely that the deprotonated form of G^C forms the RNTs detected by DLS and observed by SEM.

It is possible that a population of deprotonated species exists in the form of nanotubes and is not detectable by NMR. To test this idea, an experiment was carried out to find if 100% of G^C modules are seen by NMR. A ^{1}H NMR spectrum of a 1:1 mixture of **2-2** with p-chloro-iodobenzene – a non assembling molecule – was recorded in the concentration range of 230 – 3 mM in DMSO. This experiment established that the ratio of integrals for the resonances of **2-2** and the reference compound remained constant at 1:1 ratio. This indicates that each molecule of **2-1** gives a NMR signal. Therefore, it is likely that deprotonated species are in fast equilibrium with RNTs, which were observed by TEM, SEM and AFM.

Titration of **2-2** with triethylamine in DMSO and titration of **2-1** with sodium hydroxide in water both resulted in complete disappearance of all NMR signals and gelation of the solutions. This could be due to the formation of high molecular weight RNTs in which isotropic averaging of chemical shift tensors due to molecular tumbling is too limited to be detectable by solution NMR. It is therefore necessary to study the deprotonated G^C by solid state NMR techniques.

If it is the protonated species that forms large aggregates observed by DLS, EM, and AFM, then a new model of the aggregates should be devised. Protonation of N3 should destabilize G≡C triple hydrogen bond. To find out if protonation still exists after the solvent is removed, the solvent was evaporated from a solution of compound **2-2** in DMF under reduced pressure. Upon dissolution of the residue in pure DMF, the compound was found to be 100% protonated, confirming that protonation persists in the solid state. However it is unclear if the protonation site is the same in the solid state as in solution. Thus, solid state NMR is necessary to elucidate the structure of the protonated species in the solid.

2.4. Solid state NMR studies

Compound **2-4** and its deprotonated form **2-5** were synthesized (Figure 2.9) for solid state NMR studies (see experimental part).

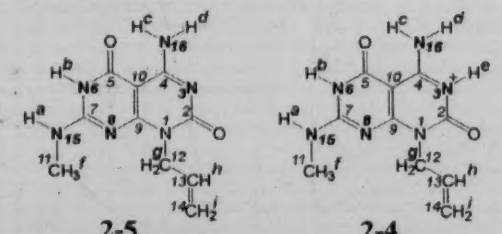

2-5 **2-4**

Figure 2. 9. Deprotonated G^C (2-5) and protonated G^C (2-4) self-assembling modules. The nitrogens in bold-face type have been ^{15}N-labeled.

(A) Peak assignments

Solid-state ^{1}H NMR typically suffers from poor spectral resolution due primarily to the strong ^{1}H-^{1}H dipolar couplings and narrow ^{1}H chemical shift range. By performing solid-state ^{1}H NMR experiments at a high magnetic field and with fast magic-angle spinning, it is possible to obtain relatively well-resolved ^{1}H NMR spectra of solids. Figure 2.10a displays ^{1}H MAS NMR spectra of the G^C samples obtained with the state-of-the-art in solid-state NMR spectroscopy, with regards to magnetic field strength (21.1 T) and magic-angle spinning frequency (60 kHz). Nearly all proton sites are resolved in these spectra. With this high resolution, it is possible to probe in detail the molecular arrangements of the G^C self-assembling modules. The first step is to assign the peaks.

With ^{15}N-enriched samples, it is straightforward to obtain ^{15}N NMR spectra of the G^C samples (Figure 2.10b). In each case, the five peaks arising from the five ^{15}N-labelled sites are clearly resolved and there are significant differences in the ^{15}N chemical shifts between the two samples.

The spinning sideband profiles in the ^{15}N CP MAS spectra obtained at slow MAS frequencies (Figure 2.11) reveal the ^{15}N chemical shift tensors for each nitrogen (Table 2.3). In **2-4**, only one of the nitrogens (at 170.5 ppm) has a chemical shift anisotropy with a significantly larger magnitude than the others. In **2-5**, there are two nitrogens (at 176.1 and 167.3 ppm) with large chemical shift anisotropies. These peaks likely arise from the nitrogens that do not have directly attached protons. In ^{15}N CP MAS NMR spectra collected with a short CP contact time of 100 μs (not shown), these same peaks with the large chemical shift anisotropies are observed with very low signal intensity, providing a further indication that these peaks are the nitrogens without directly attached protons.

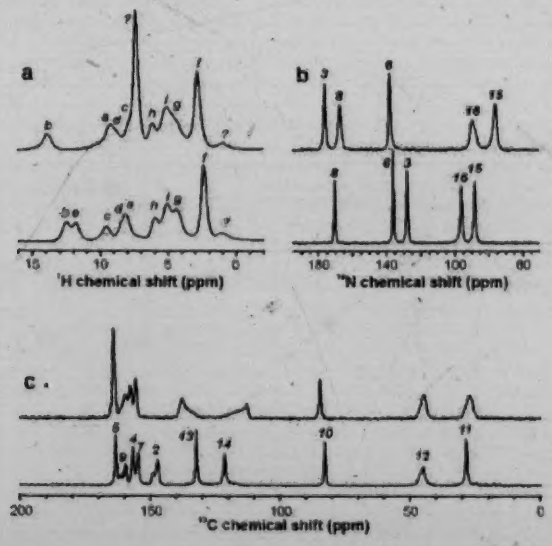

Figure 2. 10. Solid-state NMR spectra of 2-5 (*top*) and 2-4 (*bottom*): (a) ^{1}H MAS NMR spectra obtained with 60 kHz MAS at 21.1 T, (b) ^{15}N CP MAS NMR spectra obtained at 4.7 T, (c) ^{13}C CP MAS NMR spectra obtained at 4.7 T. The ^{1}H and ^{15}N peaks have been assigned based on the 2D correlation experiments while the ^{13}C peaks have been assigned based on similarities to a solution ^{13}C NMR spectrum. The peaks assigned to C2, C9, and C12 show the expected lineshapes due to the residual ^{13}C-^{14}N dipolar couplings to the neighboring quadrupolar ^{14}N nucleus (N1). The ^{1}H peaks marked with question marks are likely to be due to residual solvent molecules.

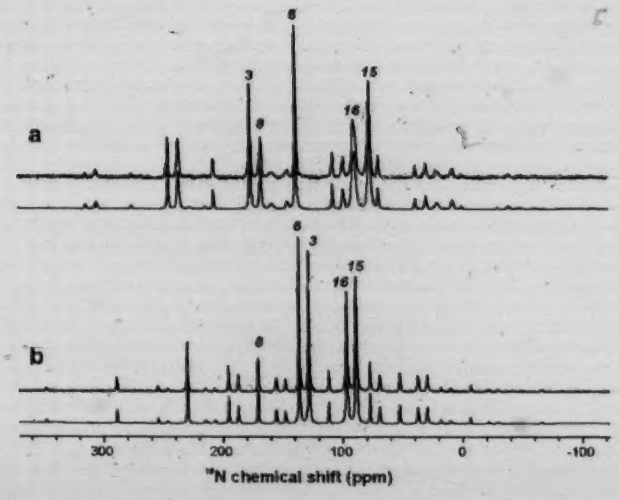

Figure 2.11. Experimental (*top*) and calculated (*bottom*) ^{15}N CP MAS NMR spectra obtained at 4.7 T of (a) 2-5 at 1.4 kHz MAS frequency and (b) 2-4 at 1.2 kHz MAS frequency. The best-fit ^{15}N chemical shift tensors values are listed in Table 2.3. The isotropic peaks are labeled.

Table 2.3. ^{15}N chemical shift tensors* determined from spinning sideband profiles in slow CP MAS spectra at 4.7 T.

	2-5			2-4		
Site	δ_{iso} (ppm)	δ_{aniso} (ppm)	η	δ_{iso} (ppm)	δ_{aniso} (ppm)	η
N3	176.1	-136.9	0.44	128.0	-66.7	0.88
N6	138.0	80.1	0.93	136.1	82.5	0.81
N8	167.3	-187.6	0.46	170.5	-189.1	0.46
N15	76.4	70.9	0.57	88.5	75.8	0.29
N16	89.2	80.0	0.49	96.3	76.3	0.70

* The isotropic value, anisotropy, and asymmetry parameters for the chemical shift interaction are related to the principal elements of the shift tensor according to $\delta_{iso} = (\delta_{xx} + \delta_{yy} + \delta_{zz})/3$, $\delta_{aniso} = \delta_{zz} - \delta_{iso}$, $\eta = (\delta_{yy} - \delta_{xx})/\delta_{aniso}$ where the principal elements are labeled and ordered according to $|\delta_{zz} - \delta_{iso}| \geq |\delta_{xx} - \delta_{iso}| \geq |\delta_{yy} - \delta_{iso}|$.

This is more clearly observed in the 2D ^{1}H-^{15}N correlation spectra (Figures 2.12a and 12d). For **2-5**, strong correlations are observed for the three nitrogens with directly attached protons, one of which (89.2 ppm) has correlations to two protons (7.8 and 8.9 ppm) and can thus be assigned to the NH_2 group (N16) and its attached protons can be assigned to H*c* and H*d*. For **2-4**, strong correlations are observed for four of the nitrogens and the NH_2 group (N16) at 96.3 ppm, with its correlations to two protons (H*c* and H*d*) at

9.5 and 8.3 ppm, is again clearly identifiable. The specific assignments of H*c* and H*d* can be made from the 2D ^{1}H-^{1}H DQ correlation spectra.

Based on their ^{1}H chemical shifts and the relative intensities, the methyl protons (H*f*) can be assigned to the peaks at 2.8 (**2-5**) and 2.4 ppm (**2-4**). For both samples, there are weak correlations between the methyl protons and the upfield ^{15}N peaks at 76.4 (**2-5**) and 88.4 ppm (**2-4**) indicating that these can be assigned to N15, the nitrogen to which the methyl group is attached. The strong ^{1}H-^{15}N correlations for N15 enables the assignment of the directly attached proton H*a* to the peaks at 9.3 (**2-5**) and 8.1 ppm (**2-4**).

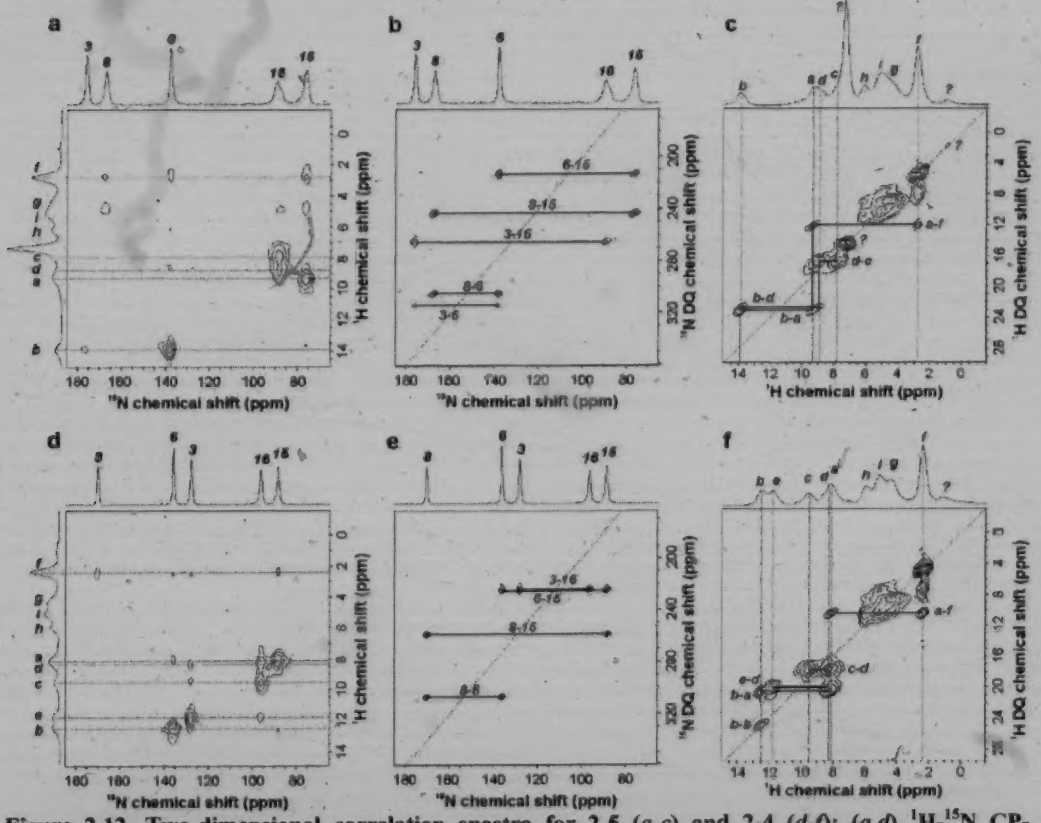

Figure 2.12. Two-dimensional correlation spectra for 2-5 (*a-c*) and 2-4 (*d-f*): (*a,d*) ^{1}H-^{15}N CP-HETCOR obtained at 21.1 T with 60 kHz MAS frequency; (*b,e*) ^{15}N-^{15}N SR26$_4^{11}$ dipolar DQ correlation obtained at 4.7 T with 4 kHz MAS frequency; (*c,f*) ^{1}H-^{1}H BABA dipolar DQ correlation obtained at 21.1 T with 60 kHz MAS frequency. The projections are the 1D spectra presented in Figure 2.10.

Table 2.4. Solid-state ^{1}H and ^{15}N isotropic chemical shifts and observed correlations* for G^C samples.

	^{1}H chemical shifts (ppm)			^{15}N chemical shifts (ppm)	
Site	**2-5**	**2-4**	**Site**	**2-5**	**2-4**
H*a*	9.3 (H*b*,H*f*) (N15)	8.1 (H*b*,H*f*) (N15)	N3	176.1 (N6,N16)	128.0 (N16) (H*e*)
H*b*	3.8 (H*a*,H*d*) (N6)	12.5 (H*a*,H*b*) (N6)	N6	138.0 (N3,N8,N15) (H*b*)	136.1 (N8,N15) (H*b*)
H*c*	7.8 (H*d*) (N16)	9.5 (H*d*) (N16)	N8	167.3 (N6,N15)	170.5 (N6,N16)
H*d*	8.9 (H*b*,H*c*) (N16)	8.3 (H*c*,H*e*) (N16)	N15	76.4 (N6,N8) (H*a*)	88.5 (N6,N8) (H*a*)
H*e*	–	11.8 (H*d*) (N3)	N16	89.2 (N3) (H*c*,H*d*)	96.3 (N3) (H*c*,H*d*)
H*f*	2.8 (H*a*)	2.4 (H*a*)			
H*g*	4.5 (H*g*,H*h*)	4.3 (H*g*,H*h*)			
H*h*	6.1 (H*g*,H*i*)	6.0 (H*g*,H*i*)			
H*i*	5.1 (H*h*,H*i*)	5.1 (H*h*,H*i*)			

*The sites listed in parentheses are those for which strong correlations are observed in 2D NMR experiments.

The other nitrogens can be assigned from the 2D ^{15}N-^{15}N DQ correlation spectra (Figures 2.12b and 2.12e). For both samples, N16 is correlated to only one other peak at 176.1 ppm in **2-5** and 128.0 ppm in **2-4.** These can therefore be assigned to N3, the only nitrogen that is in close spatial proximity to N16. N3 lacks an attached proton in **2-5**, while **2-4** has N3 with an attached proton, indicating that the additional proton H*e* (11.8 ppm) bonds to N3 upon protonation.

In both samples, N15 is correlated to two other peaks, one of which is protonated and the other is not. Of the two nitrogens that are in close spatial proximity to N15, N6 has a directly attached proton while N8 does not. Therefore, N6 is assigned to 138.0 ppm in **2-5** and 136.1 ppm in **2-4** while N8 is assigned to 167.3 ppm in **2-5** and 170.5 ppm in **2-4**. The strong ^{1}H-^{15}N correlations for N6 enable the assignment of H*b* to 13.8 ppm in **5** and 12.5 ppm in **2-4**. (An alternative assignment for **2-4** could have the proton H*b* on N8 rather than on N6, but then a significant correlation between H*b* and H*g* would be expected and this was not observed!)

The group of peaks between 4 and 6 ppm in both ^{1}H spectra belong to the protons of the allyl group. Based on relative signal intensities, the peaks near 6 ppm are assigned to H*h*. but there remains some ambiguity about the assignment of H*g* and H*i*. Based on isotropic chemical shifts, it is expected that H*i* protons would be less shielded than the H*g* protons due to the C=C double bond. Therefore the peaks near 5 ppm are assigned to H*i* and the peaks near 4 ppm are assigned to H*g*.

The peaks at 1 and 7 ppm marked with question marks are likely to be residual solvent (water or methanol) since there are no correlations with ^{15}N observed nor any ^{1}H-^{1}H correlations with any of the G^C peaks. It is possible that some of the solvent is within the nanotubes of the deprotonated G^C sample. The fact that ^{1}H-^{1}H DQ correlation peaks are observed along the diagonal for **2-5** (Figure 2.12c) suggests that the solvent has a degree of rigidity or restrained mobility. The observed correlations are likely to be internal dipolar interactions (e.g. between protons of a single water molecule). The fact that they are observed suggests that the solvent molecules lack the full (isotropic) mobility that would lead to averaging the dipolar interactions to zero. This could be consistent with the solvent molecules being located within the nanotubes in which their residual mobility is sufficient to weaken the dipolar couplings to the nuclei in the G^C units that make up the walls of the RNT but not sufficient to fully average out the much stronger internal dipolar couplings.

(B) Evidence for RNT hydrogen bonding

With the ^{1}H and ^{15}N peaks assigned from the 2D ^{1}H-^{15}N and ^{15}N-^{15}N correlation experiments, it is possible to examine some of the additional correlations, as well as the 2D ^{1}H-^{1}H correlation experiments to provide evidence for the existence of the expected

hydrogen bonding between adjacent self-complementary G^C molecules (Figure 2.13). The ^{1}H and ^{15}N solid state NMR data provides conclusive evidence that this hydrogen bonding is present in **2-5** but is *not* present in **2-4.**

There are four pieces of evidence in the solid-state NMR spectra of **2-5** that clearly indicate the existence of the expected hydrogen-bonded molecular arrangement depicted in Figure 2.13. First, the series of correlations in the ^{1}H-^{1}H 2D DQ spectrum involving H*f*, H*a*, H*b*, H*d*, and Hc, indicated by the solid lines in Figure 2.12b, are consistent with the spatial arrangement of these H sites that results upon self-complementary hydrogen-bonding of the G^C units, as shown by the solid green lines in Figure 2.13. Secondly, there is a weak but significant correlation between H*b* and N3 in the ^{1}H-^{15}N 2D HETCOR spectrum (Figure 2.12a) that is consistent with the close spatial proximity between H*b* and N3 that results from the intermolecular N6–H*b*···N3 hydrogen bond. Thirdly, the ^{15}N-^{15}N 2D DQ correlation spectrum (Figure 2.12b), which probes *through-space* dipolar couplings, has an additional correlation between N3 and N6 that can only arise from an intermolecular dipolar interaction since the intramolecular dipolar interaction between N3 and N6 is far too weak to be observed. The intensity of this correlation is weaker than the other intramolecular interactions since the distance between N3 and N6 is longer than the other nitrogen pairs (and therefore the distance-dependent dipolar coupling is weaker).

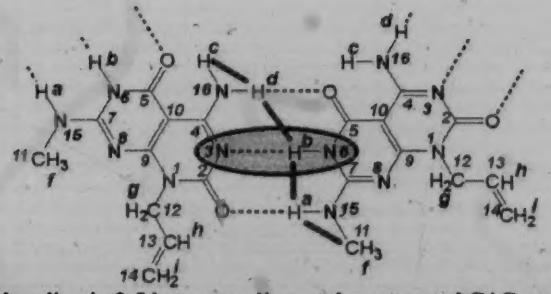

Figure 2.13. Hydrogen bonding in 2-5 between adjacent deprotonated G^C molecules in rosette nanotubes. The intermolecular interaction between N3 and N6, observed in the dipolar correlation spectrum (Figure 2.12b) and in the J-coupling INADEQUATE spectrum (Figure 2.14), is highlighted. The close spatial proximities between H atoms, observed as correlations in Figure 2.12c are also indicated.

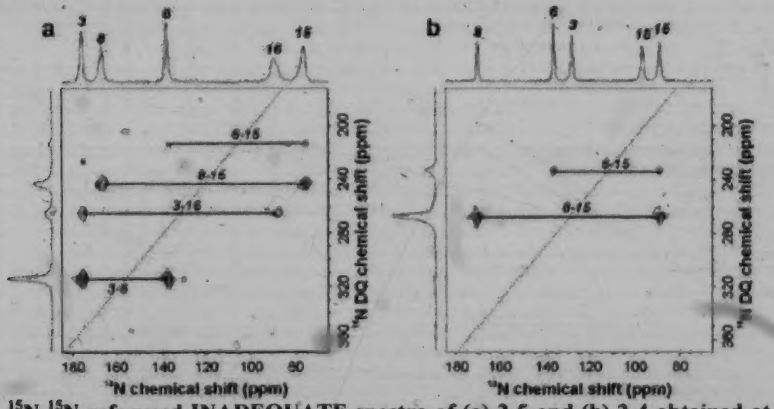

Figure 2.14. ^{15}N-^{15}N refocused INADEQUATE spectra of (a) 2-5 and (b) 2-4 obtained at 4.7 T. The strongest correlation for 2-5 arises from the intermolecular hydrogen bond mediated J-coupling between N3 and N6.

Finally, perhaps the strongest piece of evidence comes from the ^{15}N-^{15}N 2D INADEQUATE spectrum (Figure 2.14a). The INADEQUATE experiment correlates pairs of nuclear spins for which there exists a *through-bond* *J*-coupling. The spectrum shows a very strong correlation between N3 and N6. This correlation can only arise from the existence of an intermolecular hydrogen bond between N3 and N6 in which the hydrogen bond mediates the *J*-coupling between the ^{15}N spin pairs. $^{2h}J_{N-H\cdots N}$ couplings have been reported in solid-state supramolecular materials previously[92-94] and have even been measured to be in the range of 5.9 to 7.4 Hz while other two-bond ^{15}N-^{15}N *J*-

couplings have been measured to be 3.5 to 6.6 Hz. These four separate solid-state NMR observations provide unambiguous evidence for the existence of the expected hydrogen-bonded molecular arrangement of self-complementary G^C units shown in Figure 2.13.

Interestingly, these solid-state NMR observations are not observed for **2-4** which suggests that the expected hydrogen-bonded molecular arrangement is not found for the protonated G^C units. The correlations in the ^{1}H-^{1}H 2D DQ spectrum (Figure 2.12f) that are highlighted in green are mostly the intramolecular dipolar interactions that one would expect from an examination of a sole protonated G^C^{+} unit (see Figure 2.9) with the exception of the diagonal correlation for H*b* and possible weak diagonal correlations for H*c* and H*d* which arise from intermolecular dipolar interactions. Furthermore, there are no additional correlations observed in the ^{1}H-^{15}N 2D HETCOR spectrum (Figure 2.12d) nor the ^{15}N-^{15}N 2D DQ spectra that would indicate strong ^{15}N intermolecular dipolar interactions (Figure 2.12e) or hydrogen bond mediated J-couplings (Figure 2.14). The solid-state NMR results for **2-4** clearly indicate a different structure from the rosette nanotube structure of **2-5**. The structure of the protonated form remains under investigation. Microscopy and powder XRD suggest the existence of RNTs. Perhaps they exist but with a different hydrogen bonding arrangement. There is also a possibility that a hydrochloride salt is formed with close H–Cl^{-} contact, in a similar fashion to solid forms of many protonated amino acids.

Finally, the ^{13}C CP MAS spectra (Figure 2.10c) provide less conclusive, but supportive, evidence for the existence of a rosette nanotube structure for **2-5**. The ^{13}C spectrum for **2-4** shows a highly ordered structure with very well-defined peaks (note that C2, C9, and C12 have a 1:2 doublet shape due to the coupling to the quadrupolar ^{14}N

nucleus N1). However, the ^{13}C spectrum for **2-5** shows broadened line shapes for a number of the peaks (C11, C12, C13, and C14). The broadening is particularly strong for C13 and C14, resulting from a distribution of ^{13}C chemical shifts, which in turn is probably a consequence of the existence of a distribution of different local environments around C13 and C14, perhaps in bond angles and torsional angles. This suggests that the allyl groups which are on the outsides of the RNTs are highly disordered over various bonding geometries. There are no strong interactions that "lock" these groups into the same geometries throughout the entire structure like there is for the rest of the G^C unit. This ^{13}C spectrum suggests an ordered core with a disordered outside surface. Disordering of side chains attached to rosettes in solid state is consistent with data observed by single crystal X-ray diffraction for Mascal's G^C analog.[51] The dimensions of thermal ellipsoids of alkyl chain carbons increase moving away from the rosette with the most remote atoms being too disordered to be located from diffraction data.

2.5. X-ray diffraction studies

Where solid-state NMR provides clear local structural information about the hydrogen-bonded molecular arrangement, powder X-ray diffraction provides additional information about the structure on larger length scales. The diffraction pattern (Figure 2.15) has very few features, typical of a non-crystalline material. However, most of the features that are observed are consistent with a rosette nanotube structure. A strong peak, centered at a d-spacing around 3.5 Å, is likely to arise from the inter-rosette spacing in the RNTs.

A model was proposed where the nanotubes bundle into a hexagonal array, as depicted in Figure 2.15c. Formation of hexagonal arrays is very common for cylindrical objects like discotic liquid crystalline phases[95] and carbon nanotubes bundles.[96] The main reflections observed for the powder of **2-4** match very well the major expected reflections for the hexagonal model unit cell (Figure 2.15a–c). The first-order d-spacing corresponds to the perpendicular distance between opposing sides of the unit cell (approximately 22.9 Å). The peaks are heavily broadened because these nanotube bundles should certainly not be perfect, so there should be a distribution of inter-tube distances. The broad peak centered at $2\theta = 21°$ can likely be attributed to the maximum of the amorphous signal as this position is quite typical for amorphous organic compounds, such as amorphous polymers.

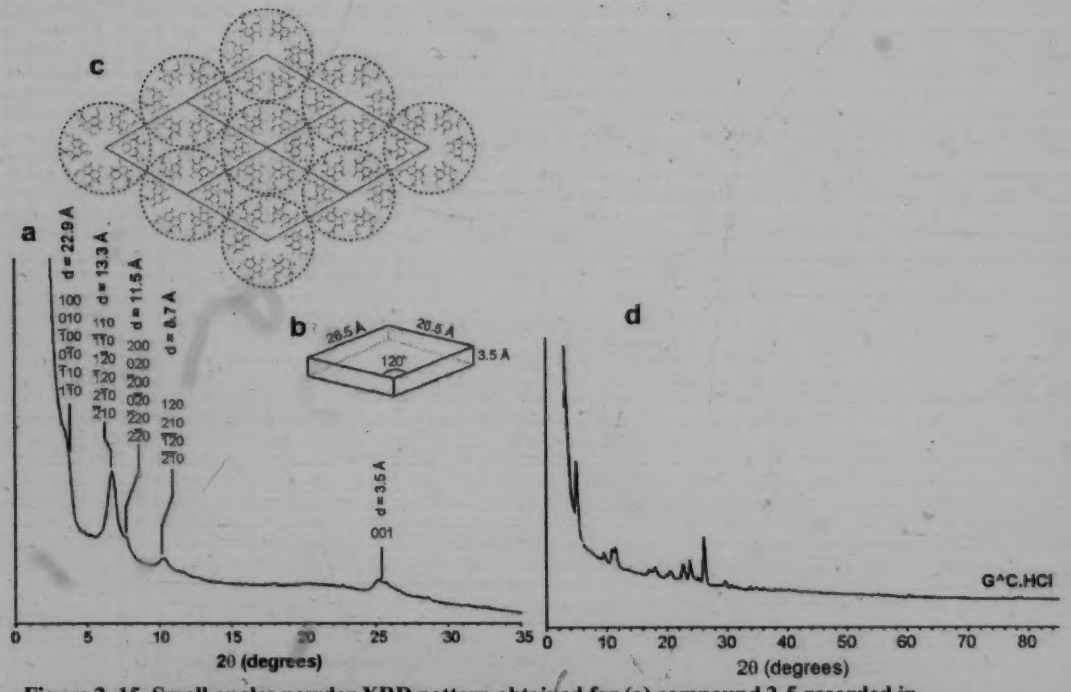

Figure 2. 15. Small angles powder XRD pattern obtained for (a) compound 2-5 recorded in transmission indexed according to hexagonal packing model (b, c). The powder of the G^C hydrochloride salt 2-4 (top) recorded at glancing angle (d).

2.6. Conclusions

Extensive 1D and 2D NMR studies of model unlabeled and ^{15}N-labeled compounds in various solvent systems allowed for the structure of the G^C module in solution to be established for the first time since it was reported in 1995. In the current work it was found that the monomeric protonated G^C molecule, rather than the free G^C base as was proposed before, gave an NMR signal. The deprotonation resulted in the disappearance of the solution NMR signal due to aggregation. By using state-of-the-art high field solid state NMR (900 MHz) and ultra fast spinning (60 kHz), the hydrogen bonding network in the RNTs that formed from deprotonated G^C was established. Four pieces of evidence were found that supported the expected hydrogen bonding in nanotubes. These include H-H and N-N intermolecular dipolar correlations and most importantly N-N intermolecular J-coupling though hydrogen bond. It should be noted that there is only one other solid state NMR instrument in the world (Lille, France) with similar capabilities, and it has been used thus far for model studies. The successful application of this solid state NMR set-up to unravel the complexity of supramolecular system is a significant advance in the field of material science.

The results of the G^C module structure studies described in Chapter 2 will change the way we think about and study G^C based nanotubes in the future. Future challenges for RNT structure investigation include obtaining crystals for X-ray diffraction analysis. For this, nanotubes or nanotube bundles with extremely high monodispersity should be prepared. To achieve this goal, a method to prepare monodisperse RNTs should be developed. Combination of high quality single crystal X-ray analysis with neutron diffraction will provide the ultimate insight into the structure of nanotubes. It would also

establish wether the RNTs are made of rosette stacks or hydrogen bonded coiled helical tapes.

It should be noted that solid state NMR and XRD are consistent with both discrete rosette and continuous helically folded hydrogen tapes (Figure 2.16). Experimental data collected thus far (NMR, XRD, TEM, AFM, UV, CD etc) does not allow us to conclusively favor one structure over the other. However, STM experiments carried out on compound **2-1** suggest the stack model (unpublished results).

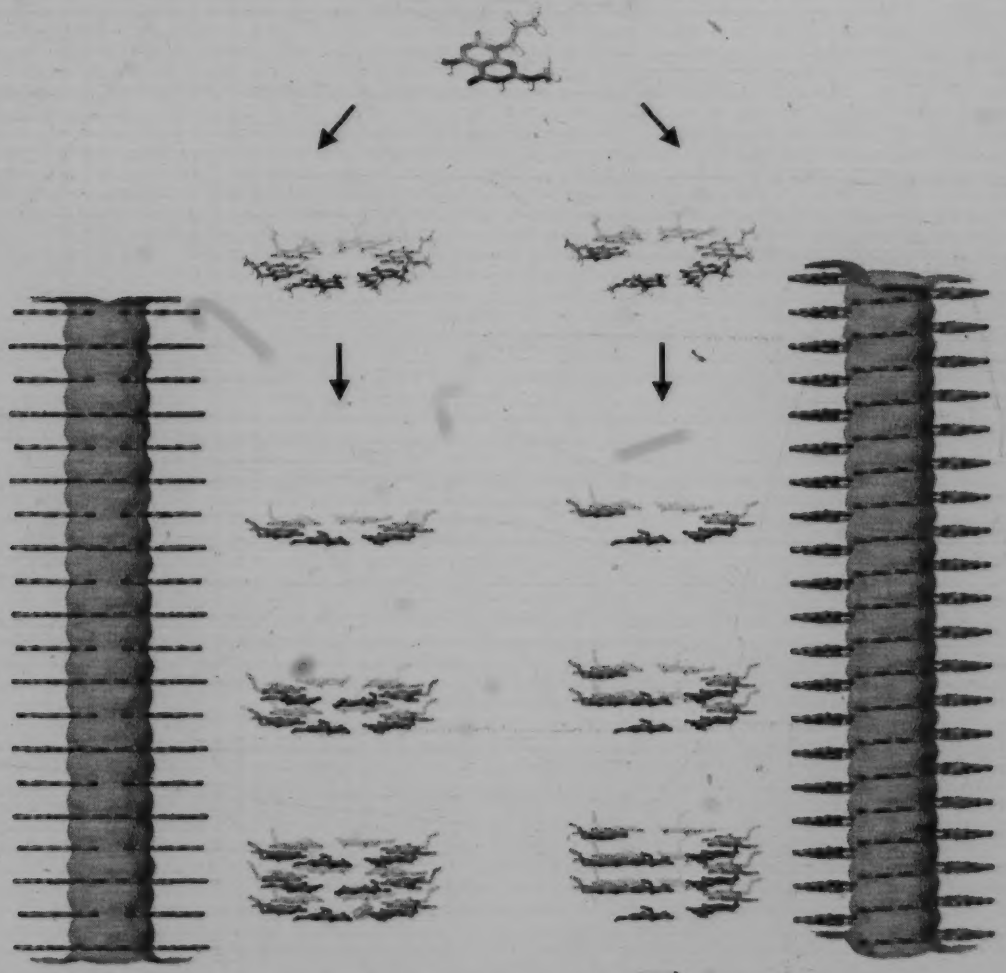

Figure 2. 16. Two possible nanotube structures: (left) rosette nanotube and (right) helical tape.

2.6. Experimental part.

Synthetic Procedures and characterization.

NMR spectra were recorded on Varian NMR spectrometers (Inova 300, 400, 500, 600 or 800) with the solvent as the internal reference. The key NMR spectra are shown. The mass spectra were performed at the Mass Spectrometry Laboratory of the University of Alberta and the Analytical Instruments Laboratory at the National Research Council of Canada's National Institute for Nanotechnology. Compounds **2-1** and **2-4-3** were prepared in this work according to previously reported procedures.[63, 78] Intermediate **2-4-7** was synthesized by Dr. Lei Fan and Dr. Souhaila Bouatra. Compiling of the spectral data and synthesis for **2-4-7** as well as the rest of the synthesis was done in this work, which is presented below, since it has not been reported previously. The synthesis and characterization of the rest of the ^{15}N labeled and non-labeled compounds was carried out in this work and it is described below. Synthetic scheme for the synthesis of non-labeled compound **2-2** is identical to the scheme given below for labeled compounds. All the reagents are commercially available from Aldrich or Fisher Scientific. Reagent grade solvents were obtained using chromatography solvent purification systems. All reactions were performed under N_2 atmosphere unless otherwise specified. For column chromatography, commercial solvents were used without purification. Chromatographic supports were silica flash Merck 60 (0.040-0.063 mm). Silica-coated TLC plates (Merck F 60_{254}) were used for monitoring reaction progress under UV light (354 nm) or by chemical staining ($KMnO_4$/acetone or ninhydrin/n-BuOH/acetic acid).

Synthetic schemes for compounds **2-4**, **2-3**, **2-7**.

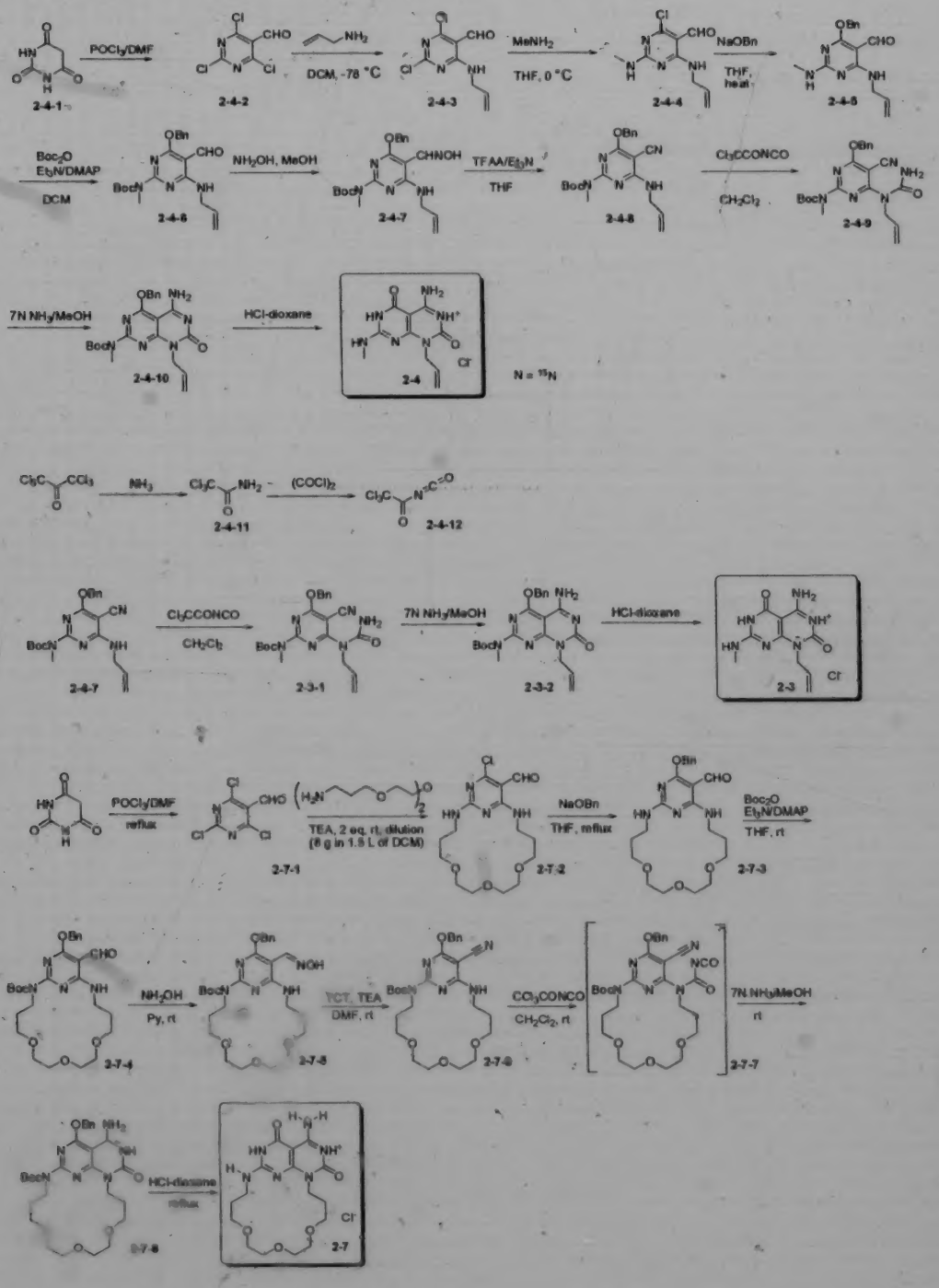

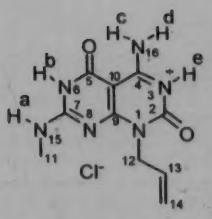

Synthesis of compound 2-2. Unlabeled analog of compound **2-4-9** (synthesis of which was previously reported[78]) (0.044 g, 0.1 mmol) was dissolved in 4M solution of HCl in dioxane (4 mL) and the mixture was heated at reflux for 2 h. The white precipitate formed was filtered, washed with CH_2Cl_2 (5 × 10 mL), and dried on a filter. Compound **2-2** was obtained as a white solid (0.028 g, 100%).

HRMS (ESI) calcd for $C_{10}H_{13}N_6O_2$ ($M+H^+$) *m/z* 249.1095, found *m/z* 249.1093.

^1H, ^{13}C and ^{15}N spectra are summarized in table 2-2. Spectra rather than their summary are given here to illustrate spectra appearance greatly dependence on the solvent nature and temperature.

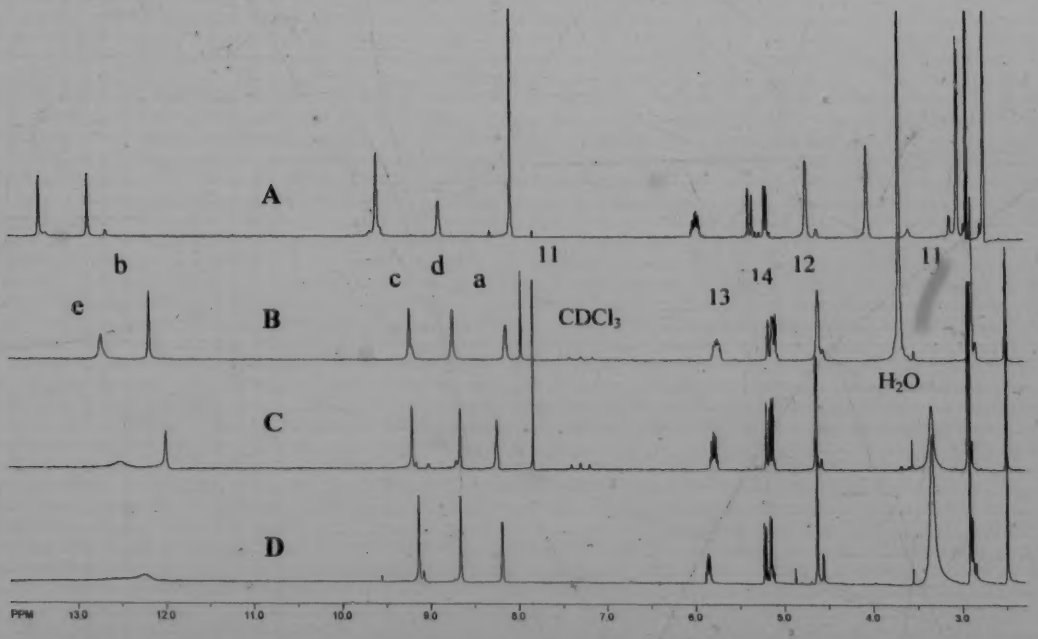

Figure 2. 17. ^1H NMR spectra of 2-2 in (A) DMF-d_7 (-60°C, 400 MHz), (B) 1:1 (v/v) $CDCl_3$–DMSO-d_6 (-40 °C, 500 MHz), (C) 1:1 (v/v) $CDCl_3$–DMSO-d_6 (0°C, 400 MHz), (D) DMSO-d_6 (27 °C, 800 MHz). Note sharpening of the NH signals as polarity of the solvent and temperature decrease. Protons c and d appear at the same chemical shift in DMF (~9.5 ppm).

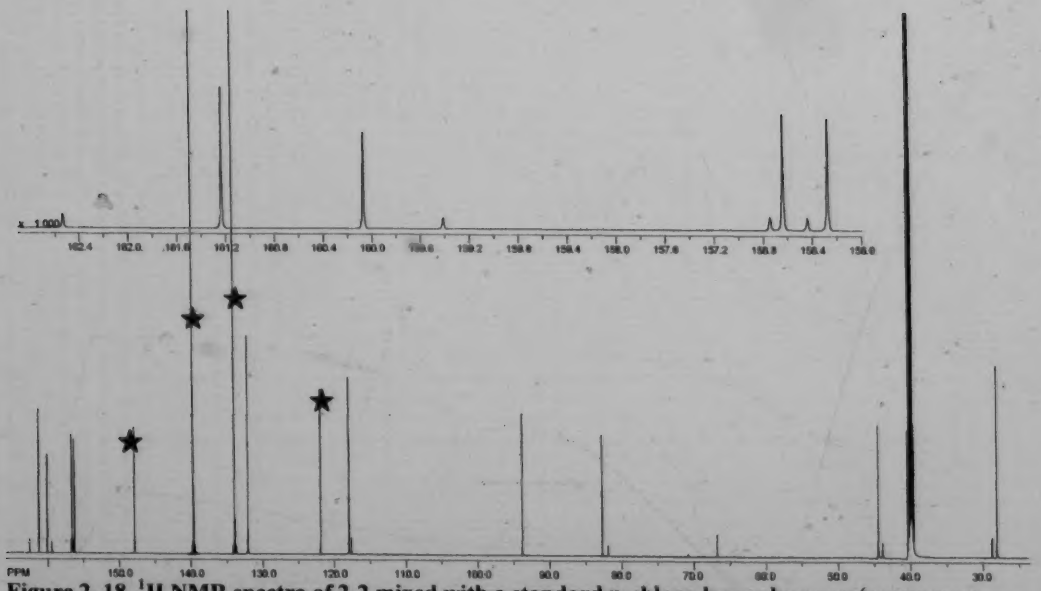

Figure 2. 18. ^{1}H NMR spectra of 2-2 mixed with a standard p-chloro-bromobenzene (resonances marked by a star) in DMSO-d_6 (27 °C, 600 MHz, acquisition time is 56 hours). Note the presence of satellite signals for every major signal of 2-2. Assignments are in Table 2.2.

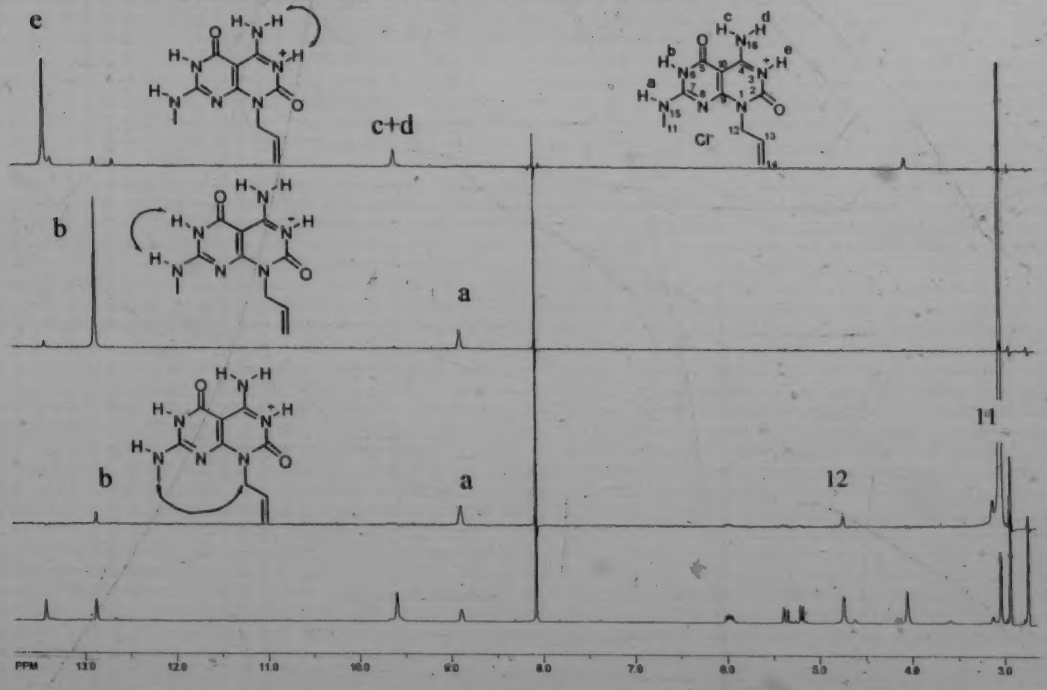

Figure 2. 19. Key NOEs observed for 2-2 in DMF-d_7 (-60 °C, 400 MHz). (A) CycleNOE spectra irradiating He, (B) CycleNOE spectra irradiating Ha, (C) CycleNOE spectra irradiating Ha, (D) ^{1}H NMR spectra of 2-2. Assignments of protons signals are based on HMQC, HMBC, and COSY (not shown).

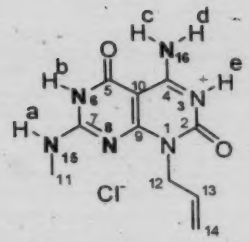

Synthesis of compound 2-3. Compound **2-3-2** (0.044 g, 0.1 mmol) was dissolved in 4M solution of HCl in dioxane (4 mL) and the mixture was heated at reflux for 2 h. The white precipitate formed was filtered, washed with CH_2Cl_2 (5 × 10 mL), and dried on a filter. Compound **2-3** was obtained as a white solid (0.028 g, 100%).

HRMS (ESI) calcd for $C_{10}H_{13}{}^{15}N_4{}^{14}N_2O_4$ ($M+H^+$) *m/z* 253.0976, found *m/z* 253.0975.

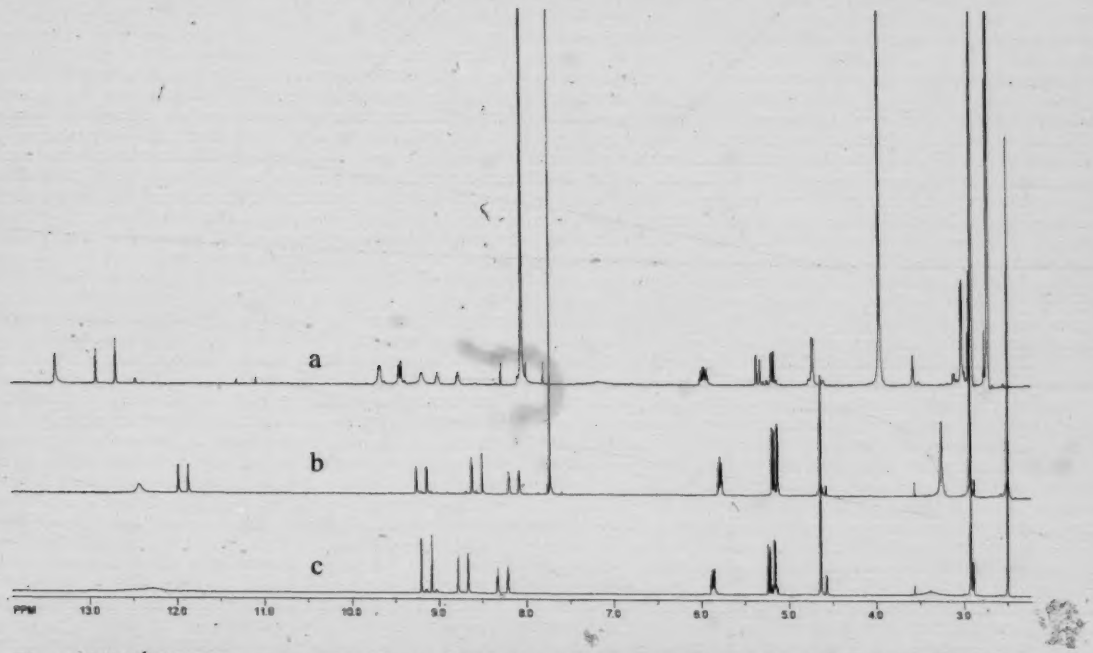

Figure 2.20. ^{1}H NMR spectra of 2-3 in (a) DMF-d_7 (-60 °C, 500 MHz), (b) 1:1 (v/v) $CDCl_3$–DMSO-d_6 (5°C, 800 MHz), (c) DMSO-d_6 (27 °C, 800 MHz). The assignments are given in Table 3.2. Note sharpening of the NH signals as polarity of the solvent and temperature decrease.

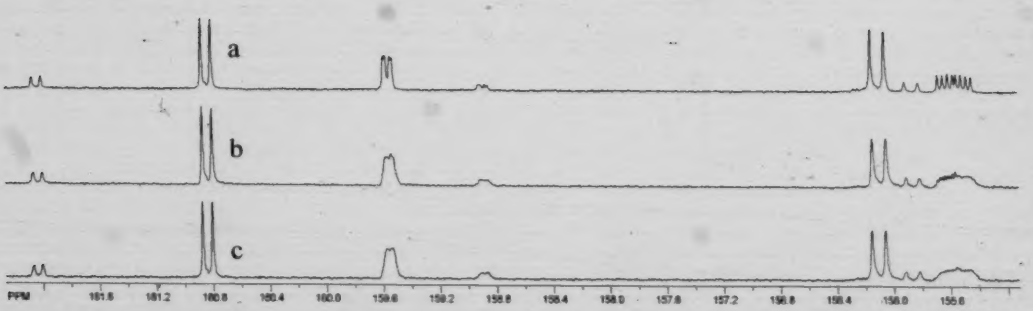

Figure 2. 21. Low field portion of ^{13}C NMR spectra of 2-3 in DMSO-d_6 (27 °C, 800 MHz) (a) fully H decoupled, (b) selective decoupling of half of Ha nuclei (presaturation of low field signal of NH doublet). Note the removal of coupling for C7 at 155.6 ppm, (c) fully H coupled. Each spectrum was collected for 18 h.

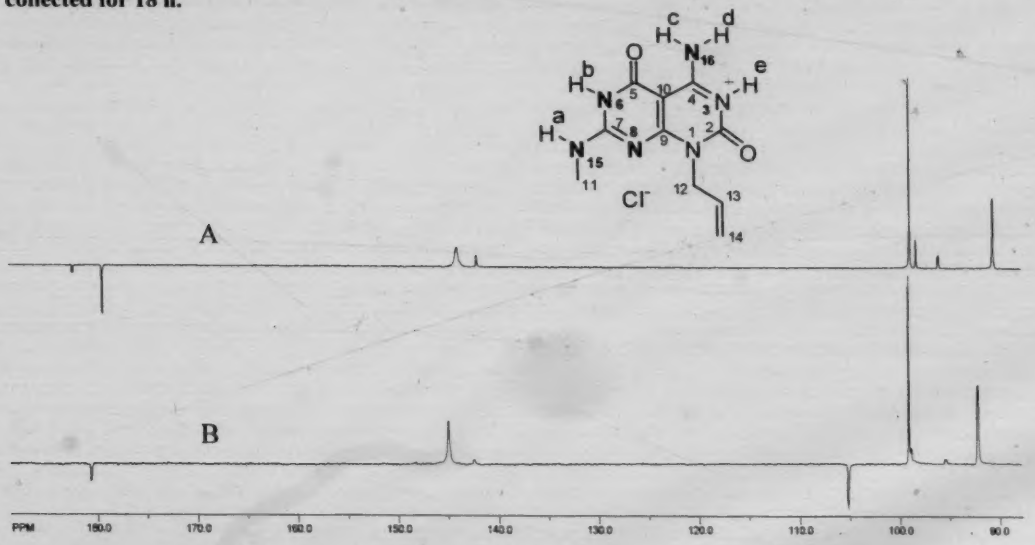

Figure 2. 22. ^{15}N NMR spectra of 2-3 in (A) DMSO-d_6 (27 °C, 800 MHz, 1 h) and (B) DMF-d_7 (-60°C, 500 MHz, 14 h). Signal at 105 ppm is DMF. Note better resolution resonance spacing for close resonances of minor and major species as well as better S/N for spectrum (A). Nitrogens with proton(s) attached have opposite (positive) phase from nitrogens with no hydrogens attached.

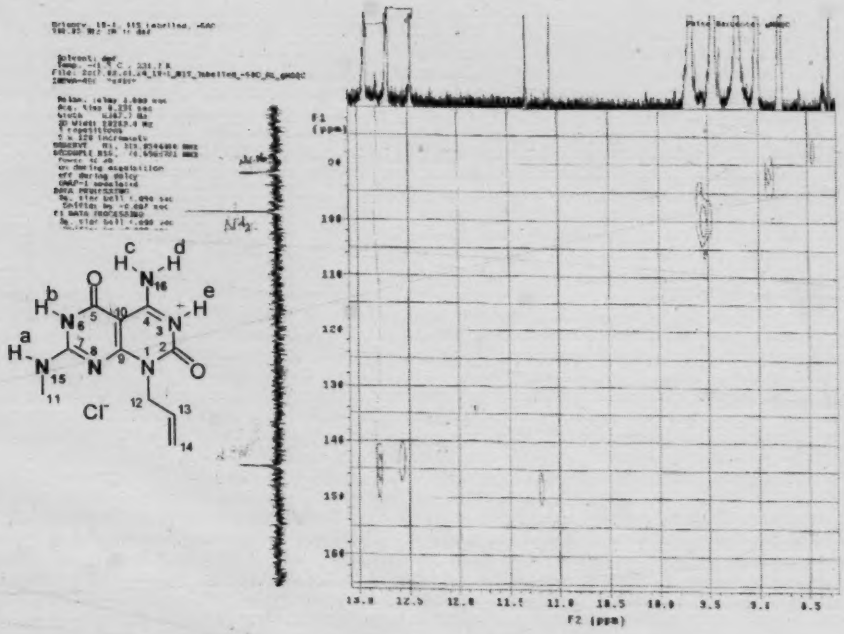

Figure 2. 23. ^{1}H-^{15}N HSQC spectrum of 2-3 in DMF-d_7 (-60 °C, 500 MHz)

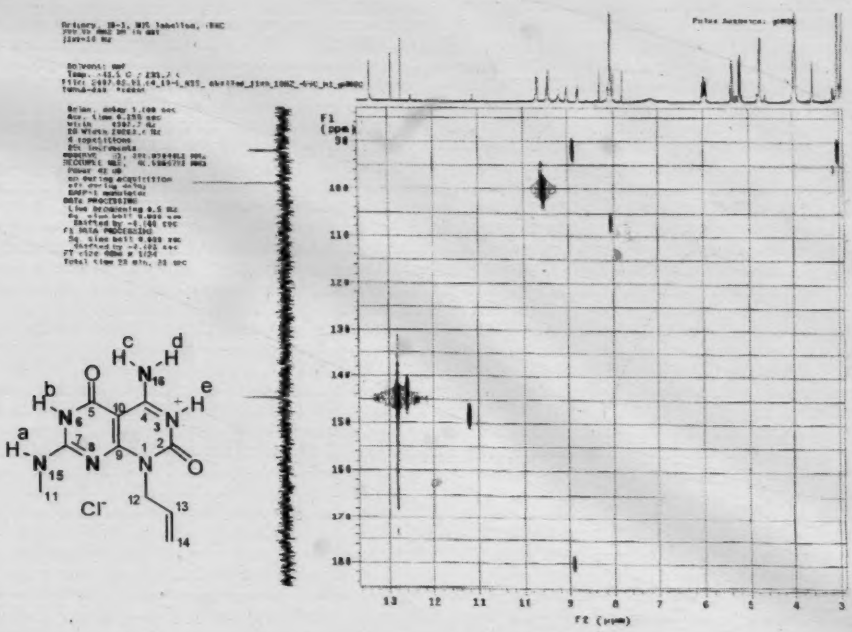

Figure 2. 24. ^{1}H-^{15}N HMQC spectrum of 2-3 in DMF-d_7 (-60 °C, 500 MHz) J_{xh} = 10 Hz

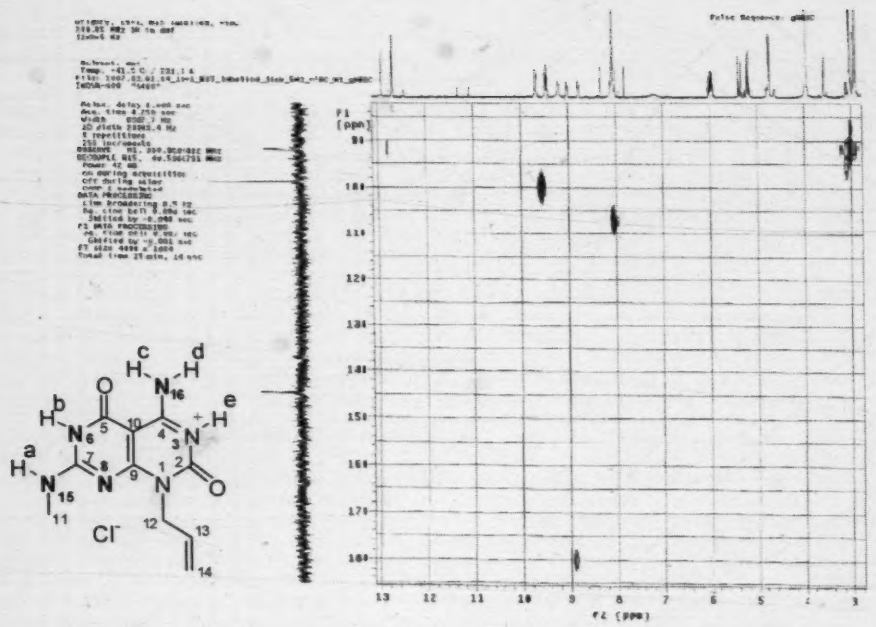

Figure 2. 25. ^{1}H-^{15}N HMQC spectrum of 2-3 in DMF-d_7 (-60 °C, 500 MHz) J_{xh} = 5 Hz. The ^{1}H-^{15}N HMQC spectrum recorded with J = 2 Hz had no correlations and is therefore not shown.

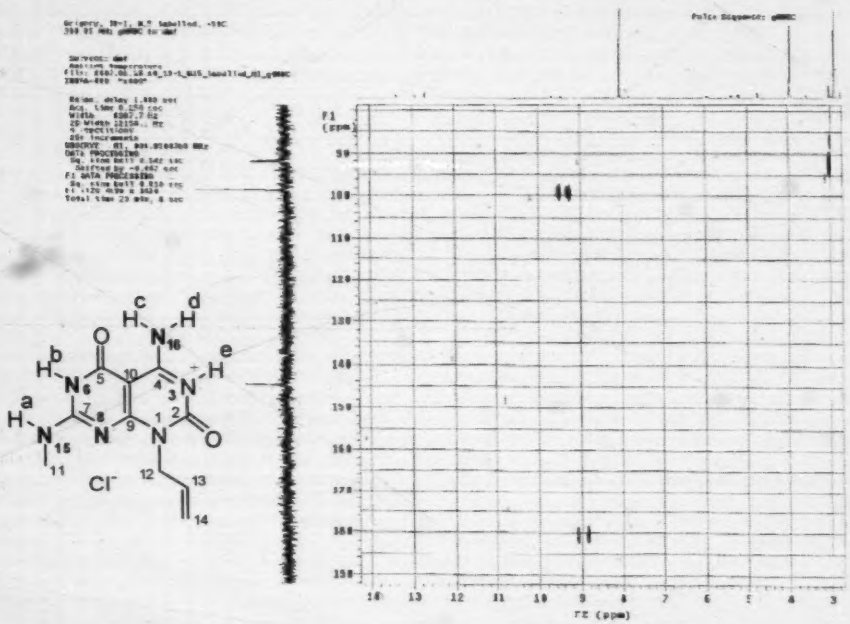

Figure 2. 26. ^{1}H-^{15}N HMBC spectrum of 2-3 in DMF-d_7 (-60 °C, 400 MHz) J_{xh} = 7 Hz.

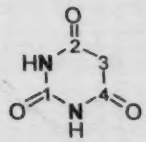

Synthesis of compound 2-4-1. In a round-bottomed flask fitted with a reflux condenser protected by a calcium chloride tube, (1.15 g, 0.05 mol) of finely cut sodium is dissolved in 63 mL of absolute alcohol. To this solution ethyl malonate (8.00 g, 0.05 mol) was added followed by urea (3.20 g, 0.05 mol) solution in 12.5 mL of hot (70°C) absolute alcohol. After being well shaken the mixture is heated at reflux for seven hours on an oil bath heated to 110°C. A white solid separated rapidly. After the completion of the reaction, 50 mL of warm (50°C) water and then enough hydrochloric acid to make the solution acidic were added. The resulting clear solution was filtered and cooled in an ice bath overnight. The white product was filtered off, washed with 10 mL of cold water, and then dried in an oven at 105-110°C for four hours. The yield of barbituric acid is (4.60 g, 68%). mp: 243°C.

^{1}H-NMR (400 MHz, DMSO) δ (ppm): 3.45 (C_3H, s, 2H), -0.91 (N, d, J_{N-H} = 92.4Hz, 2H).

^{13}C-NMR (100 MHz, DMSO) δ (ppm): 167.69 (C_2, C_4), 151.59 (C_1), 39.48 (C_3).

^{15}N-NMR (40 MHz, DMSO) δ (ppm): 154.37 (s).

High-resolution EI-MS: Calculated for $C_4H_4{}^{15}N_2O_3^+$ (M^+)/z 130.0157. Observed: *m/z* 130.0163.

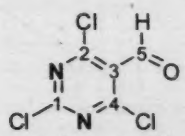

Synthesis of compound 2-4-2. Barbituric acid **2-4-1** (7.80 g, 60 mmol) was added to a stirred solution of $POCl_3$ (36 mL, 59.75 g, 389 mmol) and dimethylformamide (4.61 mL, 4.38g, 60 mmol) at rt under N_2 atmosphere. The mixture was refluxed for 15 h then allowed to cool down to rt. Excess $POCl_3$ was removed under reduced pressure (rotavap), and the resulting viscous material was carefully poured over crushed ice (150 g) while it was vigorously stirred. The resulting

brown precipitate was then filtered and dried under high vacuum. The desired compound **2-4-2** ($C_5HCl_3{}^{15}N_2O$, 10.02 g, 78%) was obtained as yellow crystalline solid. Retention factor R_f = 0.43 (10% EA/Hex). mp = 130°C.

^{1}H-NMR (400MHz, $CDCl_3$) δ (ppm): 10.42 (C_5H, s, 1H).

^{13}C-NMR (125 MHz, $CDCl_3$) δ (ppm): 184.60 (C_5), 164.07 (C_1), 123.03 (C_2, C_4).

^{15}N-NMR (50 MHz, $CDCl_3$) δ (ppm): 288.91 (s).

High-resolution EI-MS: Calculated for $C_5Cl_3{}^{15}N_2O^+$ $(M–H)^+$/z 210.9011. Observed: ***m/z*** 210.9012.

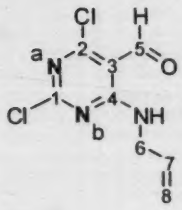

Synthesis of compound 2-4-3. To a stirred solution of **2-4-2** (4.52 g, 21.2 mmol) in CH_2Cl_2 (40 mL), allylamine (3.2 mL, 2.42 g, 42.4 mmol) was slowly added at -78 °C under N_2 atmosphere. The resulting mixture was stirred at -78 °C for 6h. The reaction was then quenched with H_2O (20 mL) and extracted with CH_2Cl_2 (180 mL). The organic layer was washed with H_2O (2 × 40 mL) and brine (100 mL), then dried over anhydrous Na_2SO_4. After filtration and evaporation of the solvent (rotavap), the crude product was purified by gravity silica gel chromatography (0-2% EA/Hex). The compound **2-4-3** was obtained as colorless liquid ($C_8H_7Cl_2N^{15}N_2O$, 3.63 g, 73%). R_f = 0.33 (10% EA/Hex).

^{1}H-NMR (400 MHz, $CDCl_3$) δ (ppm): 10.30 (C_5H, s, 1H), 9.36 (NHC_6, broad (br), s, 1H), 5.94-5.85 (C_7H, m, 1H), 5.27-5.20 (C_8H, m, 2H), 4.21 (C_6H, m, 2H).

^{13}C-NMR (100 MHz, $CDCl_3$) δ (ppm): 190.40 (C_5), 165.94, 162.70 (C_1, C_2), 161.5 (C_4), 132.11 (C_7), 117.53 (C_8), 106.62 (C_3), 43.46 (C_6).

^{15}N-NMR (40 MHz, $CDCl_3$) δ (ppm): 256.01 (^{15}N*a*, d, ^{2}J= 1.8 Hz), 245.22 (^{15}N*b*, d, ^{2}J= 1.8 Hz).

High-resolution EI-MS: Calculated for $C_8H_7Cl_2{}^{15}N_2{}^{14}NO^+$ (M^+)/z 233.9980. Observed: *m/z* 233.9980.

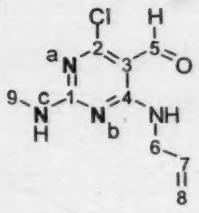

Synthesis of compound 2-4-4. To a stirred solution of **2-4-3** (3.00 g, 12.81 mmol) and methylamine hydrochloride (0.966 g, 14.09 mmol) in THF (40 mL), triethyl amine (5.4 mL, 38.4 mmol) was added at -78°C under N_2 atmosphere. The resulting mixture was stirred at -78°C for 3h. The reaction was then allowed to warm to 0°C then at rt overnight. The reaction mixture was quenched with NH_4Cl (10 mL). The solvent was removed under reduced pressure (rotavap), and the residul solid was dissolved in ethyl acetate (150 mL), washed with dH_2O (10 mL) and brine (5 mL) and dried over anhydrous Na_2SO_4. Filtration, evaporation of the solvent under reduced pressure (rotavap). The desired product **2-4-4** ($C_9H_{11}ClN^{15}N_3O$, 2.57 g, 87%) was obtained as crystalline white solid after gravity silica gel chromatography. R_f = 0.22 (10% EA/Hex). mp =156°C.

^{1}H-NMR (300 MHz, $CDCl_3$) δ(ppm): 10.05 (C_5H, s, 1H), 9.38 (NHC_6, br, s, 1H), 6.81 (HN*c*, d, J_{N-H} = 93.2Hz, 1H), 5.94-5.90 (C_7H, m, 1H), 5.27-5.15 (C_8H, m, 2H), 4.18 (C_6H, m, 2H), 3.01 (C_9, d, ^{3}J = 4.4 Hz, 3H).

^{13}C-NMR (100 MHz, $CDCl_3$) δ (ppm): 188.81 (C_5), 165.15, 162.11 (C_1, C_2), 161.9 (C_4), 133.53 (C_7), 116.39 (C_8), 101.48 (C_3), 42.87 (C_6), 28.17 (C_9).

^{15}N-NMR (40 MHz, $CDCl_3$) δ(ppm): 226.50 (N*b*, dd, $^2J_1$= 7.9 Hz, $^2J_2$= 6.8 Hz), 194.83 (N*a*, dd, $^2J_1$= 7.9 Hz, $^2J_2$= 6.1 Hz), 90.96 (N*c*, dd, $^2J_1$= 6.8 Hz, $^2J_2$= 6.1 Hz).

High-resolution ESI-MS: Calculated for $C_9H_{12}Cl^{15}N_3{}^{14}NO^+$ $(M+H^+)/z$ 230.0605. Observed: *m/z* 230.0607.

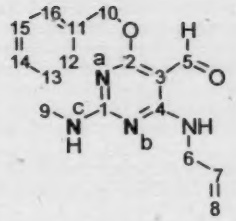

Synthesis of compound 2-4-5. Benzyl alcohol (0.67 g, 0.64, 6.1 mmol) was added to a stirred suspension of 95% NaH (0.183 G, 7.01 mmol) in THF (10 mL) at rt under N_2 atmosphere. After 15 min, the solution was cooled to 0ºC then a solution of compound **2-4-4** (0.7g, 3.05 mmol) in THF (20 mL) was added. The mixture was allowed to warm to rt then it was refluxed for 22 h. The mixture was then cooled to 0ºC and carefully quenched with saturated NH_4Cl (5 mL). The solvent was removed under reduced pressure (rotavap), and the residual solid was dissolved in diethyl ether (Et_2O), washed with dH_2O (100 mL) and brine (50 mL) and dried over anhydrous Na_2SO_4. Filtration, evaporation of the solvent under reduced pressure (rotavap) followed by gravity silica gel chromatography (0 to 5% EA/Hex) yielded **2-4-5** as a white solid ($C_{16}H_{18}N^{15}N_3O_2$, 0.75 g, 82%). R_f = 0.51 (30% EA/Hex). mp= 56ºC.

^{1}H-NMR (400 MHz, $CDCl_3$) δ(ppm): 10.01 (C_5H, s, 1H), 9.36 (NHC_6, br, s, 1H), 7.39-7.32 ($C_{12}H$-$C_{16}H$, m, 5H), 5.94-5.93 (C_7H, br, m, 1H), 5.49-5.13 (C_8H, $C_{10}H$, m, 4H), 4.19 (C_6H, br, s, 2H), 3.01 (C_9, s, 3H).

^{13}C-NMR (125 MHz, $CDCl_3$) δ (ppm): 185.88 (C_5), 171.26 (C_4), 163.32, 163.29 (C_1, C_2), 136.60 (C_{11}), 134.34 (C_7), 128.38, 127.77, 126.82 (C_{12}-C_{16}), 115.81 (C_8), 92.72 (C_3), 67.37 (C_{10}), 42.53 (C_6), 28.09 (C_9).

^{15}N-NMR (40 MHz, $CDCl_3$) δ(ppm): 195.57 (N*b*, br, d, ^2J = 6.6 Hz), 188.31 (N*a*, br, d, ^2J = 6.6 Hz), 87.91 (N*c*, m).

High-resolution ESI-MS: Calculated for $C_{16}H_{19}{}^{15}N_3{}^{14}NO_2{}^+$ $(M+H^+)/z$ 302.1414. Observed: *m/z* 302.1420.

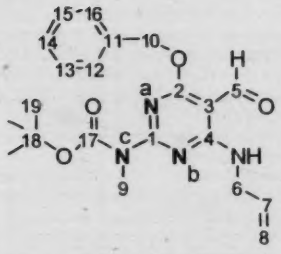

Synthesis of compound 2-4-6. To a stirred solution of compound **2-4-5** (1.16 g, 3.8 mmol), 4-N,N-dimethylaminopyridine (0.235 g, 1.9 mmol) and THF (20 mL), triethylamine (Et_3N) (1.16 g, 1.61 mL, 11.5 mmol) was added at rt under N_2 atmosphere. After stirring for 5 min, Boc_2O (1.26 g, 5.77 mmol) was added, and the mixture was stirred at rt for 18h. The reaction was quenched with dH_2O (5 mL) followed by removal of the solvent under reduced pressure (rotavap). The residual solid was dissolved in EA (100 mL) and washed with 10% aqueous citric acid (10 mL), dH_2O (2×10 mL), 5% aqueous $NaHCO_3$ (10 mL), and brine (10 mL). After drying the organic layer over anhydrous Na_2SO_4, filtration, and removal of the solvent under reduced pressure (rotavap), the residue compound **2-4-6** ($C_{21}H_{26}N^{15}N_3O_4$, 1.27 g, 83%) was obtained as a white crystalline solid. R_f = 0.38 (10% EA/Hex). mp = 54 °C.

^{1}H-NMR (400 MHz, $CDCl_3$) δ(ppm): 10.14 (C_5H, s, 1H), 9.22 (NHC_6, br, t, 1H), 7.42-7.35 (C_{12}H-C_{16}H, m, 5H), 5.93-5.91 (C_7H, m, 1H), 5.48 (C_{10}H, s, 2H), 5.25-5.13 (C_8H, m, 2H), 4.18 (C_6H, m , 2H), 3.38 (C_9H, s, 3H), 1.55 (C_{19}, s, 9H).

^{13}C-NMR (100 MHz, $CDCl_3$) δ(ppm): 187.65 (C_5), 171,48 (C_4), 162.74, 162.68 (C_1, C_2), 153.90 (C_{17}), 136.32 (C_{11}), 134.08 (C_7), 128.54, 128.20, 128.05 (C_{12}-C_{16}), 116.23 (C_8), 94.29 (C_3), 81.92 (C_{18}), 68.24 (C_{10}), 43.02 (C_6), 34.99 (C_9), 28.21 (C_{19}).

^{15}N-NMR (40 MHz, $CDCl_3$) δ(ppm): 212.21 (N*b*, dd, $^2J_1 = {}^2J_2$= 5.6 Hz d), 209.54 (N*a*, dd, $^2J_2$ = 5.6 Hz, $^2J_3$ = 5.0 Hz), 120.80 (N*c*, dd, $^2J_1$ = 5.6 Hz, $^2J_3$ = 5.0 Hz).

High-resolution ESI-MS: Calculated for $C_{21}H_{26}{}^{15}N_3{}^{14}NO_4Na^+$ $(M+Na^+)/z$ 424.1757. Observed: *m/z* 424.1760.

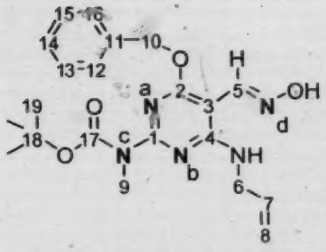

Synthesis of compound 2-4-7. To a stirred solution of **2-4-6** (1.42 g, 3.5 mmol) in pyridine (17 mL) hydroxylamine hydrochloride (0.491 g, 6.97 mmol) was added at rt under N_2 atmosphere. The mixture was refluxed for 3h then cooled to rt and quenched with dH_2O (10 mL). The solvent was removed (rotavap) and residual solid was dissolved in EA (100 mL), washed with dH_2O (20 mL) and brine (10 mL). The organic layer was dried over anhydrous Na_2SO_4, filtered, and evaporated to dryness (rotavap) to yield compound **2-4-7** ($C_{21}H_{27}N^{15}N_3O_4$, 1.60 g, 100%). R_f = 0.50 (30%EA/Hex).

^{1}H-NMR (300 MHz, $CDCl_3$) δ(ppm): 8.48 (C_5H, d, ^4J= 1.8 Hz, 1H), 8.05 (NHC_6, t, ^3J= 6.5 Hz, 1H), 7.60 (NOH, br, s, 1H), 7.41-7.28 (C_{12}H-C_{16}H, m, 5H), 5.99-5.89 (C_7H, m, 1H), 5.44 (C_{10}H, s, 2H), 5.28-5.10 (C_8H, m, 2H), 4.25-4.18 (C_6H, m, 2H), 3.41 (C_9H, s, 3H), 1.56 (C_{19}, s, 9H).

^{13}C-NMR (125 MHz, $CDCl_3$) δ (ppm): 166.88 (C_4), 160.16, 158.96 (C_1, C_2), 154.03 (C_{17}), 145.42(C_5), 136.74 (C_{11}), 134.76 (C_7), 128.33, 127.95 (C_{12}-C_{16}), 115.37 (C_8), 88.05 (C_3), 81.16 (C_{18}), 67.94 (C_{10}), 43.24 (C_6), 34.70 (C_9), 28.23 (C_{19}).

^{15}N-NMR (50 MHz, $CDCl_3$) δ (ppm): 348.01 (N*d*, s), 217.52 (N*b*, dd, $^2J_1 = {}^2J_2$= 5.4 Hz), 212.91 (N*a*, dd, $^2J_2$ = 5.4 Hz, $^2J_3$ = 5.0 Hz), 79.43 (N*c*, d, $^2J_1$ = 5.4 Hz, $^2J_3$ = 5.0 Hz).

High-resolution ESI-MS: Calculated for $C_{21}H_{26}{}^{15}N_4{}^{14}NO_4{}^+$ $(M+H^+)/z$ 418.2017. Observed: *m/z* 418.2017.

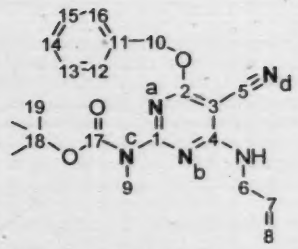

Synthesis of compound 2-4-8. Compound **2-4-7** (1.44g, 3.45 mmol), Et_3N (1.44 mL, 1.04g, 10.35 mmol), and THF (35 mL) were cooled to 0°C then trifluoroacetic anhydride (0.72 mL, 1.08 g, 5.17 mmol) was slowly added. After stirring for 15 min, the mixture was allowed to warm to rt then it was refluxed for 5 h. After cooling down to rt the reaction was quenched with dH_2O (10 mL) and the solvent was removed under reduced pressure (rotavap). The residual solid was dissolved in EA (150 mL), washed with dH_2O (2×30 mL), 10% aqueous citric acid (15 mL), dH_2O (30 mL), 5% aqueous $NaHCO_3$ (30 mL), and brine (30 mL). The organic layer was dried over anhydrous Na_2SO_4, filtered, and evaporated to dryness under reduced pressure (rotavap). Compound **2-4-8** was obtained as a white solid ($C_{21}H_{25}N^{15}N_4O_3$, 1.13g, 82%) after gravity silica gel chromatography (3% EA/Hex). R_f = 0.64 (30% EA/Hex). mp= 68°C.

^{1}H-NMR (400 MHz, $CDCl_3$) δ (ppm): 7.44-7.31 (C_{12}H-C_{16}H, m, 5H), 5.92-5.86 (C_7H, m, 1H), 5.46 (C_{10}H, s, 2H), 5.24 (C_8H, d, ^{3}J= 17.2, 1H), 5.18 (C_8H, d, ^{3}J= 10.4, 1H), 4.16 (C_6H, t, ^{3}J= 5.6 Hz, 2H), 3.35 (C_9H, s, 3H), 1.54 (C_{19}, s, 9H).

^{13}C-NMR (100 MHz, $CDCl_3$) δ (ppm): 170.21 (C_4), 163.89, 162.30 (C_1, C_2), 153.52 (C_{17}), 135.82 (C_{11}), 133.60 (C_7), 128.39, 128.08, 127.89 (C_{12}-C_{16}), 117.06 (C_8), 114.70 (C_5), 81.97 (C_{18}), 68.52 (C_{10}), 43.57 (C_6), 34.49 (C_9), 28.10 (C_{19}).

^{15}N-NMR (40 MHz, $CDCl_3$) δ (ppm): 274.65 (N*d*, s), 211.48 (N*a*, dd, $^2J_1$ = 6.0 Hz, $^2J_2$ = 1.4 Hz), 211.17 (N*b*, dd, $^2J_2$ = 6.0 Hz, $^2J_3$ = 1.4 Hz), 119.56 (N*c*, t, $^2J_1 = {}^2J_3$ = 6.0 Hz).

High-resolution ESI-MS: Calculated for $C_{21}H_{25}{}^{15}N_4{}^{14}NO_3Na^+$ ($M+Na^+$)/z 422.1731. Observed: *m/z* 422.1744.

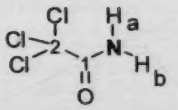

Synthesis of compound 2-4-11. Hexachloroacetone (35.33 g, 22.35 mL, 0.13 mol) in $CHCl_3$ (75 mL) was cooled to -178°C with under N_2 atmosphere. $^{15}NH_3$ gas was then added upon stirring over 3 h while the reaction mixture maintained at under -80°C. Then the mixture was allowed warm to -10°C for 1 h. Filtration and drying at rt under vacuum, yielded compound **2-4-11** as a white solid ($C_2H_2Cl_3{}^{15}NO$, 19.02 g, 95%). mp= 142°C.

^{1}H-NMR (400 MHz, $CDCl_3$) δ (ppm): 7.54 (H*a* or H*b*, d, J = 90.0 Hz, 1H). 7.27 (H*b* or H*a*, d, J = 90.0 Hz, 1H)

^{13}C-NMR (125 MHz, DMSO-d_6) δ (ppm): 162.95 (C_1), 93.11(C_2).

^{15}N-NMR (50 MHz, DMSO-d_6) δ (ppm): 102.02 (s).

ESI-MS Calculated for H_2CNO^+ $(M\text{-}CCl_3)^+$/z, 44. Observed, *m/z*, 44(100%).

FTIR (KBr, rt), (cm^{-1}): 3364-3177 (NH_2), 1688 (C=O), 1611 (C-N), 750-850 (C-Cl).

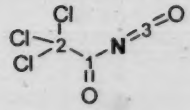

Synthesis of compound 2-4-12. In a 250-mL round-bottomed flask fitted with a magnetic stirrer, a thermometer, and a condenser carrying a calcium chloride tube (10.0 g. 0.06 mol) of **2-4-11** and 40 mL of 1.2-DCE were added. The mixture is cooled in an ice bath to 0 °C and stirred while (7.76 g. 5.18 mL, 0.6 mol) of oxalyl chloride was added all at once. The mixture was removed from the ice bath, stirred for 1 hour, and then heated to reflux at 83 °C with stirring for 24 hours. The solvent was distilled at 83 °C under atmosphere pressure. Distillation at 50-55 °C (130 mm Hg) yielded **2-4-12** (4.4 g. 60%), b.p. 80–85 °C (20 mm.), as a colorless liquid.

^{13}C-NMR (125 MHz, CD_3CN) δ (ppm): 159.79 (C_1), 131.38 (C_3), 92.28 (C_2).

^{15}N-NMR (50 MHz, DMSO-d_6) δ (ppm): 246.79 (s)

Infrared IR (KBr, rt), γ (cm^{-1}): 2243 (N=C=O), 1758 (C=O).

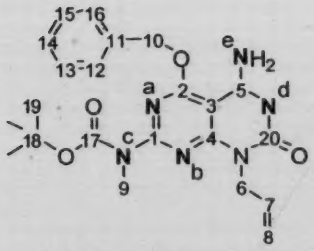

Synthesis of compound 2-4-10. To a solution of compound **2-4-9** (0.95 g, 2.38 mmol) in CH_2Cl_2 (18 mL), trichloroacetyl isocyanate **2-4-12** (2.7 g, 1.71 mL, 14.27 mmol) was added drop wise at 0 °C over a period of 15 min under N_2 atmosphere. After stirring for 2 hours at 0 °C, the mixture was allowed to warm to rt and was stirred for overnight. The solution of 7M NH_3 in CH_3OH (60 mL) was added under N_2 atmosphere at rt for 3h. Excess CH_3OH was removed under reduced pressure (rotavap) and the desired compound **2-4-10** was obtained as white solid ($C_{22}H_{26}N^{15}N_5O_4$, 0.53 g, 50%) after gravity silica gel chromatography (30-100% Hex/EA). R_f= 0.26 (50% Hex/EA). mp= 192 °C.

^{1}H-NMR (400 MHz, $CDCl_3$) δ(ppm): 7.47-7.39 (C_{12}H-C_{16}H, m, 5H), 6.95 (HN*e*, dd, ^1J = 93 Hz, ^2J = 6.79 Hz, 1H), 6.25-6.46 (HN*e*, br, m, 1H), 6.00-5.91 (C_7H, m, 1H), 5.60 (C_{10}H, s, 2H), 5.24 (C_8H, m, 2H), 4.16 (C_6H, m, 2H), 3.45 (C_9H, s, 3H), 1.59 (C_{19}, s, 9H).

^{13}C-NMR (100 MHz, $CDCl_3$) δ (ppm): 166.51 (C_4), 161.06, 161.00, (C_1, C_2), 160.52 (C_5), 155.69 (C_{17}), 153.31 (C_{20}), 153.08 (C_{21}, C_{24}), 135.10 (C_{11}),132.61 (C_7), 129.19, 128.80, (C_{12}-C_{16}), 117.66 (C_8), 86.16 (C_3), 82.81 (C_{22}, C_{25}), 77.59 (C_{18}), 70,32 (C_{10}), 44.91 (C_6), 35.17(C_9), 28.51 (C_{19}).

^{15}N-NMR (40 MHz, $CDCl_3$) δ(ppm): 218.95 (N*b*, dd, ^2J= 5.6 Hz, ^2J= 1.2 Hz), 216.83 (N*a*, dd, ^2J= 5.6 Hz, ^2J= 1.2 Hz), 200.61 (N*e*, d, ^2J= 5.8 Hz), 120.74 (N*d*, d, ^2J = 5.8 Hz), 120.74 (N*c*, dd, $^2J_1 = {}^2J_2 = 6.0$ Hz).

High-resolution ESI-MS: Calculated for $C_{22}H_{26}{}^{15}N_5{}^{14}NO_4Na^+$ $(M+Na^+)/z$ 466.1759. Observed: *m/z* 466.1801.

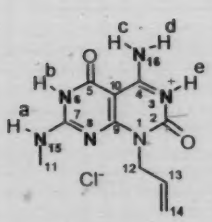

Synthesis of compound 2-4. Compound **2-4-10** (0.044 g, 0.1 mmol) in was dissolved in 4M solution of HCl in dioxane (4 mL) and the mixture was refluxed for 2 h. The white precipitate formed was filtered, washed with CH_2Cl_2 (5 × 10 mL), and dried on a filter. Compound **2-4** was obtained as a white solid (0.028 g, 100%).

HRMS (ESI) calcd for $C_{10}H_{13}{}^{15}N_5{}^{14}NO_4$ $(M+H^+)$ *m/z* 254.0977, found *m/z* 254.0978.

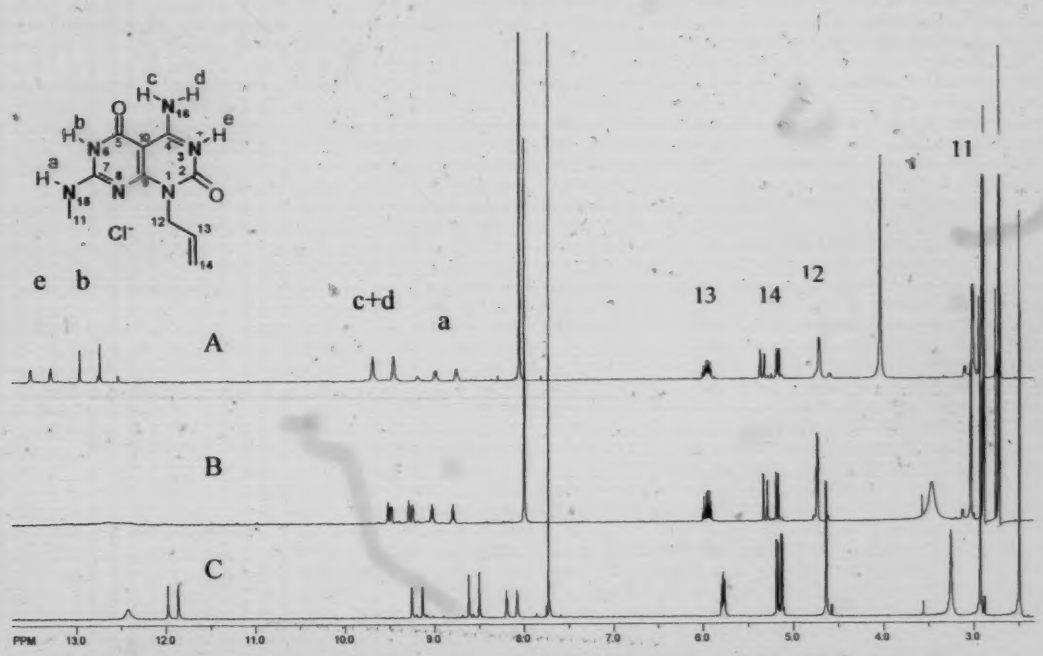

Figure 2. 27. ^{1}H NMR spectra of 2-4 in (A) DMF-d_7 (-50 °C, 500 MHz), (B) DMF-d_7 (27°C, 500 MHz), (C) 1:1 (v/v) $CDCl_3$–DMSO-d_6 (5 °C, 800 MHz). The assignments are given in Table 3.2. Note sharpening of the NH signals as polarity of the solvent and temperature decrease. Note that signal c and d overlap at -60 °C and are resolved at +27 °C.

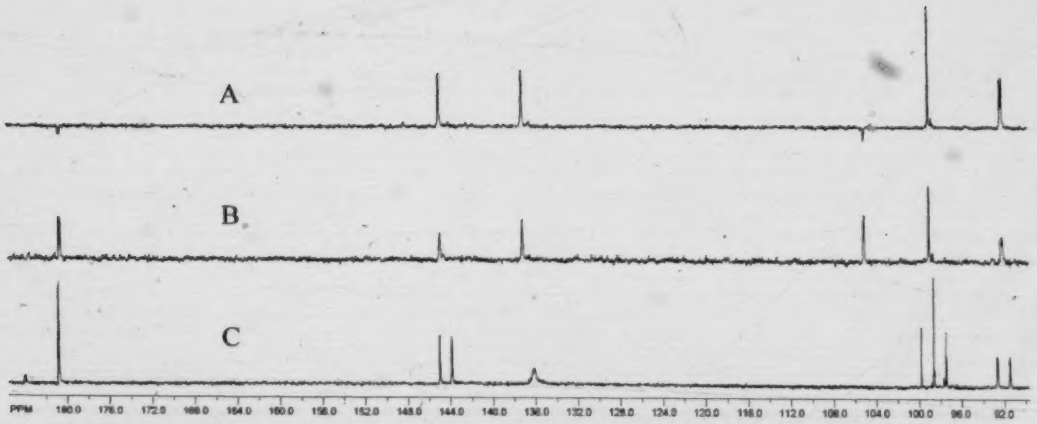

Figure 2. 28. ^{15}N NMR spectra of 2-4 in (A) DMF-d_7 (27 °C, 400 MHz, 10 hours, with NOEs) and (B) DMF-d_7 (27 °C, 500 MHz, 10 hours, no NOEs), 1:1 (v/v) $CDCl_3$–DMSO-d_6 (25 °C, 800 MHz) (27 °C, 500 MHz, 10 hours, no NOEs, coupled to H). Signal at 105 ppm in (A, B) is DMF.

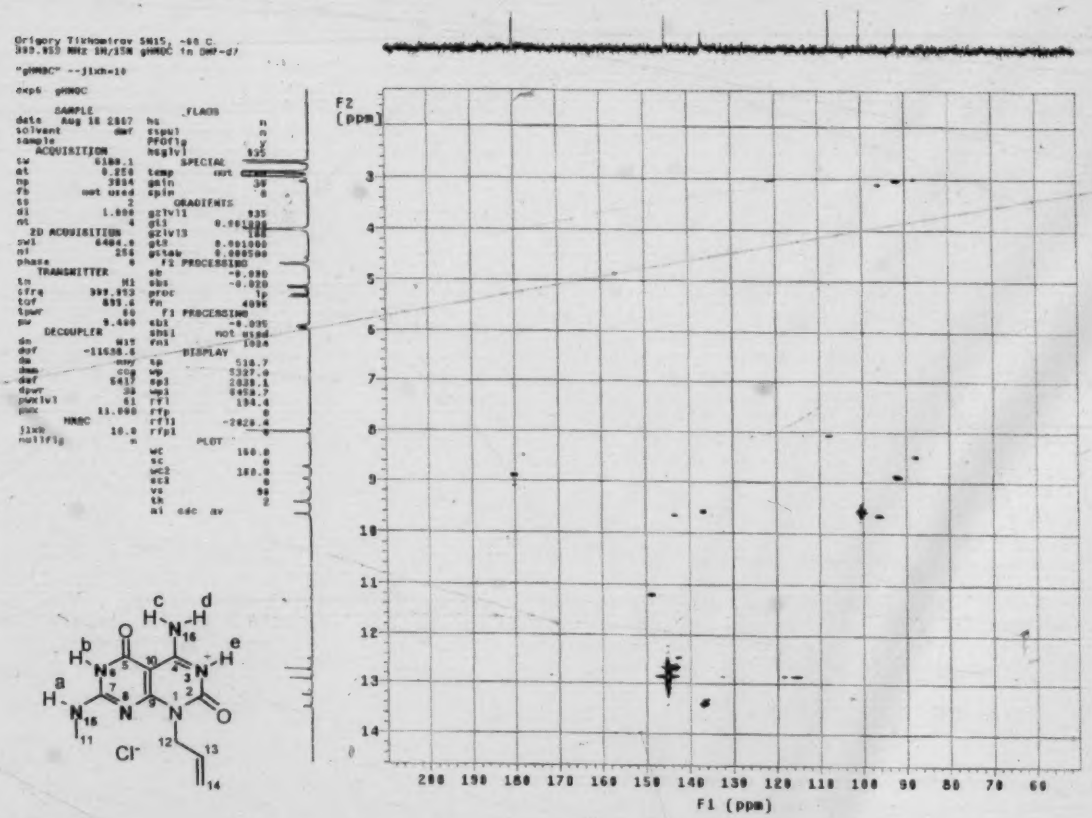

Figure 2. 29. ^{1}H-^{15}N HMQC spectrum of 2-4 in DMF-d_7 (-60 °C, 400 MHz) J_{xh} = 10 Hz.

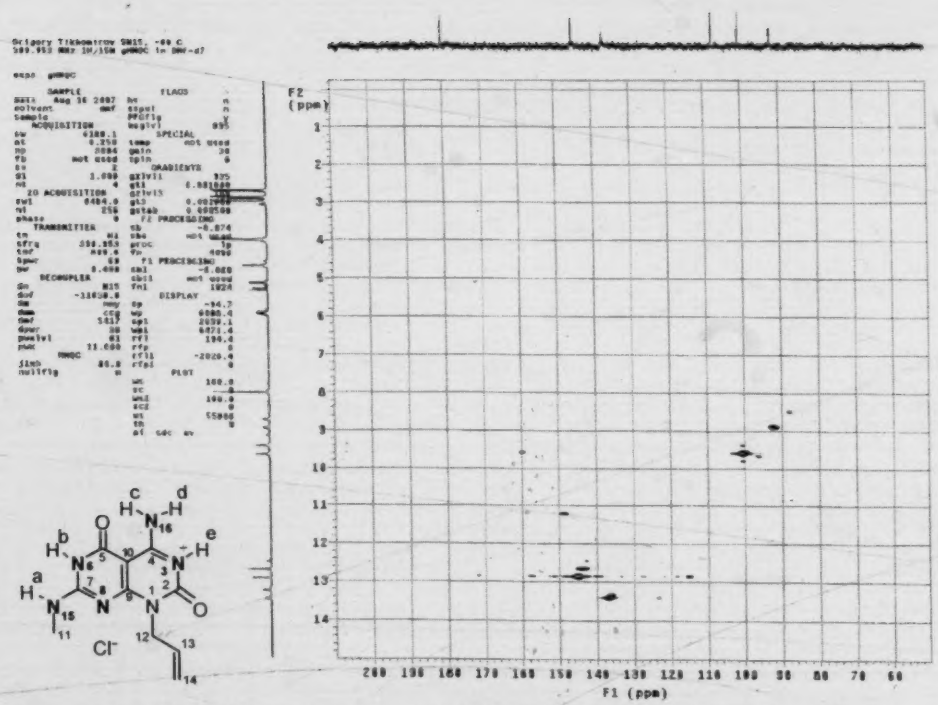

Figure 2. 30. ^{1}H-^{15}N HMQC spectrum of 2-4 in DMF-d_7 (-60 °C, 400 MHz) J_{1xh} = 90 Hz.

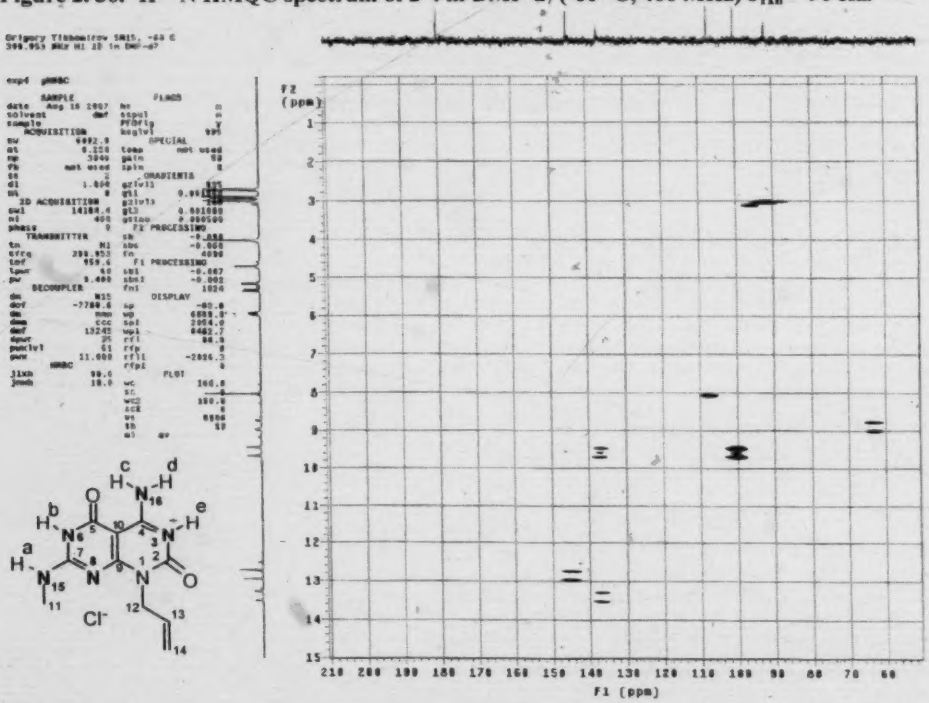

Figure 2. 31. ^{1}H-^{15}N HMBC spectrum of 2-4 in DMF-d_7 (-60 °C, 400 MHz) J_1 = 90 Hz, J_n = 10 Hz.

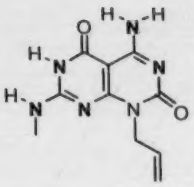

Synthesis of compound 2-5. 40 mg (0.141 mM) of **2-4** were dissolved in 200 mL of methanol (HPLC grade). 7M NH_3 (5 mL, 35 mM, 250 fold excess) in methanol was added to the solution. Immediate precipitation occurred. Solvent and excess ammonia were removed under reduced pressure and the precipitated was washed with water (5×20 mL) to remove NH_4Cl.

HRMS (ESI) calcd for $C_{10}H_{13}{}^{15}N_5{}^{14}NO_4$ (M+H$^+$) *m/z* 254.0977, found *m/z* 254.0975.

Compound **2-5** does not five NMR spectra in solution. Solid state NMR of **2-5** was discussed in detail before.

HRMS (ESI) calcd for $C_{10}H_{13}{}^{15}N_5{}^{14}NO_4$ (M+H$^+$) *m/z* 254.0977, found *m/z* 254.0975.

Sample for SEM was obtained by 5 min sonication of compound 5 in hot methanol and then drop casting the saturated solution on a carbon coated copper grid. Solubility of **5** in methanol is less than 0.1 g/L.

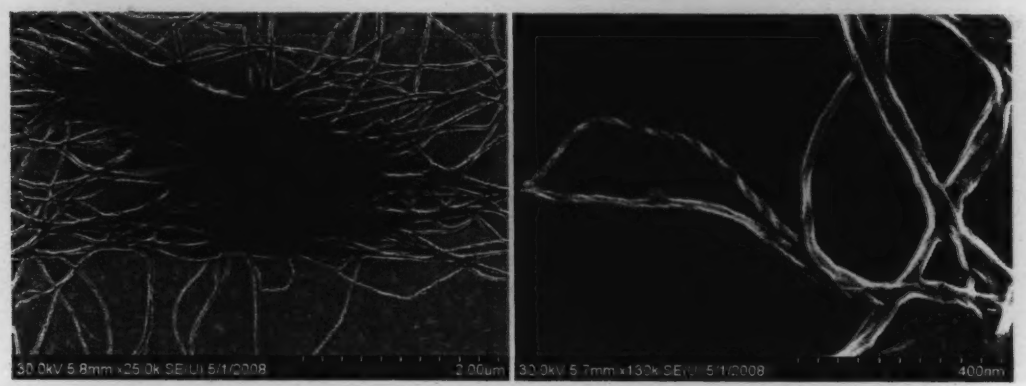

Figure 2. 32. SEM images of 2-5 (<0.1 mg/mL, MeOH, carbon film).

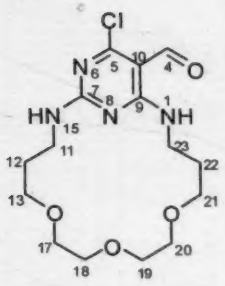

Synthesis of compound 2-7-2. To a solution of compound 2,4,6-Trichloro-pyrimidine-5-carbaldehyde (**2-7-1**) (21.22 g, 91.5 mmol) in THF (*1000 mL!*), 4,7,10-trioxa-1,13-tridecanediamine (20.1 g, 20.0 mL, 91.5mmol), followed by triethylamine (18.5 g, 25.5 mL, 183 mmol) were added slowly at 0°C under N_2 atmosphere. The reaction mixture was stirred at rt for 14 hs. The reaction was quenched with saturated aqueous NH_4Cl (10 mL) and the solvent was removed under reduced pressure (rotovap). The solid obtained was dissolved in CH_2Cl_2 (200 mL). The organic layer was washed with dH_2O (2 × 100 mL) and brine (50 mL), then dried over anhydrous Na_2SO_4. After filtration and evaporation of the solvent (rotovap) the crude product was purified by gravity silica gel chromatography (5 to 10%). The desired compound **2-7-2** was obtained as a white solid (1.31 g, 4%).

R_f = 0.40 (15% EA/Hex). mp = 162 °C

^{1}H NMR (400 MHz, $CDCl_3$) δ (ppm): 10.00 (HC_5, major, s, 1H), 10.21 (HC_5, minor, s), 9.19 ($HNC_{1'}$, major, t, J = 4.2 Hz, 1H), 9.04 ($HNC_{1'}$, minor, t, J = 4.2 Hz, 1H), 5.54 ($HNC_{1'}$, br. s, 1H), 3.70 – 3.43 (H11,13, 17, 18, 19, 20, 21, 23, m, 16H), 1.88 – 1.66 (H12, 22, m, 4H)

^{13}C NMR (100 MHz, $CDCl_3$) δ (ppm): 188.9 (C_4), 167.0, 165.9, 162.6 (C_5, C_7, C_9), 102.6 (C_{10}), 71.26, 71.08, 70.77, 70.25, 69, 56, 68.78, 68.65, 67.61 ($C_{11,13,17,18,19,20,21,23}$), 67.3 ($C_{24}$), 31.5, 30.5 ($C_{12,22}$)

HRMS (ESI) calcd for $C_{15}H_{24}ClN_4O_4$ (M+H)/z, 359.1481. Observed 359.1480.

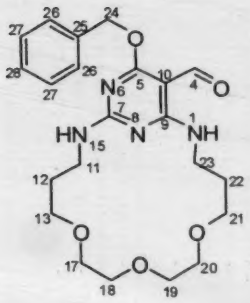

Synthesis of compound 2-7-3 Benzyl alcohol (0.57 g, 0.55 mL, 5.3 mmol) was added to a stirred suspension of 95% NaH (0.51 g, 21.2 mmol) in THF (10 mL) at rt under N_2 atmosphere. After 15 min the solution was cooled to 0°C, then a solution of compound **7-2** (1.90 g, 5.3 mmol) in THF (40 mL) was added. The mixture was allowed to warm to rt, then it was refluxed for 24 h. The mixture was then cooled to 0°C and carefully quenched with sat NH_4Cl (10 mL). The solvent was removed under reduced pressure (rotovap), and the residual solid was dissolved in Et_2O, washed with dH_2O (100 mL) and brine (50 mL) and dried over anhydrous Na_2SO_4. Filtration, evaporation of the solvent under reduced pressure (rotovap) followed by silica gel chromatography (5 to 10% EA/Hex) yielded **2-7-3** as a white solid (2.00 g, 88%).

R_f = 0.35 (15% EA/Hex). mp = 163 °C

^{1}H NMR (400 MHz, $CDCl_3$) δ (ppm): 9.95 (HC_5, major, s, 1H), 9.12 ($HNC_{1'}$, major, t, J = 4.6 Hz, 1H), 9.03 (HNC_{23}, minor, t, J = 4.6 Hz, 1H), 7.42 – 7.22 (H26, 27 ,28, m, 5H) 5.32 (H24, s, 2H), 5.11 (HNC_{15}, t, = 4.6 Hz, 1H), 3.70 – 3.45 (H11,13, 17, 18, 19, 20, 21, 23, m, 16H), 1.90 – 1.76 (H12, 22, m, 4H)

^{13}C NMR (100 MHz, $CDCl_3$) δ (ppm): 185.9 (C_4), 163.7, 162.9, 160.6 (C_5, C_7, C_9), 136.7 (C_{25}), 128.5, 127.9, 127.7 ($C_{26, 27, 28}$), 102.6 (C_{10}), 71.26, 71.08, 70.77, 70.25, 69, 56, 68.78, 68.65, 67.61 ($C_{11, 13, 17, 18, 19, 20, 21, 23}$), 56.2 ($C_{24}$) 30.3, 30.1 ($C_{12, 22}$)

HRMS (ESI) calcd for $C_{22}H_{31}N_4O_5$ (M+H)/z, 431.2289. Observed 431.2289.

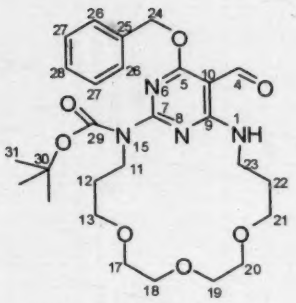

Synthesis of compound 2-7-4 To a stirred solution of compound **2-7-3** (0.89 g, 2.1 mmol), DMAP (0.25 g, 1.1 mmol) and THF (30 mL), Et_3N (0.67 g, 0.9 mL, 6.3 mmol) was added at rt under N_2 atmosphere. After stirring for 5 min, Boc_2O (0.54 g, 2.5 mmol) was added, and the mixture was stirred at rt for 20 h. The reaction was quenched with dH_2O (10 mL) followed by the removal of the solvent under reduced pressure (rotovap). The residual solid was dissolved in EA (200 mL) and washed with 10 % aqueous citric acid (50 mL), dH_2O (2 × 50 mL), 5% aqueous $NaHCO_3$ (50 mL) and brine (50 mL). After drying the organic layer over anhydrous Na_2SO_4, filtration and removal of the solvent under reduced pressure 9rotovap), the residue was purified by flash silica gel chromatography (0 to 8 % EA/Hex). The desired compound **2-7-4** (0.98 g, 90%) was obtained as a white crystalline solid.

R_f = 0.40 (15% EA/Hex). mp = 105 °C

^{1}H NMR (400 MHz, $CDCl_3$) δ (ppm): 10.07 (HC_5, s, 1H), 9.05 (HN1, t, J = 5.3 Hz, 1H), 7.44 – 7.24 (H26, 27, 28, m, 5H) 5.45 (H24, s, 2H), 4.03 (H11, m, 2H), 3.70 – 3.45 (H13, 17, 18, 19, 20, 21, 23, m, 16H), 2.00 – 1.80 (H12, 22, m, 4H), 1.53 ((H31, m, 9H)

^{13}C NMR (100 MHz, $CDCl_3$) δ (ppm): 187.5 (C_4), 171.3 (C_{29}) , 162.7, 161.4, 153.4 (C_5, C_7, C_9), 136.3 (C_{25}), 128.5, 128.2, 128.1 ($C_{26, 27, 28}$), 94.2 (C_{10}), 81.8 (C_{11}), 71.16, 70.86, 70.21, 70.02, 69.56, 68.72, 68.28 ($C_{13, 17, 18, 19, 20, 21, 23}$), 46.0 ($C_{24}$), 38.84 ($C_{30}$), 30.1, 29.4 ($C_{12, 22}$), 28.3 ($C_{31}$)

HRMS (ESI) calcd for $C_{27}H_{39}N_4O_7$ (M+H)/z, 531.2813. Observed 531.2814.

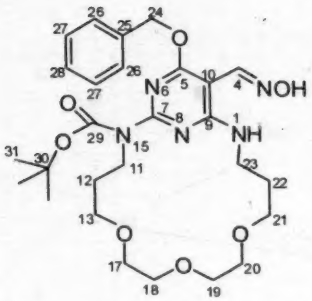

Synthesis of compound 2-7-5. To a stirred solution of **2-7-4** (0.530 g, 1.0 mmol) in pyridine (20 mL) $NH_2OH{\cdot}HCl$ (0.139 g, 2.0 mmol) was added at rt. The mixture was stirred for 3 h. Pyridine was removed under reduced pressure and the residual solid was dissolved in EA (200 mL), washed with dH_2O (50 mL) and brine (25 mL). The organic layer was dried over anhydrous Na_2SO_4, filtered, and evaporated to dryness under reduced pressure to yield compound **2-7-5** (0.545 g, 100%), that was used in the next step without purification. R_f = 0.20 (15% EA/Hex).

HRMS (ESI) for $C_{27}H_{40}N_5O_7$ ($M+H^+$) *m/z* calcd 546.2922, found 546.2924.

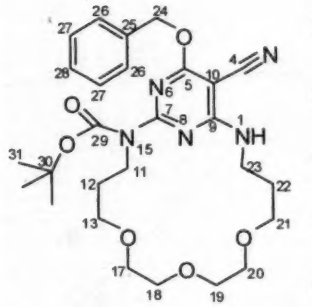

Synthesis of compound 2-7-6 2,4,6-Trichloro-[1,3,5]triazine (TCT, 0.366 g, 2.0 mmol) was added to DMF (3 mL), at r.t. After the formation of a white solid (thick suspension formed), the reaction was monitored by TLC until complete disappearance of TCT, Then **2-7-5** (0.567 g, 1.0 mmol) in DMF (5 mL) was added. After the addition (instant brown coloring and heating up occured), triethylamine (0.3 mL, 2 mmol) was added, and the mixture was stirred at room temperature, monitored by TLC until completion (8 h). Water (10 mL) was added, and the product was extracted with 50 mL of EA, and the organic phase washed with 15 mL of a saturated solution of K_2CO_3, followed by 10% citric acid, water, and brine. The organic layer was dried over Na_2SO_4 and the solvent evaporated to yield pure **2-7-6** as a white solid (0.516 g, 98%).

R_f = 0.25 (15% EA/Hex). mp = 152 °C

^{1}H NMR (400 MHz, $CDCl_3$) δ (ppm): 7.54 – 7.14 (H26, 27, 28, m, 5H) 5.42 (H24, s, 2H), 5.15 (HN1, br.s., 1H), 4.02 (H11, m, 2H), 3.70 – 3.45 (H13, 17, 18, 19, 20, 21, 23, m, 16H), 2.00 – 1.80 (H12, 22, m, 4H), 1.54 ((H31, m, 9H)

^{13}C NMR (100 MHz, $CDCl_3$) δ (ppm): 170.4 (C_{29}) , 164.2, 160.5, 153.3 (C_5, C_7, C_9), 136.0 (C_{25}), 128.5, 128.2, 128.1 ($C_{26, 27, 28}$), 115.1 (C_4), 94.2 (C_{10}), 81.8 (C_{11}), 71.10, 70.91, 70.20, 70.15, 69.42, 68.58, 68.32 ($C_{13, 17, 18, 19, 20, 21, 23}$), 45.9 ($C_{24}$), 39.7 ($C_{30}$), 30.1, 29.2 ($C_{12, 22}$), 28.2 ($C_{31}$)

HRMS (ESI) calcd for $C_{27}H_{39}N_4O_7$ (M+H)/z, 528.2817. Observed 528.2817.

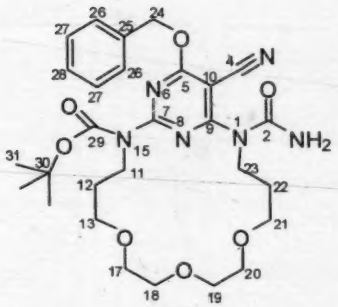

Synthesis of compound 2-7-7. To a solution of compound **2-7-6** (0.30 g, 0.56 mmol) in CH_2Cl_2 (10 mL), N-trichlorometylcarbonylisocyanate (0.56 g, 0.40 mL, 3.4 mmol) was added at 0°C under N_2 atmosphere. After stirring for 1h at 0°C, the mixture was allowed to warm to rt and was stirred for an additional 48 h. The reaction mixture was cooled to 0°C and carefully quenched with dH_2O (10 mL, exothermic reaction!) followed by 5% aqueous $NaHCO_3$ (10 mL). The product was extracted with CH_2Cl_2 (100 mL) and the resulting organic layer was washed with dH_2O (2 × 50 mL), and brine (100 mL) and dried over anhydrous Na_2SO_4. After filtration and evaporation of the organic solvent under reduced pressure (rotovap), TLC of **2-7-7** showed two spots with R_f = 0.70 and 0.20 (50% EA/Hex). The mixture was used in the next step without separation.

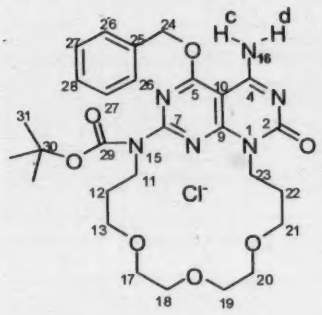

Synthesis of compound 2-7-8. A solution of compound **2-7-7** (0.30 g, 0.56 mmol) in CH_2Cl_2 (8 mL) and 7N NH_3 in CH_3OH was stirred under N_2 atmosphere at rt for 5 h. Solvents were removed under reduced pressure (rotovap) and the desired compound **2-7-8** was obtained as a white paraffin-like solid (0.18 g, 61%), which was pure as shown by MS and NMR. R_f = 0.15 (EA). mp = 164 °C

^{1}H NMR (400 MHz, $CDCl_3$) δ (ppm): 7.52 – 7.40 (H26, 27, 28, m, 5H), 5.42 (Hc, s, 1H), 5.42 (Hd, br.s., 1H), 5.60 (H24, s, 2H), 4.15 (H23, m, 2H), 4.02 (H11, m, 2H), 3.70 – 3.45 (H13, 17, 18, 19, 20, 21, m, 16H), 2.00 – 1.87 (H12, 22, m, 4H), 1.56 (H31, m, 9H)

^{13}C NMR (100 MHz, $CDCl_3$) δ (ppm): 166.5 (C_5), 160.65, 160.60, 156.0, (C_4, C_7, C_9), 152.9 (C_2), 134.0 (C_{25}), 128.5, 128.2, 128.1 ($C_{26, 27, 28}$), 114.1 (C_4), 85.8 (C_{10}), 82.4 (C_{30}), 71.10, 70.91, 70.20, 70.15, 69.42, 68.58, 68.32 ($C_{13, 17, 18, 19, 20, 21, 23}$), 46.2 ($C_{24}$), 41.1 ($C_{30}$), 28.9, 28.4 ($C_{12, 22}$), 28.2 ($C_{31}$).

HRMS (ESI) calcd for $C_{28}H_{39}N_6O_7$ (M+H)/z, 571.2875. Observed 571.2863.

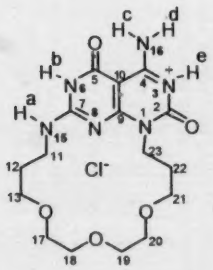

Synthesis of compound 2-7. Compound **2-7-8** (0.086 g, 0.15 mmol) in was dissolved in 4M solution of HCl in dioxane (4 mL) and the mixture was refluxed for 2 h. The white precipitate formed was filtered, washed with CH_2Cl_2 (5 × 10 mL), and dried on a filter. Compound **2-7** was obtained as a white solid (0.057 g, 100%). HRMS (ESI) calcd for $C_{16}H_{25}N_6O_5$ (M+H$^+$) *m/z* 381.1881, found *m/z* 381.1851.

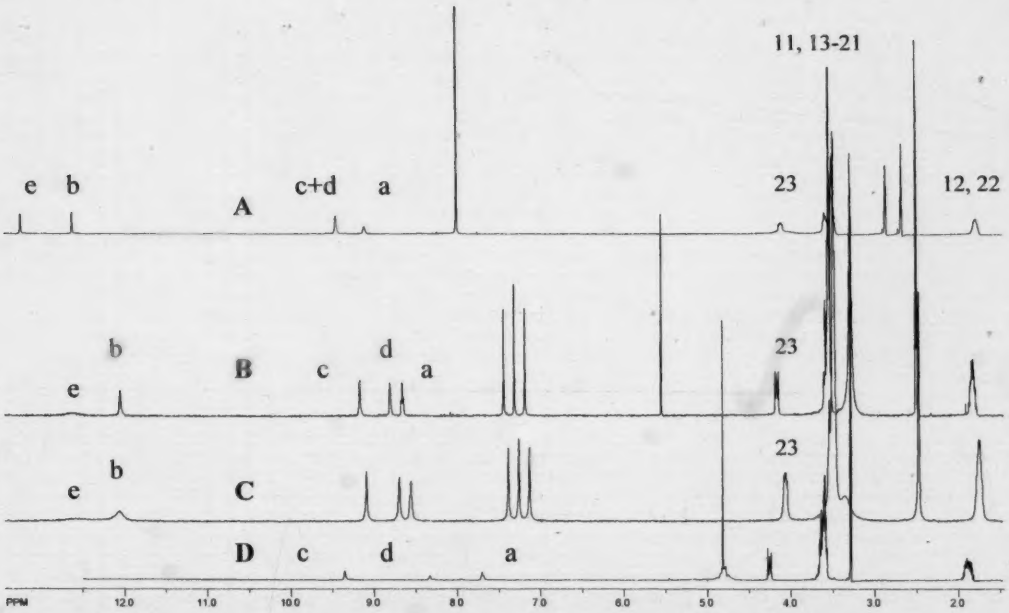

Figure 2. 33. ^{1}H NMR spectra of 2-7 in (A) DMF-d_7 (-60 °C, 400 MHz), (B) 1:1 (v/v) CD_2Cl_2–DMSO-d_6 (27 °C, 400 MHz), (C) DMSO-d_6 (27 °C, 400 MHz), (D) CD_3OH (27 °C, 400 MHz, presaturation). Note sharpening of the NH signals as polarity of the solvent and temperature decrease.

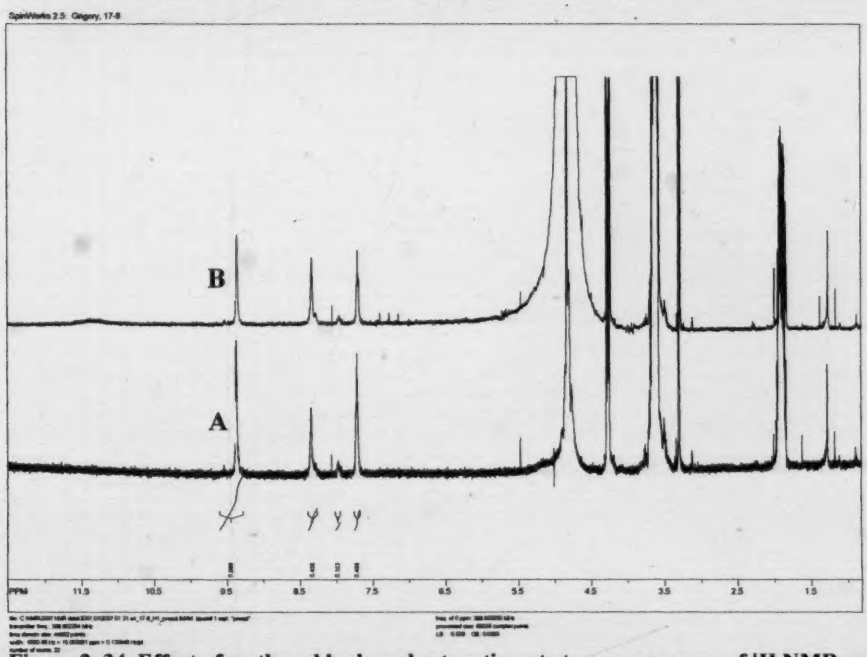

Figure 2. 34. Effect of methanol hydroxyl saturation at rt on appearance of 'H NMR spectra of 2-7 in CD_3OH. Note the integral ratio of Hd and Hc which is 0.44 if the presaturation is used and 0.70 with no presaturation.

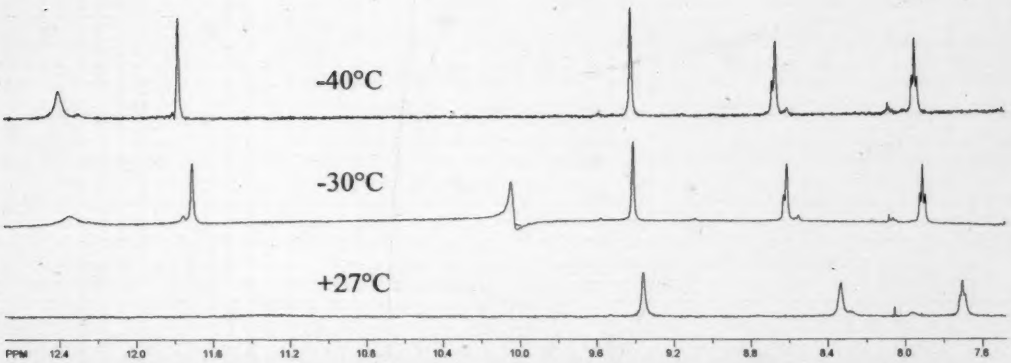

Figure 2. 35. Effect of temperature on appearance of low field portion of ^{1}H NMR spectra of 2-7 in CD_3OH (no presaturation used). Note complete absence of Hb and He at room temperature also observed for water solutions of 1. Note the presence of satellite peaks for NH signals. Unphased signal at ~10 ppm is an artifact (offset transfer of frequency).

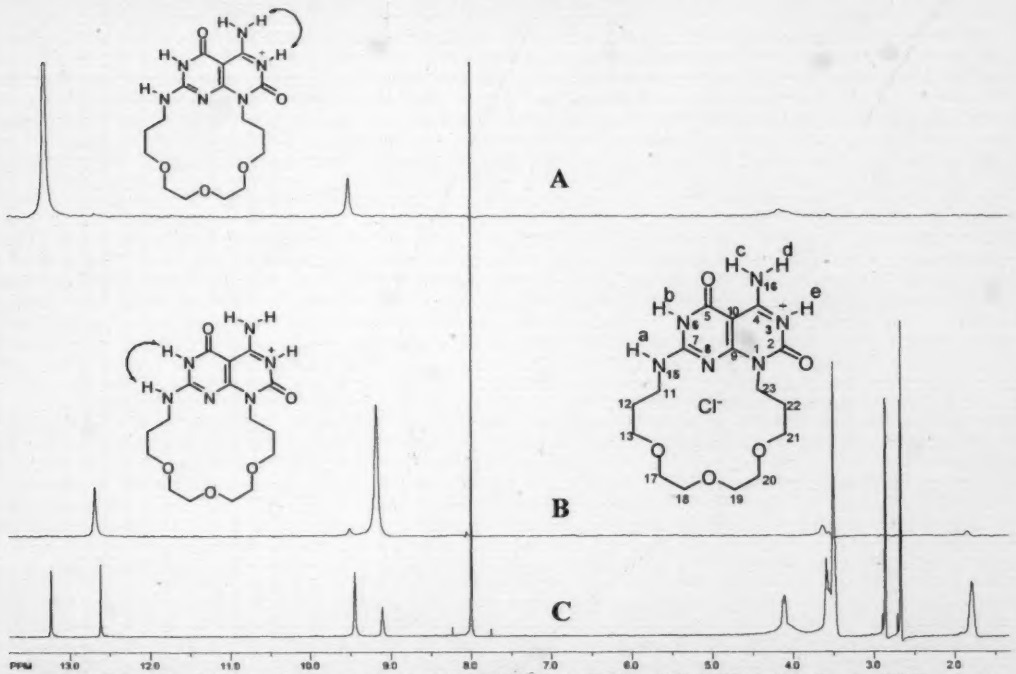

Figure 2. 36. Key NOEs observed for 2-7 in DMF-d_7 (-50 °C, 400 MHz). (A) Cycle NOE spectra saturating He, (B) Cycle NOE spectra saturating Ha, (C) ^{1}H NMR spectra for comparison. Assignments of protons signals are based on HMQC, HMBC, and COSY (not shown).

SEM characterization of 2-2 drop cast on carbon film from NMR tubes.

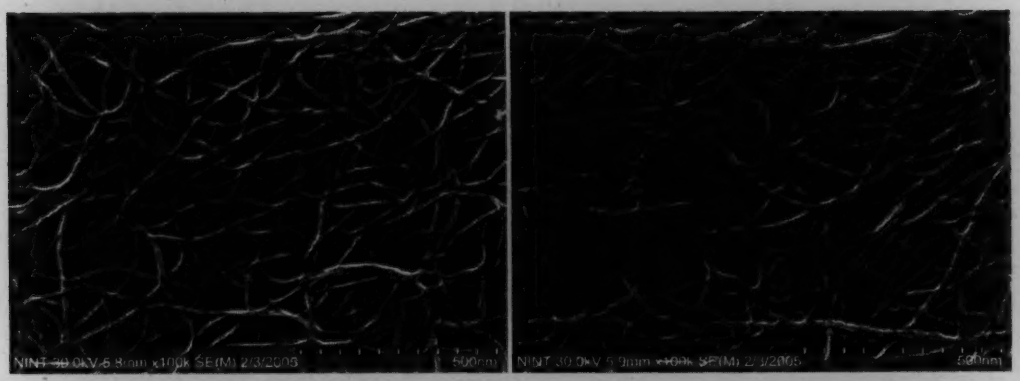

Figure 2. 37. SEM images of 2-2 (7 mg/mL, DMSO, carbon film).

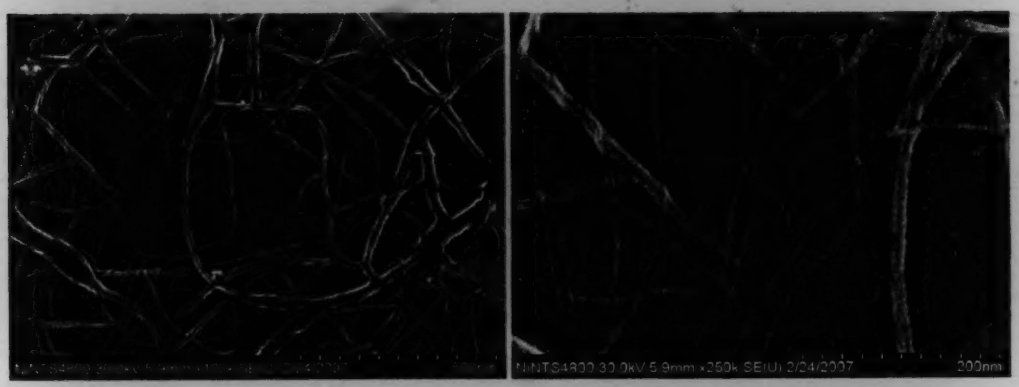

Figure 2. 38. SEM images of 2-2 (4 mg/mL, 1:1 (v/v) $CDCl_3$–DMSO-d_6, carbon film).

Figure 2. 39. SEM images of 2-2 (3 mg/mL, 3:1 (v/v) $CDCl_3$–DMSO-d_6, carbon film).

Figure 2. 40. SEM images of 2-2 (2.4 mg/mL, CD_3OH, carbon film).

Figure 2. 41. SEM images of 2-2 (4.3 mg/mL, DMF-d_7, carbon film).

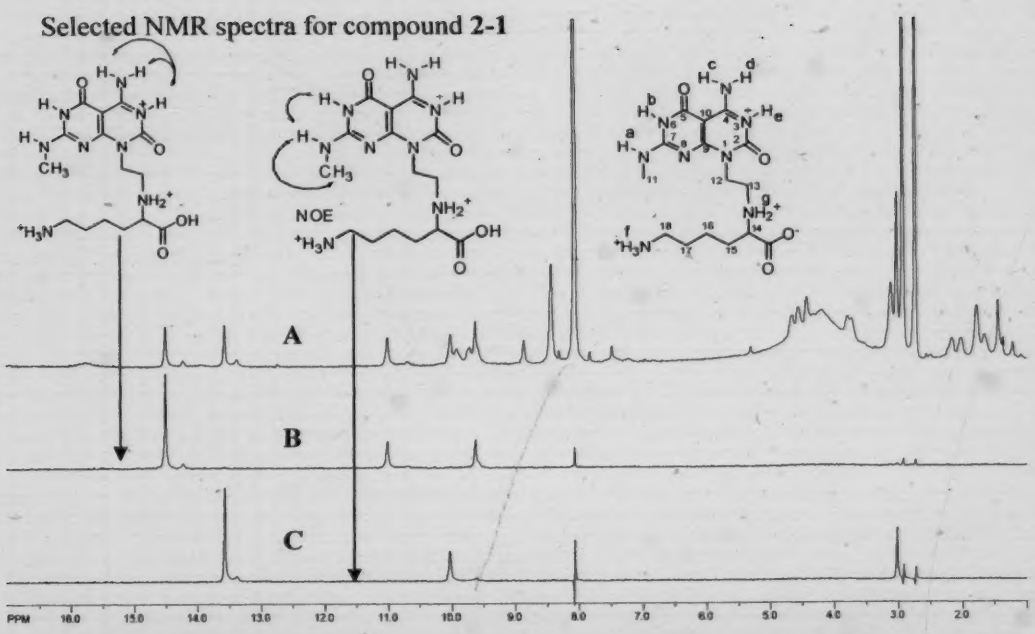

Figure 2. 42. Key NOEs observed for 2-1 in DMF-d_7 (-60 °C, 400 MHz). (A) ^{1}H NMR spectrum, (B) cycle NOE spectrum obtained after irradiation of He, (C) cycle NOE spectrum obtained after irradiation of Hb. Assignments are made based on HMBC, HMQC, and COSY.

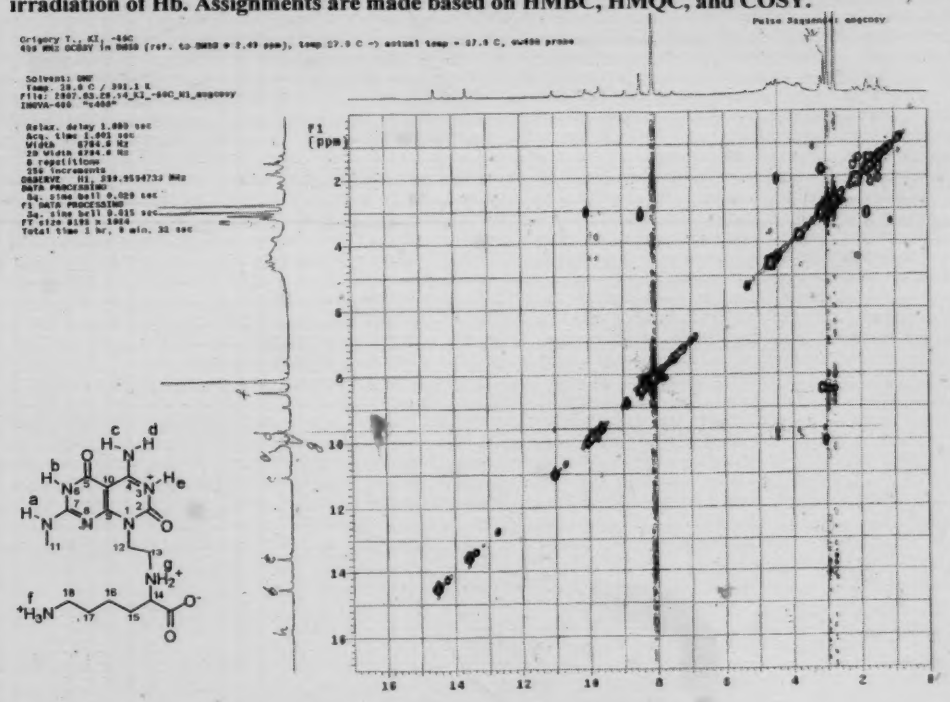

Figure 2. 43. COSY spectrum of 2-1 in in DMF-d_7 (-60 °C, 400 MHz).

Solid State NMR. Ultrahigh-field solid-state ^{1}H MAS NMR and two-dimensional ^{1}H-^{1}H and ^{1}H-^{15}N correlation experiments were carried out on a Bruker AVANCE-II 900 instrument with a 21.1 T magnetic field strength and operating at 900.08 and 91.20 MHz (National Ultra-high Field NMR Facilities in Ottawa). Larmor frequencies for ^{1}H and ^{15}N, respectively. The experiments were performed with a 1.3 mm double resonance CP MAS probe enabling a MAS frequency of 60 kHz. The ^{1}H MAS NMR spectra were obtained with 16 scans and a recycle delay of 5 s. The ^{1}H-^{1}H 2D DQ correlation experiments employed one rotor period (16.67 μs) of back-to-back (BABA) DQ excitation and reconversion. The ^{1}H 90° pulse length was 1.5 μs. The sweep width in the DQ dimension was 30 kHz and the States method was used for quadrature detection in the indirect dimension.[97-99] Two experiments, each with 16 scans, were acquired at each of the 40 t_1 increments. The 2D ^{1}H-^{15}N CP-HETCOR experiments employed 1 ms of ^{1}H to ^{15}N cross-polarization with ^{1}H and ^{15}N nutation frequencies of 40 and 100 kHz, respectively. Weak ^{1}H cw decoupling with a ^{1}H nutation frequency of 10 kHz was applied during the acquisition period. The sweep width in the indirect ^{1}H dimension was 30 kHz and the States method was used for quadrature detection in the indirect dimension. Two experiments, each with 16 scans were acquired at each of the 24 t_1 increments. The recycle delay in these 2D experiments was 5 s.

Solid-state ^{13}C and ^{15}N CP MAS NMR and two-dimensional ^{15}N-^{15}N correlation experiments were carried out on a Bruker AVANCE 200 instrument with a 4.7 T magnetic field strength and operating at 200.5, 50.42, 20.32 MHz Larmor frequencies for ^{1}H, ^{13}C, and ^{15}N, respectively. The experiments were performed with a 7 mm double resonance CP MAS probe. The ^{13}C and ^{15}N experiments were carried out at MAS

frequencies of 7 and 4 kHz with cross-polarization contact times of 2 and 10 ms, respectively, employing recycle delays of 5 s and SPINAL-64 ^{1}H decoupling with a ^{1}H nutation frequency of 46 kHz during the acquisition period. The ^{13}C and ^{15}N CP MAS NMR spectra were acquired with 8000 and 64 scans, respectively. The 2D ^{15}N-^{15}N DQ correlation experiments were performed with the $SR26_4^{11}$ symmetry-based dipolar recoupling sequence with 8 ms of DQ excitation and reconversion with a ^{15}N recoupling nutation frequency of 26 kHz and a ^{1}H cw decoupling nutation frequency of 77 kHz. The 2D ^{15}N-^{15}N refocused INADEQUATE experiment was carried at a MAS frequency of 4 kHz MAS with a half-echo delay time of 10 ms. During the DQ excitation, evolution, and reconversion periods, ^{1}H SPINAL-64 decoupling was applied with a ^{1}H nutation frequency of 46 kHz. For both ^{15}N-^{15}N correlation experiments, the States method was used for quadrature detection in the indirect dimension and 64 t_1 increments, each with two experiments, were acquired. The dipolar $SR26_4^{11}$ spectra were acquired with 16 scans per experiment while the J-coupling INADEQUATE spectra were acquired with 128 scans per experiment.

^{1}H and ^{13}C chemical shifts were referenced to TMS using adamantane as a secondary reference by setting the ^{1}H signal to 1.74 ppm and the downfield ^{13}C signal to 38.48 ppm. ^{15}N chemical shifts were referenced to liquid ammonia using glycine as a secondary reference by setting the ^{15}N signal to 32.1 ppm. The shifts can be converted to the chemical shift scale referenced with respect to CH_3NO_2 by subtracting 379.5 ppm.

X-ray Powder Diffraction. Samples were prepared according to the following two methods. Method 1: A thin film was prepared on an amorphous glass cover slip (SPI

supplies no. 1021, 22 mm diameter and 0.15 mm thick) by drop-casting a solution (0.25 g/L in) and drying it, then repeating this cycle ca. 200×. Method 2: A solution of compound **2-4** (0.25 g/L MeOH) was concentrated at room temperature under atmospheric pressure. Powder of **2-5** was prepared as described above for solid state NMR samples. The resulting powder was then ground and placed between two amorphous tapes. The samples were analyzed on a Bruker D8 Discover equipped with Cu K_α source and Bruker HiStar GADDS detector. The first sample was analyzed in a glancing angle, and the second was investigated in transmission mode using a beam stopper. Control experiments with the glass slide and the tape were carried out as well.

3. Assembly of Hydrophobic Organic Nanotubes

3.1. Objectives

Assembly of organic molecules into higher order aggregates has been previously studied and discussed, with a nanotubular architecture being the target. Most of the nanotubes obtained were characterized as either polydisperse single tubes or mixtures of randomLy oriented polydisperse nanotubular assemblies. To realize the full potential of this promising class of materials, a strategy to assemble nanotubes into larger, uniform, micrometer sized architectures has to be developed. This is particularly important for integrating nanotubes into functional devices, thus merging bottom up and top down nanofabrication approaches.

Self-assembled nanotubes have fascinating properties as highlighted in Chapter 1. In order to use these one-dimensional structures for applications (electronic devices, storage and delivery systems, templating architectures, etc.) their surface functionality and processing needs to be tailored to control higher order architectures.

The main goal of this study is to take a conventional system – Rosette Nanotubes – and study their higher order self-organization, or inter-RNT interactions. *Assembly of self-assembled* nanotubes is conceptually an attempt to understand and control hierarchical multi-step self-assembly processes that mimic complex biological systems. Developing methods to control nanotube organization could potentially allow for the development of a multitude of nanotube-based functional nano and micro-structures.

3.2. Overview of known nanotubes assemblies

Analysis of the literature related to self-assembled nanotubes shows that individual nanotubes have been the ultimate supramolecular target. Subsequent association of the nanotubes has rarely been reported. In fact, the aggregation of nanotubes has been considered undesirable and was avoided in order to better characterize individual nanotubes. Even though a number of interesting nanotube aggregates/arrays made of individual nanotubes were observed judging from published images, they were not sufficiently characterized. It was reported, for instance, that self-assembled nanotubes can organize into discrete bundles[37] that can assume a helical organization.[31, 37, 64] Lipid nanotubes can form continuous hexagonal phases if they are liquid crystalline.[45, 100]

Formation of various nanotube bundles and other nanotube aggregates is known for carbon,[101, 102] inorganic,[103, 104] hybrid silica,[105] and peptide[106] nanotubes. The formation of the nanotubes is concomitant with the growth of the corresponding bundles. In most cases the shape and the size of the resulting nanotube structures are not controllable. The highest level of aggregate morphology control has been achieved for CNT bundles using a combination of lithography and directed growth.[107] In summary, there are very few studies reported on the hierarchical self-assembly of organic self-assembling nanotubes into larger structures because the assembly of nanotubes as a target structure has been the focus of much of the research done so far.

3.3. Design

In order to control nanotubes' organization, it is important to understand the forces that govern intertubular interactions. Modulation of these interactions was used as a means to assemble many of the mentioned bundles. Covalent bonds, van der Waals

interactions, metal coordination, and hydrogen bonding between the tubes have been reported to maintain the architectures.[103, 106, 108] While stronger intertubular interactions (e.g. covalent bonds and metal coordination) often yield more robust nanotube assemblies compared to those based on noncovalent interactions, the bundling process is controlled kinetically rather than thermodynamically. This often limits our control over the assembly processes. Using weak noncovalent interactions could lead to thermodynamic control over bundling. If self-assembly is performed in solution, the energy of intertubular interactions depends on the balance of the nanotube-nanotube and nanotube-solvent interaction energies. The interaction energy between nanotubes in turn depends on the functional groups (FG) expressed on their outside walls. The nanotube – solvent interaction energy depends on the exterior FG and on the nature of the solvent.

In order to control the degree of bundling so as to assemble a large number of diverse morphologies, it is necessary to develop a strategy to fine tune the interaction energies. This can be achieved by appending the nanotubes with different FG and assembling them in one solvent, or, alternatively, by using one FG and assembling the nanotubes in various solvents. A number of Rosette Nanotubes with polar FGs like amino acids and crown ethers have been shown to assemble into a morphologically limited number of architectures, featuring mostly single nanotubes and thicker bundles in water and methanol.[62-64, 78] However, limited solubility of such polar derivatives in nonpolar organic solvents does not allow for control over higher order aggregation via solvent variation. Variation of solvent appears to have an advantage over FG variation since it eliminates the necessity to carry out the synthesis of new derivatives with different FG. A large variety of organic solvents with low polarity are readily available. One of the most

common ways to improve solubility of organic compounds in such solvents is attachment of long alkyl chains to the molecules. In the current work, several synthetic approaches were explored to synthesize G^C modules with hydrophobic FG. Moreover, solubility of RNTs in low polarity solvents will allow for a number of new applications to be explored.

3.4. Synthesis

The first synthetic approach takes advantage of a large library of hydrophobic amines (Figure 3.1) developed by Percec et al.[109] These amines can be attached to the G^C module via reductive amination.

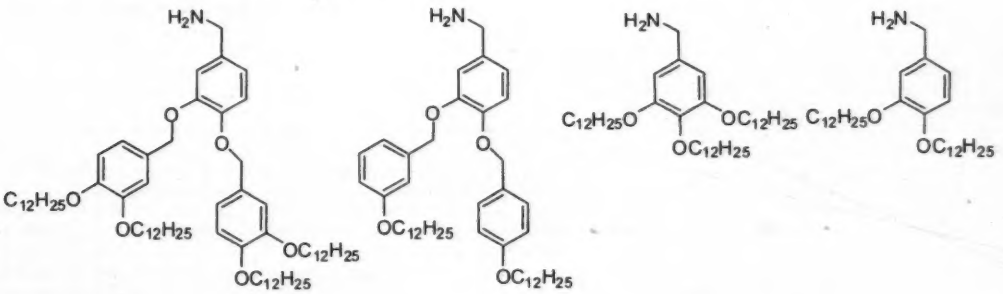

Figure 3. 1. Examples of Percec's amines.

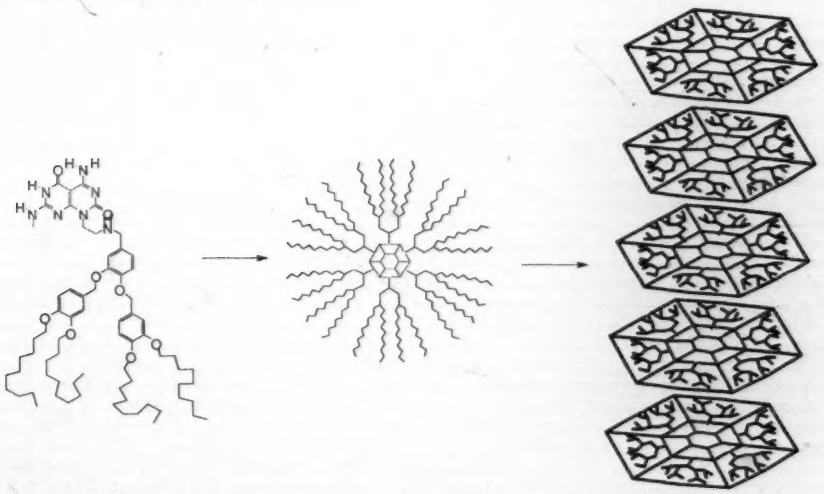

Figure 3. 2. Schematic representation of the assembly of a RNT from G^C module functionalized with dendritic amines.

Unfortunately, preliminary stability tests, even under mild acidic conditions required for the final deprotection step, led to amine decomposition at the benzylic positions. An attempt to functionalize the G^C motif via coupling of the G^C bearing allyl group module with commercially available aryl halides using the Heck reaction conditions did not proceed.

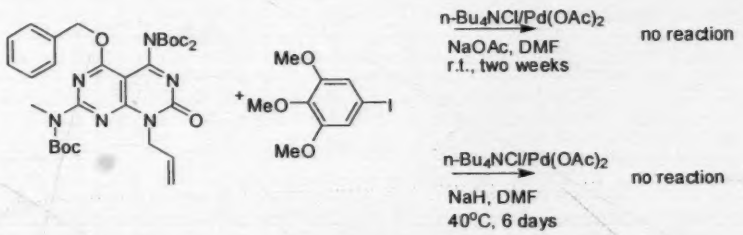

Figure 3. 3. Attempts to functionalize G^C module via Heck reaction.

Cross metathesis attempts between the same G^C module and *p*–bromostyrene using Grubbs' second generation catalyst were equally unsuccessful.

The strategy wherein the alkyl chains are introduced early in the synthetic scheme was found to work. Compounds **1a–f** were thus synthesized in nine steps from a common precursor (2,4,6–trichloropyrimidine–5–carbaldehyde) in 17–43% overall yield (81–91% average stepwise yield) (Figure 3.4). The allyl group in compounds **1a–f** was introduced as a handle for further chemical derivatization. All compounds were characterized by NMR spectroscopy, HR–MS (ES–CI), and elemental analysis.

Selective monosubstitution at position 4 of 2,4,6–trichloropyrimidine–5–carbaldehyde was achieved by S_NAr at –78°C in the presence of 1 equiv. of amine (Figure 3.4). This selectivity was attributed to a directing effect resulting from either the

formation of a stable hydrogen bond between the carbaldehyde and the amine, or the formation of a transient carbinolamine species between the aldehyde and the amine. In agreement with these hypotheses, higher temperatures (0–25 °C), led to a mixture of 2– and 4–monosubstituted, as well as 2,4–disubstituted products.

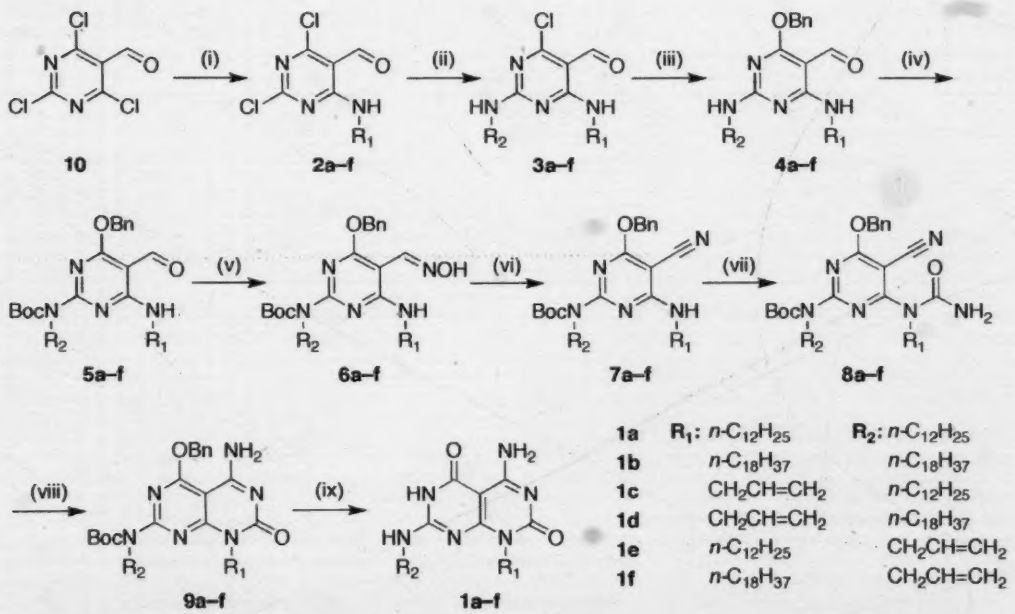

Figure 3. 4. Synthetic scheme used to synthesize G^C derivatives 1a-f. (i) R_1NH_2, Et_3N, DCM, –78 °C. (ii) R_2NH_2, Et_3N, DCM, 0 °C. (iii) BnOH, NaH, THF, reflux. (iv) Boc_2O, DMAP, Et_3N, DCM, rt. (v) NH_2OH·HCl, TEA, MeOH, reflux; or NH_2OH·HCl, pyridine, rt. (vi) $(CF_3CO)_2O$, Et_3N, THF, reflux; or CDI, TEA, $CHCl_3$, reflux; or TCT, TEA, DMF, rt. (vii) $Cl_3CCONCO$, DCM, rt; or ClCONCO, TEA, DCM, rt. (viii) 7M NH_3 in MeOH, rt. (ix) 4M HCl in 1,4-dioxane. Adapted with permission from ref [110]. Copyright 2008 American Chemical Society.

The second S_NAr to form **3a–f** proceeded smoothly with 1 equiv. of amine. When R_1=R_2, 2 equiv. of amine were added to 2,4,6–trichloropyrimidine–5–carbaldehyde at room temperature. In contrast with all other compounds, **3j** and **3k** were prepared from 4–allylamino–2,6–dichloropyrimidine–5–carbaldehyde, which was isolated as a by–product of the first S_NAr. The third S_NAr required the use of a stronger nucleophile

(benzyl alkoxide) and elevated temperature (THF reflux), due to deactivation of the pyrimidine ring by the electron donating alkylamines. The first Boc protection occurred selectively at the 2–amino position. The 4–amino group is less nucleophilic because the nitrogen is engaged in an intramolecular H–bond with the neighbouring carbonyl group.

Conversion of aldehydes **5a–f** into the corresponding nitriles **7a–f** was carried out in two steps. Aldehydes **5a–f** were first converted to the corresponding oximes and then, depending on the nature of the R groups, they were dehydrated using either TFAA, carbonyldiimidazole, or trichlorotriazine under basic conditions.

Treatment of **7a–f** with the more stable *N*–trichloroacetyl isocyanate or with *N*–(chlorocarbonyl) isocyanate resulted in mixed ureas **8a–f**. The former had to be used in large excess (up to 4 equiv.) to drive the reaction to completion in a reasonable period of time because of its lower reactivity. *N*–(chlorocarbonyl) isocyanate on the other hand, was used in stoichiometric amounts. However, this reagent must be freshly distilled and used under strictly anhydrous conditions as it decomposes and releases HCl in sufficient quantities to induce Boc deprotection. Bicyclic compounds **9a–f** were obtained in excellent yield upon basic work up, or treatment of the crude product **8a–f** with concentrated ammonia in methanol. Final deprotection in 4M HCl/dioxane yielded target compounds **1a–f** in 98% average yields as monohydrochloride salts. It is particularly noteworthy that all intermediate compounds in the synthesis of **1a** could be isolated by selective precipitation in methanol (i.e. no chromatography). It is quite possible that **1b–f** and the compounds leading to them could also be subjected to the same selective precipitation method.

3.5. Self-assembly studies

The samples were prepared by sonication (20 s) and heating to reflux of a solution of compounds **1a–f** in a chosen solvent and subsequent casting on a carbon film. Eight solvents were chosen which cover a wide range of polarities, from very nonpolar hexanes to very polar DMSO. As previously discussed, the assembly should be greatly influenced by the polarity of the solvent. Representative HRSEM images of **1a–f** assembled in various solvents at 0.25 g/L are summarized in Figure 3.5.

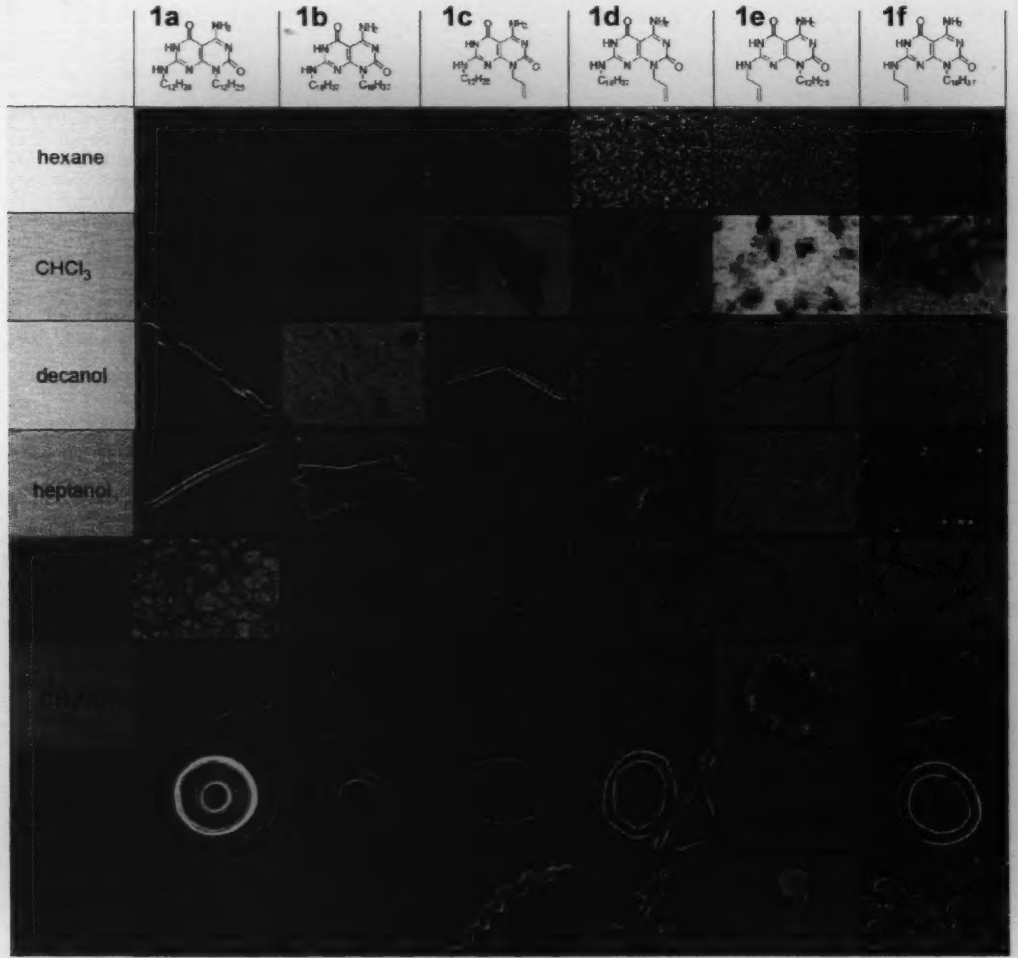

Figure 3. 5. Summary of the morphologies obtained from 1a–f in the solvents indicated (0.25 g/L).

The data are presented according to solvent. SEM studies in each solvent are followed by detailed studies of a representative morphology (normally assembled from 1a) by TEM and AFM. SEM allows one to survey large areas of a sample, providing high contrast and 3D view of a structure. TEM provides quantitative lateral (x, y) and AFM provides height (z) information with sub nanometer resolution for dimensions of nano-assemblies. The time and concentration dependence studies are given for the most interesting morphologies. Discussion of the results concludes this section. It should be noted that all the observed morphologies, except for **1a** and **1b** in nitromethane, are monodisperse and represent at least ~90% of all the aggregates observed by electron microscopy. All the assembly and SEM experiments were carried out three at least times.

(A) Self-assembly studies in hexane

Compound **1a** is soluble in hexanes up to ca. ~0.5 g/L, which achieves the goal of making RNTs soluble in nonpolar solvents. Tapping mode atomic force microscopy (TM-AFM) imaging of a sample cast from this solution showed the formation of thick multilayers of RNTs, from which it was difficult to discern individual RNTs. Drop-casting of a 0.25 g/L solution on mica resulted in networks of RNTs comprised of single nanotubes (Figure 3.7) with an outer diameter in the range of 3.5-5 nm. This variability is well known for dispersed soft materials[111, 112] and results from a tip-induced compression in tapping mode. Scanning electron microscopy (SEM) images (Figure 3.6) revealed high-aspect-ratio nanostructures with an outer diameter of 4.8 ± 0.5 nm consistent with the calculated diameter (4.9 nm). Dynamic light scattering (DLS) experiments showed the formation of relatively large aggregates in solution with a broad distribution centered at 700 nm (Figure 3.8A).

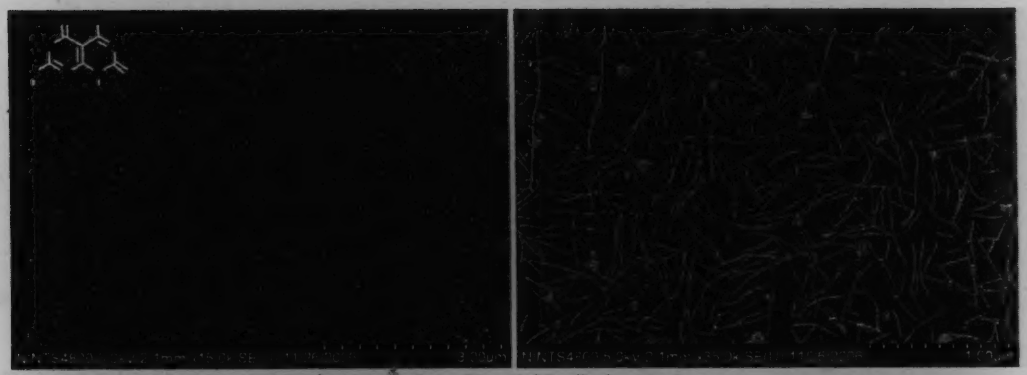

Figure 3. 6. SEM images of 1a cast on carbon film (0.25 g/L, hexane).

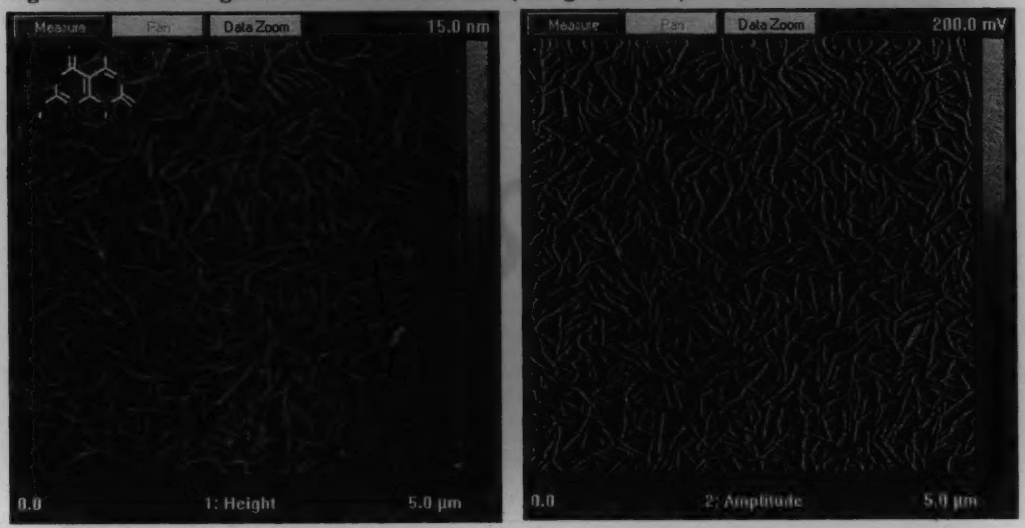

Figure 3. 7. Height and amplitude (right) AFM images of 1a cast on carbon film (0.25 g/L, hexane)

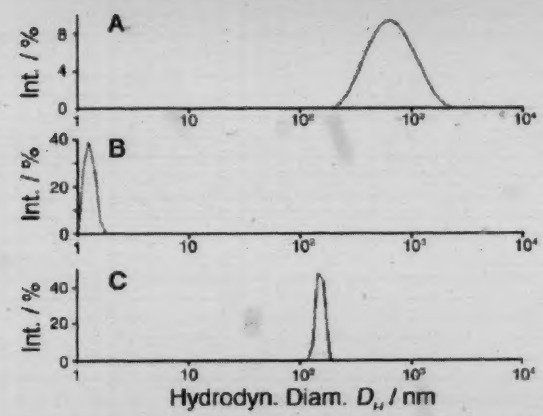

Figure 3. 8. Dynamic light scattering (DLS) regularization diagram showing the hydrodynamic diameter (DH) for compound 1a (0.25 g/L) versus scattering intensity in hexane (A) methanol (B), and chloroform (C).

Similarly to **1a**, compounds **1b–f** formed dispersed arrays of single nanotubes. A day-old solution cast on the substrate resulted in thick bundles that were difficult to resolve by SEM. However, deposition of the solutions after 10 minutes of ageing resulted in well dispersed nanotubes (Figure 3.8 – 2.11). A higher tendency of **1b–f** to aggregate compared to **1a** can be explained by the stronger intertubular hydrophobic interactions due to the increase of side chain(s) length or/and introduction of an allyl group.

It was not possible to stain any of the single nanotubes for TEM, since methanol – the solvent for uranyl acetate (staining agent) – disrupts self-assembly. Attempts to use other commercially available staining agents: silver tetraphenylporphyrin (a more hydrophobic staining agent), OsO_4, nanotungsten, or sodium molybdate did not improve the contrast.

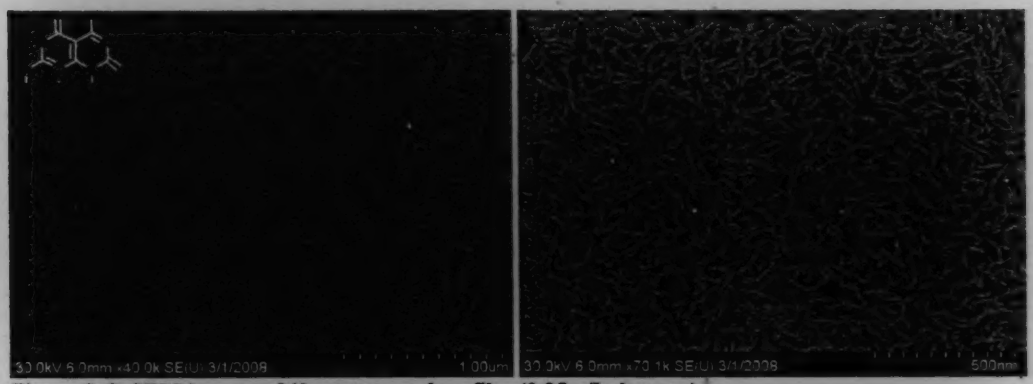

Figure 3. 9. SEM images of 1b cast on carbon film (0.25 g/L, hexane).

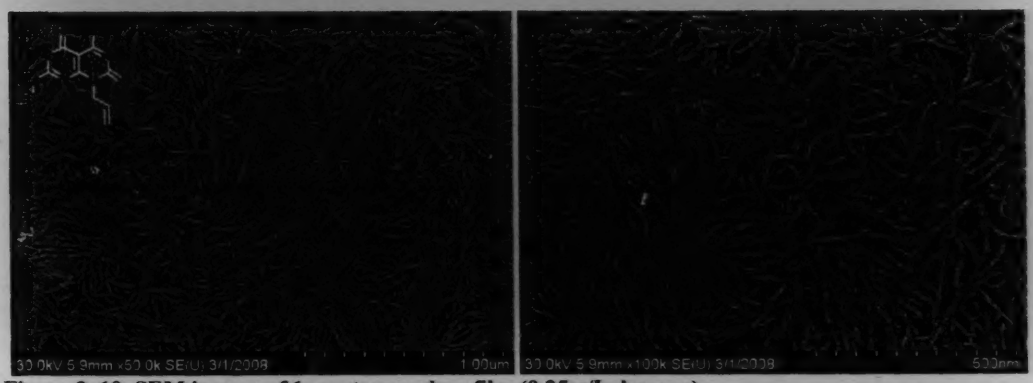

Figure 3. 10. SEM images of 1c cast on carbon film (0.25 g/L, hexane).

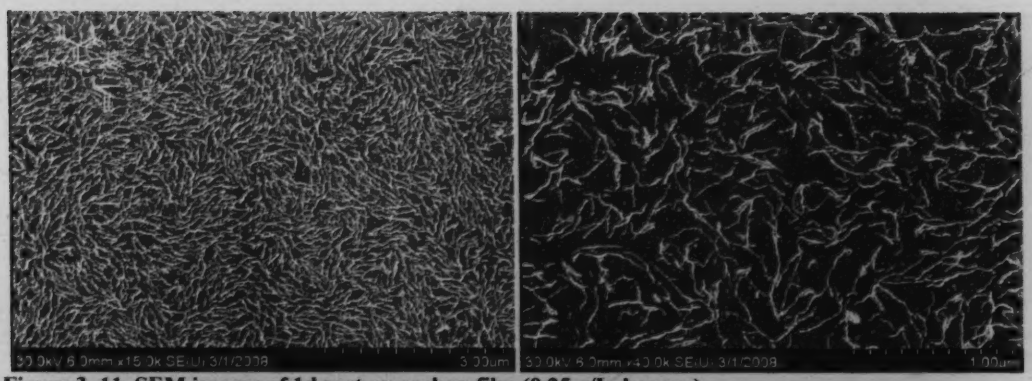

Figure 3. 11. SEM images of 1d cast on carbon film (0.25 g/L, hexane).

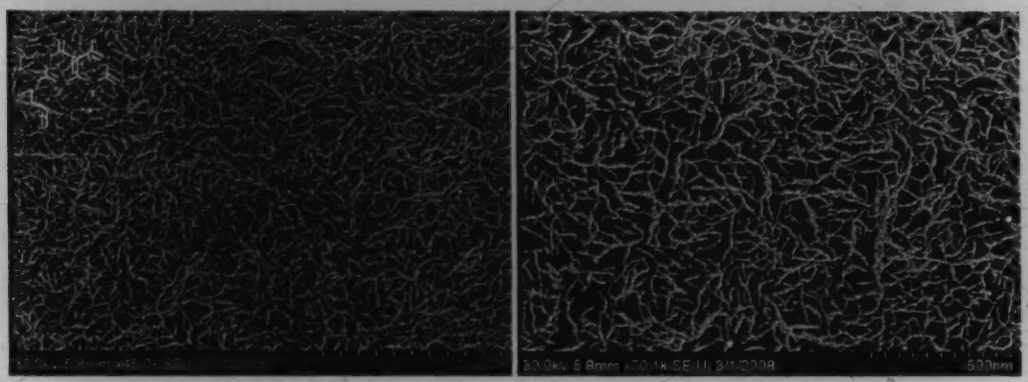

Figure 3. 12. SEM images of 1e cast on carbon film (0.25 g/L, hexane).

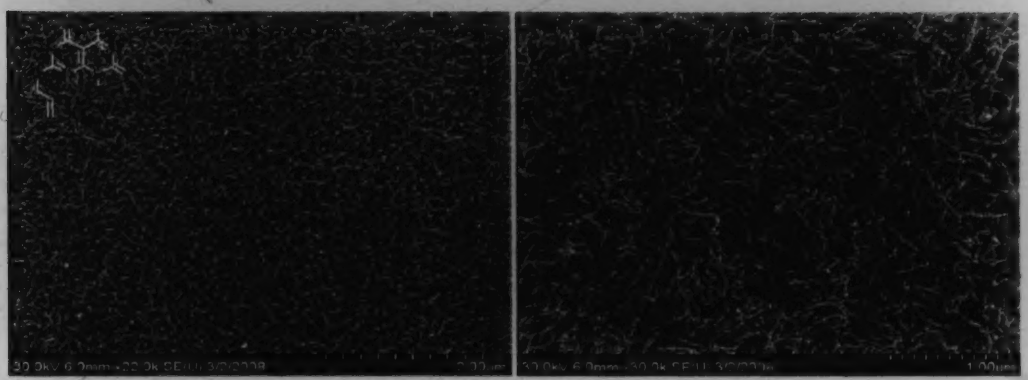

Figure 3. 13. SEM images of 1f cast on carbon film (0.25 g/L, hexane).

(B) Self-assembly studies in chloroform

Interestingly, in chloroform, compound **1a** (0.25 g/L) underwent an unexpected hierarchical self-assembly process to generate discrete prolate nanospheroids. SEM, TEM, and TM-AFM (Figure 3.14 – 3.16) revealed relatively uniform spheroids 1300 ± 200 nm (PDI = 1.02) along the main axis, 260 ± 30 nm (PDI = 1.01) along the short axis, and 60 ± 30 nm (PDI = 1.17) in thickness. TM-AFM imaging (Figures 3.16) revealed terraces on their surfaces with 4.6 ± 0.4 nm steps, consistent with the calculated van der Waals diameter of a RNT (4.9 nm), and thus suggesting that these superstructures are made up of RNT monolayers. Furthermore, sheet fragments featuring the same height were observed on the substrate surface around the nanospheroids, suggesting their likely role as precursors in the formation of these superstructures. The multilayered nature of these nanospheroids can be clearly seen in the TM-AFM phase images (Figure 3.15). The supramolecular organization of the nanospheroids was further investigated by selected area electron diffraction (SAED) and X-ray powder diffraction (XRD). SAED gave two rings corresponding to *d* spacing values of 4.5 (d_1) and 2.2 (d_2) nm in addition to less-well-defined rings corresponding to 0.7, 0.41, and 0.28 nm (Figure 3.17). XRD gave two strong reflections at 4.21 and 2.07 nm and three weak reflections at 0.69, 0.43, and 0.27 nm (Figure 3.18). The results of SAED and XRD are remarkably consistent and in agreement with a lamellar organization of RNT monolayers, as depicted in Figure 1D. Notably, the ratio of the first and second strong *d* values of ~0.5 (SAED, 2.2:4.5; XRD, 2.07:4.21) is consistent with a lamellar multilayered mesophase.[113-115] Furthermore, the largest *d* spacing (SAED, 4.5 nm; XRD, 4.21 nm) is consistent with the measured RNT diameter (4.8 ± 0.5 nm) and nanospheroid terrace thickness (4.6 ± 0.4 nm), suggesting

that the RNTs are the basic building block of the lamellar architecture of the nanospheroids.

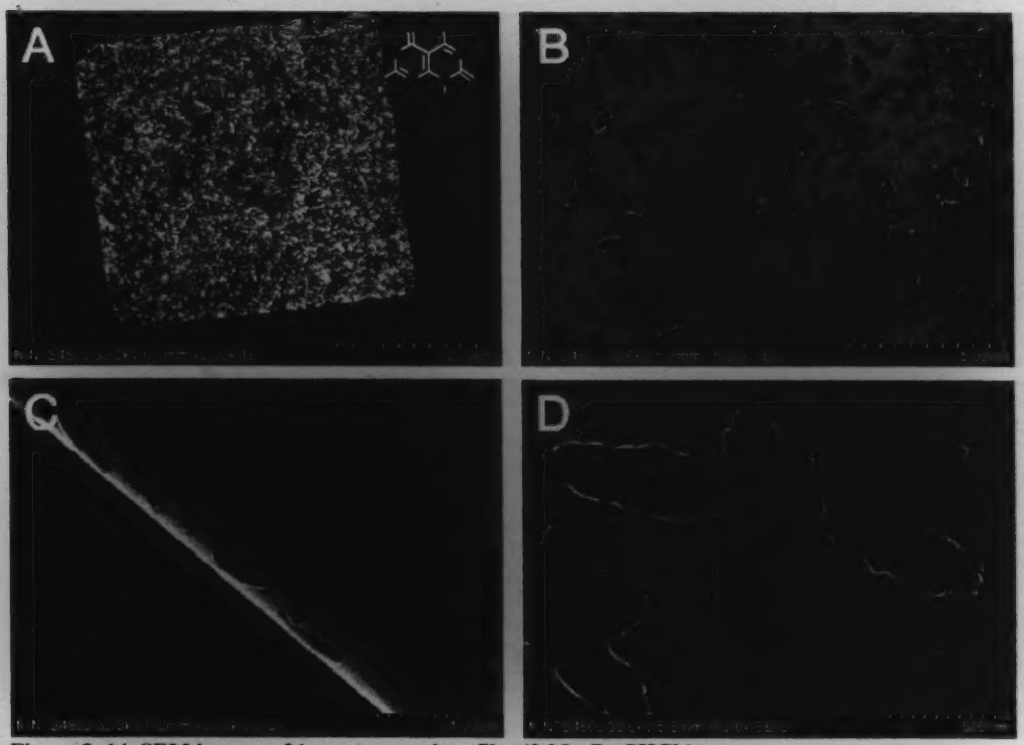

Figure 3. 14. SEM images of 1a cast on carbon film (0.25 g/L, $CHCl_3$).

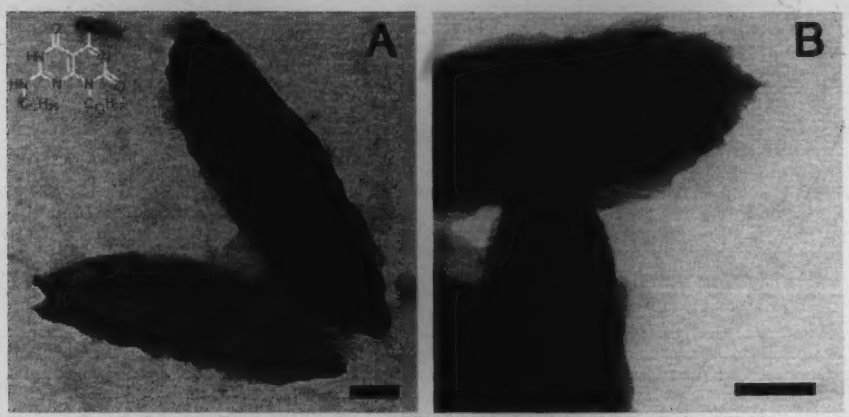

Figure 3. 15. Energy filtered (zero loss) TEM images of 1a (0.25 g/L in $CHCl_3$) on carbon-coated grid showing the lamellar organization of the spheroids. Scale bars = 100 nm.

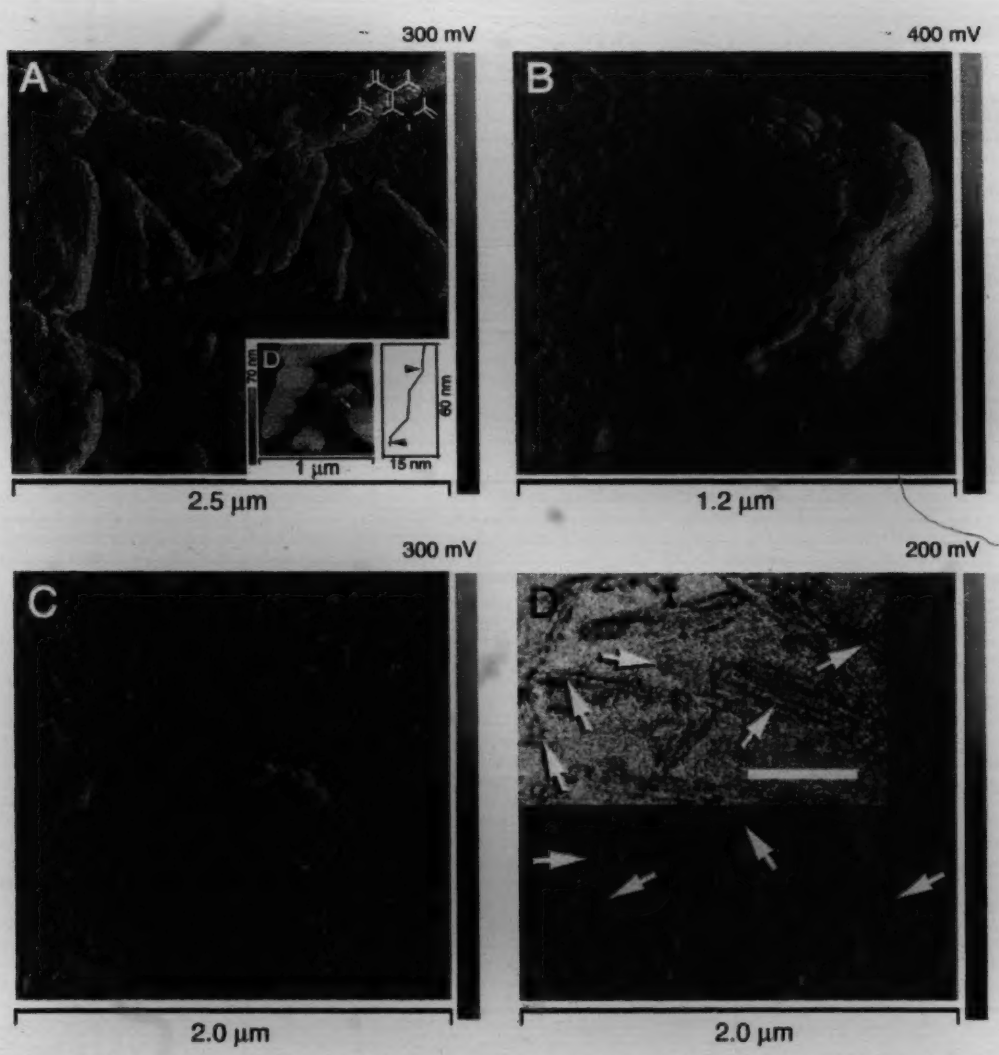

Figure 3. 16. (A–C) TM-AFM amplitude images of compound 1a (0.25 g/L) cast from $CHCl_3$ on mica showing background material surrounding nanospheroids. High resolution TM-AFM image (D) obtained with ultra sharp AFM tips (radius of curvature is 1 nm) and negatively stained TEM image (using 2% uranyl acetate in MeOH, scale bar = 200 nm) revealing individual RNTs (white arrows, 4.4 ± 0.3 nm) aligned in a parallel fashion within sheet fragments that make up the nanospheroids.

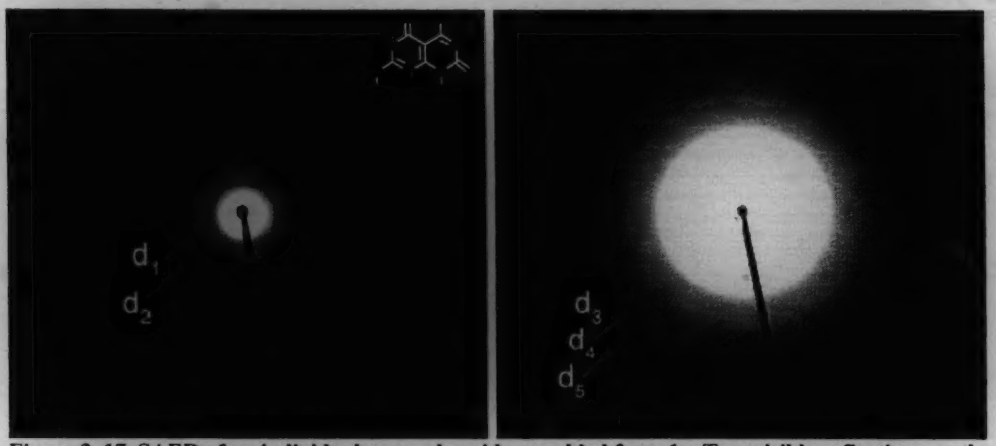

Figure 3. 17. SAED of an individual nanospheroid assembled from 1a. Two visible reflections on the left image correspond to 4.5 (d_1) and 2.2 (d_2) nm. Additional weak reflections corresponding to 0.70 (d_3), 0.41 (d_4) and 0.28 (d_5) nm were revealed by adjusting the contrast (right image).

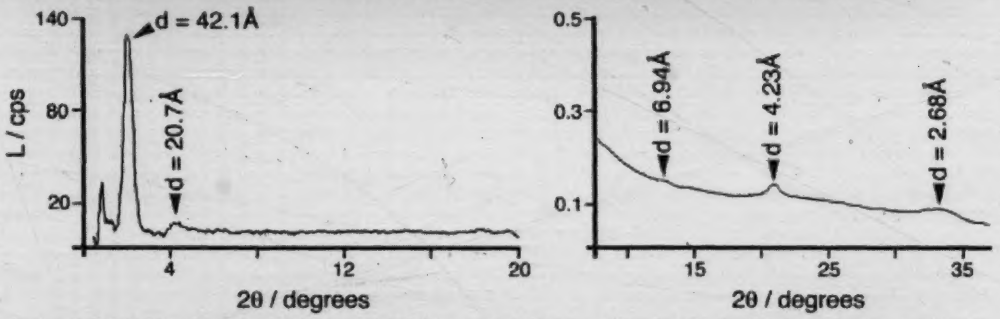

Figure 3. 18. XRD spectrum of nanospheroids prepared according to Method 1 (low angles, left) and Method 2 (high angles, right) described in experimental part. Peak at 2θ ~0.95 is from direct x-ray beam (+1.5 to –1.5). The diffraction peaks at 2θ values of 2.09 and 4.26 correspond to 'd' spacings of 42.1 and 20.7 Å.

While high-resolution TEM (HR-TEM) on negatively stained samples of the nanospheroids confirmed their lamellar organization (Figure 3.15), it did not resolve the supramolecular organization of the sheets because of their thickness and the inability of the hydrophilic staining agent to penetrate the hydrophobic barrier generated by the amorphous interpenetrating C12 side chains between the RNTs. However, TM-AFM with ultra sharp AFM tips (Figure 3.16) and HR-TEM of thin sheet fragments around the nanospheroids revealed the presence of aligned RNTs along their main axes.

The fact that nanotubes assembled in hexane were not stable to a solution of staining agent in methanol raised the possibility of complete disassembly in this solvent. Thus drop-casting **1a** from methanol (0.25 g/L) on mica gave uniform coverage with a surface roughness under 1 nm, whereas on HOPG the surface roughness exceeded 10 nm. On both surfaces, however, the RNTs were not observed by both TM-AFM and SEM (Figure 3.19). DLS experiments on the same solution showed the presence of particles ~1-2 nm (Figure 3.8), confirming the absence of RNTs or aggregates thereof in this solvent.

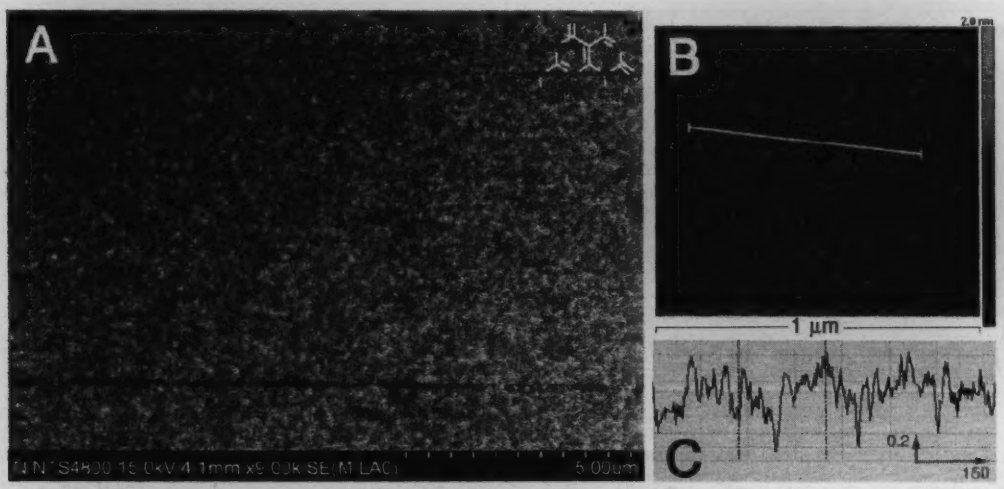

Figure 3. 19. SEM micrograph (A), TM-AFM height image (B) and height profile (C) of compound 1 (0.25 g/L) cast from methanol on HOPG (A) and mica (B). The (x,y) scale in C is in nm.

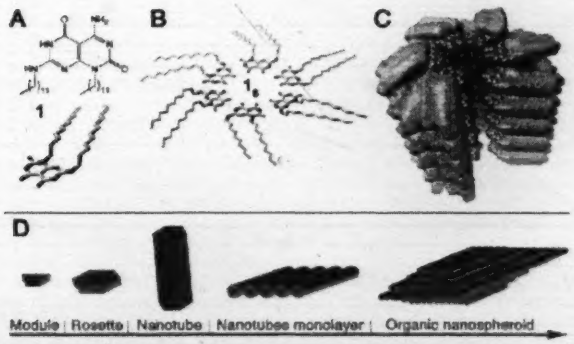

Figure 3. 20. Hierarchical self-assembly of organic nanospheroids. G^C derivative 1 (A), and resulting rosette (B) and rosette nanotube (RNT) (C). One module was removed from each rosette along the RNT wall to unveil the inner channel (red). The RNTs self-organize into monolayers, which then form 'flattened' prolate nanospheroids according to the schematic representation in (D). Reproduced with permission from ref [116]. Copyright 2008 American Chemical Society.

To establish that the hierarchical states captured in methanol, chloroform and hexane are in a dynamic relationship, a solution of **1a** in chloroform (3.0 g/L) was readily disassembled or converted to a dispersion of RNTs upon dilution to 0.25 g/L in hot methanol or hexane, respectively (Figure 3.21).

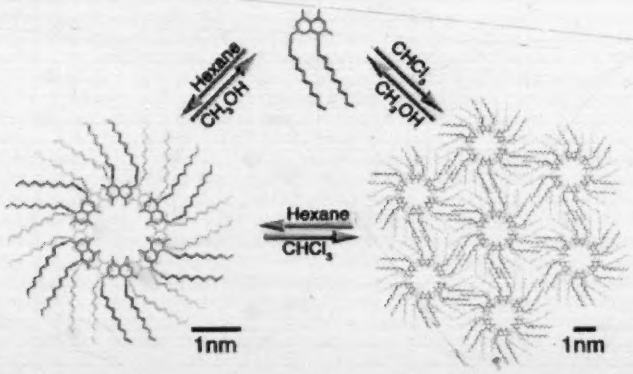

Figure 3. 21. Solvent promoted transition between three levels of hierarchical self-assembly for 1a. Reproduced with permission from ref [116]. Copyright 2008 American Chemical Society.

On the basis of the experimental results, it is clear that the hierarchical self-assembly of **1a** is highly dependent on solvation free energy. In methanol, the C12 alkyl chains are poorly solvated, leading most likely to the formation of micellar aggregates in which the G^C motif is exposed to solvent. In hexane, the alkyl chains are well solvated whereas

the base is not due to its relatively polar character. In this solvent, rosette formation and stacking interactions are driven not by the hydrophobic effect as previously shown for the water-soluble derivatives of the G^C base,[112] but rather by polar stacking interactions between bases and, to a smaller extent, via interchain van der Waals interactions on the periphery of the RNTs. The low polarity of hexane was also anticipated to promote intermodular H-bonding. In chloroform, the rationale for RNT formation is similar to that proposed for hexane. However, their subsequent self-organization into lamellar mesostructures results from RNTs' lower solvation free energy in chloroform, and preferred solute-solute (i.e., interchain van der Waals) interactions. The formation of spheroidal shapes suggests an anisotropy along the nanoparticle's main axes, in agreement with the formation of a 3D supramolecular assembly with two physically distinct surfaces. The first, along the main axis of the nanospheroids, is covered with C12 chains protruding from the RNT walls. The second surface covers the two diametrically opposed ends of the nanospheroids and is composed of a mosaic of rosette disks, as schematically shown in Figure 3.72. The prolate shape assumed by this architecture reflects a stronger inter-rosette stacking versus interchain van der Waals interactions. The prolate shape suggests also a stronger inter-nanotube van der Waals interaction within versus between layers.

Compounds **1b-f** form morphologies that are quite similar to the one formed by **1a** in chloroform (Figure 3.17 – 2.25). From the SEM images for **1b-d** it is obvious that the main axis of RNTs is aligned with the longest dimension of a nanospheroid, since single RNTs and their bundles can be seen protruding from the opposing edges of the structures. In addition, striations running along the main axis of the structures can be seen on the

surface of structures assembled from **1b-d**, corroborating the hierarchical model proposed for **1a**. Compound **1b** generally forms more diffuse/less compact structures compared to **1a,** possibly the result of higher solvation energy for RNT made of **1b**. Compounds **1c, d** generally form larger structures compared to **1a-c**. This could be due to the stronger intertubular solvophobic interactions because of substitution of an alkyl chain by the allyl group. Structures assembled from **1e, f** are less uniform and buried into a layer of a background material on the carbon grid. This distinct morphology might be linked to the presence of allyl substituent attached to the left hand side nitrogen, since it is the common feature in both compounds.

Figure 3. 22. SEM images of 1b cast on carbon film (0.25 g/L, $CHCl_3$)

Figure 3. 23. SEM and S(T)EM (right) images of 1b cast on carbon film (0.25 g/L, $CHCl_3$).

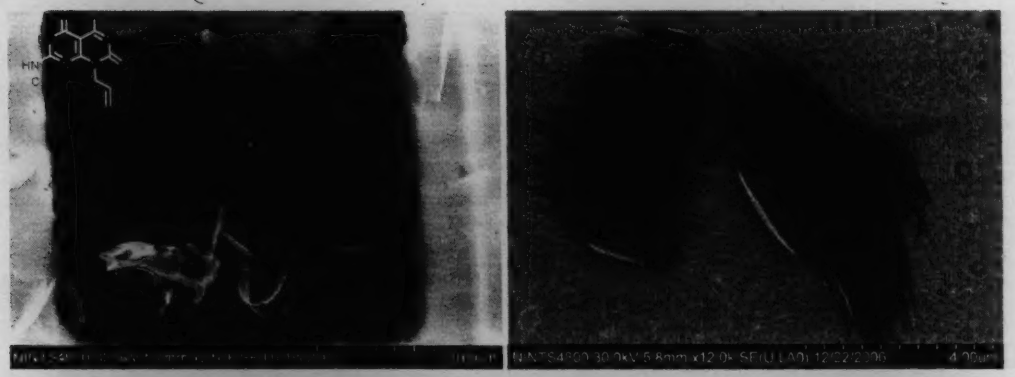

Figure 3. 24. SEM images of 1c cast on carbon film (0.25 g/L, $CHCl_3$).

Figure 3. 25. SEM images of 1d cast on carbon film (0.25 g/L, $CHCl_3$).

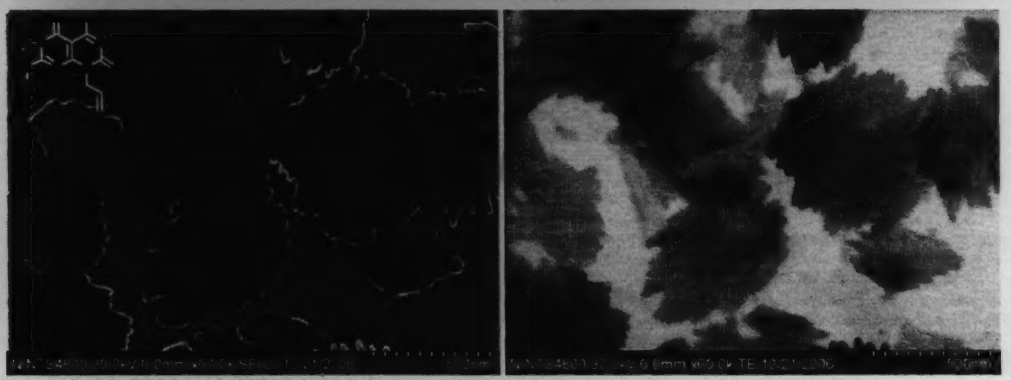

Figure 3. 26. SEM and STEM (right) images of 1d cast on carbon film (0.25 g/L, $CHCl_3$)

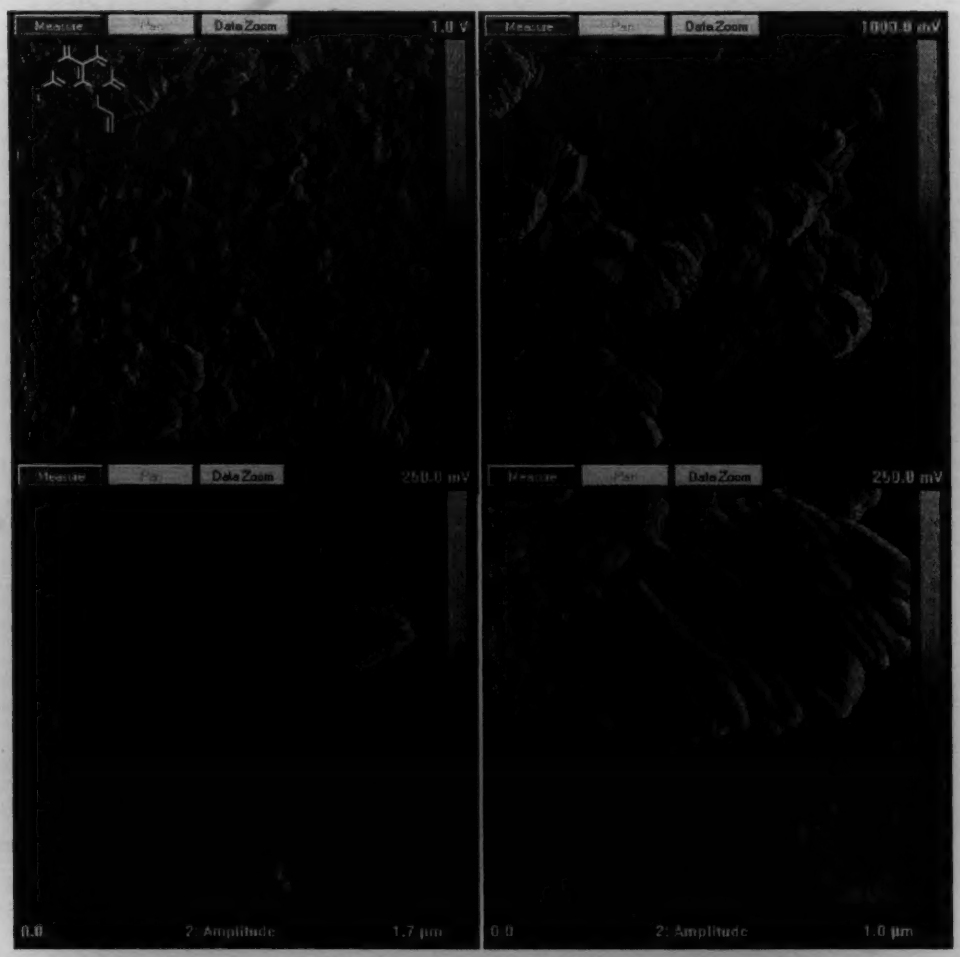

Figure 3. 27. TM-AFM amplitude images of compound 1d on mica (0.25 g/L, $CHCl_3$)

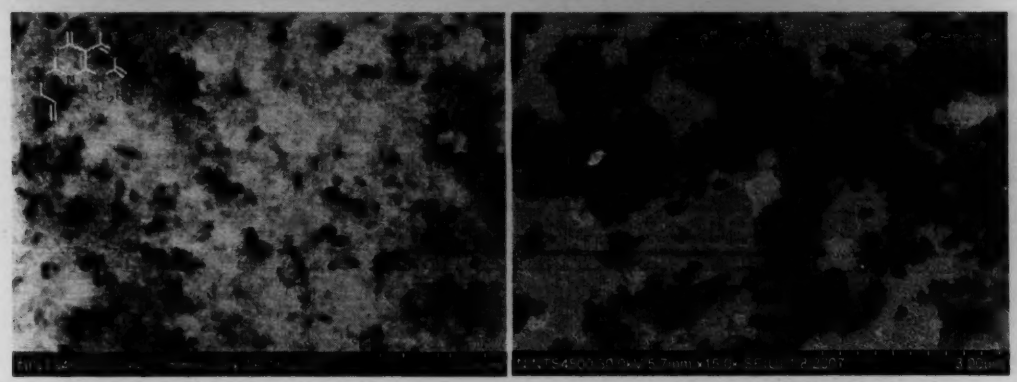

Figure 3. 28. SEM images of 1e cast on carbon film (0.25 g/L, $CHCl_3$).

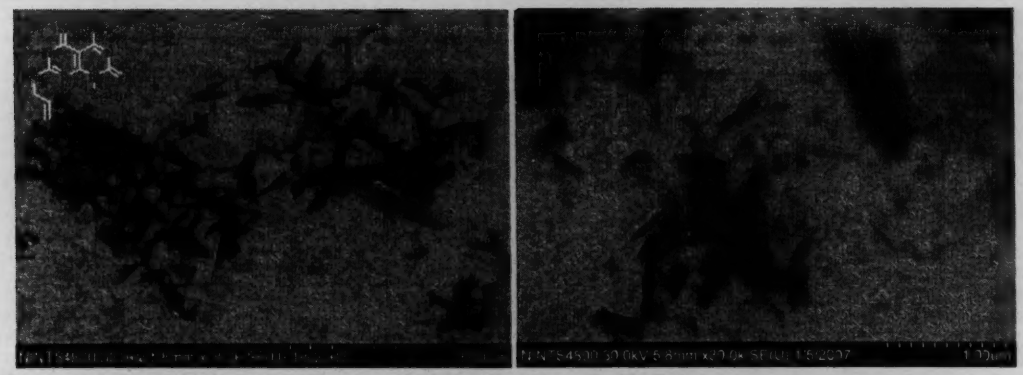

Figure 3. 29. SEM images of 1f cast on carbon film (0.25 g/L, $CHCl_3$).

(B) Concentration and time dependent studies in chloroform for 1a

In order to understand the self-assembly process the concentration and time dependance of **1a** morphology in chroroform was studied.

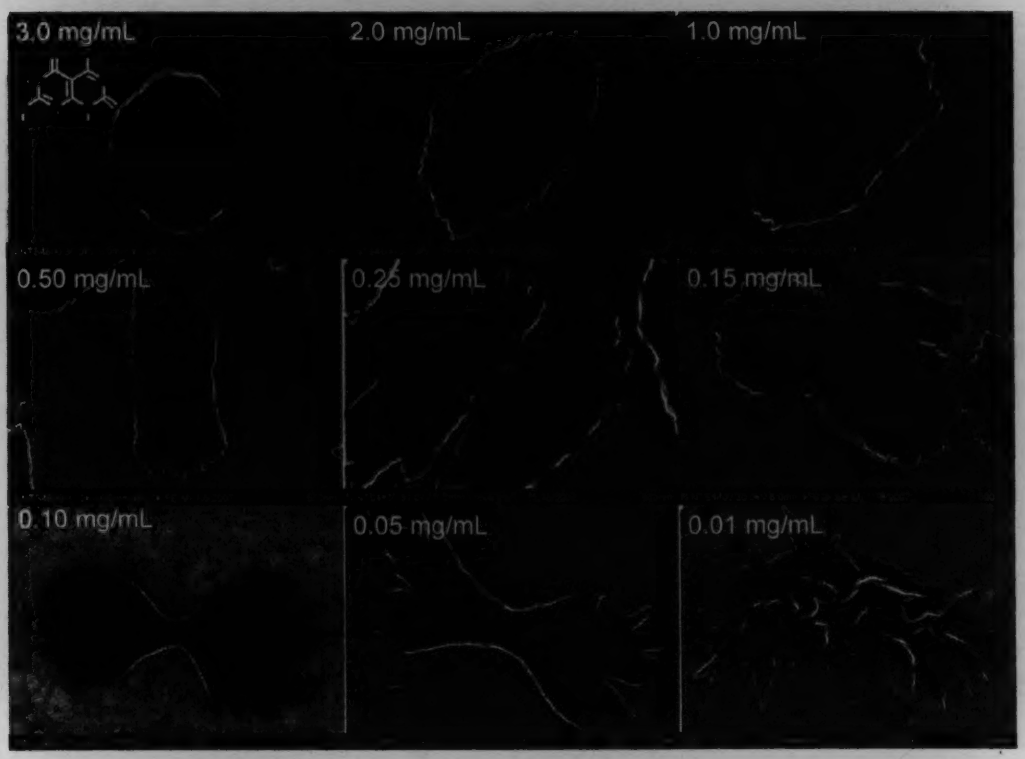

Figure 3. 30. Concentration dependence of 1a morphology (time = 1 hour).

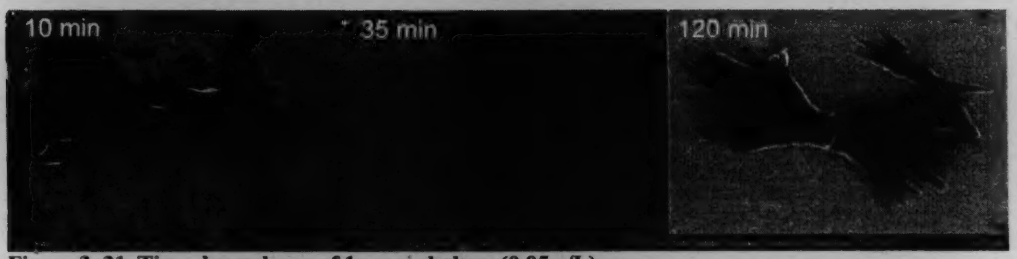

Figure 3. 31. Time dependence of 1a morphology (0.05 g/L).

Figure 3. 32. Time dependence of 1a morphology (0.10 g/L).

Figure 3. 33. Time dependence of 1a morphology (0.25 g/L).

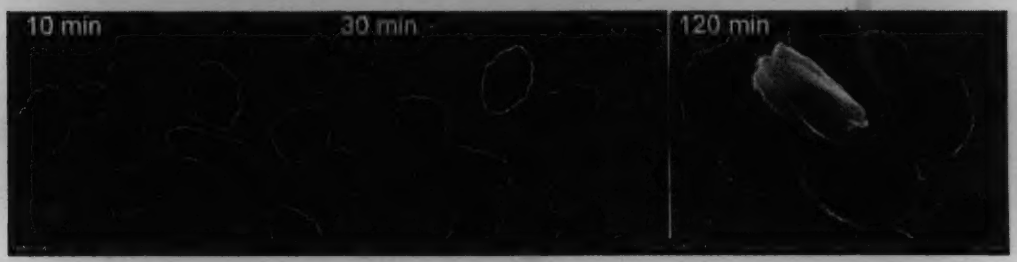

Figure 3. 34. Time dependence of 1a morphology (3.0 g/L).

It is clear from these experiments that morphology of **1a** is concentration-dependent (Figure 3.30). Oblate but not prolate spheroids are dominant at high concentration (3 g/L). Lowering the concentration to 0.25 g/L results in a gradual increase of the spheroid aspect ratio. Oblate and prolate spheroids at 0.25 g/L transform into what we call "bowties" or "hay stacks" when the concentration is further lowered. Folds start to appear on the surface of the architectures. The appearance of the fold can be seen upon tilting of the stage in SEM instrument (Figure 3.35). At concentrations of 0.1 and 0.5 g/L, one large fold is located in the center of spheroids perpendicular to the structure's longest dimension. Smaller structures without folds are observed at concentrations equal or lower than 0.01 g/L.

Figure 3. 35. SEM images of the bow ties assembled from 1a with instrument's stage tilted 30°.

Interestingly, bowties give the same SAED pattern as nanospheroids, which indicates that they also have the lamellar organization proposed for nanospheroids. TEM imaging of bowties revealed their multilayered structure (Figure 3.36) to be very similar to the one observed for nanospheroids. Also, single nanotubes and their bundles protruding at the edges of the structures (Figure 3.37) were observed. AFM imaging showed the presence of nanotube monolayer fragments similar to the ones observed for nanospheroids, thus confirming their common origin (Figure 3.38).

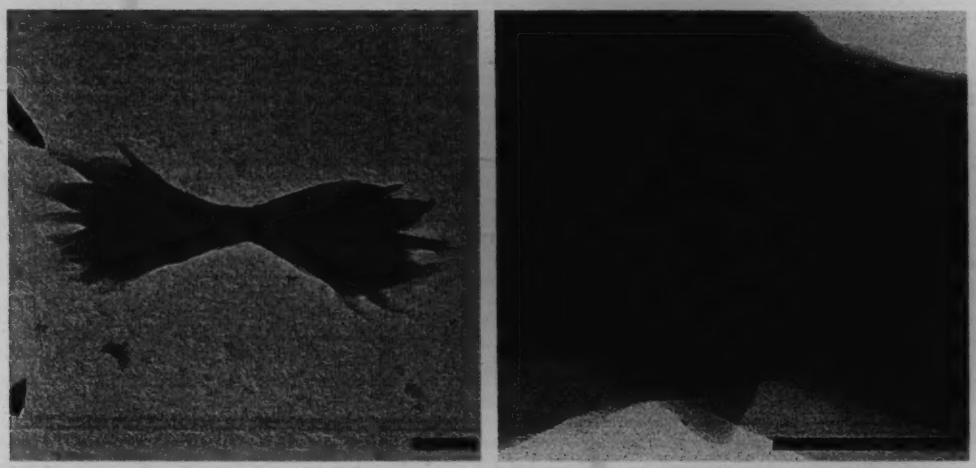

Figure 3. 36. TEM images of unstained "bow ties" assembled from 1a. Scale bars are 100 nm.

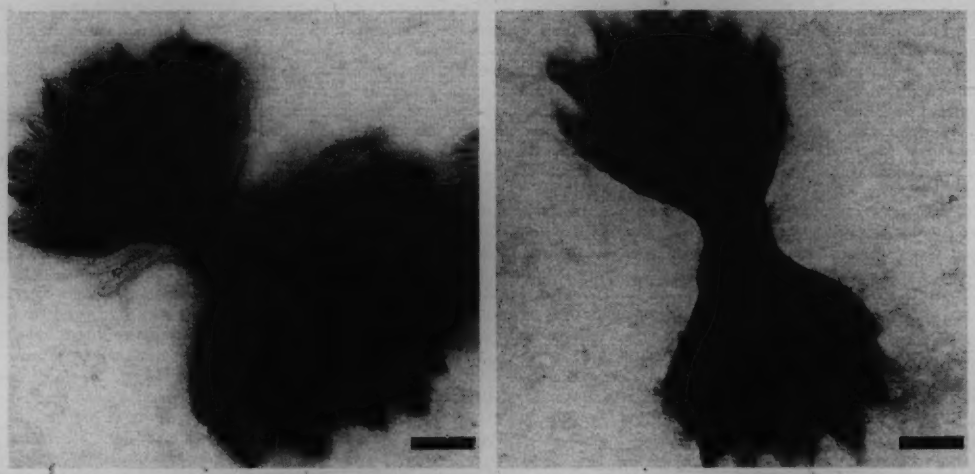

Figure 3. 37. TEM images of "bow ties" assembled from 1a and stained with uranyl acetate. Scale bars are 100 nm.

Time dependent studies at selected concentrations (Figures 3.31. – 3.34) showed that it takes at least an hour for a morphology to reach its final shape at concentrations <1.0 g/L. Very little time-dependence was found for concentrations above 1 g/L and the final morphology was assembled within a few minutes. This is most likely due to the fact that higher concentration causes faster assembly.

Figure 3. 38. TM-AFM images of bow ties assembled from 1a in cast on carbon film (0.1 g/L, $CHCl_3$).

Mechanism of nanobowties formation

It is important to understand the mechanism of the assembly of these fascinating sheaf-like structures, i.e. "bow-ties" or "hay-stacks", since the process can potentially be used to fabricate other functional organic nanostructures via supramolecular polymerization. No organic structures with an analogous morphology were found in the literature. However, a number of morphologically similar architectures exist in inorganic chemistry. Both naturally occurring macroscopic mineral[117, 118] and synthetic nano- and microcrystals[119-121] were reported to form sheaf structures. It is believed by mineralogists that the sheaf structures form by crystal splitting during their growth. Figure 3.39.A shows drawings of successive stages of splitting during crystal growth. An individual crystal splits apart, forming a number of subindividuals (simple splitting), a sheaflike structure, or, in its final form, a spherulitic structure. Different minerals are found to have different "splitting ability", depending on their crystal structure. For example, aragonite (the orthorhombic phase of $CaCO_3$) has a higher splitting ability than calcite (the

rhombohedral phase of $CaCO_3$) and therefore tends to form split acicular crystals or frostwork-like structures.

Although not completely understood, crystal splitting may occur due to several reasons, but generally splitting is associated with fast crystal growth. With other conditions being the same, crystal growth depends strongly on the solution oversaturation. Punin et al. suggested[118] that splitting is only possible if the oversaturation exceeds a certain "critical" level, which is specific for each mineral and the given conditions. Other factors that have been found to cause crystal splitting are mechanical splitting, when extra molecules appear in some layers of its crystallographic network, and chemical splitting, when certain ions (e.g., Mg^{2+} and Ca^{2+}) are present in the parent solution.[117] Depending on the level of supersaturation or impurity concentration (which can change during growth), minerals can take on different degrees of splitting, resulting in a number of subforms of split crystals (Figure 3.39.B-E). Figure 3.39.B is a picture of a quartz rod without splitting while panels C and D of Figure 3.39. show the late stage of simple splitting and early stage of sheaf splitting of quartz, respectively. Figure 3.39E shows a wavellite (an aluminum phosphate mineral) spherulite. Panels F-I show representative TEM images of an inorganic synthetic Bi_2S_3 nanostructures with different forms of splitting.[121] Panels 3.39.J-M show representative SEM images illustrating the evolution of "hay stacks" assembled from RNTs (this work).

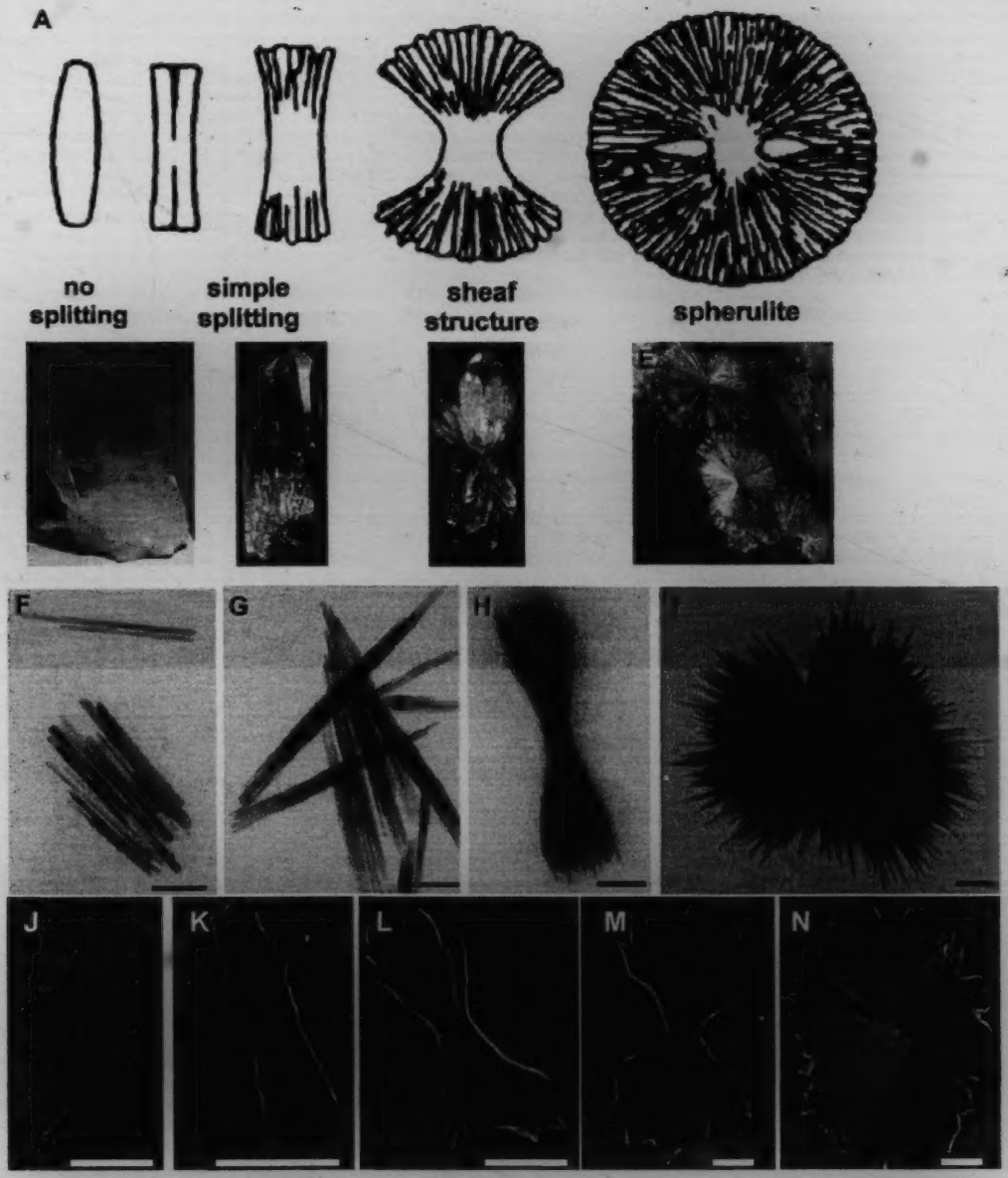

Figure 3. 39 Schematic illustration of crystal splitting (A) and examples of different forms of splitting in minerals (B-E), inorganic nanostructures (F-I), and synthesized in this work RNTs bowties (J-N). All the scale bars in panels F-I are 100 nm. Adapted with permission from ref 110. Copyright 2008 American Chemical Society. Splitting of the bowties' edges into RNTs bundles and eventually into individual tubes is especially clear in TEM images (Figure 3.37). All the scale bars in panels J-N are 200 nm.

Striking similarity with inorganic structures may indicate similar mechanism for the hay stack formation observed in this work. It is instructional to consider supramolecular polymerization as a crystallization process. It is clear that solvophobic interactions drive both the crystallization of inorganic structures and the assembly of organic nanotubes. Anisotropy in inorganic crystal growth arises from the difference in energy of various crystallographic planes, whereas for RNT bowties there are two different forces: π-π stacking fueling nanotube elongation and weaker van der Waals interactions driving nanotube bundling. Both of these forces are electrostatic in nature. Coulomb forces that dominate in the formation of inorganic structures are stronger than the π-π stacking and van der Waals interactions. The latter two have broader energy "well" potentials; therefore, the distance between two interacting species is more variable. This could explain higher flexibility of the sheaf structures observed in this work as well as the presence of the folds. The folds that are particularly obvious in the center of the bowties (Figures 3.35 – 3.37), arise most likely from mechanical stress caused by the splitting during growth process.

(C) Self-assembly studies in decanol

In decanol (Figures 3.40 – 3.46), which is a more hydrophilic solvent compared to hexane, compounds **1a-f** were expected to form bundles of RNTs as they did in chloroform. Indeed, no single tubes were observed for any of the compounds. Compounds **1a, c, e** formed nanorods several microns long and 100 – 300 nm in width. TEM studies of **1a** nanorods revealed the presence of nanotubes aligned along the main axis of the nanorods (Figure 3.27). Compounds **1b, d, f** did not form distinct nanorods, but instead assembled into sheets made of few nanotube monolayers. While the lateral

dimensions of the sheets were found to be quite polydisperse, their thickness was found to be quite uniform, on average made up of 2–3 RNT monolayers based on SEM image analysis.

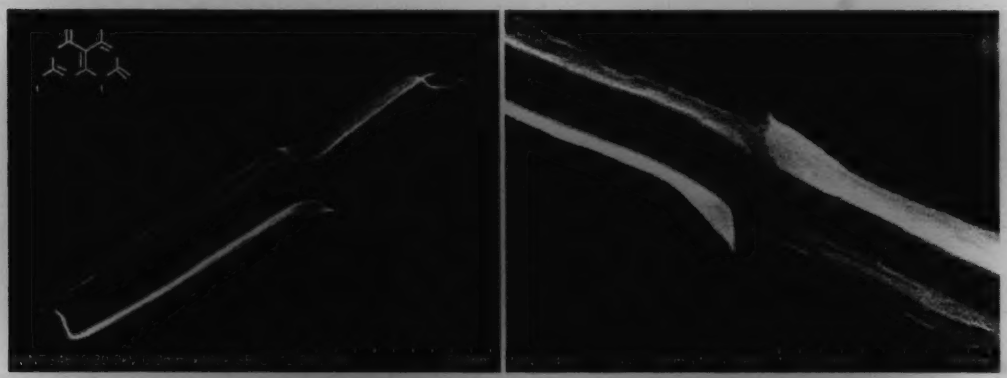

Figure 3. 40. SEM images of 1a cast on carbon film (0.25 g/L, decanol).

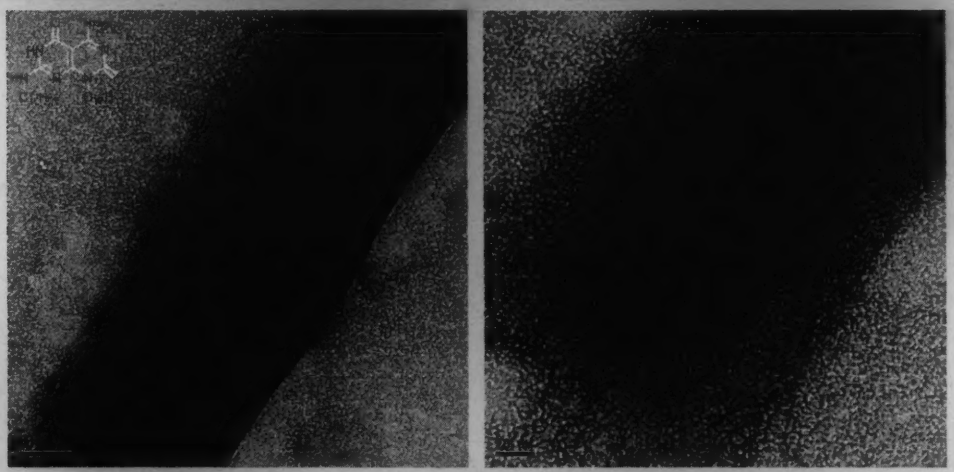

Figure 3. 41. TEM images 1a cast on carbon film stained with uranyl acetate (0.25 g/L, decanol). Measured nanotubes diameter is 4.6 ± 0.5 nm.

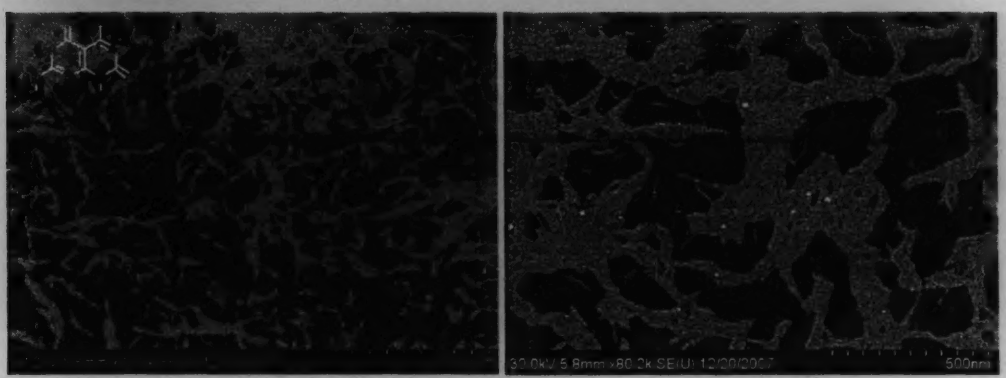

Figure 3. 42. SEM images of 1b cast on carbon film (0.25 g/L, decanol).

Figure 3. 43 SEM images of 1c cast on carbon film (0.25 g/L, decanol).

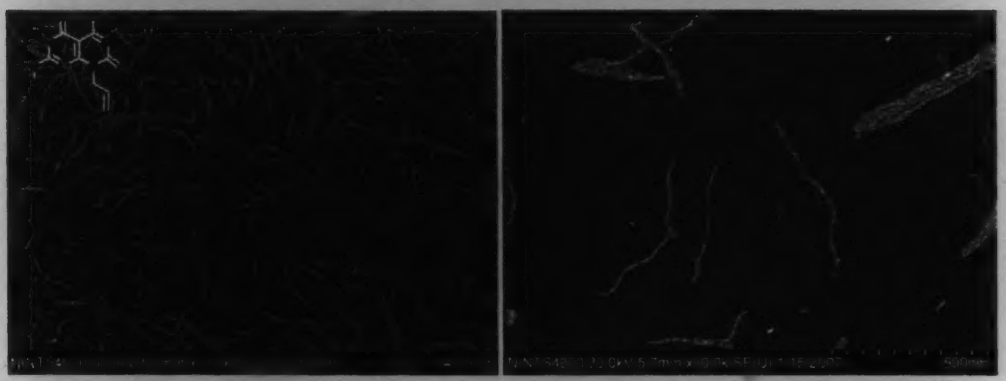

Figure 3. 44 SEM images of 1d cast on carbon film (0.25 g/L, decanol)

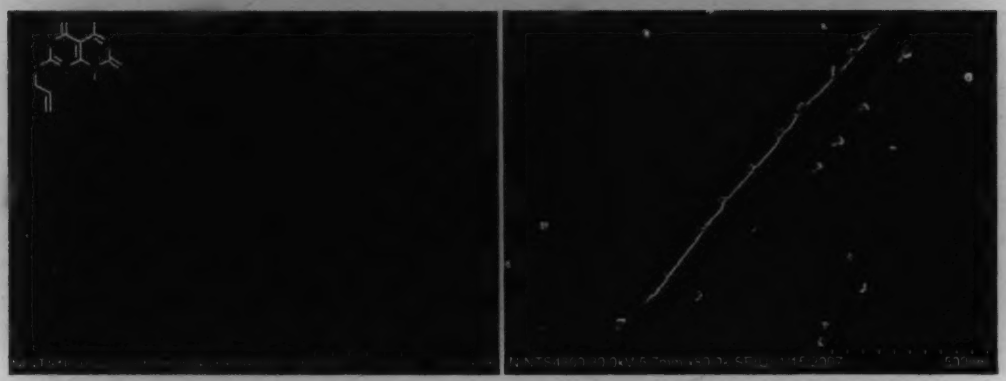

Figure 3. 45 SEM images of 1e cast on carbon film (0.25 g/L, decanol)

Figure 3. 46 SEM images of 1f cast on carbon film (0.25 g/L, decanol)

(D) Self-assembly studies in heptanol

In heptanol (Figures 3.47 – 3.43) only **1a** formed nanorods similar to the ones observed in decanol. However, the nanorods were thinner and shorter in heptanol. **1b, e, f** formed multilayered nanotube sheets similar to **1a, c, e** in decanol. The sheets were noticeably thicker in heptanol, probably due to higher polarity of the solvent. **1c, d** formed long polydisperse RNTs bundles network. Coexistent with the bundles network compound **1d** formed an unexpected architecture – reminiscent of the bowties observed in chloroform. This architecture is most likely made up of "wrinkled" nanotube monolayers. Similar architectures that could be the precursors of the "wrinkled" structures were found for compound **1b** in heptanol. TEM studies of **1a** nanorods revealed the presence of nanotubes aligned along the main axis of the nanorods (Figure 3.48) just as in decanol. Also, for some of the compounds, individual nanotubes were observed by SEM, along with the main nanostructures.

Figure 3. 47 SEM images of 1a cast on carbon film (0.25 g/L, heptanol)

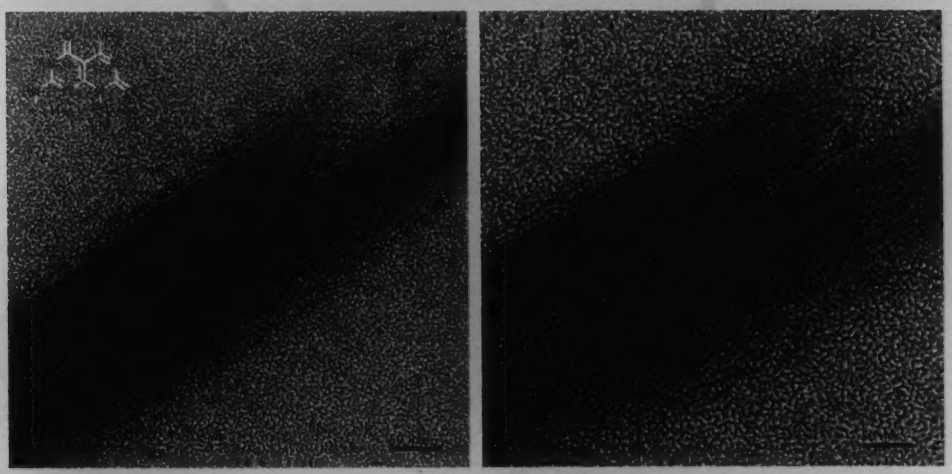

Figure 3. 48 TEM images 1a cast on carbon film stained with uranyl acetate (0.25 g/L, heptanol). Measured nanotubes diameter is 4.5 ± 0.5 nm.

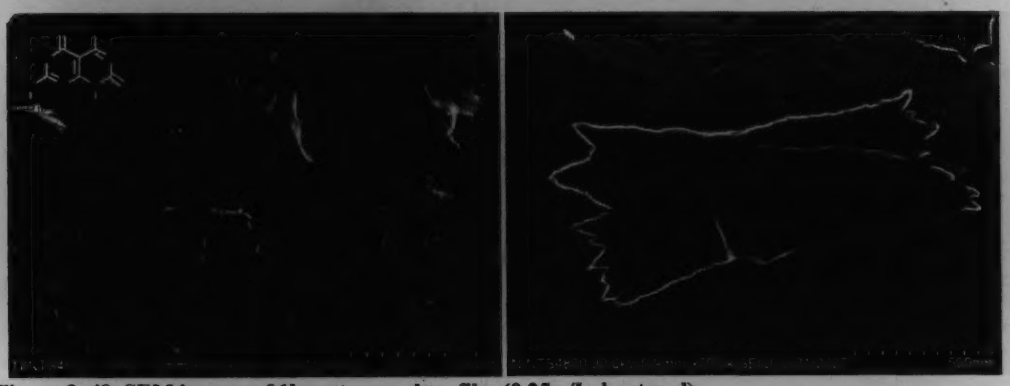

Figure 3. 49. SEM images of 1b cast on carbon film (0.25 g/L, heptanol).

Figure 3. 50. SEM images of 1c cast on carbon film (0.25 g/L, heptanol).

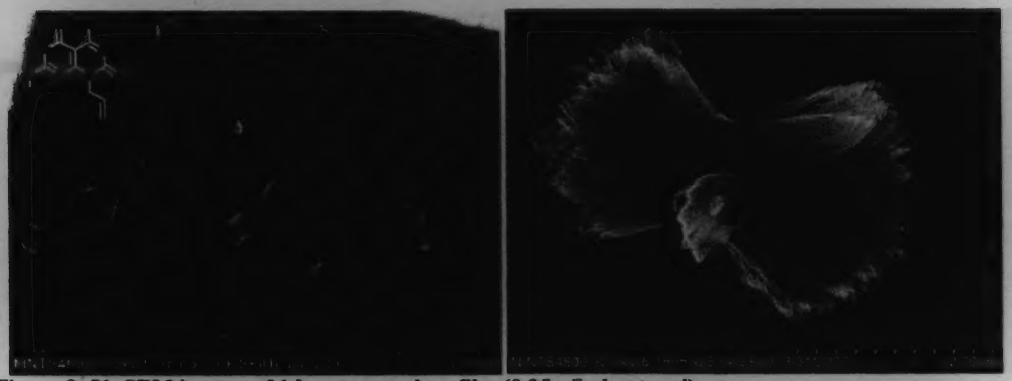

Figure 3. 51. SEM images of 1d cast on carbon film (0.25 g/L, heptanol).

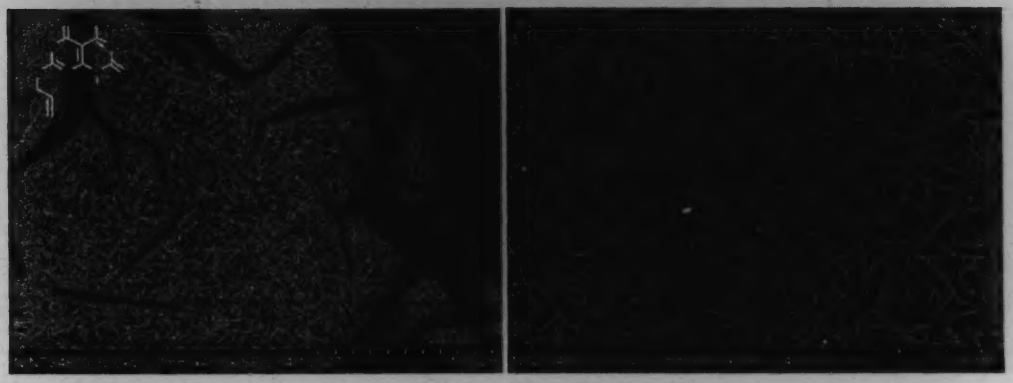

Figure 3. 52 SEM images of 1e cast on carbon film (0.25 g/L, heptanol)

Figure 3. 53. SEM images of 1f cast on carbon film (0.25 g/L, heptanol).

(E) Self-assembly studies in butanol

In butanol (Figures 3.54 – 3.60) all the compounds formed RNT bundles and networks. In case of compound **1b** the bundle network coexists with a population of thin wrinkled sheets. In the alcohol solvent series, the order/crystallinity of the nanostructures decreases as the length of the alcohol's alkyl chain decreases (solvent polarity increases). This is probably due to more kinetic rather than equilibrium growth dynamics of the bundles. TEM studies of the bundle networks assembled from **1a** revealed the presence of RNTs aligned along the main axis of the nanorods just as in decanol (Figure 3.55).

Figure 3. 55. TEM images 1a cast on carbon film stained with uranyl acetate (0.25 g/L, butanol). Measured nanotubes diameter is 4.7 ± 0.6 nm.

Figure 3. 56. SEM images of 1b cast on carbon film (0.25 g/L, butanol).

Figure 3. 57. SEM images of 1c cast on carbon film (0.25 g/L, butanol).

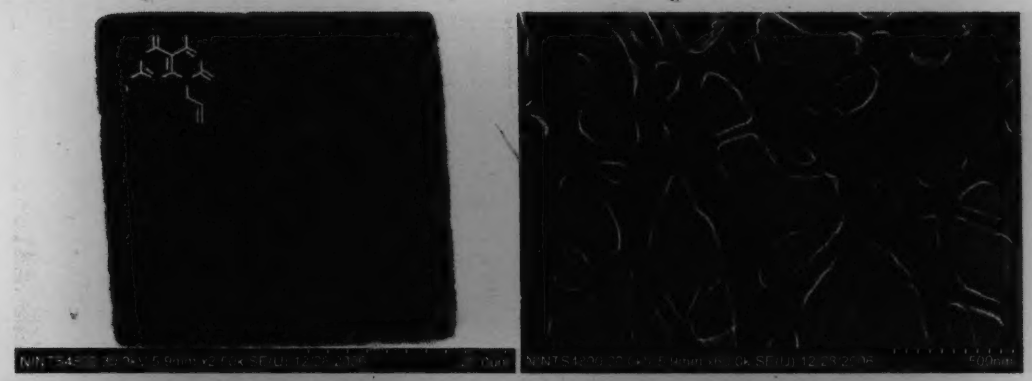

Figure 3. 58. SEM images of 1d cast on carbon film (0.25 g/L, butanol).

Figure 3. 59. SEM images of 1e cast on carbon film (0.25 g/L, butanol).

Figure 3. 60. SEM images of 1f cast on carbon film (0.25 g/L, butanol).

(F) Self-assembly studies in nitromethane

Assembly of the compounds in nitromethane (Figures 3.61 – 3.68) provided the most diverse set of morphologies. Compounds **1a, b** form a number of coexisting nanoarchitectures in the solvent including rod-like, shoe sole-like, and flower-like structures with dimensions up to three micrometers. Multilayered structure of thick sheet structures formed by **1a** were observed by SEM (Figure 3.61). Moreover, periodic wave-like fold with period of ~ 75 nm were observed for the same structures (Figure 3.63).

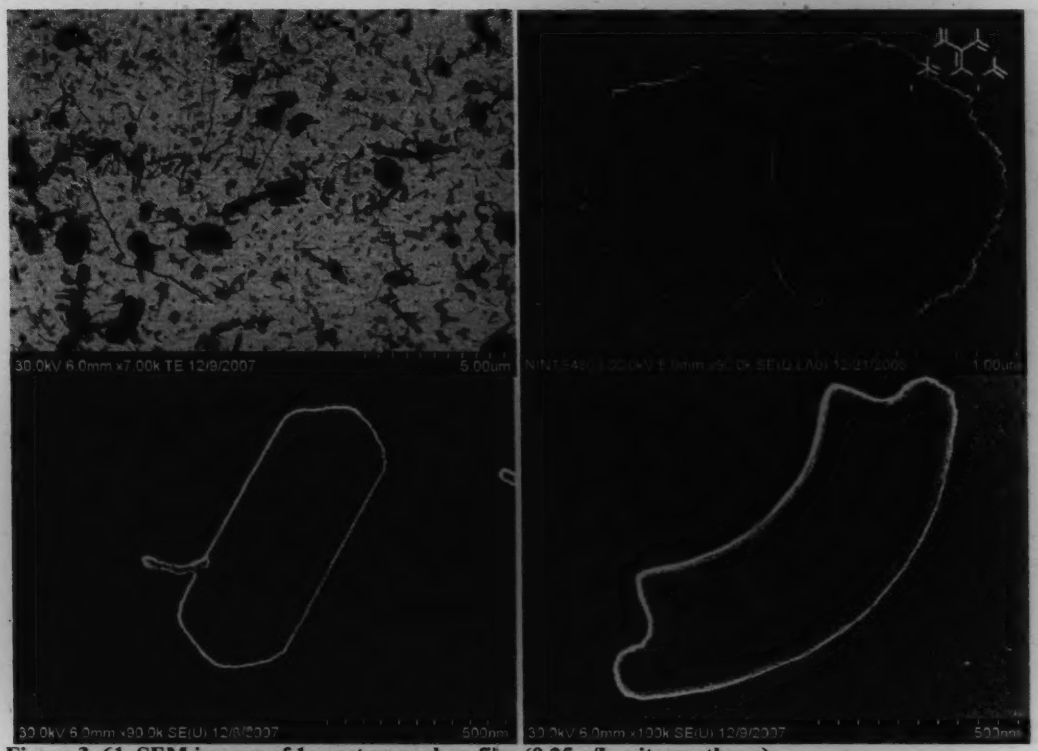

Figure 3. 61. SEM images of 1a cast on carbon film (0.25 g/L, nitromethane)

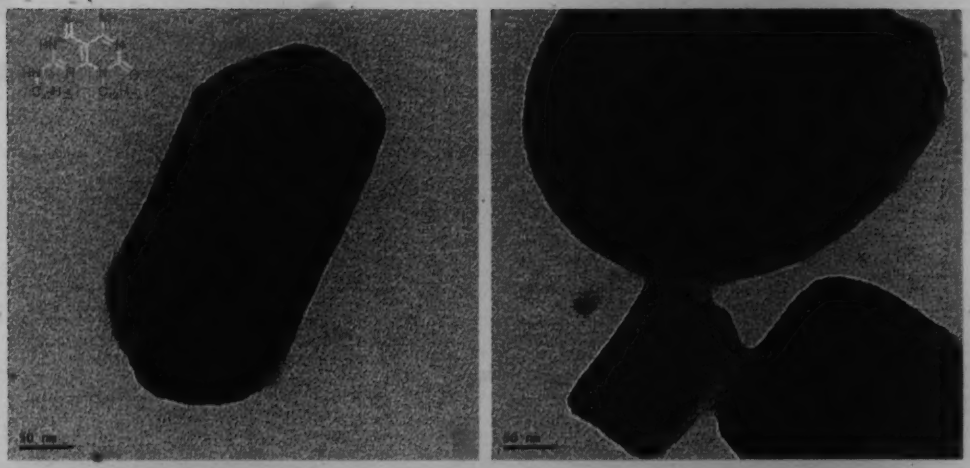

Figure 3. 62 Cryo-TEM images 1a cast on carbon film stained with uranyl acetate (0.25 g/L, nitromethane). Measured nanotubes diameter is 4.7 ± 0.3 nm.

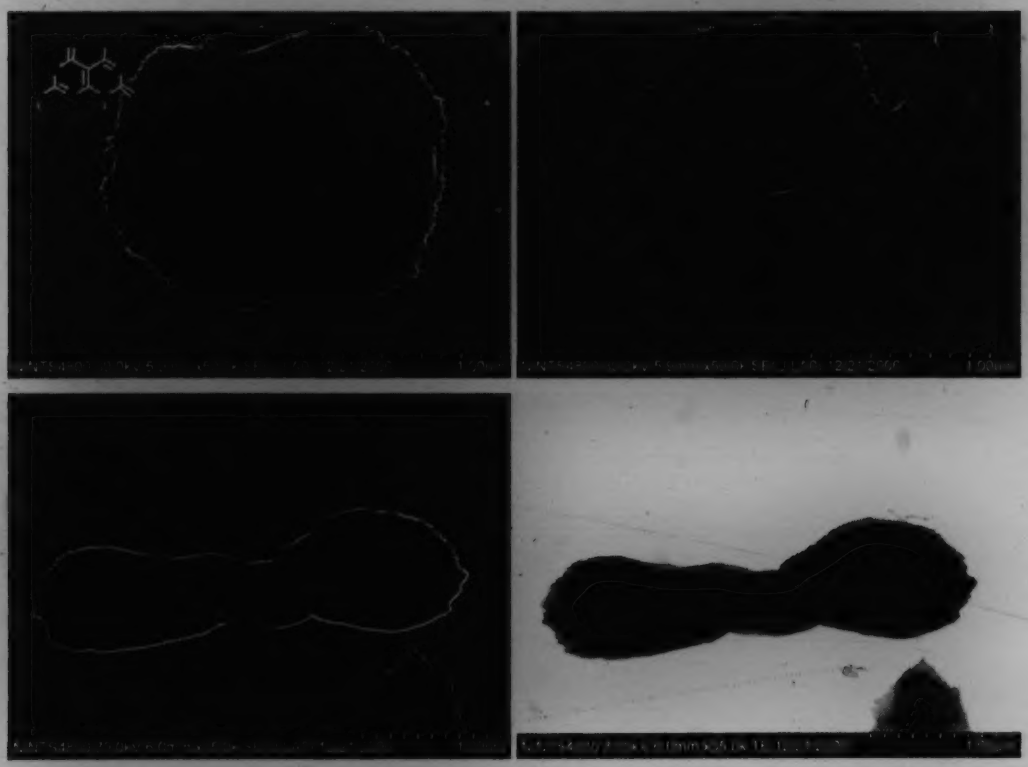

Figure 3. 63. SEM images of 1a cast on carbon film (0.25 g/L, nitromethane) demonstrating multilayered structure and the presence of periodic folds.

Compounds **1c, d** formed nanorod structures reminiscent of those assembled from **1a, c, d** in decanol. However, the rods in nitromethane are cylindrical as opposed to prolate rods in decanol. The nanorods of **1c** and **1d** have diameters of 43 ± 6 nm and 52 ± 7 nm respectively. The nanorods assembled from **1c, d** have more bending points and therefore appear to be more flexible than the ones assembled from **1a, c, d** in decanol.

Compounds **1e, f** form flower-like structures that most likely consist of wrinkled multilayered RNT sheets observed previously stuck to one another. It is unclear why **1c, 1d** form only rods, and **1e** and **1f** assemble into flower-like structures, but it is most likely related to the difference in the molecular structure of G^C modules in which positions of alkyl and allyl substituents are switched for these two different morphologies. TEM studies of the various nanostructures present in **1a** assemblies revealed that they are all made of nanotubes (Figure 3.62).

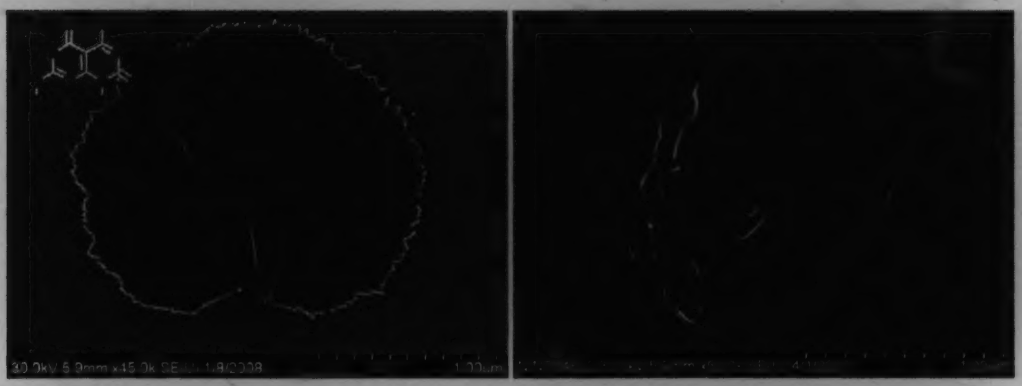

Figure 3. 64. SEM images of 1b cast on carbon film (0.25 g/L, nitromethane).

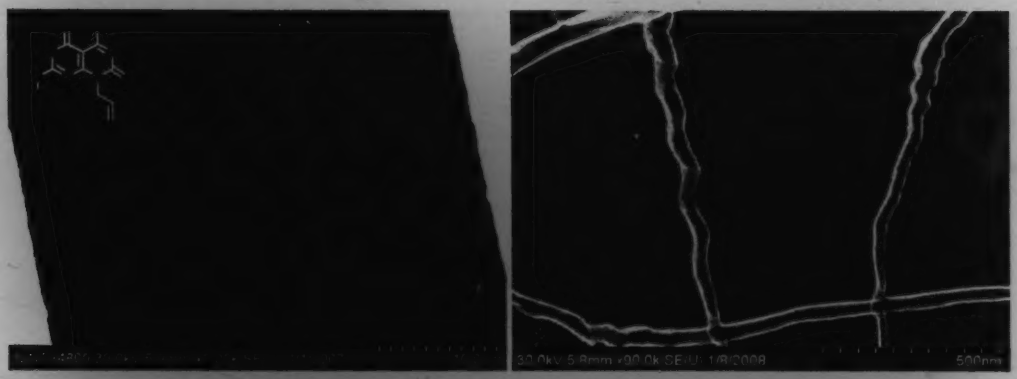

Figure 3. 65. SEM images of 1c cast on carbon film (0.25 g/L, nitromethane).

Figure 3. 66. SEM images of 1d cast on carbon film (0.25 g/L, nitromethane).

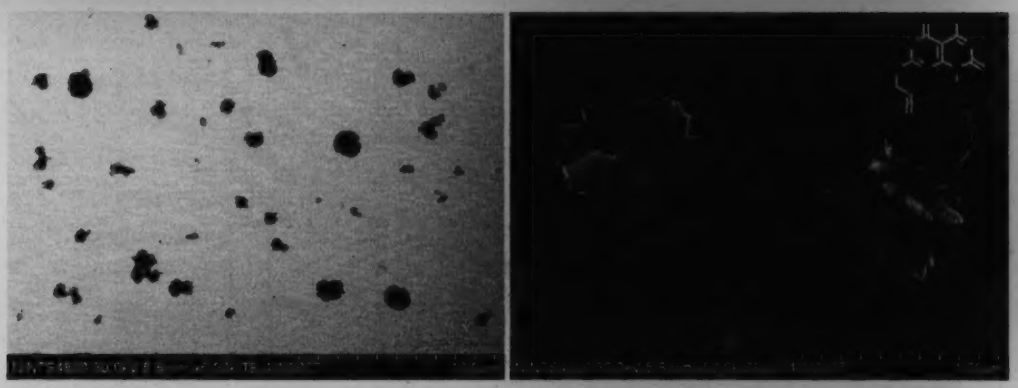

Figure 3. 67. SEM images of 1e cast on carbon film (0.25 g/L, nitromethane).

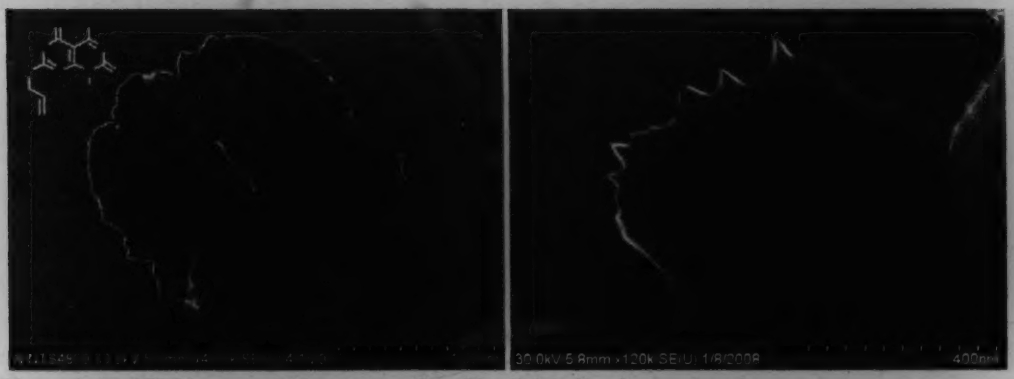

Figure 3. 68. SEM images of 1f cast on carbon film (0.25 g/L, nitromethane).

(G) Self-assembly studies in DMF

Self-assembly in dimethylformamide provided the most intriguing architectures – nanodonuts (Figures 3.70 – 3.77). Individual nanodonuts with sizes from 150 to 1000 nm and thicknesses from 50 to 150 nm were found for compounds **1a, b, c, f**. Donuts embedded into the ropes that are made of nanotube bundles were found for **1d, e**. The yields estimated from SEM images and the concentration range at which nanodonuts where observed are summarized below. The yield was found by dividing area covered by the donuts by total area covered by both donuts and ropes.

compound	**1a**	**1b**	**1c**	**1d**	**1e**	**1f**
Concentration range, g/L	0.1-6.0	0.1-3.0	0.1-3.0	0.5-5.0	0.25-1.0	0.25-1.0
Yield, % at (concentration*)	95 (3)	90 (3)	60 (3)	10 (2)	5 (1)	50 (1)

*The concentration at which the estimated yield was the highest given (g/L).

The structure of the donuts formed from **1a** was studied by SEM, TEM, and AFM. TEM images of stained donuts show the presence of nanotubes with diameter of 4.4 ± 0.5 nm aligned along the donuts perimeter. High contrast in AFM amplitude images has

allowed measuring the nanotubes diameter 4.7 ± 0.3, which corroborates TEM measurements. Both values are consistent with the diameter of the nanotubes obtained from modeling studies.

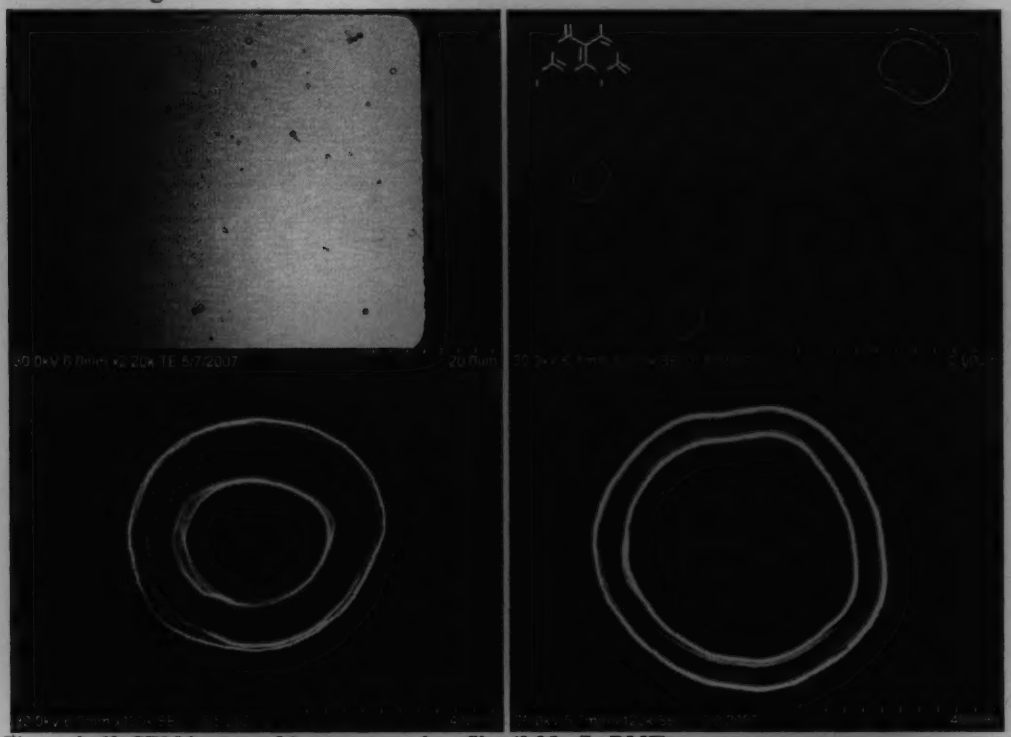

Figure 3. 69. SEM images of 1a cast on carbon film (0.25 g/L, DMF).

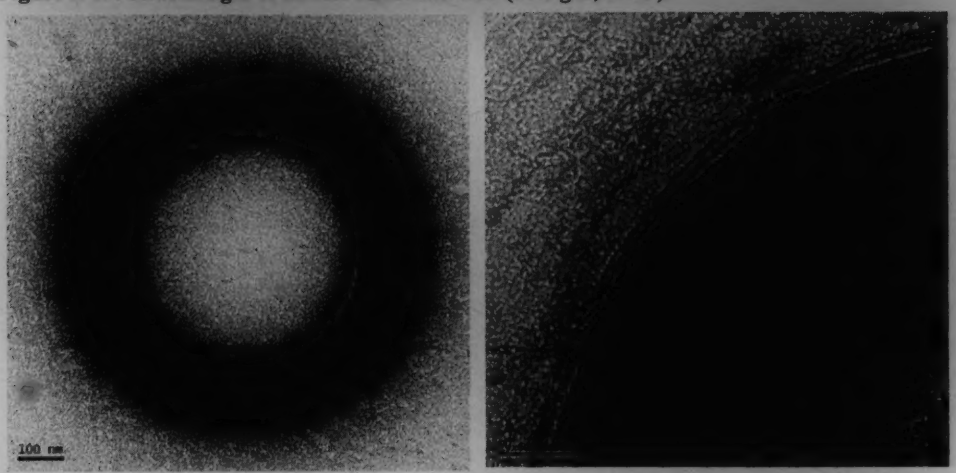

Figure 3. 70. TEM images 1a cast on carbon film stained with uranyl acetate (0.25 g/L, DMF). Measured nanotubes diameter is 4.4 ± 0.5 nm.

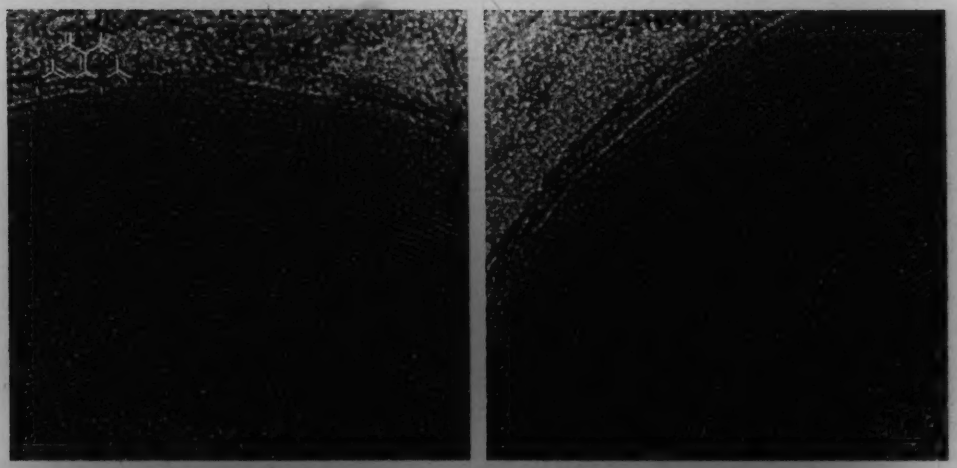

Figure 3. 71. TEM images 1a cast on carbon film stained with uranyl acetate (0.25 g/L, DMF).

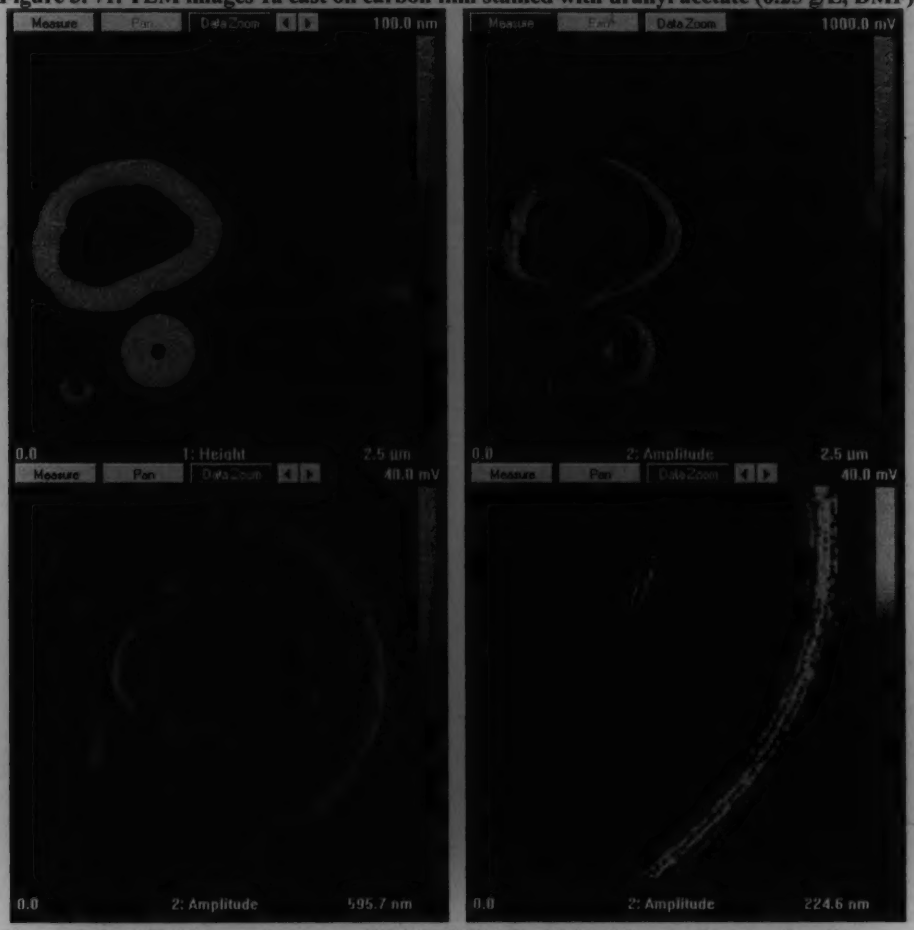

Figure 3. 72. AFM images 1a cast on HOPG (0.25 g/L, DMF). Measured nanotubes diameter is 4.7 ± 0.3 nm.

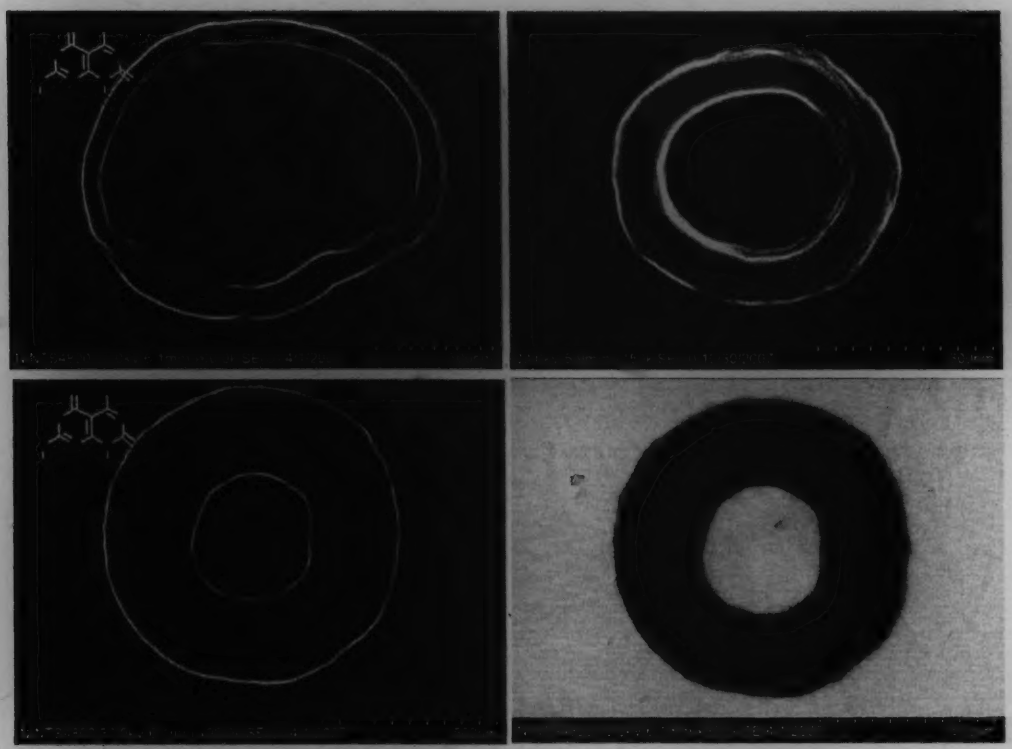

Figure 3. 73. SEM images 1b cast on carbon film (0.25 g/L, DMF)

Figure 3. 74. SEM images 1c cast on carbon film (0.25 g/L, DMF).

Figure 3. 75. SEM images 1d cast on carbon film (0.25 g/L, DMF).

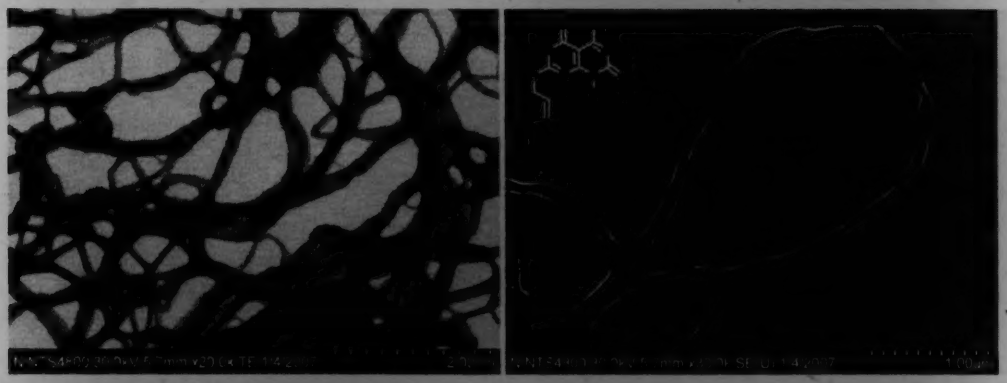

Figure 3. 76. SEM images 1e cast on carbon film (0.25 g/L, DMF).

Figure 3. 77. SEM images 1f cast on carbon film (0.25 g/L, DMF).

The donuts were also imaged at various accelerating voltages to find optimal conditions for imaging (Figure 3.78). Sample "charging" makes voltages below 10 keV impractical for imaging. Stage tilting was also used for imaging (Figure 3.79).

Figure 3. 78. SEM images of 1a donuts at 30 kV (left) and 1 kV electron beam accelerating voltages.

Figure 3. 79. SEM images of 1a donuts on tilted stage.

In order to understand the principle governing the donut self-assembly process, the concentration, time, and temperature dependent evolution of **1a** morphology in DMF was investigated by SEM. The shape of the donuts was found to be generally independent of the concentration of **1a** (Figure 3.80). The density of the donuts covering the grid was found to be proportional to the concentration. Larger populations of ropes and donuts stuck to one another were found at higher concentrations.

Evolution of the morphologies assembled at different temperatures was monitored by SEM (Figures 3.81 – 3.83). Formation of ribbons of mono and multilayers of nanotubes at 0 °C was accompanied by the formation of loops on the nanotube ends.

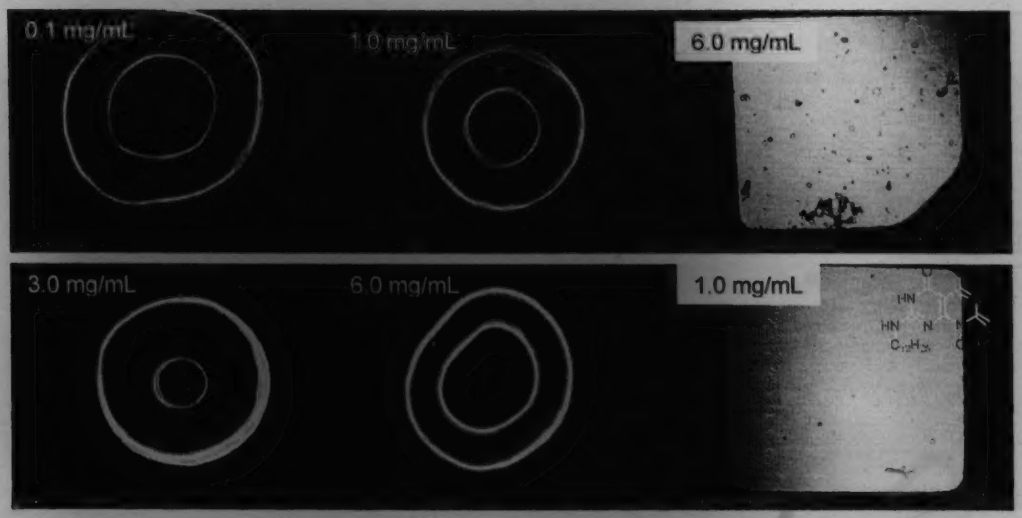

Figure 3. 80. SEM images of 1a assembled at different concentrations.

Figure 3. 81. Time dependence of 1a sonicated for 10 sec at 0 °C and assembled at 0 °C (0.25 mg/mL).

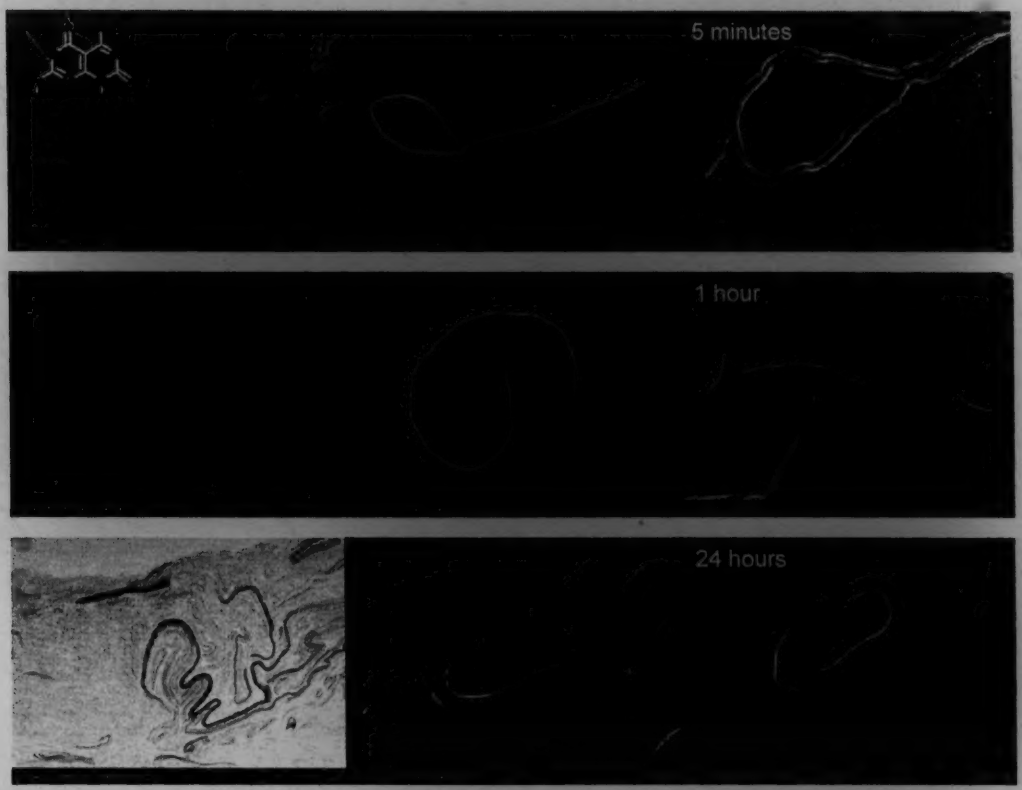

Figure 3. 82. Time dependence of 1a sonicated for 10 sec at 25 °C and assembled at 25 °C (0.25 mg/mL).

Figure 3. 83. 1a boiled for 10 seconds cast on carbon film (0.25 mg/mL, DMF).

Formation of thicker RNT bundles and their progressive folding was observed at 25 °C. Assembling **1a** for longer than a day resulted in more loop formation, but it did not yield "perfect" donuts. Ideal donuts (Figure 3.83) were observed only when solution was boiled. Self-assembly at DMF's boiling point (153 °C) is very fast and yields donuts after only 10 seconds (Figure 3.83).

Mechanism of nanodonut formation

To understand the mechanism of donut formation a literature search was performed with the goal to find similar morphologies. A variety of materials were found to form similar nanoring structures: porphyrin derivatives,[122-126] metal nanoparticles,[127-129] amphiphilic dumbbell molecules,[130] macromolecules,[38, 131, 132] biopolymers,[133-139] carbon nanotubes[140, 141] and carbon nanotube bundles.[96, 142, 143]

A number of mechanisms for ring structure formation were proposed. However only two mechanisms were well established: (A) ring formation resulting from surface force phenomena during solvent evaporation[122, 127, 144] (drying effect), and (B) covalent linking of a high aspect ratio nanostructure.[131, 140, 141] Spooling of flexible circular strands and few other mechanism were proposed as well.[135-137, 145].

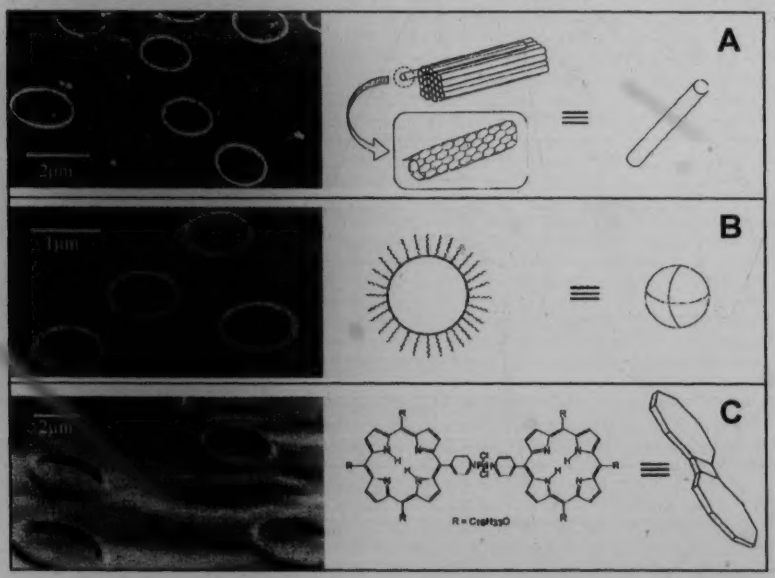

Figure 3. 84. Examples of nanorings obtained by drying effect from (A) CNT bundles,[37] (B) metal nanoparticles,[28] (C) porphyrin derivative.[122] SEM images (left) and corresponding scheme (right). Adapted with permission from ref[144]. Copyright 1998 Wiley Interscience.

(A) *Drying effect* (Figure 3.84). Consider the particular case of a drop of a dilute organic solution of alkylthiol-passivated silver nanocrystals[127] placed on a substrate.

Upon evaporation of the solvent, 0.1±5 μm diameter rings are observed in high yield. As the thickness of the evaporating film becomes thinner than the equilibrium thickness t_e, there is a balance between the disjoining pressure and spreading coefficient contributions to the free energy. At this point, holes nucleate and begin to grow in order to restore this optimum film thickness. It is significant that nucleation of holes starts only when the film has thinned down to nanometer-sized dimensions. Furthermore, as the holes grow they push out the metal particles along their advancing rim (three-phase contact line). Finally, the resulting ring of particles gets "stuck" when the friction between the particles and the substrate can no longer be overcome by the force acting radially outward to thicken the film. This model implies that for a specific particle size, solvent, and substrate, the ring diameter is expected to vary inversely with particle concentration. Also, the ring sizes should all be the same for any given sample, even if their associated holes began to grow at different times. It is very unlikely that donut assembly is due to drying effect in this work, since drying should be very dependent on surface properties. Furthermore, the donuts were obtained on different surfaces varying from hydrophilic mica and glass, to hydrophobic HOPG and amorphous carbon.

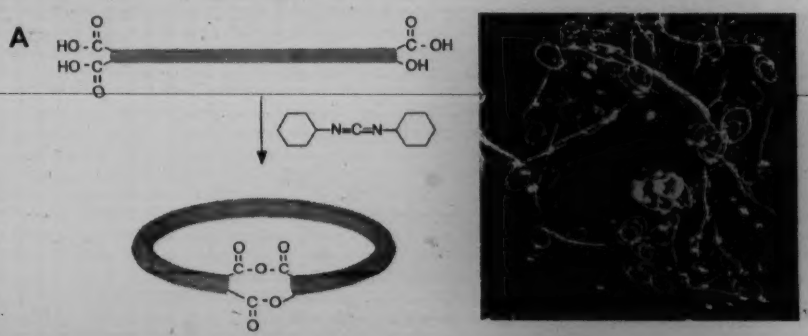

Figure 3. 85. An example of CNTs covalently closed into rings.[141] (A) Scheme of the process. (B) AFM image of the nanorings on mica (scale bar = 10 μm). Adapted with permission from ref [141]. Copyright 2008 American Association for the Advancement of Science.

(B) *Covalent linking* mechanism is straightforward. Two functions attached to opposing ends of a high aspect ratio structure can be chemically attached to each other. In this case the length of the structure should be more than its persistence length.[129] For example, Shinkai et al.[141] reported covalent linking of carbon nanotubes via ester and anhydride formation (Figure 3.85). Under certain conditions CNTs were reported to form seamLess single CNT rings during their growth process.[140]

It is very unlikely that the mechanism of donut formation in this work is similar to the covalent linking process described in the literature, since the forces that would cause RNTs to form seamLess circular assemblies are too weak. It is unclear from EM images if there are seamLess tube rings present in donuts, since staining of hydrophobic nanotubes poses a problem and it is impossible to have all of a single donut in perfect focus due to its large size and variations in thickness along the perimeter. No seamLess circular RNTs were found in AFM images. Donut formation due to nanoscale solvent whirlpool formations during drying were also ruled out since both drop casting and spin casting (deposition of the drop on a rotating at 2000 rpm substrate) yielded the donuts with the same appearance. Formation of a long circular strand with its subsequent spooling into a donut is thermodynamically unfavorable. On the basis of time, temperature, and structure studies of derivatives **1a-f** in DMF the following donut formation mechanisms are proposed.

(I) Loop templating rings. This mechanism illustrated in the Figure 3.86, can be devided into several steps: (A) single nanotubes form bundles (B, C) that start to bend to form loops (D, E, F). Each loop then serves as a template for donut formation as more

tube bundles adhere to the loops in a circular fashion (G, H). A donut formed in this way (I) is released and the loop continues to serve as a nucleation site for subsequent donuts.

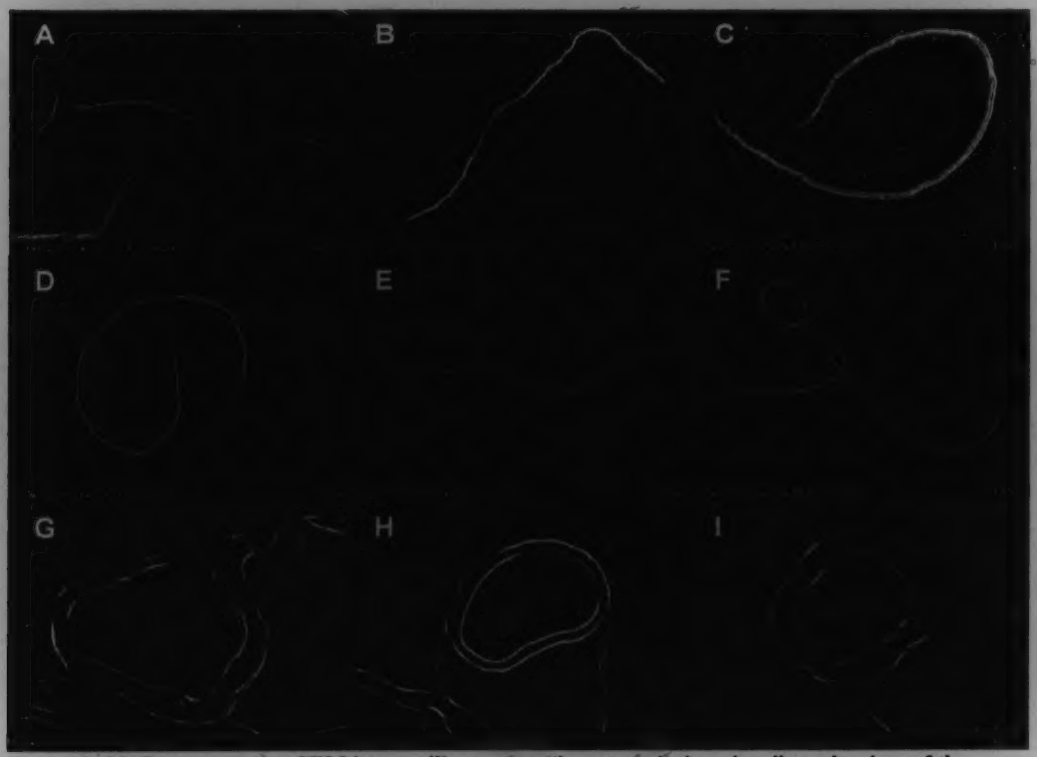

Figure 3. 86. Representative SEM images illustrating "loop templating rings" mechanism of the donuts formation.

(II) Coiling of nanotube ribbons (Figure 3.87). It was noticed that RNTs tend to form sheets or ribbons in the early stages of their growth (A, B). The ribbons further thicken via nanotube aggregation from the solution (C). When the supply of nanotubes is depleted, the solvophobic forces that are quite strong for **1a** in DMF, force the ribbons to coil (D–I). Coiling can start in the middle of the ribbon (D) or from one of its ends (E). Energy-filtered TEM revealed multilayered structure of the donuts (panels J, K, M, N), that can be seen to some extent in the AFM image (O). Panel L shows a RNT ribbon in an early coiling stage.

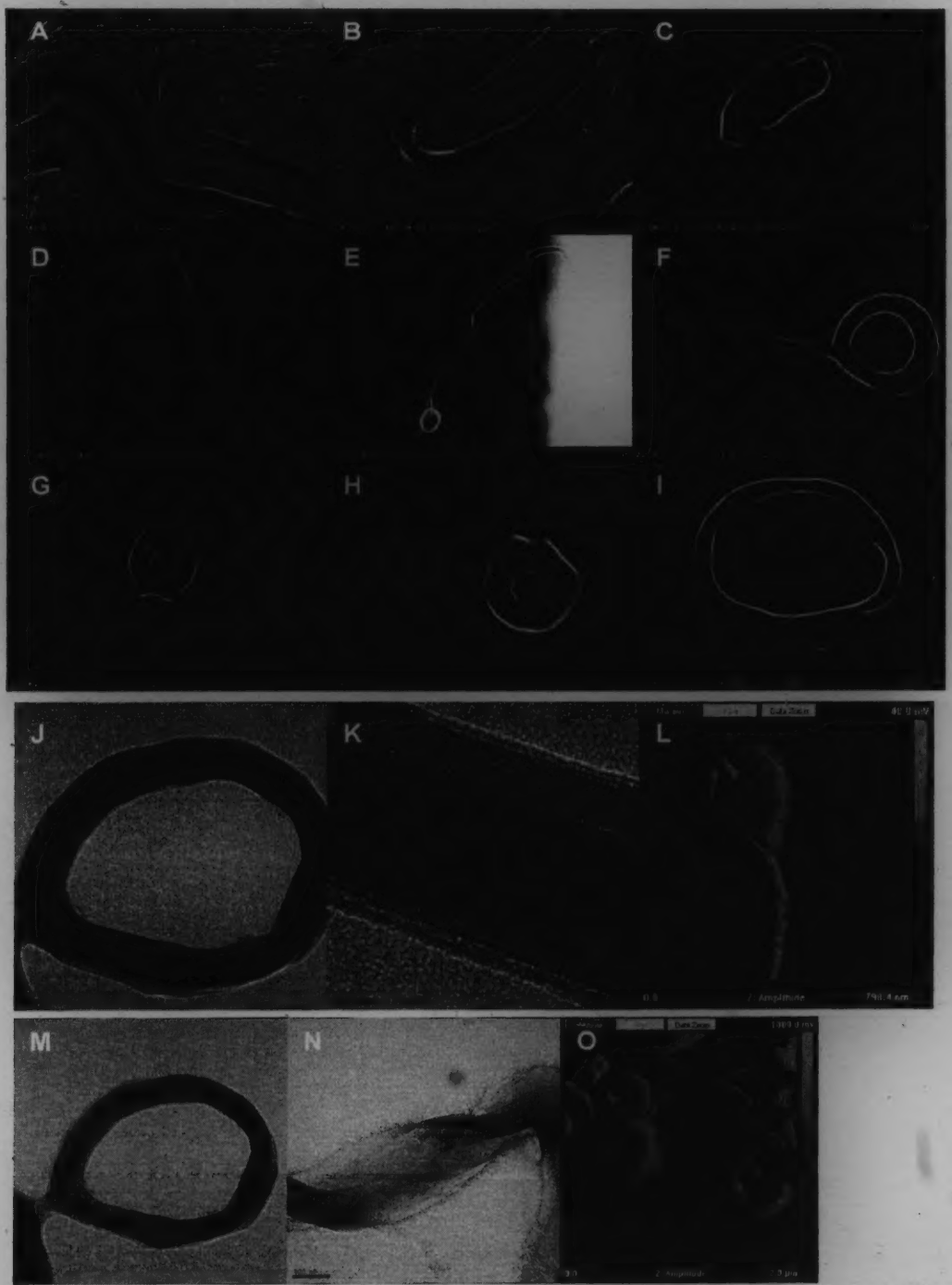

Figure 3. 87 Representative SEM images illustrating "coiling of nanotube ribbons" mechanism of the donuts formation (A-I). Energy filtered TEM images of unstained donuts showing layered structure of donuts (J, K, M, N). AFM amplitude image of nanodonuts (L, O).

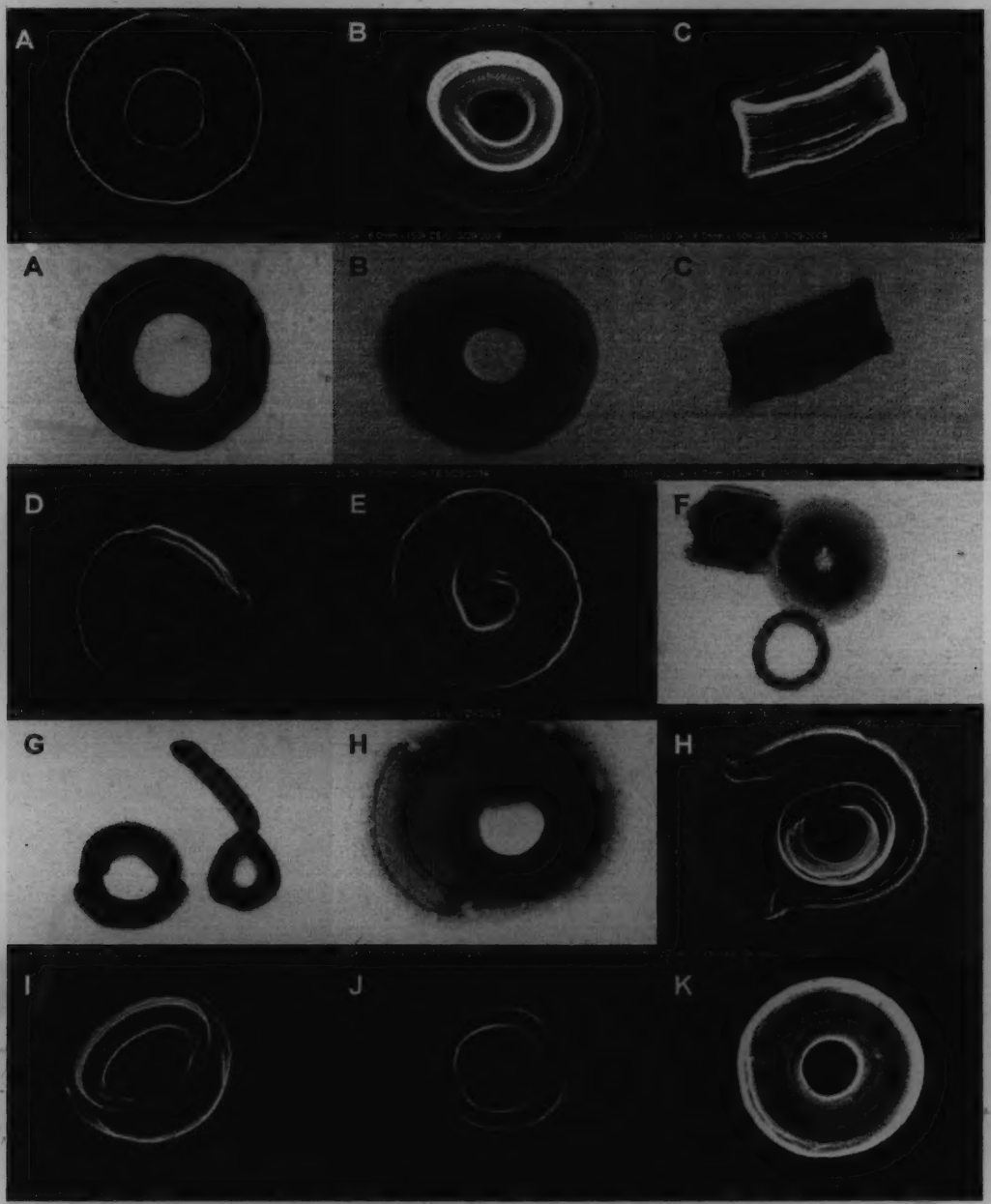

Figure 3. 88. Representative SEM images illustrating concentric rolling ribbons mechanism. The same letter is used for bright and dark field SEM imaging modes of the same area.

(III) Concentric rolling of the ribbons (Figure 3.88). In the early stages, this mechanism is topologically similar to mechanism (II). However, if the sheets/ribbons formed in the early stages are very wide, the thickening of the ribbons, driven by

solvophobic interactions, proceeds not via coiling but through radial folding of the concentric nanotube sheets. Initially the sheets can be flat (A, B) or cylindrical (C). Flat sheets can start to roll to either from the inner edge (A) or the outer edge (B). Brighter area of the concentric sheets in scattering mode indicate elevation of the structure ("edge effect"), that correspond to larger thickness in transmission mode, thus confirming the suggested structure. Cylindrical ribbons can roll from both edges simultaneously (e.g. panel F). Panels D, G–K show progressive rolling of flat ribbons to form a "perfect" donut eventually (K). Panel F shows that cylindrical and flat sheets at different stages of folding coexist in the same mixture. Panel E illustrates the possibility that flat sheets may form from cylindrical ones. A fold protruding into the inner circle (E) is most likely caused by mechanical stress developed during such flattening.

Certain donuts were found to have a helical twist around the perimeter (Figure 3.89) indicating that they may be formed from coiled ribbons. Mechanism (II) should be dominant in this case.

(IV) Internal end-to-end fusion (Figure 3.90). This mechanism is well illustrated by the image of snake biting its own tale. Certain "imperfections" were sometimes observed in the structure of donuts by SEM (Figure 3.90) that might be the seams left after the ends of a thick nanotube bundle met each other to fuse into a ring. It however appears to be an unlikely mechanism, since RNTs tend to form very long bundles that cannot form the donuts with observed dimensions. The "imperfections" are most likely the creases formed while relieving the mechanical stress of folding/twisting of the donuts.

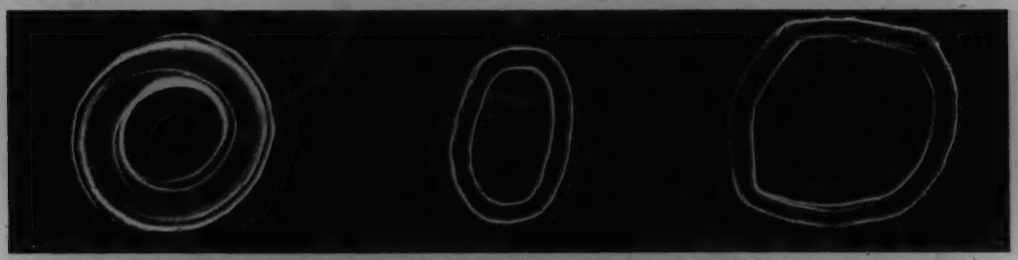

Figure 3. 89. SEM images illustrating helical twist along the some donuts' perimeter.

Figure 3. 90. SEM images illustrating "internal end-to-end fusion" mechanism.

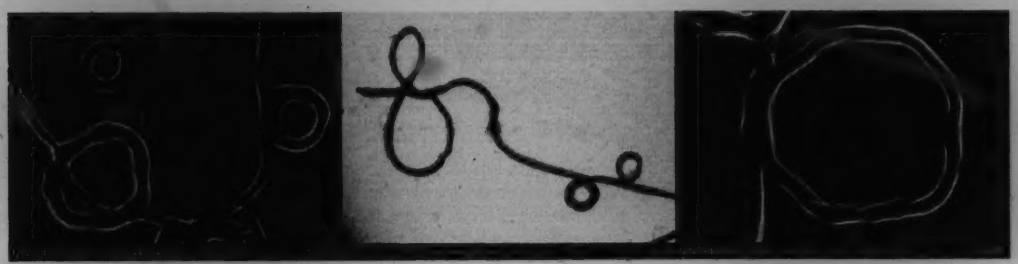

Figure 3. 91. SEM images illustrating "budding" mechanism.

(V) **Budding mechanism** (Figure 3.91). This mechanism proceeds via loop formation. During the dynamic process where the inner structure of the bundles could be in a fluid state (see the explanation in the next paragraph) the donut "buds off" to become independent.

Some of the donuts look so "perfect" (e.g. Figures 3.80, 3.83) that it makes one think that they are made up of an array of seamLess single RNT rings. As was mentioned

before, it was not possible to trace a single RNT along the perimeter of a donut to prove or disprove the hypothesis. However it is possible that during the late stages of donut evolution a curtain like state may be present wherein the nanotubes within the donuts are in a semi-liquid-crystalline state (due to long alkyl chains presence and high temperature). In order to minimize the mechanical stress developed during the folding process they may form seamLess structures.

It is most likely that several mechanisms particularly I, II, and III contribute significantly to the pathways to donut formation.

(H) Self-assembly studies in DMSO

In dimethysulfoxide (Figures 3.92 – 3.98) compounds **1a–f** form a large variety of nanostructures. Very thick bundles of nanotubes up to 500 nm in diameter are formed from **1a–c**. Interestingly, periodic wave-like (**1a, b**) or helical staircase-like (**1c**) bundles were observed. This is probably due to the mechanical stress caused by the helical twist in the bundle structure. TEM studies of **1a** bundles revealed the presence of nanotubes aligned along the main axis of the structures (Figure 3.93). Deviating from the trend observed for **1a–c**, **1d** formed octopus-like structures. These structures may be the result of sheaflike structure evolution into spherulites by the splitting mechanism observed for **1a–c** in chloroform. Compound **1e** formed thick (up to two microns in diameter) but relatively short (around 3.5 microns on average) tadpole-like structures. The mechanism of formation of these structures is unclear at this stage.

Unexpectedly **1f** formed platelets. They are similar to nanospheroids observed for **1a** in chloroform, even though the platelets are more polydisperse (50 – 1000 nm in lateral

dimension and ~20 nm in thickness). It is unclear however if they are made of nanotubes or lipid bilayers. The latter possibility appears to be a reasonable explanation since DMSO is a much more hydrophilic solvent compared to chloroform and might cause such a drastic structural change.

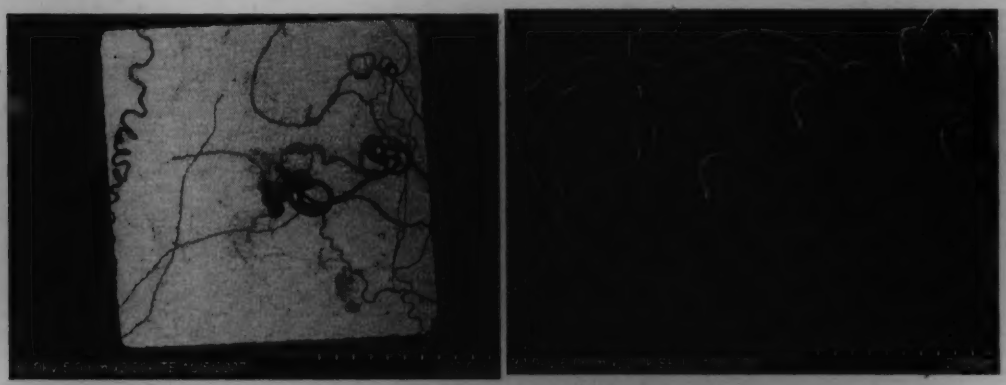

Figure 3. 92. SEM images 1f cast on carbon film (0.25 g/L, DMSO).

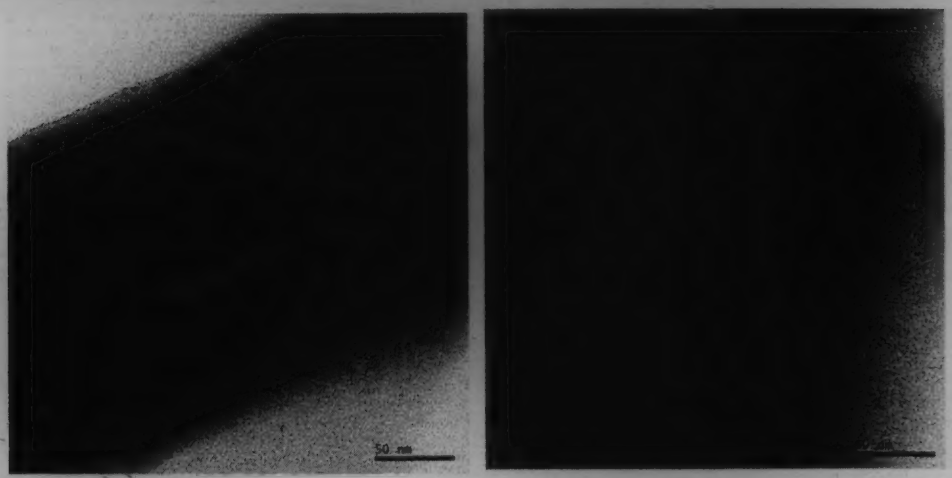

Figure 3. 93. TEM images 1a cast on carbon film stained with uranyl acetate (0.25 g/L, DMSO). Measured nanotubes diameter is 4.4 ± 0.5 nm.

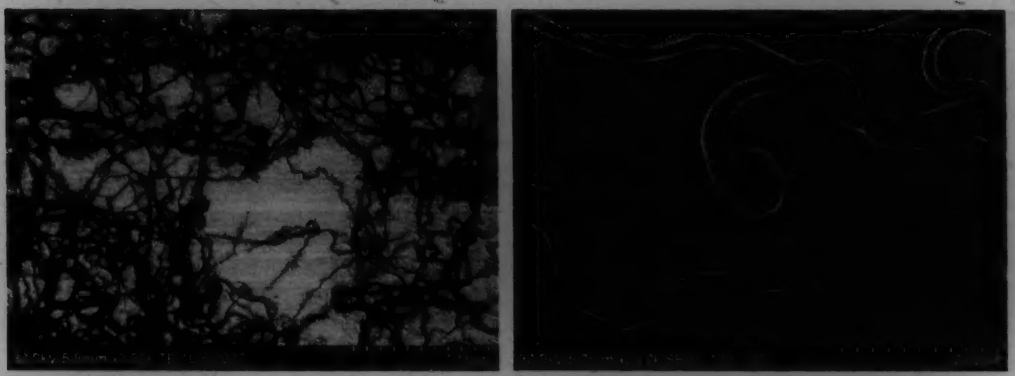

Figure 3. 94. SEM images 1b cast on carbon film (0.25 g/L, DMSO).

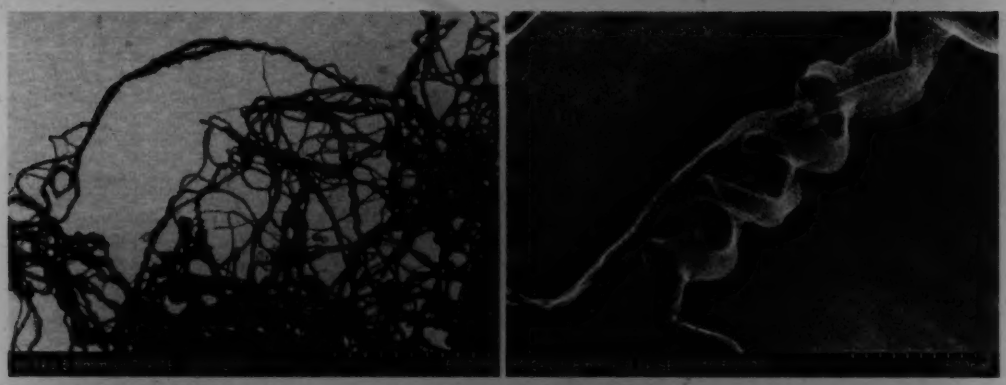

Figure 3. 95. SEM images 1c cast on carbon film (0.25 g/L, DMSO).

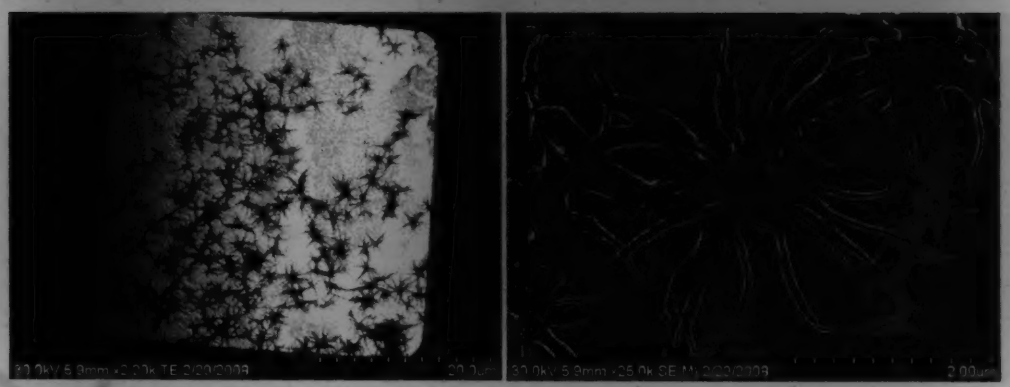

Figure 3. 96. SEM images 1d cast on carbon film (0.25 g/L, DMSO).

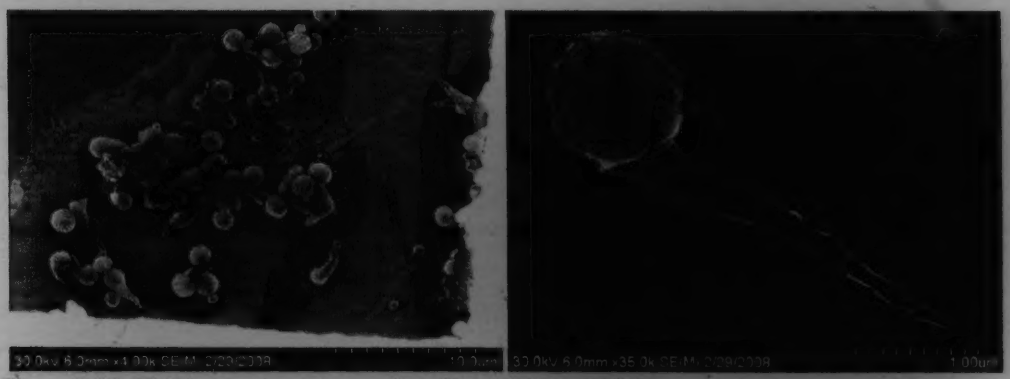

Figure 3. 97. SEM images 1e cast on carbon film (0.25 g/L, DMSO).

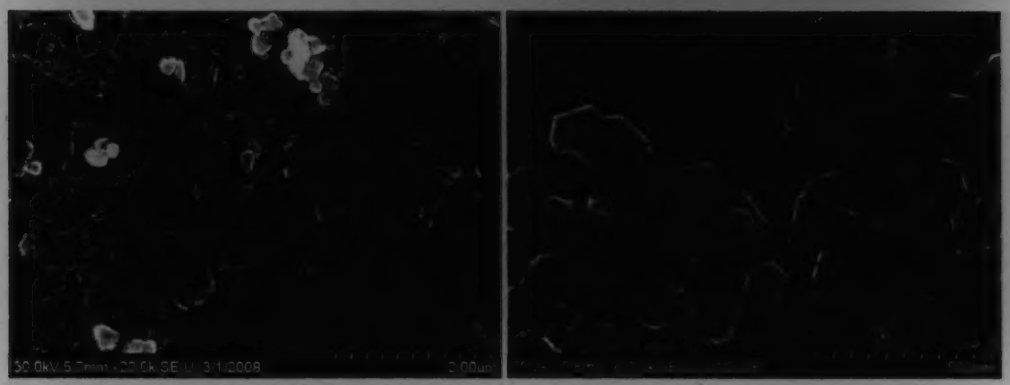

Figure 3. 98. SEM images 1f cast on carbon film (0.25 g/L, DMSO).

3.6. Conclusions

In this chapter, it was demonstrated that the same small molecule can be assembled into a large variety of nanostructures. (e.g. Figure 3.99). In spite of the high polydispersity of the RNTs generated after the first two assembly levels (hydrogen bonding and π-π stacking), the third level of hierarchical self-assembly dictates the length of the tubes within the final aggregate. Thus, control over the morphology at higher hierarchical levels was shown. This is the first reported systematic attempt to control assembly of nanotubes that are themselves hierarchically self-assembled nanostructures.

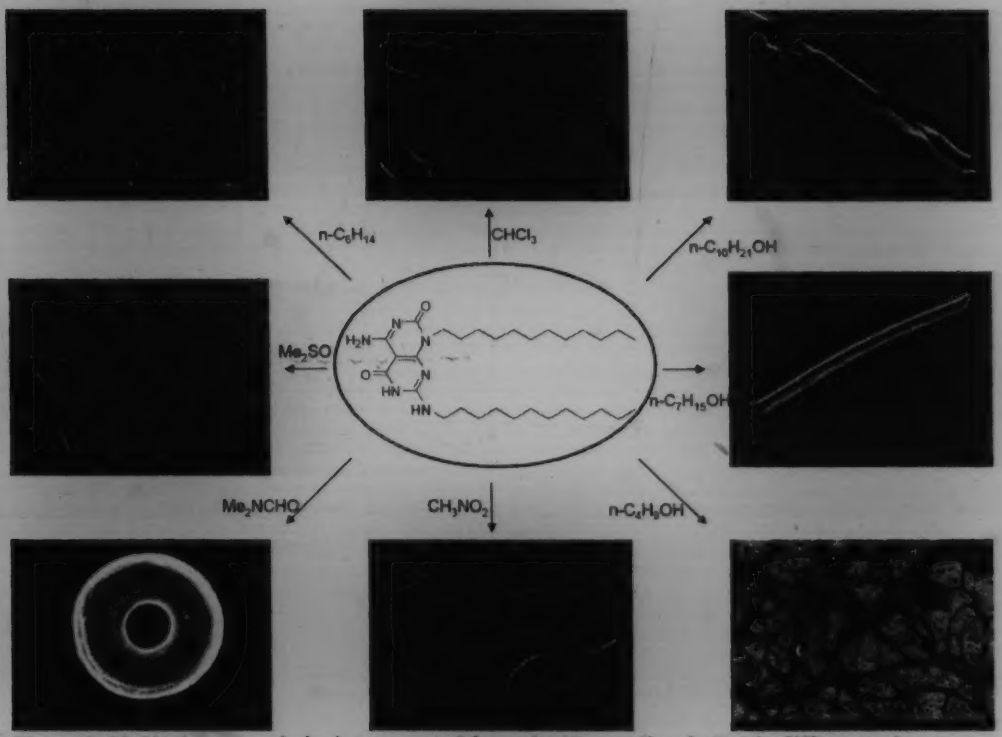

Figure 3. 99. Various morphologies generated from the same molecule (1a) in different solvents.

It was shown that RNT aggregation depends to a large extent on the nature of the solvent. The size of the aggregates generally increases as the polarity of a solvent increases. Eight solvents covering the polarity scale provided most of the *solvent polarity – assembly morphology* correlations were discussed. The correlations found can be used for designing functional materials with desired dimensions. For example, if individual well dispersed nanotubes are needed (e.g. for fabrication of hydrophobic thin film coatings) low polarity hexane should be used for their assembly. If larger mechanically stable nanotube bundles are desired (e.g. for multichannel storage and delivery systems) dimethylsulfoxide should be used for their assembly. The control over thickness of RNT bundles makes it possible to generate nanostructured materials with mechanical properties.

General correlations between solvent polarity and resulting morphology present a valuable contribution to the field of self-assembled nanotubes, as they can be used for rational design of functional RNT-based materials. Even though correlations found here may not transfer directly to other classes of self-assembled materials, the paradigm of solvent control for morphologically diverse architecture generation has a great potential in materials science, e.g. in the field of supramolecular polymers.[146]

RNTs soluble in low polarity solvents were synthesized for the first time. Solubility in nonpolar solvents opens the door for the development of many exciting and practically useful applications for this field. For instance, RNTs can be used for transporting of hydrophilic molecules in nonpolar media (e.g. drug delivery through biological membranes or water coalescence for oil upgrading) and for making nanotube-based materials with liquid crystalline properties. In addition, solubility in nonpolar solvents allows better control over placement and integration into microscale devices via e.g. Langmuir-Blodgett[110] or self-propelled drop[147] techniques.

The next step should be the incorporation of functional substituents into G^C motif while keeping the long alkyl chains around the nanotubes that respond to solvent control. For instance, appending G^C modules with a photoactive functional group and assembling them in DMF should allow fabrication of a cyclic array of conjugated chromophores. Such an array is typical for naturally occurring light harvesting systems and can be used for development of their artificial analogs.[148] While alkyl chains were shown to be successful in mediating intertubular interactions in low polarity media, it would be important to extend this concept to polar solvents (e.g. water and methanol).

3.8. Experimental part

General procedures.

NMR spectra were recorded on Varian NMR spectrometers (Inova 300, 400, 500) with the solvent as the internal reference. The key NMR spectra are shown. The mass spectra were performed at the Mass Spectrometry Laboratory of the University of Alberta and the Analytical Instruments Laboratory at the National Research Council of Canada's National Institute for Nanotechnology. Compound **1f** was synthesized by Dr. Fenton Heirtzler. The self-assembly of **1f** was studied in this work. All the reagents are commercially available from Aldrich or Fisher Scientific. Reagent grade solvents were obtained using chromatography solvent purification systems. THF was distilled over Na/benzophenone prior to use. All reactions were performed under N_2 atmosphere unless otherwise specified. For column chromatography, commercial solvents were used without purification. Chromatographic supports were silica flash Merck 60 (0.040-0.063 mm). Silica-coated TLC plates (Merck F 60_{254}) were used for monitoring reaction progress under UV light (354 nm) or by chemical staining ($KMnO_4$/acetone or ninhydrin/n-BuOH/acetic acid). All samples for SEM were prepared in triplicates.

Synthesis.

Experimental procedures are given for the synthesis of compounds **2a – 8a, 1a**. The synthesis of the corresponding **c - f** compounds is analogous to the one for the **a** scheme unless otherwise specified.

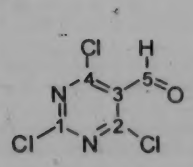

Dimethylformamide (24 mL, 0.31 Mol) was added to $POCl_3$ (188 mL, 2.02 Mol) stirred under N_2. After the initial warmth had subsided, barbituric acid (40 g, 0.31 mol) was added in one portion. The resulting suspension was heated under reflux. A yellow solution, which darkened within 2-3 h, was formed. After a total of 14 h, the mixture was cooled to ambient temperature. Excess $POCl_3$ was recovered from the reaction vessel by direct distillation under reduced pressure (105 mbar, heated water bath)[a] and the residual solid was carefully hydrolysed through addition of crushed ice (1 kg) and DCM,[b] accompanied by mechanical stirring with a spatula. Extraction of the mixture with DCM (4×300 mL), filtering through celite/cotton to remove the emulsion formed, washing with water (3×200 mL), a saturated, aqueous $NaHCO_3$ solution (2×50 mL; removed red colour in solution) then saturated aqueous brine (200 mL), drying (Na_2SO_4) and finally solvent removal (rotavap) gave a yellow solid.[c] Hot filtration from acetone and recrystallization (refrigerator) from the same medium gave the product in two crops of pale yellow prismatic crystals ($C_5HN_2OCl_3$, 39.2 g, 60%). Spectral data for 2,4,6-trichloro-pyrimidine-5-carbaldehyde have already been reported.[62]

^1H NMR (300 MHz, $CDCl_3$): 10.38 (C_5, s, 1H).

(a) The use of a rotavap is not recommended because corrosive liquids and gases (HCl) form during this reaction. A reduced pressure distillation apparatus with a KOH trap is recommended. When carrying out a synthesis on >200g of barbituric acid, evaporation of excess $POCl_3$ was not performed, since it makes quenching of very viscous residue very difficult. Instead, the reaction mixture was poured on 6 kg of ice. Recrystallization from EA worked well for this scale.

[b] The use of small amounts of DCM is recommended.

[c] The relatively low solubility of the compound in DCM may complicate the separatory funnel operations. Any beige-coloured solid is the product.

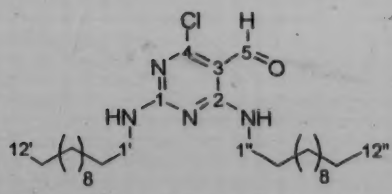

Synthesis of 3a. Method #1. To a solution of 2,4,6-trichloro-pyrimidine-5-carbaldehyde (8.0 g, 37.8 mmol) in THF (100 mL), dodecylamine (14.01 g, 75.6 mmol) and Et_3N (7.6 g, 10.5 mL, 75.6 mmol) were added sequentially and slowly at 0°C under N_2 atmosphere. The reaction mixture was stirred for 1 h at 0°C then at rt for 8 h. The reaction was quenched with saturated aqueous NH_4Cl (10 mL) and the solvent was removed under reduced pressure (rotovap). The solid obtained was dissolved in of DCM (200 mL). The organic layer was washed with dH_2O (2×100 mL) and brine (50 mL) then dried over anhydrous Na_2SO_4. After filtration and evaporation of the solvent (rotovap) the crude product was purified by gravity silica gel chromatography (0–5% EA/Hex). The desired compound **3a** was obtained as a white solid ($C_{29}H_{53}ClN_4O$, 8.8 g, 53%).

Synthesis of 3a. Method #2. To a stirred solution of 2,4,6-trichloro-pyrimidine-5-carbaldehyde (12.7 g, 60 mmol) in THF (200 mL), dodecylamine (23.2 g, 125 mmol), followed by Et_3N (16.8 mL, 121 mmol) were added at room temperature under N_2 atmosphere. The reaction mixture was heated at reflux for 18 h. The mixture was cooled in an ice/water bath and acidified by addition of HCl solution (1M, 20 mL). After separation of the organic layer, followed by its dilution with distilled water (300 mL), a solid precipitated. Gravity filtration, extensive washing with water and drying in vacuum

over P_4O_{10} afforded the crude product. Dissolution of the crude material in $CHCl_3$ to give a saturated solution, and subsequent re-precipitation with CH_3OH (1/10 v/v) yielded **2a** as a white solid ($C_{29}H_{53}ClN_4O$, 30.1 g, 98% yield).

R_f = 0.70 (15% EA/Hex, SiO_2). mp = 95 °C.

^1H NMR (400 MHz, $CDCl_3$) δ (ppm): 10.10 (HC_5, minor, s), 10.01 (HC_5, major, s, 1H), 9.28 ($HNC_{1''}$, major, t, J = 4.2 Hz, 1H), 9.06 ($HNC_{1''}$, minor, br, s, 1H), 5.65 ($HNC_{1'}$, t, J = 4.2 Hz, 1H), 5.38 ($HNC_{1'}$, br, s, 1H), 3.46 ($HC_{1'}$+ $HC_{1''}$, m, 4H), 1.58 ($HC_{2'}$+$HC_{2''}$, m, 4H), 1.30–1.20 ($HC_{3'}$–$HC_{11'}$ + $HC_{3''}$–$HC_{11''}$, m, 32H), 0.87 ($HC_{12'}$ + $HC_{12''}$, t, J = 6.7 Hz, 6H).

^{13}C NMR (100 MHz, $CDCl_3$) δ (ppm): 188.4 (C_5), 165.7, 162.4, 160.9 (C_1, C_2, C_4), 101.7 (C_3), 41.57, 40.7 ($C_{1'}$, $C_{1''}$), 31.9–26.5 ($C_{2'}$–$C_{11'}$, $C_{2''}$–$C_{11''}$), 14.1 ($C_{12'}$, $C_{12''}$).

FTIR (cm^{-1}): 3254, 3111, 2954, 2915, 2915, 2847, 1649, 1596, 1566.

HRMS (ESI): Calculated for ($C_{29}H_{53}ClN_4O$ +H^+)/z, 509.3980. Observed 509.3981.

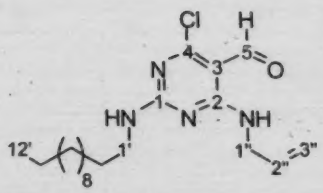

Synthesis of 3c. This compound was synthesized from 4-allylamino-2,6-dichloro-pyrimidine-5-carbaldehyde using general Method #1 with 1 equivalent of dodecylamine. Compound **3c** was obtained as a white solid ($C_{20}H_{33}ClN_4O$, 13.6 g, 81%). R_f = 0.65 (15% EA/Hex, SiO_2). mp = 54 °C.

^1H NMR (400 MHz, $CDCl_3$) δ (ppm): 10.05 (HC_5, minor, s), 10.02 (HC_5, major, s, 1H), 9.35 ($HNC_{1''}$, major, br, s, 1H), 9.14 ($HNC_{1''}$, minor, br, s), 5.90 ($HC_{2'}$, m, 1H), 5.69 ($HNC_{1''}$, t, major, J = 5.6 Hz, 1H), 5.36 ($HNC_{1''}$, minor, t, J = 5.6 Hz), 5.19 ($HC_{3''}$, m, 2H), 4.13 ($HC_{1''}$, major, dddd, $J_1 = J_2 = 5.6$ Hz, $J_3 = J_4 = 1.6$ Hz, $J_2 = 5.6$ Hz, 2H), 4.06 ($HC_{1''}$,

minor, app. t), 3.44 ($HC_{1'}$, minor, dt, J_1 = 13.6 Hz, J_2 = 6.8 Hz), 3.39 ($HC_{1'}$, major, dt, J_1 = 13.2 Hz, J_2 = 6.9 Hz, 2H), 1.56 ($HC_{2'}$, m, 2H), 1.34–1.20 ($HC_{3'}$–$HC_{11'}$, m, 18H), 0.86 ($HC_{18'}$, t, J = 6.8 Hz, 3H).

^{13}C NMR (100 MHz, $CDCl_3$) δ (ppm): 188.2 (C_5), 165.5, 162.2, 160.8 (C_1, C_2, C_4), 133.6 ($C_{2''}$), 116.4 ($C_{3''}$), 101.8 (C_3), 43.0, 41.6 ($C_{1'}$, $C_{1''}$), 32.0–22.8 ($C_{2'}$–$C_{11'}$), 14.2 ($C_{12'}$).

HRMS (ESI): Calculated for ($C_{20}H_{33}ClN_4O$ +H^+)/z 381.2416. Observed *m/z* 381.2417.

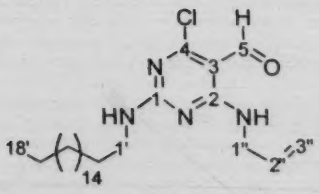

Synthesis of 3d. This compound was synthesized from 4-allylamino-2,6-dichloro-pyrimidine-5-carbaldehyde[1] using Method 2.1 with 1 equivalent of octadecylamine. Compound **3d** was obtained as a white powder ($C_{26}H_{45}ClN_4O$, 34.7 g, 59%).

R_f = 0.60 (15% EA/Hex, SiO_2). mp = 96 °C.

^{1}H NMR (400 MHz, $CDCl_3$) δ (ppm): 10.05 (HC_5, minor, s), 10.02 (HC_5, major, s, 1H), 9.35 ($HNC_{1'}$, major, t, J = 4.2 Hz, 1H), 9.14 ($HNC_{1'}$, minor, br, s), 5.89 ($HC_{2''}$, m, 1H), 5.72 ($HNC_{1''}$, t, J = 5.6 Hz, 1H), 5.19 ($HC_{3''}$, m, 2H), 4.13 ($HC_{1''}$, major, dddd, J_1 = J_2 = 5.6 Hz, J_3 = J_4 = 1.6 Hz, J_2 = 5.6 Hz, 2H), 4.06 ($HC_{1''}$, minor, app. t), 3.44 ($HC_{1'}$, minor, dt, J_1 = 13.6 Hz, J_2 = 6.8 Hz), 3.39 ($HC_{1'}$, major, dt, J_1 = 13.2 Hz, J_2 = 6.9 Hz, 2H), 1.56 ($HC_{2'}$, m, 2H), 1.34–1.20 ($HC_{3'}$–$HC_{17'}$, m, 30H), 0.86 ($HC_{18'}$, t, J = 6.4 Hz, 3H).

^{13}C NMR (100 MHz, $CDCl_3$) δ (ppm): 188.2 (C_5), 165.5, 162.2, 160.8 (C_1, C_2, C_4), 133.6 ($C_{2''}$), 116.43 ($C_{3''}$), 101.8 (C_3), 43.0, 41.6 ($C_{1'}$, $C_{1''}$), 32.0–22.8 ($C_{2'}$–$C_{17'}$), 14.2 ($C_{18'}$).

HRMS (ESI): Calculated for ($C_{26}H_{45}ClN_4O$ +H^+)/z 465.3355. Observed *m/z* 465.3354.

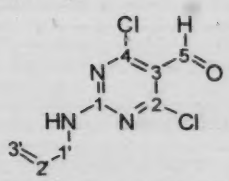

Synthesis of 4-allylamino-2,6-dichloro-pyrimidine-5-carbaldehyde. 2-Allylamino-2,6-dichloro-pyrimidine-5-carbaldehyde was obtained as a white crystalline powder ($C_8H_6Cl_2N_3O$, 16.2 g, 14%) after evaporation of the second fraction collected during flash chromatography in the synthesis of 4-allylamino-2,6-dichloro-pyrimidine-5-carbaldehyde.

R_f = 0.35 (15% EA/Hex, SiO_2). mp = 108 °C.

The bulk of 2-allylamino-2,6-dichloro-pyrimidine-5-carbaldehyde can be separated from ortho derivative by dissolving the crude mixture obtained after work-up in the reaction of 2,4,6-trichloro-pyrimidine-5-carbaldehyde with allylamine in DCM (400 mL per 100 g of 2,4,6-trichloro-pyrimidine-5-carbaldehyde) and cooling at –4 °C overnight . The desired product precipitates selectively and can be washed from its ortho isomer with cold DCM.

^{1}H NMR (600 MHz, $CDCl_3$) δ (ppm): 10.26 (C_5H, s, 1H), 6.18 ($HNC_{1'}$, br. s, 1H), 5.90 ($HC_{2'}$, m, 1H), 5.30 ($HC_{3'}$, m, 2H), 4.17 ($HC_{1'}$, m, 2H).

^{13}C NMR (100 MHz, $CDCl_3$) δ (ppm): 184.9 (C_5), 165.2 (C_1), 160.2 (C_2), 132.5 ($C_{2'}$), 117.6 (C_3), 114.4 ($C_{3'}$), 44.2 ($C_{1'}$).

HRMS (EI): Calculated for ($C_8H_7Cl_2N_3O$ +H^+)/z 230.9966. Observed 230.9971.

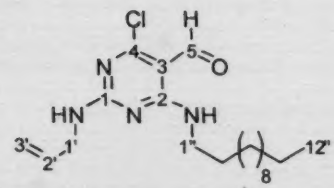

Synthesis of 3e. This compound was synthesized from 2-allylamino-2,6-dichloro-pyrimidine-5-carbaldehyde using general Method #1 with 1 equivalent of dodecylamine. The target compound was obtained as a white powder ($C_{20}H_{32}ClN_4O$, 22.0 g, 78%).

R_f = 0.65 (15% EA/Hex, SiO_2). mp = 87 °C.

^{1}H NMR (400 MHz, CCl_4:DMSO–d_6 4:1 (v/v)) δ (ppm): 9.90 (HC_5, minor, s), 9.87 (HC_5, major, s, 1H), 9.25 ($HNC_{1''}$, major, t, J = 5.6, 1H), 9.07 ($HNC_{1'}$, minor, J = 5.6, 1H), 8.22 ($HNC_{1''}$, t, major, J = 5.8 Hz, 1H), 5.36 ($HNC_{1''}$, minor, t, J = 5.6 Hz), 5.89 ($HC_{2'}$, m, 1H), 5.14 ($HC_{3'}$, m, 2H), 4.13 ($HC_{1'}$, m, 2H), 3.24 ($HC_{1'}$, m, 2H), 1.49 ($HC_{2''}$, m, 2H), 1.30–1.20 ($HC_{3''}$–$HC_{11''}$, m, 18H), 0.85 ($HC_{18''}$, t, J = 6.8 Hz, 3H).

^{13}C NMR (100 MHz, $CDCl_3$) δ (ppm): 188.3 (C_5), 165.6, 162.2, 160.8 (C_1, C_2, C_4), 133.6 ($C_{2''}$), 116.4 ($C_{3''}$), 101.8 (C_3), 43.0, 41.6 ($C_{1'}$, $C_{1''}$), 32.0–22.8 ($C_{2''}$–$C_{11'}$), 14.2 ($C_{12'}$).

HRMS (EI): Calculated for ($C_{20}H_{32}ClN_4O$ +H^+)/z 380.2343. Observed *m/z* 380.2342.

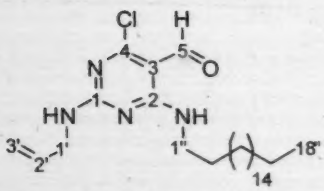

Synthesis of 3f. This compound was synthesized from 2-allylamino-2,6-dichloro-pyrimidine-5-carbaldehyde using general Method #1 with 1 equivalent of octadecylamine. The desired compound **3f** was obtained as a white powder ($C_{26}H_{45}ClN_4O$, 3.40 g, 89%). R_f = 0.60 (15% EA/Hex, SiO_2). mp = 108 °C.

^{1}H NMR (400 MHz, $CDCl_3$) δ (ppm): 10.06 (HC_5, minor, s), 10.03 (HC_5, major, s, 1H), 9.29 ($HNC_{1'}$, major, br, s, 1H), 9.09 ($HNC_{1'}$, minor, br, s), 5.90–5.84 ($HC_{2'}$, m, 1H overlapping with $HNC_{1''}$, major, 1H), 5.43 ($HNC_{1''}$, minor, br, s), 5.19 ($HC_{3'}$, m, 2H), 4.2–4.04 ($HC_{1'}$, major overlapping with $HC_{1'}$ minor, app. t, J = 5.6 Hz, 2H), 4.06 ($HC_{1''}$, minor, app. t), 3.49 ($HC_{1'}$, major, dt, J_1 = 13.2 Hz, J_2 = 6.9 Hz, 2H), 3.41 ($HC_{1''}$, minor, dt, J_1 = 13.1 Hz, J_2 = 6.0 Hz), 1.61 ($HC_{2''}$, m, 2H), 1.38–1.24 ($HC_{3''}$–$HC_{17''}$, m, 30H), 0.88 ($HC_{18''}$, t, J = 6.8 Hz, 3H).

^{13}C NMR (100 MHz, $CDCl_3$) δ (ppm): 188.5 (C_5), 165.8, 162.3, 160.8 (C_1, C_2, C_4), 133.8 ($C_{2''}$), 116.56 ($C_{3'}$), 101.9 (C_3), 43.9, 40.7 ($C_{1'}$, $C_{1''}$), 31.9–22.7 ($C_{2''}$–$C_{17''}$), 14.1 ($C_{18''}$).

HRMS (ESI): Calculated for ($C_{26}H_{45}ClN_4O$ +H^+)/z 465.3355. Observed *m/z* 465.3355.

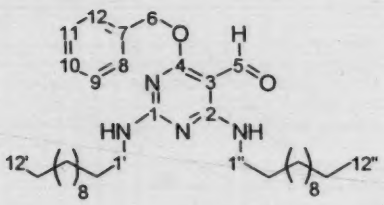

Synthesis of 4a (Method #3). Benzyl alcohol (0.99 g, 0.91 mL, 8.8 mmol) was added to a stirred suspension of NaH (95%, 0.84 g, 35.8 mmol) in THF (10 mL) at rt under N_2 atmosphere. After 15 min the solution was cooled to 0°C, then a solution of **3a** (4.48 g, 8.8 mmol) in THF (40 mL) was added. The mixture was allowed to warm to rt, then it was refluxed for 24 h. The mixture was then cooled to 0°C and carefully quenched with saturated NH_4Cl (10 mL). The solvent was removed (rotovap), and the residual solid was dissolved in Et_2O, washed with dH_2O (100 mL) and brine (50 mL), and dried over anhydrous Na_2SO_4. Filtration, evaporation of the solvent under reduced pressure (rotovap) followed by silica gel chromatography (0–5% EA/Hex) yielded **4a** as a white solid ($C_{36}H_{60}N_4O_2$, 4.00 g, 79%).

Synthesis of 4a (Method #4). Benzyl alcohol (1.8 mL, 18 mmol) was added to a stirred suspension of NaH (95%, 0.84 g, 35 mmol) in THF (10 mL) at room temperature under N_2 atmosphere. After 15 min the solution was cooled to 0 °C, then a solution of **3a** (7.9 g, 16 mmol) in THF (100 mL) was added. The mixture was allowed to warm to room temperature then it was refluxed for 20 h. the reaction mixture was cooled to 0 °C and the solvent was removed under reduced pressure (rotovap). The residual solid was dissolved in Et_2O, washed with dH_2O (3×100 mL), saturated brine (50 mL) and dried over anhydrous Na_2SO_4. The solvent was evaporated under reduced pressure (rotovap). Dissolution of the crude material in EA to give a saturated solution, and subsequent

precipitation by addition of CH_3OH (1/10 v/v) yielded **4a** as a white solid ($C_{36}H_{60}N_4O_2$, 8.91 g, 99%). R_f = 0.45 (15% EA/Hex, SiO_2).

R_f = 0.45 (6% CH_3CN/Toluene). mp = 94 °C.

^1H NMR (400 MHz, DMSO–d_6) δ (ppm): 9.82 (HC_5, s, 1H), 9.03 ($HNC_{1''}$, major, t, J = 4.2 Hz, 1H), 7.42–7.22 ($HNC_{1'}$ overlapping with HC_8–HC_{12}, 6H), 5.40 (HC_6, s, 2H), 3.41, 3.28 ($HC_{1'}$, dt, J = 13.2 Hz, J = 5.6 Hz, 2H; $HC_{1''}$, dt, J = 13.2 Hz, J = 5.6 Hz, 2H), 1.52 ($HC_{2'}$+$HC_{2''}$, m, 4H), 1.30–1.20 ($HC_{3'}$–$HC_{11'}$ + $HC_{3''}$–$HC_{11''}$, m, 32H), 0.83 ($HC_{12'}$ + $HC_{12''}$, t, J = 6.8 Hz, 6H).

^{13}C NMR (100 MHz, $CDCl_3$) δ (ppm): 185.8 (C_5), 171.5, 163.5, 162.3 (C_1, C_2, C_4), 136.7 (C_7), 128.5, 127.9, 127.7 ($C_{8\text{-}12}$), 92.8 (C_3), 67.3 (C_6), 41.4, 40.4 ($C_{1'}$, $C_{1''}$), 31.9–22.7 ($C_{2'}$–$C_{11'}$, $C_{2''}$–$C_{11''}$), 14.1 ($C_{12'}$, $C_{12''}$).

FTIR (cm^{-1}): 3331, 3258, 2953, 2912, 2847, 1631, 1593, 1576, 1539, 1518, 1208, 1111.

HRMS (ESI): Calculated for ($C_{36}H_{60}N_4O_2$ +H^+)/z 465.3355. Observed *m/z* 465.3354.

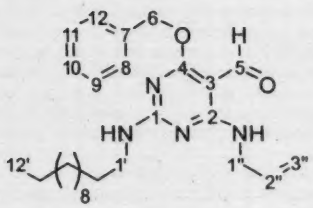

Synthesis of 4c. This compound was obtained from **3c** as a white solid ($C_{27}H_{39}N_4O_2$, 8.90 g, 92%) using Method #3.

R_f = 0.40 (15% EA/Hex, SiO_2). mp = 94 °C.

^1H NMR (400 MHz, $CDCl_3$) δ (ppm): 9.84 (HC_5, major, s, 1H), 9.82 (HC_5, minor, s), 9.21 ($HNC_{1''}$, major, br, s, 1H), 9.09 ($HNC_{1''}$, minor, br, s), 7.30–7.14 (m, HC_8–HC_{12}, 5H overlapping with $CDCl_3$), 5.82 ($HC_{2''}$, m, 1H), 5.44–5.00 ($HC_{3''}$ overlapping with HC_6, 4H), 4.05 ($HC_{1''}$, app. t, J = 5.2, 2H), 3.30 ($HC_{1'}$, m, 2H), 1.47 ($HC_{2'}$, m, 2H), 1.30–1.16 ($HC_{3'}$–$HC_{11'}$, m, 18H), 0.80 ($HC_{12'}$, t, J = 6.8 Hz, 3H).

^{13}C NMR (100 MHz, $CDCl_3$) δ (ppm): 185.7 (C_5), 165.5, 162.9, 160.8 (C_1, C_2, C_4), 136.4 (C_7), 134.4 ($C_{2''}$), 128.4, 127.9, 127.5 ($C_{8\text{-}12}$), 115.7 ($C_{3''}$), 92.8 (C_3), 67.3 (C_6), 42.8, 41.5 ($C_{1'}$, $C_{1''}$), 31.9–22.7 ($C_{2'}$–$C_{11'}$), 14.2 ($C_{12'}$).

HRMS (ESI): Calculated for ($C_{27}H_{39}N_4O_2$ + Na^+)/z 475.3044. Observed *m/z* 475.3042.

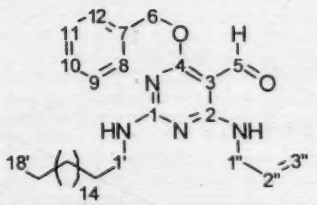

Synthesis of 4d. This compound was obtained from **3d** as a white solid ($C_{33}H_{52}N_4O_2$, 27.04 g, 88%) using Method #3. R_f = 0.45 (15% EA/Hex, SiO_2). mp = 107 °C.

^{1}H NMR (400 MHz, $CDCl_3$) δ (ppm): 10.02 (HC_5, minor, s, 1H), 10.01 (HC_5, major, s), 9.36 ($HNC_{1''}$, major, br, s, 1H), 9.21 ($HNC_{1''}$, minor, br, s), 7.41–7.28 (m, HC_8–HC_{12}, 5H), 5.95 ($HC_{2''}$, m, 1H), 5.48–5.14 ($HC_{3''}$ overlapping with HC_6 and $NHC_{1'}$, 5H), 4.18 ($HC_{1''}$, major, app. t, J = 5.4, 2H), 4.11 ($HC_{1''}$, br. s, 2H), 3.43 ($HC_{1'}$, dt, J = 13.0 Hz, J = 6.7 Hz, 2H), 1.59 ($HC_{2'}$, m, 2H), 1.40–1.00 ($HC_{3'}$–$HC_{11'}$, m, 30H), 0.89 ($HC_{18'}$, t, J = 6.2 Hz, 3H).

^{13}C NMR (100 MHz, $CDCl_3$) δ (ppm) for major peaks: 185.9 (C_5), 171.5, 163.5, 162.3 (C_1, C_2, C_4), 136.7 (C_7), 134.6 ($C_{2''}$), 128.5, 128.0, 127.7 ($C_{8\text{-}12}$), 115.9 ($C_{3''}$), 92.9 (C_3), 42.8, 41.4 ($C_{1'}$, $C_{1''}$), 31.9–22.7 ($C_{2'}$–$C_{11'}$), 14.1 ($C_{12'}$).

HRMS (ESI): Calculated for ($C_{33}H_{52}N_4O_2$ +H^+)/z 537.4163. Observed *m/z* 537.4166.

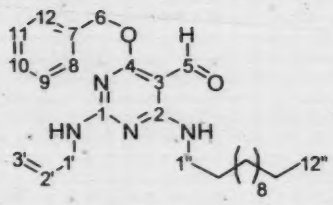

Synthesis of 4e. This compound was obtained from **3e** as a white solid ($C_{33}H_{52}N_4O_2$, 27.04 g, 88%) using Method #3. R_f = 0.45 (15% EA/Hex, SiO_2). mp = 107 °C.

^{1}H NMR (400 MHz, $CDCl_3$) δ (ppm): 10.02 (HC_5, minor, s, 1H), 10.01 (HC_5, major, s), 9.36 ($HNC_{1''}$, major, br, s, 1H), 9.21 ($HNC_{1''}$, minor, br, s), 7.41–7.28 (m, HC_8–HC_{12}, 5H), 5.95 ($HC_{2''}$, m, 1H), 5.48–5.14 ($HC_{3''}$ overlapping with HC_6 and $NHC_{1'}$, 5H), 4.18 ($HC_{1''}$, major, app. t, J = 5.4, 2H), 4.11 ($HC_{1''}$, br. s, 2H), 3.43 ($HC_{1'}$, dt, J = 13.0 Hz, J = 6.7 Hz, 2H), 1.59 ($HC_{2'}$, m, 2H), 1.40–1.00 ($HC_{3'}$–$HC_{11'}$, m, 30H), 0.89 ($HC_{18'}$, t, J = 6.2 Hz, 3H).

^{13}C NMR (100 MHz, $CDCl_3$) δ (ppm) for major peaks: 185.9 (C_5), 171.5, 163.5, 162.3 (C_1, C_2, C_4), 136.7 (C_7), 134.6 ($C_{2''}$), 128.5, 128.0, 127.7 ($C_{8\text{-}12}$), 115.9 ($C_{3''}$), 92.9 (C_3), 42.8, 41.4 ($C_{1'}$, $C_{1''}$), 31.9–22.7 ($C_{2'}$–$C_{11'}$), 14.1 ($C_{12'}$).

HRMS (ESI): Calculated for ($C_{33}H_{52}N_4O_2$ +H^+)/z 537.4163. Observed *m/z* 537.4166.

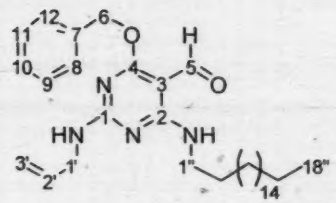

Synthesis of 4f. This compound was obtained from **3f** as a white solid ($C_{27}H_{40}N_4O_2$, 2.93 g, 91%) using Method #3. R_f = 0.50 (15% EA/Hex, SiO_2). mp = 89 °C.

^{1}H NMR (500 MHz, $CDCl_3$) δ (ppm): 10.01 (HC_5, major, s, 1H), 10.02 (HC_5, minor, br. s, 1H), 9.38 ($HNC_{1''}$, minor, br. s), 9.21 ($HNC_{1''}$, minor, br. s), 7.60–7.35 (m, HC_8–HC_{12}, 5H), 6.00 ($HC_{2''}$, m, 1H), 5.53–5.15 ($HC_{3''}$ overlapping with HC_6 and $NHC_{1'}$, 5H), 4.22 ($HC_{1''}$, major, br. s, 2H), 4.13 ($HC_{1''}$, minor, br. s), 3.46 ($HC_{1''}$, major, m, 2H), 3.46 ($HC_{1'}$, m, 2H), 1.64 ($HC_{2''}$, m, 2H), 1.42–1.28 ($HC_{3'}$–$HC_{11'}$, m, 30H), 0.94 ($HC_{18'}$, t, J = 7.4 Hz, 3H).

^{13}C NMR (100 MHz, $CDCl_3$) δ (ppm) for major peaks: 185.9 (C_5), 171.5, 163.5, 162.3 (C_1, C_2, C_4), 136.7 (C_7), 134.6 ($C_{2''}$), 128.5, 128.0, 127.7 ($C_{8\text{-}12}$), 115.9 ($C_{3''}$), 92.9 (C_3), 42.8, 41.4 ($C_{1'}$, $C_{1''}$), 31.9–22.7 ($C_{2'}$–$C_{11'}$), 14.1 ($C_{12'}$).

HRMS (ESI): Calculated for ($C_{27}H_{40}N_4O_2$ +H^+)/z 453.3230. Observed *m/z* 453.33232.

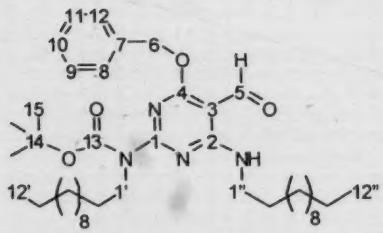

Synthesis of 5a (Method #5). To a stirred solution of compound **4a** (2.5 g, 4.25 mmol) and DMAP (0.26 g, 2.17 mmol) in THF (30 mL), Et_3N (1.28 g, 1.77 mL, 12.8 mmol) was added at rt under N_2 atmosphere. After stirring for 5 min, Boc_2O (1.11 g, 5 mmol) was added, and the mixture was stirred at rt for 20 h. The reaction was quenched with dH_2O (10 mL) followed by removal of the solvent (rotovap). The residual solid was dissolved in EA (200 mL) and washed with 10% aqueous citric acid (50 mL), dH_2O (2×50 mL), 5% aqueous $NaHCO_3$ (50 mL) and brine (50 mL). After drying the organic layer over anhydrous Na_2SO_4, filtration and removal of the solvent (rotovap), the residue was purified by flash silica gel chromatography (0–8% EA/Hex). The desired compound **5a** ($C_{41}H_{68}N_4O_4$, 2.63 g, 91%) was obtained as a white crystalline solid. **5a** can also be purified by selective precipitation from EA, with MeOH as counter-solvent (1/10 v/v).

R_f = 0.75 (15% EA/Hex, SiO_2). mp = 39 °C.

^1H NMR (400 MHz, $CDCl_3$) δ (ppm): 10.11 (HC_5, s, 1H), 9.14 ($HNC_{1''}$, t, J = 5.6 Hz, 1H), 7.43–7.32 (m, HC_8–HC_{12}, 5H), 5.46 (HC_6, s, 2H), 3.87 ($HC_{1'}$, m, 2H), 3.49 ($HC_{1''}$, m, 2H), 1.65 ($HC_{2'}$+$HC_{2''}$, m, 4H), 1.55 (HC_{15}, s, 9H), 1.34–1.22 ($HC_{3'}$–$HC_{11'}$ + $HC_{3''}$–$HC_{11''}$, m, 32H), 0.88 ($HC_{12'}$ + $HC_{12''}$, t, J = 7.0 Hz, 6H).

^{13}C NMR (100 MHz, $CDCl_3$) δ (ppm): 187.5 (C_5), 171.5, 162.8, 161.7 (C_1, C_2, C_4), 153.7 (C_{13}), 136.4 (C_7), 128.5, 128.1, 128.0 ($C_{8\text{-}12}$), 94.2 (C_3), 81.6 (C_{14}), 68.1 (C_6), 47.8 ($C_{1'}$), 40.8 ($C_{1''}$), 31.9–22.7 ($C_{2'}$–$C_{11'}$, $C_{2''}$–$C_{11''}$), 28.2 (HC_{15}), 14.1 ($C_{12'}$, $C_{12''}$).

FTIR (cm^{-1}) 3292, 3090, 2981, 2920, 2852, 1718, 1640, 1579, 1518, 1216, 1073.

HRMS (ESI): Calculated for ($C_{41}H_{68}N_4O_4$ +H^+)/z, 681.5313. Observed *m/z* 681.5316.

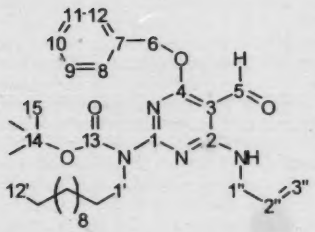

Synthesis of 5c. This compound was obtained from **4c** as a fluffy white powder ($C_{32}H_{48}N_4O_2$, 6.29 g, 95%) using Method #5. R_f = 0.65 (15% EA/Hex, SiO_2). mp = 79 °C.

^{1}H NMR (400 MHz, $CDCl_3$) δ (ppm): 10.16 (HC_5, s, 1H), 9.22 ($HNC_{1''}$, t, J = 5.8 Hz, 1H), 7.42–7.28 (m, HC_8–HC_{12}, 5H), 5.87 ($HC_{2''}$, m, 1H), 5.45 (HC_6, s, 2H), 5.27–5.07 ($HC_{3''}$, m, 2H), 4.25 ($HC_{1''}$, dddd, J_1 = J_2 = 5.6 Hz, J_3 = J_4 = 1.5 Hz, 2H), 3.84 ($HC_{1'}$, m, 2H), 1.63 ($HC_{2'}$, m, 2H), 1.52 (HC_{15}, s, 9H), 1.30–1.22 ($HC_{3'}$–$HC_{11'}$, m, 18H), 0.87 ($HC_{12'}$, t, J = 6.8 Hz, 3H).

^{13}C NMR (100 MHz, $CDCl_3$) δ (ppm): 187.5 (C_5), 171.4, 162.7, 161.6 (C_1, C_2, C_4), 153.6 (C_{13}), 136.3 (C_7), 134.1 ($C_{2''}$), 128.5, 128.1, 127.9 ($C_{8\text{-}12}$), 116.1 ($C_{3''}$), 94.3 (C_3), 81.7 (C_{14}), 68.1 (C_6), 47.7 ($C_{1'}$), 42.9 ($C_{1''}$), 31.9–22.6 ($C_{2'}$–$C_{11'}$), 28.1 (HC_{15}), 14.1 ($C_{12'}$).

HRMS (ESI): Calculated for ($C_{32}H_{48}N_4O_2$ +H^+)/z 553.3748. Observed *m/z* 553.3748.

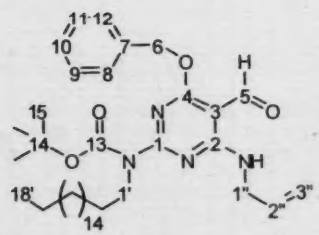

Synthesis of 5d. This compound was obtained as a white crystalline solid ($C_{38}H_{60}N_4O_4$, 4.95 g, 94%) from **4d** using Method #5. R_f = 0.70 (15% EA/Hex). mp = 84 °C.

^{1}H NMR (400 MHz, $CDCl_3$) δ (ppm): 10.12 (HC_5, s, 1H); 9.19 ($HNC_{1''}$, t, J = 5.6 Hz, 1H), 7.41–7.29 (m, HC_8–HC_{12}, 5H), 5.89 ($HC_{2''}$, m, 1H), 5.45 (HC_6, s, 2H), 5.23–5.10 ($HC_{3''}$, m, 2H), 4.15 ($HC_{1''}$, dddd, $J_1 = J_2 = 5.6$ Hz, $J_3 = J_4 = 1.6$ Hz, 2H), 3.85 ($HC_{1'}$, m, 2H), 1.64 ($HC_{2'}$, m, 2H), 1.53 (HC_{15}, s, 9H), 1.30–1.22 ($HC_{3'}$–$HC_{17'}$, m, 30H), 0.86 ($HC_{12'}$, t, J = 7.2 Hz, 3H).

^{13}C NMR (100 MHz, $CDCl_3$) δ (ppm): 187.2 (C_5), 171.1, 162.5, 161.3 (C_1, C_2, C_4), 153.4 (C_{13}), 136.1 (C_7), 133.9 ($C_{2''}$), 128.3, 127.9, 127.7 ($C_{8\text{-}12}$), 115.9 ($C_{3''}$), 94.1 (C_3), 81.5 (C_{14}), 68.0 (C_6), 47.6 ($C_{1'}$), 42.9 ($C_{1''}$), 31.8–22.6 ($C_{2'}$–$C_{17'}$), 28.1 (HC_{15}), 14.0 ($C_{12'}$).

HRMS (ESI): Calculated for ($C_{38}H_{60}N_4O_4$ +H^+)/z 637.4687. Observed *m/z* 637.4698.

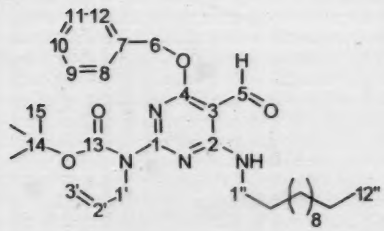

Synthesis of 5e. This compound was obtained as a white powder ($C_{32}H_{48}N_4O_2$, 6.97 g, 95%) from **4e** using Method #5. R_f = 0.65 (15% EA/Hex). mp = 89 °C.

^{1}H NMR (300 MHz, $CDCl_3$) δ (ppm): 10.18 (C_5H, s, 1H), 9.21 ($HNC_{1''}$, t, J = 5.6 Hz, 1H), 7.47–7.41 (m, HC_8–HC_{12}, 5H), 6.00 ($HC_{2'}$, m, 1H), 5.52 (HC_6, s, 2H), 5.22–5.10 ($HC_{3'}$, m, 2H), 4.56 ($HC_{1'}$, m, 2H), 3.57 ($HC_{1''}$, m, 2H), 1.60–1.55 ($HC_{2'}$, m, overlapping with HC_{15}, s, 11H), 1.40–1.26 ($HC_{3'}$–$HC_{11'}$, m, 18H), 0.88 ($HC_{12'}$, t, J = 7.0 Hz, 3H).

^{13}C NMR (100 MHz, $CDCl_3$) δ (ppm): 187.9 (C_5), 172.2, 164.0, 163.3 (C_1, C_2, C_4), 153.8 (C_{13}), 136.2 (C_7), 134.5 ($C_{2'}$), 128.3, 128.3, 128.1 ($C_{8\text{-}12}$), 116.3 ($C_{3'}$), 94.8 (C_3), 82.2 (C_{14}), 68.3 (C_6), 49.7 ($C_{1'}$), 40.9 ($C_{1''}$), 31.9–22.7 ($C_{2''}$–$C_{11''}$), 28.2 (HC_{15}), 14.2 ($C_{18'}$).

HRMS (ESI): Calculated for ($C_{32}H_{48}N_4O_2$ +H^+)/z 553.3748. Observed *m/z* 553.3749

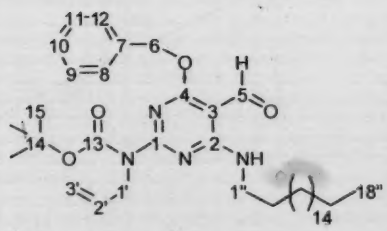

Synthesis of 5f. This compound was obtained as a white powder ($C_{38}H_{60}N_4O_4$, 1.92 g, 91%) from **4f** using Method #5.

R_f = 0.85 (15% EA/Hex). mp = 74 °C.

^{1}H NMR (500 MHz, $CDCl_3$) δ (ppm): 10.12 (HC_5, s, 1H), 9.15 ($HNC_{1''}$, t, J = 5.6 Hz, 1H), 7.44–7.31 (m, HC_8–HC_{12}, 5H), 5.95 ($HC_{2'}$, m, 1H), 5.46 (HC_6, s, 2H), 5.22–5.10 ($HC_{3'}$, m, 2H), 4.51 ($HC_{1'}$, m, 2H), 3.50 ($HC_{1''}$, dt, J = 12.8 Hz, J = 6.9 Hz, 2H), 1.56 ($HC_{2''}$, m, 2H), 1.54 (HC_{15}, s, 9H), 1.36–1.24 ($HC_{3''}$–$HC_{17''}$, m, 30H), 0.88 ($HC_{18''}$, t, J = 7.0 Hz, 3H).

^{13}C NMR (100 MHz, $CDCl_3$) δ (ppm): 187.6 (C_5), 171.6, 162.8, 161.4 (C_1, C_2, C_4), 153.3 (C_{13}), 136.4 (C_7), 134.2 ($C_{2'}$), 128.5, 128.2, 128.1 ($C_{8\text{-}12}$), 116.2 ($C_{3'}$), 94.3 (C_3), 81.9 (C_{14}), 68.2 (C_6), 49.7 ($C_{1'}$), 40.8 ($C_{1''}$), 31.9–22.7 ($C_{2''}$–$C_{17''}$), 28.2 (HC_{15}), 14.1 ($C_{18'}$).

HRMS (ESI): Calculated for ($C_{38}H_{60}N_4O_4$ +H^+)/z 637.4687. Observed: *m/z* 637.4684.

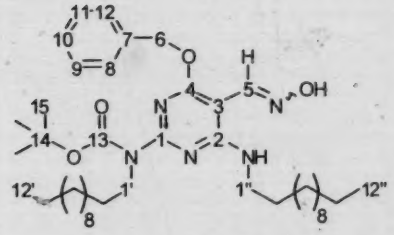

Synthesis of 6a (Method #6). To a stirred solution of **5a** (1.18 g, 1.8 mmol) in anhydrous MeOH (100 mL), $KHCO_3$ (4.23 g, 42.2 mmol) and hydroxylamine hydrochloride (0.25 g, 3.6 mmol) were added at rt under N_2 atmosphere. The resulting slurry was refluxed for 3 h then cooled to rt and quenched with dH_2O (10 mL). The solvent was removed under reduced pressure and the residual solid was dissolved in EA (200 mL), washed with dH_2O (50 mL) and brine (25 mL). The organic layer was dried over anhydrous Na_2SO_4. Filtration, evaporation of the solvent under reduced pressure (rotovap) followed by silica gel

chromatography (0–10% EA/Hex) yielded **6a** as a white solid ($C_{41}H_{69}N_5O_4$, 0.97 g, 81%).

Synthesis of 6a (Method #7). To a stirred solution of **5a** (1.53 g, 2.3 mmol) in pyridine (30 mL), $NH_2OH{\cdot}HCl$ (0.31 g, 4.5 mmol) was added at rt. The mixture was stirred for 3 h. Pyridine was removed under reduced pressure and the residual solid was dissolved in EA (200 mL), washed with dH_2O (50 mL) and brine (25 mL). The organic layer was dried over anhydrous Na_2SO_4, filtered, and evaporated to dryness (rotavap) to yield compound **6a** ($C_{41}H_{70}N_5O_4$, 1.56 g, quantitative), that was used in the next step without purification. R_f = 0.37 (15% EA/Hex).

^{1}H NMR (400 MHz, $CDCl_3$) δ (ppm): 8.55 (HC_5, s, 1H), 7.85 ($HNC_{1''}$, t, J = 6.0 Hz, 1H), 7.43 – 7.30 (m, HC_8 – HC_{12}, 5H), 6.84 (HO, s, 1H), 5.40 (HC_6, s, 2H), 3.82 ($HC_{1'}$, m, 2H), 3.51 ($HC_{1''}$, m, 2H), 1.69 – 1.58 ($HC_{2'}$+$HC_{2''}$, m, 4H), 1.53 (HC_{15}, s, 9H), 1.34 – 1.24 ($HC_{3'}$–$HC_{11'}$ + $HC_{3''}$–$HC_{11''}$, m, 32H), 0.89 ($HC_{12'}$ + $HC_{12''}$, t, J = 7.0 Hz, 6H).

^{13}C NMR (100 MHz, $CDCl_3$) δ (ppm): 167.3 (C_5), 160.9, 159.2, 154.1 (C_1, C_2, C_4), 153.7 (C_{13}), 136.9 (C_7), 128.4, 128.0, 127.9 ($C_{8\text{-}12}$), 87.1 (C_3), 80.9 (C_{14}), 68.0 (C_6), 47.9 ($C_{1'}$), 41.3 ($C_{1''}$), 32.0 – 22.7 ($C_{2'}$–$C_{11'}$, $C_{2''}$–$C_{11''}$), 28.2 (HC_{15}), 14.2 ($C_{12'}$, $C_{12''}$).

FTIR (cm^{-1}) 3311, 3034, 2954, 2911, 2847, 1697, 1567, 1525, 1278, 1079.

HRMS (ESI): Calculated for ($C_{41}H_{69}N_5O_4$ +H^+)/z 695.5422. Observed 695.5426.

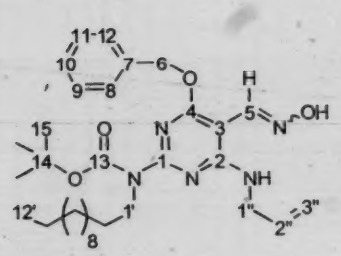

Synthesis of 6c. This compound was obtained from **5c** ($C_{32}H_{49}N_5O_4$, 4.08 g, 97%) using Method #6. R_f = 0.40 (15% EA/Hex). HRMS (ESI): Calculated for ($C_{32}H_{49}N_5O_4$ +H^+)/z 568.3857. Observed *m/z* 568.3856.

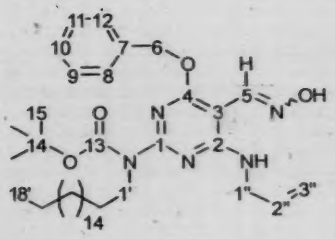

Synthesis of 6d. This compound was obtained from **5d** using Method #6 ($C_{38}H_{61}N_5O_4$, 5.40 g, 95%). R_f = 0.35 (15% EA/Hex). HRMS (ESI): Calculated for ($C_{38}H_{61}N_5O_4$+H^+)/z 652.4796. Observed *m/z* 652.4798.

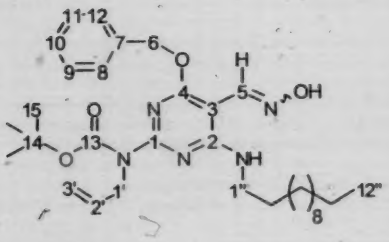

Synthesis of 6e. This compound was obtained from **5e** ($C_{32}H_{49}N_5O_4$, 4.18 g, 97%) using Method #6. R_f = 0.35 (15% EA/Hex). HRMS (ESI): Calculated for ($C_{32}H_{49}N_5O_4$ +H^+)/z 568.3857. Observed *m/z* 568.3856.

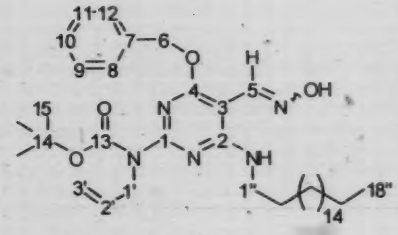

Synthesis of 6f. This compound was obtained from **5f** ($C_{38}H_{61}N_5O_4$, 1.52 g, 97%) using Method #11. R_f = 0.35 (15% EA/Hex). HRMS (ESI): Calculated for ($C_{38}H_{61}N_5O_4$ +H^+)/z 652.4796. Observed *m/z* 652.4795.

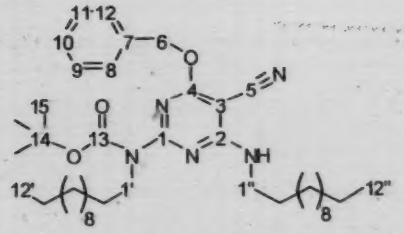

Synthesis of 7a (Method #8). Compound **6a** (11.0 g, 15.8 mmol) was dissolved in THF (130 mL) and cooled to 0 °C in an ice bath. After addition of Et_3N (7 mL, 50.2 mmol) to the solution, TFAA (4.4 mL, 31.6 mmol) was added over 30 min. After stirring for 15 min, the mixture was allowed to

warm up to rt then it was refluxed for 5 h. After cooling to rt, the reaction was quenched with dH_2O and the solvent was evaporated under reduced pressure (rotavap). The residual solid was dissolved in EA (600 mL), washed with dH_2O (3×50 mL), 5% aqueous $NaHCO_3$ (2×50 mL), brine (50 mL), then dried over anhydrous Na_2SO_4. The solvent was removed (rotovap) and the residual solid was precipitated in CH_3OH to yield **7a** as a white solid ($C_{41}H_{67}N_5O_3$, 10.2 g, 92% yield). R_f = 0.72 (15% EA/Hex). mp = 77 °C.

^{1}H NMR (400 MHz, $CDCl_3$) δ (ppm): 7.45–7.26 (m, HC_8–HC_{12}, 5H), 5.45 (HC_6, s, 2H), 5.36 ($HNC_{1''}$, t, J = 5.2 Hz, 1H), 3.84 ($HC_{1'}$, m, 2H), 3.48 ($HC_{1''}$, dt, J_1 = 7.2 Hz, J_1 = 13.2 Hz, 2H), 1.63–1.57 ($HC_{2'}$+$HC_{2''}$, m, 4H), 1.54 (HC_{15}, s, 9H), 1.34–1.24 ($HC_{3'}$–$HC_{11'}$ + $HC_{3''}$–$HC_{11''}$, m, 32H), 0.89 ($HC_{12'}$ + $HC_{12''}$, t, J = 7.0 Hz, 6H).

^{13}C NMR (100 MHz, $CDCl_3$) δ (ppm): 170.2 (C_4), 164.1, 160.7 (C_1, C_2), 153.3 (C_{13}), 136.5 (C_7), 128.4, 128.0, 127.8 ($C_{8\text{-}12}$), 115.0 (C_5), 82.1 (C_{14}), 68.5 (C_3), 68.2 (C_6), 47.3 ($C_{1'}$), 41.0 ($C_{1''}$), 31.8–22.5 ($C_{2'}$–$C_{11'}$, $C_{2''}$–$C_{11''}$), 28.2 (HC_{15}), 14.0 ($C_{12'}$, $C_{12''}$).

FTIR (cm^{-1}) 3303, 3176, 2915, 2849, 2221, 1751, 11706, 1610, 1587, 1214, 1125.

HRMS (ESI): Calculated for ($C_{41}H_{67}N_5O_3$ +H^+)/z 678.5317. Observed *m/z* 678.5313.

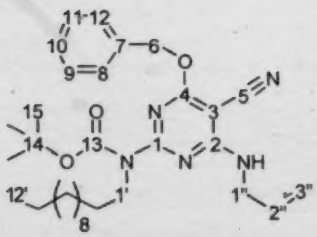

Synthesis of 7c. This compound was obtained as a white solid ($C_{32}H_{47}N_5O_3$, 3.83 g, 92%) from **6c** using Method #8.

Synthesis of 7c (Method #9). [149] 2,4,6-Trichloro-[1,3,5]triazine (TCT, 3.66 g, 20.0 mmol) was added to DMF (6 mL) at rt leading to the formation of a thick white suspension. The reaction was monitored by TLC until complete disappearance of TCT. Addition of **6c** (5.67 g, 10 mmol) in DMF (15 mL) to this suspension led instantly to brown coloration and heating.

Et_3N (2.78 mL, 20 mmol) was added, and the mixture was stirred at rt for 8 h. dH_2O (20 mL) was added and the product was extracted with EA (50 mL). The organic phase was washed with saturated aqueous K_2CO_3 (15 mL), 10% citric acid, dH_2O, and brine. The organic layer was dried over Na_2SO_4, filtered, and the solvent evaporated to yield pure **6c** as a white solid ($C_{32}H_{47}N_5O_3$, 5.38 g, 98%). R_f = 0.50 (15% EA/Hex). mp = 108 °C. ^{1}H NMR (400 MHz, $CDCl_3$) δ (ppm): 7.42–7.27 (m, HC_8–HC_{12}, 5H), 5.87 ($HC_{2''}$, m, 1H), 5.44 (HC_6, s, 2H), 5.42 ($HNC_{1''}$, t, J = 5.6 Hz, 1H), 5.25–5.07 ($HC_{3''}$, m, 2H), 4.12 ($HC_{1''}$, dddd, $J_1 = J_2 = 5.6$ Hz, $J_3 = J_4 = 1.5$ Hz, 2H), 3.81 ($HC_{1'}$, m, 2H), 1.63–1.56 ($HC_{2'}$, m, 2H), 1.51 (HC_{15}, s, 9H), 1.30–1.22 ($HC_{3'}$–$HC_{11'}$, m, 18H), 0.86 ($HC_{12'}$, t, J = 6.8 Hz, 3H).

^{13}C NMR (100 MHz, $CDCl_3$) δ (ppm): 170.3 (C_4), 164.7, 160.3 (C_1, C_2), 153.1 (C_{13}), 135.7 (C_7), 133.5 ($C_{2''}$), 128.2, 127.9, 127.6 ($C_{8\text{-}12}$), 116.8 ($C_{3''}$), 114.6 (C_5), 81.7 (C_{14}), 68.8 (C_3), 68.4 (C_6), 47.7 ($C_{1'}$), 43.5 ($C_{1''}$), 31.8–22.6 ($C_{2'}$–$C_{11'}$), 28.1 (HC_{15}), 14.0 ($C_{12'}$). HRMS (ESI): Calculated for ($C_{32}H_{47}N_5O_3$ +H^+)/z 550.3752. Observed *m/z* 550.3769.

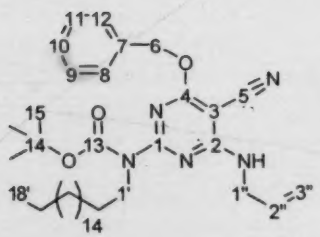

Synthesis of 7d. This compound was obtained from **6d** as a white solid ($C_{38}H_{59}N_5O_3$, 5.18 g, 93% yield) using Method #8. R_f = 0.50 (15% EA/Hex). mp = 108 °C. ^{1}H NMR (400 MHz, $CDCl_3$) δ (ppm): 7.44–7.28 (m, HC_8–HC_{12}, 5H), 5.85 ($HC_{2''}$, m, 1H), 5.47 (HC_6, s, 2H), 5.43 ($HNC_{1''}$, t, J = 5.6 Hz, 1H), 5.22 ($HC_{3''}$, m, 2H), 4.15 ($HC_{1''}$, dddd, $J_1 = J_2 = 5.6$ Hz, $J_3 = J_4 = 1.5$ Hz, 2H), 3.84 ($HC_{1'}$, m, 2H), 1.66–1.59 ($HC_{2'}$, m, 2H), 1.54 (HC_{15}, s, 9H), 1.34–1.24 ($HC_{3'}$–$HC_{17'}$, m, 30H), 0.89 ($HC_{18'}$, t, J = 6.8 Hz, 3H).

^{13}C NMR (100 MHz, $CDCl_3$) δ (ppm): 170.3 (C_4), 164.1 (C_2), 160.6 (C_1), 153.4 (C_{13}), 136.0 (C_7), 133.7 ($C_{2''}$), 128.5, 128.2, 127.9 ($C_{8\text{-}12}$), 117.1 ($C_{3''}$), 114.8 (C_5), 81.9 (C_{14}), 69.0 (C_3), 68.5 (C_6), 47.8 ($C_{1'}$), 43.7 ($C_{1''}$), 31.9– 22.7 ($C_{2''}$–$C_{17'}$), 28.1 (HC_{15}), 14.1 ($C_{18''}$). HRMS (ESI): Calculated for ($C_{38}H_{59}N_5O_3$ +H^+)/z 634.4691. Observed *m/z* 634.4690.

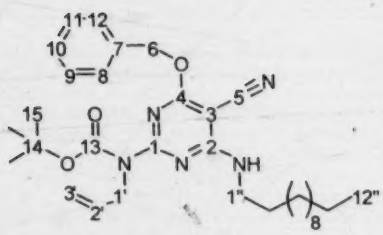

Synthesis of 7e. This compound was obtained from **6e** as a white powder ($C_{32}H_{47}N_5O_3$, 3.80 g, 94%) using Method #9.

R_f = 0.65 (15% EA/Hex). mp = 97 °C.

^{1}H NMR (400 MHz, $CDCl_3$) δ (ppm): 7.42–7.26 (m, HC_8–HC_{12}, 5H), 5.89 ($HC_{2'}$, m, 1H), 5.44 (HC_6, s, 2H), 5.33 ($HNC_{1''}$, t, J = 5.6 Hz, 1H), 5.14 ($HC_{3'}$, m, 2H), 4.17 ($HC_{1'}$, m, 2H), 3.45 ($HC_{1''}$, dt, J_1 = 6.2 Hz, J_2 = 13.8 Hz, 2H), 1.63–1.59 ($HC_{2''}$, m, 2H), 1.55 (HC_{15}, s, 9H), 1.34–1.24 ($HC_{3''}$–$HC_{17''}$, m, 30H), 0.88 ($HC_{18''}$, t, J = 6.8 Hz, 3H).

^{13}C NMR (100 MHz, $CDCl_3$) δ (ppm): 170.3 (C_4), 164.2 (C_2), 160.5 (C_1), 153.0 (C_{13}), 136.1 (C_7), 134.3 ($C_{2'}$), 128.4, 128.2, 128.0 ($C_{8\text{-}12}$), 116.3 ($C_{3'}$), 115.0 (C_5), 81.2 (C_{14}), 69.0 (C_3), 68.5 (C_6), 49.7 ($C_{1'}$), 41.9 ($C_{1''}$), 31.9–22.7 ($C_{2''}$–$C_{11''}$), 2.1 (HC_{15}), 14.1 ($C_{18''}$). HRMS (ESI): Calculated for ($C_{32}H_{47}N_5O_3$ +H^+)/z 550.3752. Observed *m/z* 550.3754.

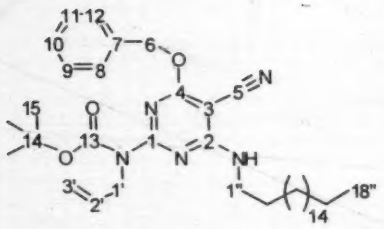

Synthesis of 7f. This compound was obtained from **6f** as a white powder ($C_{38}H_{59}N_5O_3$, 1.29 g, 96%,) using Method #9. R_f = 0.70 (15% EA/Hex). mp = 109 °C.

^{1}H NMR (400 MHz, $CDCl_3$) δ (ppm): 7.44–7.28 (m, HC_{8}–HC_{12}, 5H), 5.90 ($HC_{2'}$, m, 1H), 5.45 (HC_6, s, 2H), 5.34 ($HNC_{1''}$, t, J = 5.6 Hz, 1H), 5.13 ($HC_{3'}$, m, 2H), 4.15 ($HC_{1'}$, m, 2H), 3.47 ($HC_{1''}$, dt, J_1 = 5.8 Hz, J_2 = 13.2 Hz, 2H), 1.61–1.57 ($HC_{2''}$, m, 2H), 1.56 (HC_{15}, s, 9H), 1.34–1.24 ($HC_{3''}$–$HC_{17''}$, m, 30H), 0.88 ($HC_{18''}$, t, J = 6.8 Hz, 3H).

^{13}C NMR (100 MHz, $CDCl_3$) δ (ppm): 170.4 (C_4), 164.2 (C_2), 160.4 (C_1), 153.0 (C_{13}), 136.0 (C_7), 134.0 ($C_{2'}$), 128.5, 128.2, 128.0 ($C_{8\text{-}12}$), 116.3 ($C_{3'}$), 114.9 (C_5), 81.0 (C_{14}), 69.0 (C_3), 68.6 (C_6), 49.7 ($C_{1'}$), 41.6 ($C_{1''}$), 31.9–22.7 ($C_{2''}$–$C_{17''}$), 28.1 (HC_{15}), 14.1 ($C_{18''}$). HRMS (ESI): Calculated for ($C_{38}H_{59}N_5O_3$ +H^+)/z 634.4691. Observed *m/z* 634.4672.

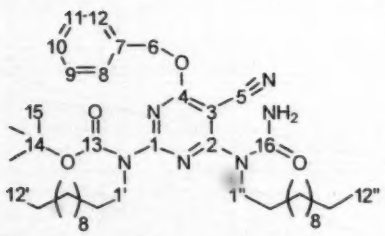

Synthesis of 8a (Method #10). To a solution of compound **7a** (0.41 g, 0.6 mmol) in DCM (50 mL), N-trichlorometylcarbonylisocyanate (0.23 g, 0.14 mL, 1.2 mmol) was added at 0°C under N_2 atmosphere. After stirring for 1h at 0 °C, the mixture was allowed to warm to rt and was stirred for an additional 48 h. The reaction mixture was cooled to 0 °C and carefully quenched with dH_2O (10 mL, exothermic reaction!) followed by 5% aqueous $NaHCO_3$ (10 mL). The product was extracted with DCM (300 mL) and the resulting organic layer was washed with dH_2O (2×50 mL), brine (100 mL), and dried over anhydrous Na_2SO_4. After filtration and evaporation of the solvent (rotovap), the residual solid was used in the

next step without further purification. R_f = 0.75 and 0.25 (50% EA/Hex) corresponding to the mixed urea (**8a**) and the cyclized products (**9a**, next step).

Synthesis of 7a (Method #11). To a solution of **6a** (2.8 g, 4.1 mmol) and DIEA (5 mL) in DCM (40 mL), N-(chlorocarbonyl) isocyanate (1.98 mL, 24.6 mmol) was added at 0 °C under N_2 atmosphere. After stirring for 1 h at 0 °C, the mixture was allowed to warm to room temperature and was stirred for an additional 24 h. The reaction mixture was cooled to 0 °C and quenched slowly with saturated Na_2CO_3 solution (20 mL). The product was extracted with DCM (300 mL), washed with dH_2O (3×50 mL), brine (100 mL), and dried over anhydrous Na_2SO_4. After evaporation of the solvent (rotovap), the product was precipitated in CH_3OH to give **8a** as a white solid ($C_{42}H_{68}N_6O_4$, 2.80 g, 94%).

^{1}H NMR (400 MHz, $CDCl_3$) δ (ppm): 7.44 – 7.32 (m, HC_8 – HC_{12}, 5H), 5.51 (HC_6, s, 2H), 4.19 ($HC_{1'}$, m, 2H), 3.89 ($HC_{1''}$, m, 2H), 1.63 – 1.57 ($HC_{2'}$+$HC_{2''}$, m, 4H), 1.73 – 1.56 ($HC_{3'}$–$HC_{11'}$ + $HC_{3''}$–$HC_{11''}$, m, 32H), 1.54 (HC_{15}, s, 9H), 0.89 ($HC_{12'}$ + $HC_{12''}$, t, J = 6.8 Hz, 6H).

^{13}C NMR (100 MHz, $CDCl_3$) δ (ppm): 172.3 (C_4), 163.7, 158.2 (C_1, C_2), 155.3 (C_{13}), 153.5 (C_{16}), 135.2 (C_7), 128.6, 128.3, 127.2 ($C_{8\text{-}12}$), 113.9 (C_5), 83.1 (C_{14}), 69.4 (C_3), 68.2 (C_6), 47.8 ($C_{1'}$), 46.0 ($C_{1''}$), 31.8 – 22.5 ($C_{2'}$–$C_{11'}$, $C_{2''}$–$C_{11''}$), 22.1 (HC_{15}), 14.0 ($C_{12'}$, $C_{12''}$).

FTIR (cm^{-1}) 3399, 3283, 3037, 2953, 2921, 2851, 2219, 1744, 1725, 1677, 1577, 1525, 1084.

HRMS (ESI): Calculated for ($C_{42}H_{68}N_6O_4$ +H^+)/z 721.5375. Observed *m/z* 721.5371.

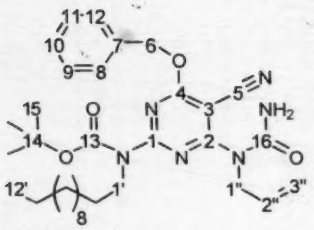

Synthesis of 8c. This compound was obtained from **7c** as a white powder (1.29 g, 98%) using Method #11. R_f = 0.65 and 0.20 (50% EA/Hex) corresponding to mixed urea (**8c**) and the cyclized products (**9c**, next step).

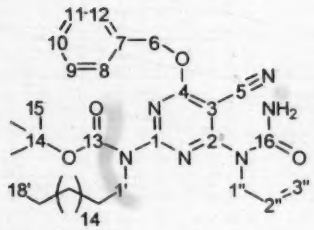

Compound 8d. This compound was obtained as a white powder (3.04 g, 95%) from **7d** using Method #11. R_f = 0.70 and 0.25 (50% EA/Hex) corresponding to mixed urea (**8d**) and the cyclized products (**9d**, next step).

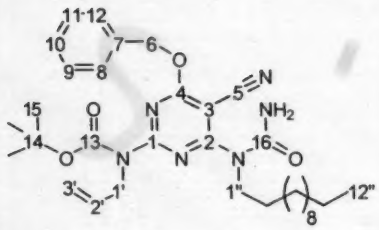

Synthesis of 8e. This compound was not isolated. Compound **7e** converted directly to **9e** using Method #11.

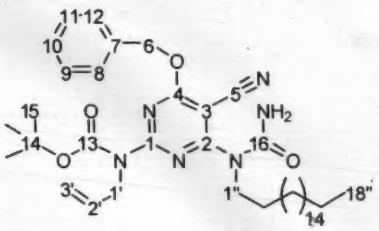

Synthesis of 8f. This compound was not isolated. Compound **7f** converted directly to **9f** using Method #11.

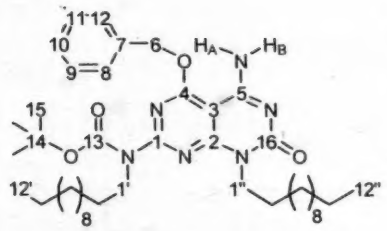

Synthesis of 9a (Method #12). A solution of **8a** (0.20 g, 0.28 mmol) in DCM (8 mL) and 7N NH_3 in CH_3OH were stirred under N_2 atmosphere at rt for 5 h. The solvents were removed under reduced pressure (rotovap) and the desired compound **9a** was obtained as a white paraffin-like solid ($C_{42}H_{68}N_6O_4$, 0.20 g, quantitative). R_f = 0.25 (50% EA/Hex).

^{1}H NMR (400 MHz, $CDCl_3$) δ (ppm): 7.45–7.26 (m, HC_8–HC_{12}, 5H), 6.92 (sh.s, H_A, 1H), 6.52 (H_B, br. s, 1H), 5.58 (HC_6, s, 2H), 4.17 ($HC_{1'}$, m, 2H), 3.93 ($HC_{1''}$, dt, J_1 = 7.2 Hz, J_1 = 13.2 Hz, 2H), 1.72-1.62 ($HC_{2'}$+$HC_{2''}$, m, 4H), 1.57 (HC_{15}, s, 9H), 1.34–1.22 ($HC_{3'}$–$HC_{11'}$ + $HC_{3''}$–$HC_{11''}$, m, 32H), 0.88 ($HC_{12'}$ + $HC_{12''}$, t, J = 7.2 Hz, 6H).

^{13}C NMR (100 MHz, $CDCl_3$) δ (ppm): 166.4 (C_4), 160.7, 160.6, 160.6, (C_1, C_2, C_5) 156.0 (C_{13}), 153.0 (C_{16}), 135.0 (C_7), 129.0, 128.9, 128.6 ($C_{8\text{-}12}$), 85.9 (C_3), 82.3 (C_{14}), 70.0 (C_6), 48.1 ($C_{1'}$), 42.9 ($C_{1''}$), 31.9–22.7 ($C_{2'}$–$C_{11'}$, $C_{2''}$–$C_{11''}$), 28.2 (HC_{15}), 14.1 ($C_{12'}$, $C_{12''}$) (assignments were made based on HMBC and HMQC spectra).

HRMS (ESI): Calculated for ($C_{42}H_{68}N_6O_4$ +H^+)/z 721.5375. Observed *m/z* 721.5376.

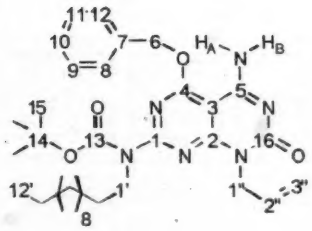

Synthesis of 9c. This compound was obtained as a white solid ($C_{33}H_{48}N_6O_4$, 5.60 g, 87% over two steps) from **8c** according to Method #12, followed by flash chromatography (0–20% EA/Hex). R_f = 0.20 (50% EA/Hex).

^{1}H NMR (400 MHz, $CDCl_3$) δ (ppm): 8.99 (H_A, br. s, major, 1H), 8.51 (H_A, br. s, minor), 7.42–7.26 (m, HC_8–HC_{12}, 5H), 7.12 (H_B, s, major, 1H), 7.07 (H_B, s, minor, 1H), 5.89 ($HC_{2''}$, m, 1H), 5.57 (HC_6, s, 2H), 5.17–5.06 ($HC_{3''}$, m, 2H), 4.75 ($HC_{1''}$, m, 2H), 3.86

($HC_{1'}$, m, 2H), 1.64–1.58 ($HC_{2'}$, m, 2H), 1.52 (HC_{15}, s, 9H), 1.30–1.18 ($HC_{3'}$–$HC_{11'}$, m, 18H), 0.82 ($HC_{12'}$, t, J = 6.8 Hz, 3H).

^{13}C NMR (100 MHz, $CDCl_3$) δ (ppm): 166.3 (C_4), 161.0, 160.2, 160.1, (C_1, C_2, C_5), 155.8 (C_{13}), 153.0 (C_{16}), 135.0 (C_7), 132.5 ($C_{2''}$), 128.9, 128.9, 128.5 ($C_{8\text{-}12}$), 117.1 ($C_{3''}$), 86.0 (C_3), 82.3 (C_{14}), 69.9 (C_6), 48.0 ($C_{1''}$), 44.5 ($C_{1'}$), 31.9– 22.7 ($C_{2'}$–$C_{17'}$), 28.1 (HC_{15}), 14.1 ($C_{18'}$).

HRMS (ESI): Calculated for $(C_{33}H_{48}N_6O_4 + H^+)/z$ 593.3810. Observed *m/z* 593.3762.

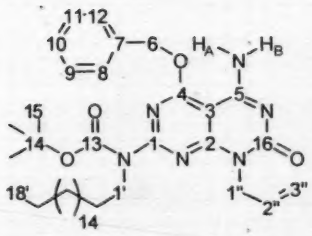

Synthesis of 9d. This compound was obtained as a white solid ($C_{39}H_{60}N_6O_4$, 0.44 g, 85% over two steps), from **8d** using Method #12, followed by flash chromatography (0–20% EA/Hex). R_f = 0.20 (50% EA/Hex).

^1H NMR (500 MHz, $CDCl_3$) δ (ppm): 7.66 (H_A, br. s, 1H), 7.43–7.32 (m, HC_8–HC_{12}, 5H), 7.01 (H_B, s, 1H), 5.92 ($HC_{2''}$, m, 1H), 5.58 (HC_6, s, 2H), 5.20–5.10 ($HC_{3''}$, m, 2H), 4.80 ($HC_{1''}$, app. d, J = 5.5 Hz, 2H), 3.86 ($HC_{1'}$, t, J = 8.0 Hz, 2H), 1.68–1.60 ($HC_{2'}$, app. p, J = 7 Hz, 2H), 1.54 (HC_{15}, s, 9H), 1.30–1.21 ($HC_{3'}$–$HC_{17'}$, m, 30H), 0.85 ($HC_{12'}$, t, J = 7.5 Hz, 3H).

^{13}C NMR (100 MHz, $CDCl_3$) δ (ppm): 166.5 (C_4), 161.0, 160.5, 160.5, (C_1, C_2, C_5), 155.6 (C_{13}), 152.6 (C_{16}), 134.8 (C_7), 132.3 ($C_{2''}$), 128.5, 128.5, 128.2 ($C_{8\text{-}12}$), 116.8 ($C_{3''}$), 85.9 (C_3), 82.1 (C_{14}), 69.6 (C_6), 47.8 ($C_{1''}$), 44.3 ($C_{1'}$), 31.8–22.6 ($C_{2'}$–$C_{11'}$), 28.0 (HC_{15}), 14.0 ($C_{12'}$).

HRMS (ESI): Calculated for $(C_{39}H_{60}N_6O_4 + H^+)/z$ 677.4749. Observed *m/z* 677.4750.

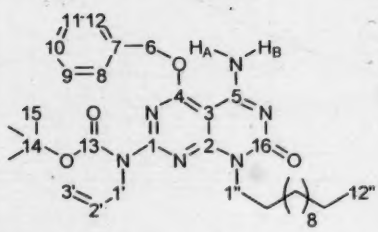

Synthesis of 9e. This compound was obtained as a white solid ($C_{33}H_{48}N_6O_4$, 1.02 g, 82% over two steps) from **7e** using Method #12, followed by flash chromatography (0–20% EA/Hex). R_f = 0.20 (50% EA/Hex).

^{1}H NMR (500 MHz, $CDCl_3$) δ (ppm): 7.51 (H_A, br. s, 1H), 7.50–7.38 (m, HC_8–HC_{12}, 5H), 7.17 (H_B, s, major, 1H), 7.07 (H_B, s, minor, 1H), 5.96 ($HC_{2''}$, m, 1H), 5.64 (HC_6, s, 2H), 5.24–5.15 ($HC_{3''}$, m, 2H), 4.58 ($HC_{1''}$, app.d, J = 5.0 Hz, 2H), 4.18 ($HC_{1'}$, t, J = 10 Hz, 2H), 1.71–1.64 ($HC_{2''}$, m, 2H), 1.58 (HC_{15}, s, 9H), 1.40–1.24 ($HC_{3''}$–$HC_{11''}$, m, 18H), 0.90 ($HC_{12'}$, t, J = 6.5 Hz, 3H).

^{13}C NMR (100 MHz, $CDCl_3$) δ (ppm): 166.3 (C_4), 161.0, 160.2, 160.1, (C_1, C_2, C_5), 155.8 (C_{13}), 153.0 (C_{16}), 135.0 (C_7), 132.5 ($C_{2''}$), 128.9, 128.9, 128.5 ($C_{8\text{-}12}$), 117.1 ($C_{3''}$), 86.0 (C_3), 82.3 (C_{14}), 69.9 (C_6), 48.0 ($C_{1''}$), 44.5 ($C_{1'}$), 31.9– 22.7 ($C_{2'}$–$C_{17'}$), 28.1 (HC_{15}), 14.1 ($C_{18'}$).

HRMS (ESI): Calculated for ($C_{33}H_{48}N_6O_4$ + Na^+)/*z* 615.3629. Observed *m/z* 615.3624.

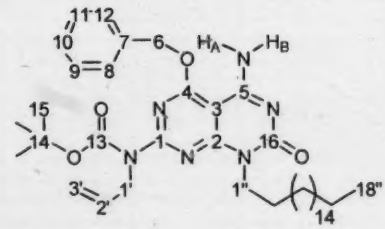

Synthesis of 9f. This compound was obtained as a white solid ($C_{39}H_{60}N_6O_4$, 0.44 g, 85% over two steps) from **7f** using Method #12, followed by flash chromatography (0–20% EA/Hex). R_f = 0.20 (50% EA/Hex).

^{1}H NMR (500 MHz, $CDCl_3$) δ (ppm): 7.66 (H_A, br. s, 1H), 7.43–7.32 (m, HC_8–HC_{12}, 5H), 7.01 (H_B, s, 1H), 5.92 ($HC_{2''}$, m, 1H), 5.58 (HC_6, s, 2H), 5.20–5.10 ($HC_{3''}$, m, 2H),

4.80 ($HC_{1''}$, app. d, J = 5.5 Hz, 2H), 3.86 ($HC_{1'}$, t, J = 8.0 Hz, 2H), 1.68–1.60 ($HC_{2'}$, app. p, J = 7 Hz, 2H), 1.54 (HC_{15}, s, 9H), 1.30–1.21 ($HC_{3'}$–$HC_{17'}$, m, 30H), 0.85 ($HC_{12'}$, t, J = 7.5 Hz, 3H).

^{13}C NMR (100 MHz, $CDCl_3$) δ (ppm): 166.5 (C_4), 161.0, 160.5, 160.5, (C_1, C_2, C_5), 155.6 (C_{13}), 152.6 (C_{16}), 134.8 (C_7), 132.3 ($C_{2''}$), 128.5, 128.5, 128.2 ($C_{8\text{-}12}$), 116.8 ($C_{3''}$), 85.9 (C_3), 82.1 (C_{14}), 69.6 (C_6), 47.8 ($C_{1''}$), 44.3 ($C_{1'}$), 31.8–22.6 ($C_{2'}$–$C_{11'}$), 28.0 (HC_{15}), 14.0 ($C_{12'}$).

HRMS (ESI): Calculated for $(C_{39}H_{60}N_6O_4 + H^+)/z$ 677.4749. Observed *m/z* 677.4750.

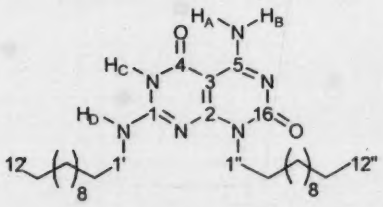

Synthesis of 1a. Method #13. Compound **9a** (0.15 g, 0.02 mmol) was dissolved in a 4M solution of HCl in dioxane (4 mL) and the mixture was refluxed for 2 h. The white precipitate formed was filtered, washed with DCM (5×10 mL), and dried on a filter. Compound **1a** was obtained as a white solid ($C_{42}H_{68}N_6O_4$, 0.11 g, quantitative).

^1H NMR (500 MHz, DMSO-d_6, 100°C) δ (ppm): 12.2–11.2 (H_C, br. s, 1H), 9.08 (H_A, s, 1H), 8.34 (H_B, s, 1H), 8.16 (H_D, s, 1H), 4.04 ($HC_{1'}$, t, J = 7.5, 2H), 3.43 ($HC_{1''}$, dt, J_1 = J_2 = 6.5 Hz, 2H), 1.68-1.58 ($HC_{2'}$+$HC_{2''}$, m, 4H), 1.38–1.24 ($HC_{3'}$–$HC_{11'}$ + $HC_{3''}$–$HC_{11''}$, m, 36H), 0.88 ($HC_{12'}$ + $HC_{12''}$, t, J = 6.5 Hz, 6H).

^1H NMR (300 MHz, $CDCl_3$, 40°C) δ (ppm): 12.7–12.2 (H_C, br. s, 1H), 9.35 (H_A, s, 1H), 9.04, 9.01 (H_B, H_D, 2H), 4.13 ($HC_{1''}$, br. s, 2H), 3.50 ($HC_{1''}$, br. s, 2H), 1.80-1.60 ($HC_{2'}$+$HC_{2''}$, m, 4H), 1.40–1.25 ($HC_{3'}$–$HC_{11'}$ + $HC_{3''}$–$HC_{11''}$, m, 36H), 0.90 ($HC_{12'}$ + $HC_{12''}$, t, J = 6.8 Hz, 6H).

^{1}H NMR (500 MHz, CF_3COOD) δ (ppm): 4.50 ($HC_{1''}$, br. s, 2H), 3.87 ($HC_{1''}$, br. s, 2H), 2.05–1.95 ($HC_{2'}$+$HC_{2''}$, m, 4H), 1.63–1.40 ($HC_{3'}$–$HC_{11'}$ + $HC_{3''}$–$HC_{11''}$, m, 36H), 1.05 ($HC_{12'}$ + $HC_{12''}$, t, J = 5.9 Hz, 6H).

^{13}C NMR (100 MHz, $CDCl_3$) δ (ppm): 165.8 (C_5), 162.8 (C_2), 157.8 (C_4), 156.8 (C_1), 151.8 (C_{16}), 84.8 (C_3), 46.5 ($C_{1''}$), 44.9 ($C_{1'}$), 33.8–24.3 ($C_{2'}$–$C_{11'}$, $C_{2''}$–$C_{11''}$), 14.6 ($C_{12'}$, $C_{12''}$) (assignments are made using HMBC and HMQC spectra of **1f**).

FTIR (cm^{-1}) 3322, 3174, 2954, 2847, 1715, 1667, 1612, 1544.

Elemental analysis: Calculated for $C_{30}H_{54}N_6O_2$–HCl: C, 63.56; H, 9.79; N, 14.83; Cl, 6.25. Found: C, 63.20; H, 9.63; N, 14.71; Cl, 6.21.

HRMS (ESI): Calculated for ($C_{42}H_{68}N_6O_4$ +H^+)/*z* 531.4381. Observed *m/z* 531.4383.

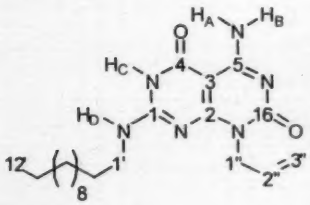

Synthesis of 1c. This compound was obtained from **9c** as a pinkish solid ($C_{21}H_{34}N_6O_2$, 149 mg, 100%) using Method #13.

^{1}H NMR (400 MHz, 5:2–CF_3COOH:CD_2Cl_2) δ (ppm): 12.0–11.0 (H_C, overlapping with TFA signal), 9.48 (H_A, s, 1H), 8.13 (H_B, s, 1H), 7.44 (H_D, major, s, 1H), 7.03 (H_D, minor, br. s), 6.11–5.92 ($HC_{2''}$, m, 1H), 5.58–5.42 ($HC_{3''}$, m, 2H), 5.02 ($HC_{1''}$, major, m, 1H), 4.91 ($HC_{1''}$, minor, m), 3.79 ($HC_{1'}$, major, m, 2H), 3.62 ($HC_{1'}$, minor, m), 1.98-1.83 ($HC_{2'}$, m, 2H), 1.60–1.16 ($HC_{3'}$–$HC_{11'}$, m, 18H), 0.99 ($HC_{12'}$, t, J = 7.2 Hz, 3H).

^{1}H NMR (400 MHz, DMSO-d_6, 100°C) δ (ppm): H_C is too broad to be observed, 9.07 (H_A, br. s, 1H), 8.80–8.58 (H_B + H_D overlapping, br. s, 2H), 5.94 –5.82 ($HC_{2''}$, m, 1H),

5.24–5.14 ($HC_{3''}$, m, 2H), 4.64 ($HC_{1''}$, app. d, J = 5.2 Hz, 2H), 3.40 ($HC_{1'}$, m, 2H), 1.60-1.53 ($HC_{2'}$, m, 2H), 1.60–1.16 ($HC_{3'}$–$HC_{11'}$, m, 18H), 0.86 ($HC_{12'}$, t, J = 6.6 Hz, 3H).

^{13}C NMR (125 MHz, 5:2–CF_3COOH:CD_2Cl_2) δ (ppm): 166.2 (C_5), 163.5 (C_2), 157.4 (C_4), 156.2 (C_1), 151.1 (C_{16}), 130.4 ($C_{2''}$), 121.4 ($C_{3''}$), 84.4 (C_3), 47.6 ($C_{1''}$), 44.6 ($C_{1'}$), 33.3–23.9 ($C_{2'}$–$C_{11'}$), 14.3 ($C_{12'}$)

Elemental analysis: Calculated for $C_{21}H_{34}N_6O_2$·HCl: C, 56.46; H, 8.04; N, 19.14. Found: C, 56.60; H, 8.06; N, 19.06.

HRMS (ESI): Calculated for ($C_{21}H_{34}N_6O_2 + H^+$)/*z* 403.2816. Observed *m/z* 403.2806.

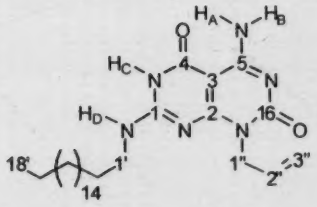

Synthesis of 1d. This compound was obtained from **9d** as white solid ($C_{27}H_{46}N_6O_2$, 191 mg, 97%) using Method #13.

^1H NMR (400 MHz, 9:1–CF_3COOH:C_6D_6) δ (ppm): 12.0–11.0 (H_C, overlapping with TFA signal), 9.04 (H_A, br. s, 1H), 8.94 (H_D, minor, br. s), 7.66 (H_B, s, 1H), 7.04 (H_D, major, s, 1H), 5.80–5.69 ($HC_{2''}$, m, 1H), 5.30–5.18 ($HC_{3''}$, m, 2H), 4.64–4.54 ($HC_{1''}$, m, 1H), 3.38 ($HC_{1'}$, major, m, 2H), 3.08 ($HC_{1'}$, minor, m), 1.63-1.49 ($HC_{2'}$, m, 2H), 1.38–1.04 ($HC_{3'}$–$HC_{17'}$, m, 18H), 0.901 ($HC_{18'}$, t, J = 7.0 Hz, 3H).

^1H NMR (300 MHz, CD_3OD) δ (ppm): 6.08–5.89 ($HC_{2''}$, m, 1H), 5.35–5.12 ($HC_{3''}$, m, 2H), 4.85–4.77 ($HNC_{1''}$, m, 1H), 3.54 ($HC_{1'}$, m, 2H), 1.77-1.62 ($HC_{2'}$, m, 2H), 1.44–1.25 ($HC_{3'}$–$HC_{17'}$, m, 30H), 0.93 ($HC_{18'}$, t, J = 6.9 Hz, 3H).

^1H NMR (500 MHz, DMSO-d_6, 60°C) δ (ppm): 12.08 (H_C, br. s, 1H), 9.14 (H_A, br. s, 1H), 8.62 (H_B, br. s, 1H), 8.43 (H_D, br. s, 1H), 5.91–5.78 ($HC_{2''}$, m, 1H), 5.20–5.03 ($HC_{3''}$,

m, 2H), 4.60 ($HC_{1''}$, br. s, 2H), $HC_{1'}$ overlaps with DMSO signal, 1.56-1.42 ($HC_{2'}$, m, 2H), 1.28–1.03 ($HC_{3'}$–$HC_{11'}$, m, 18H), 0.83 ($HC_{12'}$, t, J = 6.5 Hz, 3H).

^{13}C NMR (125 MHz, 9:1–CF_3COOH:C_6D_6) δ (ppm): 164.1 (C_5), 160.4 (C_2), 155.9 (C_4), 154.8 (C_1), 149.7 (C_{16}), 129.3 ($C_{2''}$), 120.2 ($C_{3''}$), 83.1 (C_3), 46.2 ($C_{1''}$), 43.2 ($C_{1'}$), 32.2–22.8 ($C_{2'}$–$C_{17'}$), 13.2 ($C_{18'}$)

Elemental analysis: Calculated for $C_{27}H_{46}N_6O_2$–HCl: C, 61.99; H, 9.06; N, 16.06. Found: C, 62.05; H, 9.11; N, 16.07.

HRMS (ESI): Calculated for ($C_{27}H_{46}N_6O_2 + H^+$)/*z* 487.3755. Observed *m/z* 487.3736.

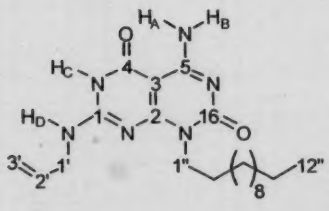

Synthesis of 1e. This compound was obtained as a white solid ($C_{21}H_{34}N_6O_2$, 27 mg, 99%) from **9e** using Method #13.

^1H NMR (400 MHz, 5:2–CF_3COOH:CD_2Cl_2) δ (ppm): 12.0–11.0 (H_C, overlapping with TFA signal), 9.51 (H_A, s, 1H), 8.17 (H_B, s, 1H), 7.55 (H_D, major, s, 1H), 7.12 (H_D, minor, br. s), 6.09–5.98 ($HC_{2'}$, m, 1H), 5.54–5.42 ($HC_{3'}$, m, 2H), 4.50–4.24 ($HC_{1''}$, m, + $HC_{1'}$, m, 4H), 1.98-1.82 ($HC_{2''}$, m, 2H), 1.60–1.31 ($HC_{3''}$–$HC_{11''}$, m, 18H), 0.96 ($HC_{12'}$, t, J = 7.2 Hz, 3H).

^{13}C NMR (125 MHz, 5:2–CF_3COOH:CD_2Cl_2) δ (ppm): 165.2 (C_5), 162.6 (C_2), 157.7 (C_4), 156.6 (C_1), 151.7 (C_{16}), 132.2 ($C_{2'}$), 126.9 ($C_{3'}$), 84.9 (C_3), 46.8, 46.4 ($C_{1'}$, $C_{1''}$), 33.5–24.1 ($C_{2''}$–$C_{11''}$), 14.4 ($C_{12''}$).

Elemental analysis: Calculated for $C_{21}H_{34}N_6O_2$–HCl: C, 56.46; H, 8.04; N, 19.14. Found: C, 56.33; H, 7.87; N, 18.93.

HRMS (ESI): Calculated for ($C_{21}H_{34}N_6O_2 + H^+$)/*z* 403.2816. Found *m/z* 403.2812.

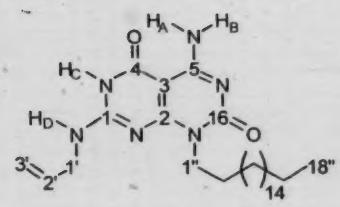

Synthesis of 1f. This compound was obtained as white solid ($C_{27}H_{46}N_6O_2$, 86 mg, 94%) from **9f** using Method #13.

^{1}H NMR (400 MHz, 5:2–CF_3COOH:CD_2Cl_2) δ (ppm): 12.0–11.0 (H_C, overlapping with TFA signal), 9.51 (H_A, s, 1H), 8.18 (H_B, s, 1H), 7.53 (H_D, major, s, 1H), 7.14 (H_D, minor, br. s), 6.11–5.98 ($HC_{2'}$, m, 1H), 5.58–5.40 ($HC_{3'}$, m, 2H), 4.50–4.25 ($HC_{1''}$, m, + $HC_{1'}$, m, 4H), 1.98-1.82 ($HC_{2''}$, m, 2H), 1.60–1.28 ($HC_{3''}$–$HC_{17''}$, m, 30H), 0.97 ($HC_{12'}$, t, J = 6.8 Hz, 3H).

^{13}C NMR (125 MHz, 5:2–CF_3COOH:CD_2Cl_2) δ (ppm): 165.2 (C_5), 162.5 (C_2), 157.6 (C_4), 156.5 (C_1), 151.6 (C_{16}), 132.2 ($C_{2'}$), 126.8 ($C_{3'}$), 85.0 (C_3), 46.8, 46.3 ($C_{1'}$, $C_{1''}$), 33.5–24.0 ($C_{2''}$–$C_{17''}$), 14.4 ($C_{18''}$)

Elemental analysis: Calculated for $C_{27}H_{46}N_6O_2$–HCl: C, 61.99; H, 9.06; N, 16.06. Found: C, 61.79; H, 8.82; N, 16.00.

HRMS (ESI): Calculated for ($C_{27}H_{46}N_6O_2 + H^+$)/*z* 487.3755. Observed *m/z* 487.3712.

Assembly and Instrumentation.

DLS Measurements. DLS experiments were performed on a Malvern Zetasizer Nano S working at a 90° scattering angle at 25 °C. The instrument is equipped with a 40 mW He-Ne laser (λ= 633 nm) and an avalanche photodiode detector. Size distributions were calculated using an inverse Laplace transform algorithm, and the hydrodynamic radii were calculated using the Stokes-Einstein equation. All samples were filtered through 0.2 μm nonsterile PVFD membranes (Whatman filters) prior to measurement. All freshly prepared samples were filtered through 0.2 μm nonsterile PVFD membranes (Whatman filters) prior to measurement. The fact that the aggregates after filtration are larger than the membrane pores used is the result of RNTs self-assembly/growth after filtration. Control experiments with only solvent filtered through membrane showed no DLS signal.

AFM. The samples were prepared by dissolving a compound in a solvent, sonicating, heating to the boiling point, then allowing the solution to age for 2 h at room temperature (or otherwise as indicated in the figure captions). Samples for AFM imaging were prepared in a Class 10000 Clean Room spin-coating 25 μL (Cookson G3-8 Desk-Top Precision Spin-Coating System) on 10 × 10 mm^2 freshly peeled Mica grade V-4 (SPI supplies) substrates. AFM measurements were performed in tapping mode (TM-AFM) at a scan rate of 2 Hz per line using a Digital Instruments/Veeco Instruments MultiMode Nanoscope IV equipped with an E scanner. Silicon cantilevers (MikroMasch USA, Inc.) with spring constants of 40 N/m were used.

Electron Microscopy. The samples were prepared by placing a carbon-coated 400-mesh copper grid on a droplet of a compound (0.25 g/L) for 5 s. The grid was then blotted and

air-dried prior to imaging. SEM images were obtained without staining at 5-30 kV accelerating voltage and a working distance of 3.0-6.0 mm on a high-resolution Hitachi S-4800 cold field emission SEM. TEM and SAED were carried out on JEOL 2200 FS TEM -200 kV Schottky field emission instrument equipped with an in-column filter. TEM images were recorded using energy filtered zero loss beam. SAED patterns were obtained by exposition on an image plate for improved contrast as opposed to the exposition on CCD camera (L = 163 mm).

X-ray Powder Diffraction. Samples were prepared according to the following two methods. Method 1: A thin film was prepared on an amorphous glass cover slip (SPI supplies no. 1021, 22 mm diameter and 0.15 mm thick) by drop-casting a solution (0.25 g/L in $CHCl_3$) and drying it, then repeating this cycle ca. 200×. Method 2: A solution of a compound (0.25 g/L $CHCl_3$) was concentrated at room temperature under atmospheric pressure. The resulting powder was then ground and placed between two amorphous tapes. The samples were analyzed on a Bruker D8 Discover equipped with Cu K_α source and Bruker HiStar GADDS detector. The first sample was analyzed in a glancing angle, and the second was investigated in transmission mode using a beam stopper. Control experiments with the glass slide and the tape were carried out as well.

4. Helical Nanotube Bundles and Their Metallization.

4.1. Objectives

As was discussed in Chapter 1, the miniaturization of electronic devices requires increasingly smaller components like diodes, transistors, and wires for their fabrication. The objectives of this Chapter are to make electrically conducting nanowires from RNTs. An improved strategy to fabricate a continuous metal nanowire has been explored whereby the aldehyde functional group expressed on the outside walls of RNTs serves to both template and reduce Ag^+ ions.

4.2. Making organic nanostructures conductive: a brief review

Several methods for generating organic high aspect ratio conducting nanostructures are known. These approaches with their advantages and limitations are discussed below.

(I) Making nanostructures conductive via *an extended conjugated π-system*. In this case, conjugation has to extend along the length of the nanostructure such as that observed in π-π stacked aromatic systems like DNA[80] and synthetic hexabenzocoronene nanotubes.[6] The conjugation can be created via polymerization, and the resulting polymer has to have a continuous array of π bonds. Some examples include oligophenylacetylene foldamers,[29] poly(3,4-ethylenedioxythiophene) poly(styrenesulfonate) nanofibers,[150] polyaniline nanoneedles,[151] and polydiacetylenes nanofibers.[152] To create a conductive band in such materials, an electron hole can be injected in the HOMO of the conjugated nanostructure or, alternatively, an electron can be injected into its LUMO. The former can be achieved via oxidation of the nanostructure[6] and the latter via photo-induced excitation of a HOMO electron promoted to the LUMO.[153] The latter mechanism is the

underlying principle in the field of photovoltaics based on organic materials. However, making a nanostructure conductive is just the first step towards miniaturization of electronic devices. The nanostructures have to be integrated into a circuit for their conductivity to be studied. The major challenge for successful integration is the creation of low resistance contacts between nanowires and the electrodes. Many approaches have been suggested.[79] Gold – sulfur linkage has been extensively used for the attachment of thiol terminated nanowires to gold electrodes. However, these contacts were found to have quite a high resistance,[154, 155] which was ascribed to the highly polar character of the Au–S bond. Using the less polar Si–C bond alternatively has allowed for alkyne-based molecular wires to be grafted on silicon surfaces[156] with much lower contact resistance. A very elegant and general approach to integration of a conductive circuit by covalently linking a nanostructure to the tip of a CNT was recently demonstrated for measuring DNA conductivity.[81] CNTs, in turn, can be integrated into a circuit relatively easily.

(II) Making nanostructures conductive via *attachment of organic groups that can be converted into nanowires*. This can be achieved by appending a diacetylene group to the nanostructure followed by polymerization to form a conjugated wire after self-assembly.[82] Any of the attached monomers can be polymerized to form the above mentioned conductive wires arrays along the nanostructure.

(III) Making nanostructures conductive via *deposition of conductive inorganic substances*. This can be achieved by appending functional groups to RNTs that have affinity for metal ions and then reducing the ions into metal.[84] If semiconductor properties are sought, the semiconductor nucleation sites can be created in the same way.

Electron transport properties can be modulated by controlling the size of metal or semiconductor nanoparticles, their spacing, density and composition.

4.3. Assembly of helical nanotube bundles.

In this work, a third approach which is based on making nanostructures conductive via deposition of a conductive inorganic substance was used. Silver metal has one of the highest electron conductivities among inorganic substances (ρ = 1.62 $\mu\Omega$-cm) and it can be obtained by reducing silver cations. Aldehydes are known to react with Ag(I) to form silver metal. In fact it is a qualitative test for formyl group (Tollen's reagent) which is known as "silver mirror reaction" due to the mirror formation on the inside walls of the reaction vessel. A G^C module bearing the aldehyde group can be easily synthesized. Its assembly should lead to a RNT with an exterior surface covered with aldehyde functionality that can be used for silver reduction to create a nanowire. A schematic representation of the idea is depicted in Figure 4.1.

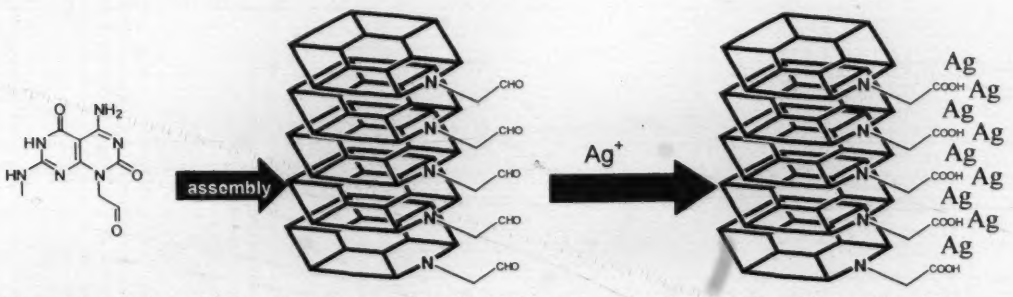

Figure 4. 1. Scheme illustrating the assembly of aldehyde functionalized RNT and its coating with silver.

Deprotection (see experimental part) to give G^C aldehyde was carried out using HCl in dioxane and proceeded in quantitative yield. The self-assembly of the G^C aldehyde was studied in various solvents in search of the most suitable medium for metallization.

Unexpectedly, *in water* G^C aldehyde formed helical structures with up to 25 nm thickness and length up to several microns (Figure 4.2). To understand the supramolecular organization of these assemblies, SEM, TEM, and AFM studies were carried out.

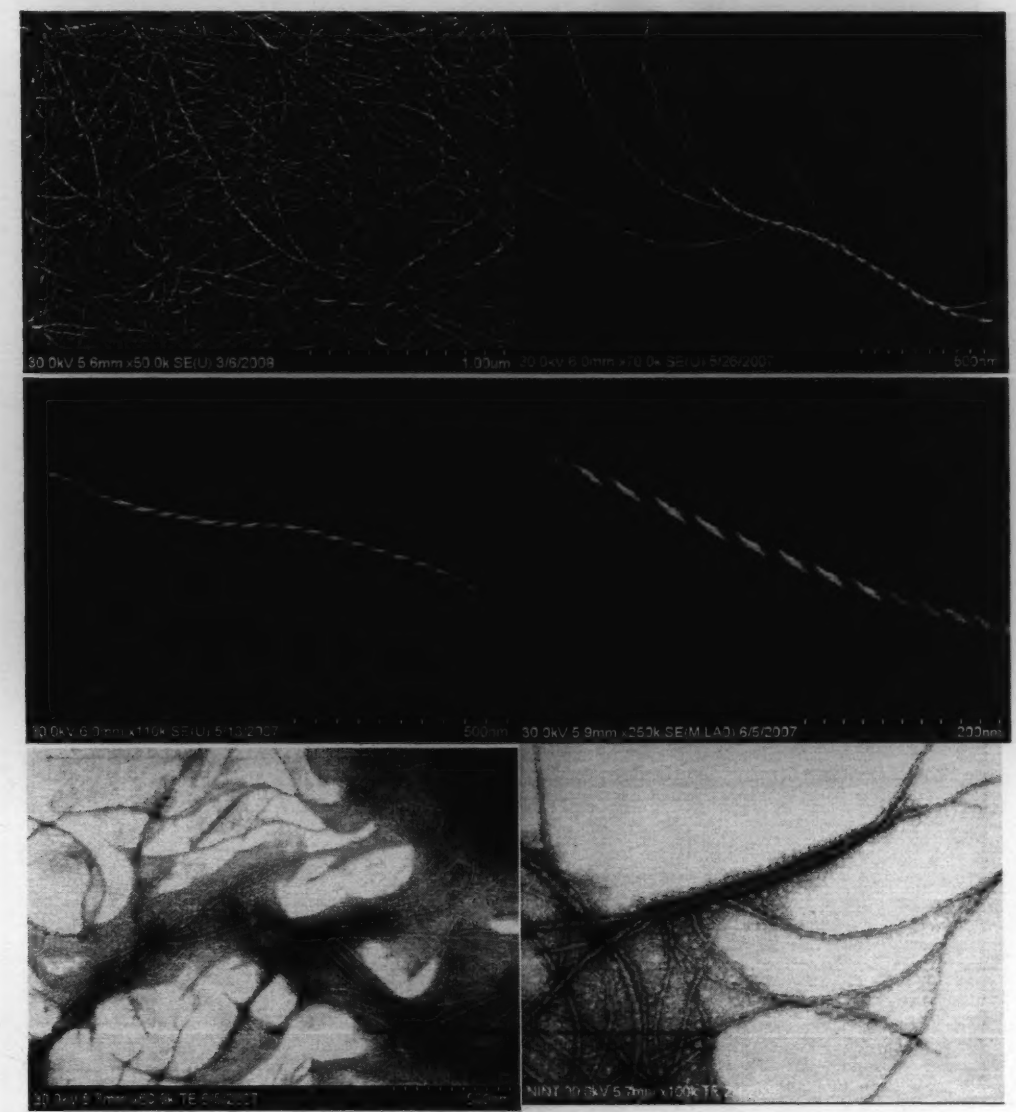

Figure 4. 2. SEM images of helical RNT bundles assembled from G^C aldehyde in water (carbon film, 1 g/L)and (bottom two images) S(T)EM of stained with uranyl acetate helical bundles.

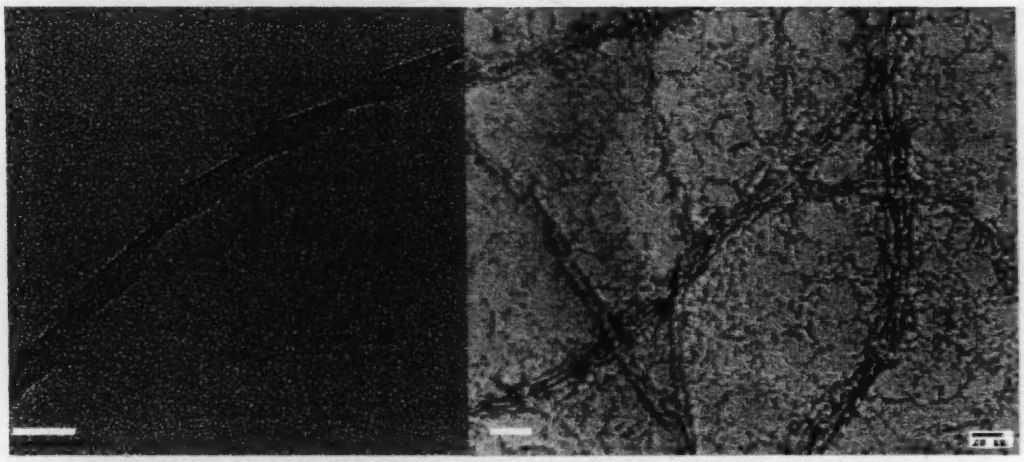

Figure 4. 3. TEM images of unstained (left) and stained (right) helical bundles (uranyl acetate) assembled in water (carbon film, 1 g/L). Scale bars are 20 nm.

Analysis of the TEM images showed that double helices (helices comprised of two single nanotubes) are the most abundant. A small number of single nanotubes were present, which allowed the tube diameter to be measured by AFM (2.2 ± 0.3 nm). The nanotube diameter obtained from TEM image analysis (2.5 ± 0.4 nm) is in agreement with AFM measurements and computer modeling (2.2 – 2.8 nm). Formation of superhelices (helices made of several helical bundles) was also observed. The helical structure of the bundles was also seen by AFM in all three imaging modes: height, amplitude and phase (Figure 4.4). The helical structure can only be revealed when using ultrahigh resolution AFM tips with a radius of curvature 1 nm. The use of regular AFM tips (radius of curvature 10 nm) does not allow for helicity to be observed, since the tip cannot penetrate the grooves of the helices. In addition the scan rate should be less than 0.5 Hz. The helical pitch was found to be dependent on the thickness of the bundle and ranges from 30 ± 5 nm for double helix (5 ± 0.6 nm thick bundle) to 150 ± 8 nm for 25 ±

3 nm thick bundle. Both right and left handed helices were observed by SEM, which is to be expected since the G^C module is achiral.

Figure 4. 4. TM-AFM height (A, C, E), amplitude (B, D, F), and phase (G) images of helical bundles assembled in water (carbon film, 1 g/L) using ultra-high resolution tips. Inset is the height profile of the double helix shown on panels E, F, and G.

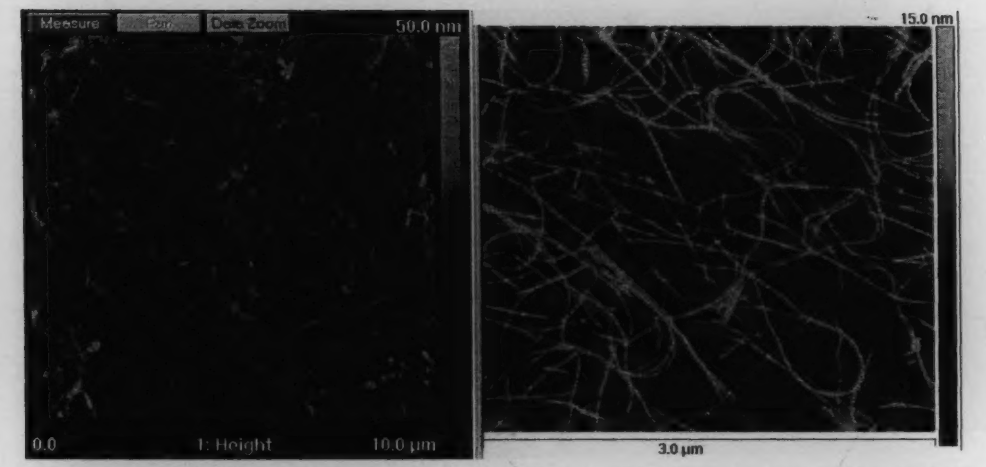

Figure 4. 5. TM-AFM height images of helical bundles assembled in water (carbon film, 1 g/L) using regular AFM tips.

To investigate the mechanism of helical bundle formation, concentration, temperature and time dependence studies were conducted. Representative SEM images of the evolution of the morphology with time at three different concentrations (0.1 g/L, 0.25 g/L, 1.0 g/L) are shown in Figures 4.6 – 4.8.

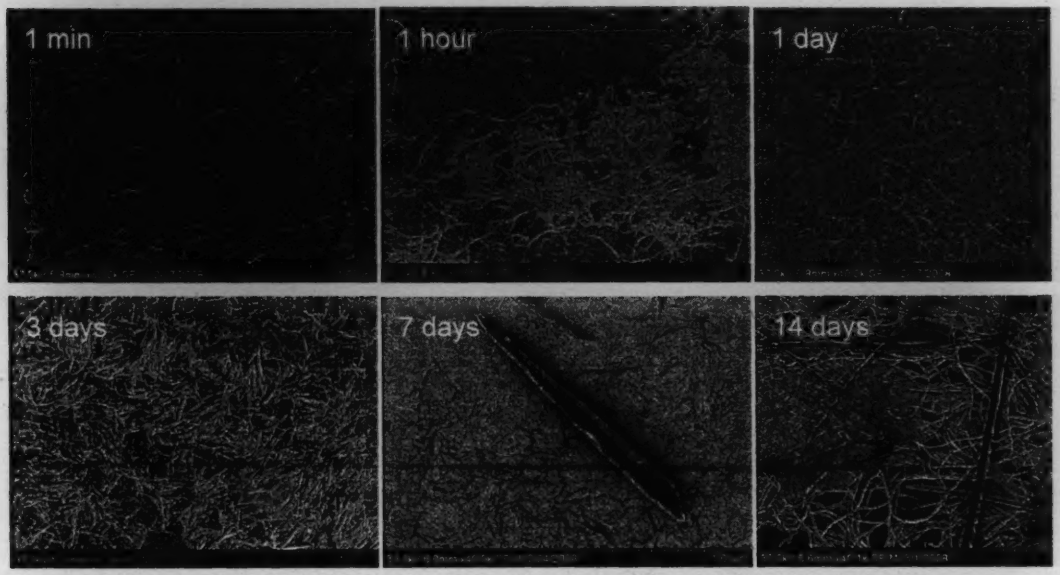

Figure 4. 6. Representative SEM images illustrating time dependence of G^C aldehyde in water (boiled, 0.1 g/L, carbon film)

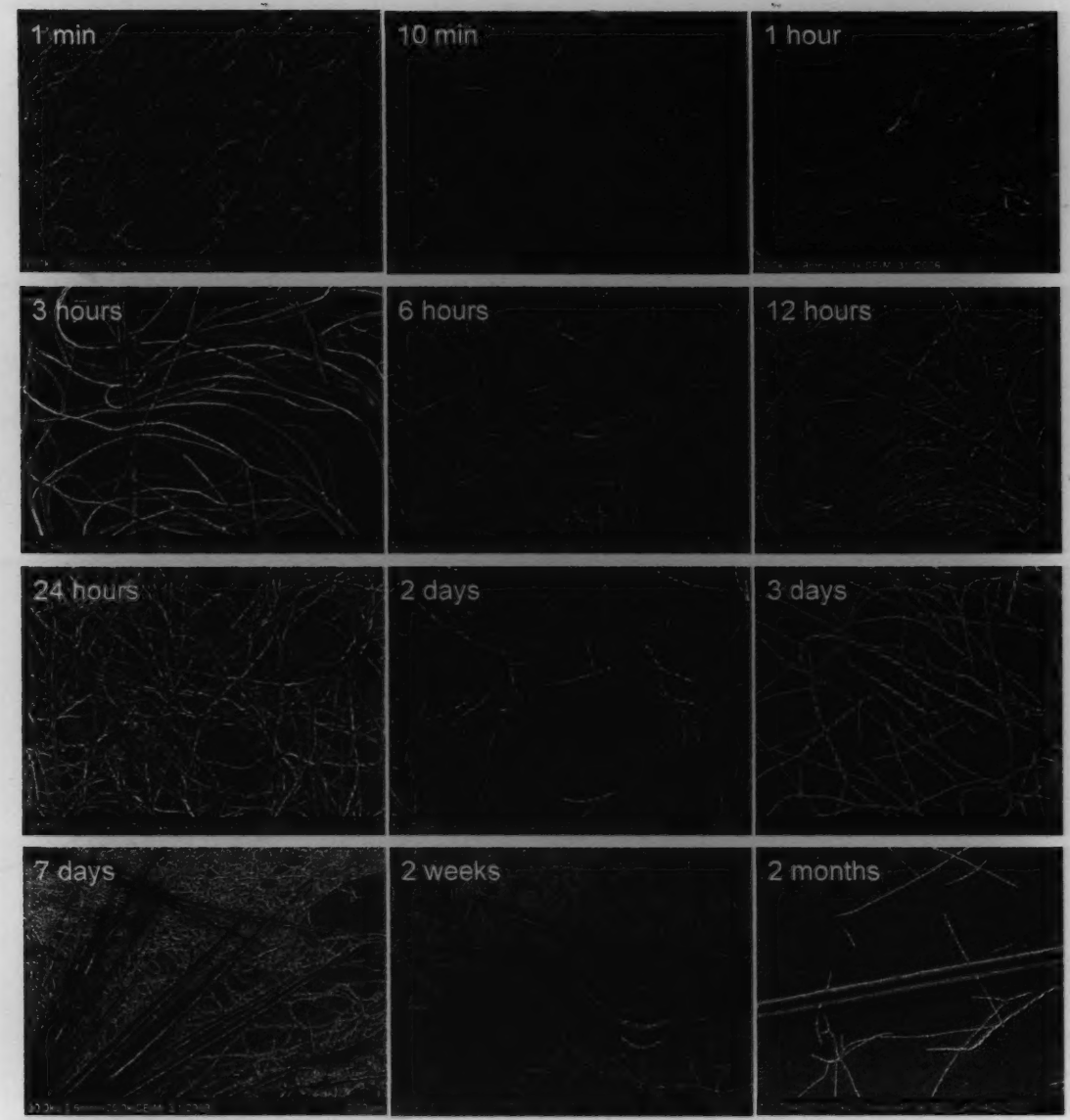

Figure 4. 7. Representative SEM images illustrating time dependence of G^C aldehyde in water (boiled, 0.25 g/L, carbon film)

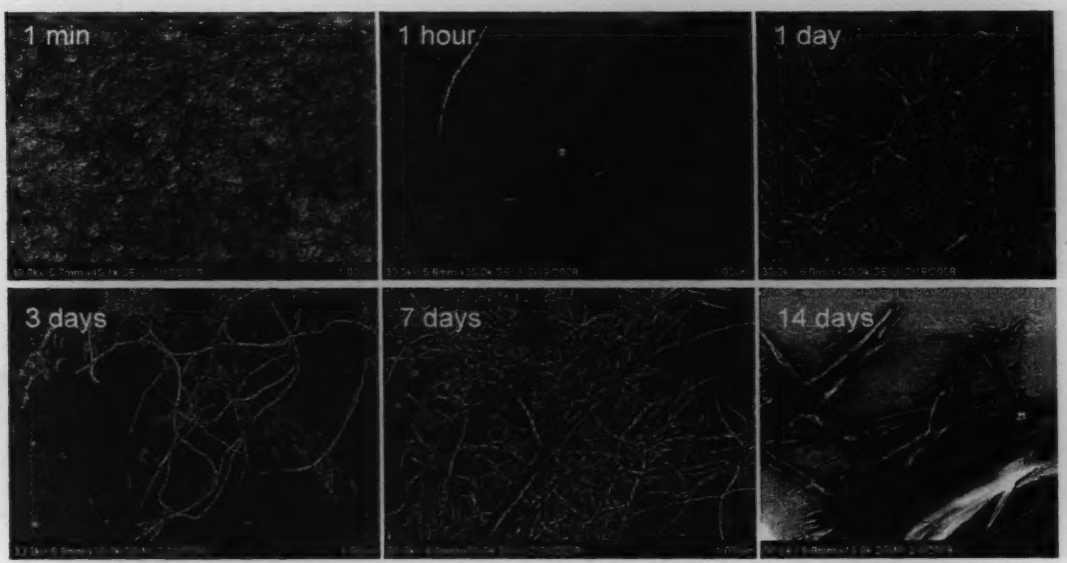

Figure 4. 8. Representative SEM images illustrating time dependence of G^C aldehyde in water (boiled, 1.0 g/L, carbon film)

As can be seen from Figures 4.6 at concentration 0.1 g/L the growth of the tubes is very slow and helical bundles are not seen till after 2 weeks of aging. Their formation is concomitant with the growth of thick nanofibers. At 0.25 g/L (Figure 4.7) the maximum accumulation of well-dispersed helical bundles is observed after three days of aging. With time, more crystalline fibers formed. The fibers further thickened and after two months became the dominant morphology coexistent with helical bundles. This suggests that the fibers form from the helical bundles. Evolution of the 1.0 g/L solution (Figure 4.8) was very similar to 0.25 g/L. Higher density of coverage and higher degree of bundling was observed for this concentration.

Heating the solution to boiling point (100°C) was shown to be crucial to the helical bundle formation. A 0.25 g/L solution that was only sonicated at room temperature showed no helical bundle formation, but only short single tubes after two weeks of aging.

Figure 4. 9. TM-AFM height images of helical bundles assembled in water (mica, 0.25 g/L aged for 2 days) using ultra sharp AFM tips.

From the time-dependence studies at 0.25 g/L, it is possible to suggest a mechanism for helix formation: (1) Single nanotubes assemble, (2) then they form ribbons of nanotubes in mono and bilayer arrangement, (3) the ribbons twist to form the helices. The fact that most of the helices are folded from mono and double layer of nanotubes was

inferred from TEM images of the helices and AFM images of the intermediate assemblies formed after two days (Figures 4.7 and 4.9). At two days, both twisted and untwisted ribbons are present. TM-AFM imaging of untwisted (flat) ribbons allowed us to measure their height, which had a bimodal distribution (76:24) with a major maximum at 2.4 ± 0.2 nm and the second one at 4.9 ± 0.5 nm. Measuring the thickness of the narrowest projection of the helical fibers by TEM gave very similar results: two populations (73:27) centered around 2.6 ± 0.3 and 5.2 ± 0.6 nm. The thickness of the ribbons corresponds to the cross-section of one or two nanotubes, which indicates that they are made of single or double ribbons of nanotubes. A very small (<5%) population of ribbons thicker than two nanotubes was observed.

Very few reports have described the formation of nanoscale helical fibers from achiral molecules with no chiral induction agents.[6, 157-161] The self-assembly of organic molecules often produces microscopic helical fibres, usually in a stereospecific way as a result of the presence of a stereogenic centre in the amphiphile.[162] Changes in morphology are often observed, from helical fibres for pure enantiomers to platelets for the racemates. However, there are notable cases where helical aggregates are formed from achiral molecules, which constitute the formation of enantiomorphic fibres. One of the most spectacular of these arises when achiral amphiphilic derivatives of the well-known melamine–barbituric acid supramolecular system are self-assembled in chloroform.

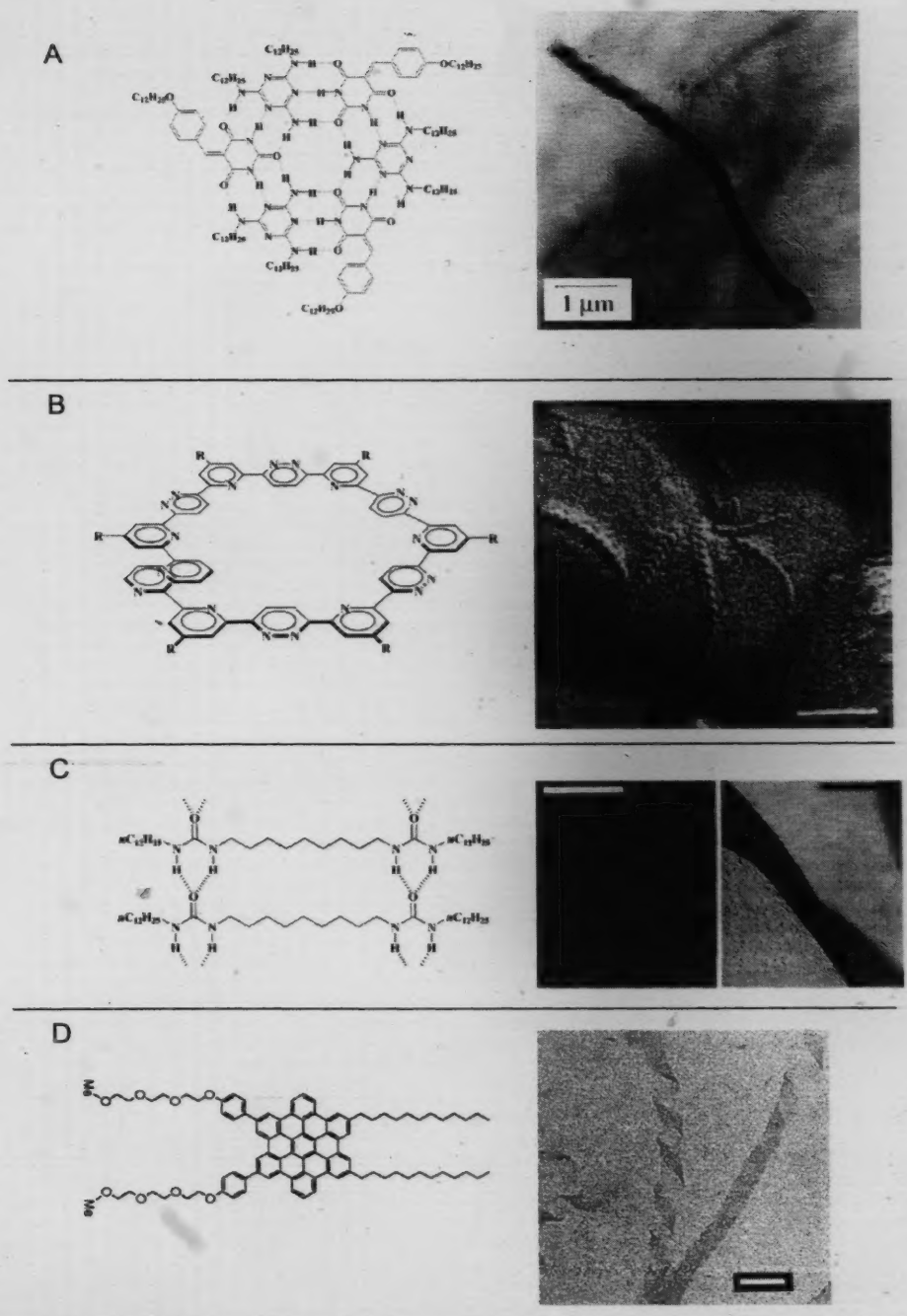

Figure 4. 10. Examples of achiral molecules assembling into helical fibers. Molecules on the left and EM pictures on the right. Adapted with permission from refs (A) 156, (B) 31, (C) 162, (D) 6.

When an equilibrated dispersion of the mixture of the two components shown in Figure 4.10A in chloroform was evaporated and stained with an ethanol/water solution of uranyl acetate, supercoiled fibers were observed by transmission electron microscopy with dimensions of approximately 10 μm length by 300 nm diameter. Both left and right-handed supercoils were observed.[157] By performing a number of control experiments, it was established that the polar solvent causes this transformation. While the exact structure of the fibers is not clear, the alkene moiety in the barbituric acid derivative makes the hexamer non-centrosymmetric, and π–π stacking does seem to be involved in supporting the chiral arrangement, which could arise from stacked discs or a helical chain.

The molecule shown in Figure 4.10B exists in a helical conformation in solution, because of the preferential *transoid* conformation of the 2,2'-bipyridine subunit. This translates into helicity on the nanometre scale.[31] The molecules aggregate through π–π stacking interactions in dichloromethane and pyridine to provide helical fibres, as observed by freeze fracture electron microscopy. The images reveal helical fibres of about 80 Å in diameter, which are "probably composed of coiled-coil bundles of two or three single supramolecular stacks".[31] In one image, produced from a dichloromethane solution, a predominance of fibers of one chirality was observed, which the authors hypothesized could arise from induction by seeds generated during the sonication process used in the preparation of the samples. More well-resolved helices, either right or left-handed, were observed when pyridine was used as a solvent.

Supramolecular sheets can also coil into helical ribbons if small distortions appear in the 2D structures. Such is the case for gels of achiral bisureas (Figure 4.10C), which form

aggregates on account of strong bifurcated hydrogen bonds between the carbonyl oxygen atom and the NH hydrogen atoms.[163] The compounds form gels in tetralin in which helically twisted fibres are observed, either right or left-handed. In butyl acetate even stronger twisting is observed. It appears that the bending in the supramolecular ribbons originates from the molecules within the sheets, which are tilted with respect to the sheet's plane.

Ribbons formed from bilayers of amphiphilic molecules (Figure 4.10D) were proposed to twist into helices due to the bending force caused by asymmetric packing of the molecules in the bilayer.[6] The asymmetric packing was proposed to be the result of offset stacking of aromatic rings due to their tendency to maximize π–π stacking interaction.

The origin of nanoscale chirality in our helical fibers should be similar to the one in melamine–barbituric acid.[157] It can be seen that stacks rotated at any angle other than 30×N degrees (where N is a natural number including 0) along the axis of the nanotube are helical. Figure 4.11 illustrates a 15° rotated arrangement of two stacks.

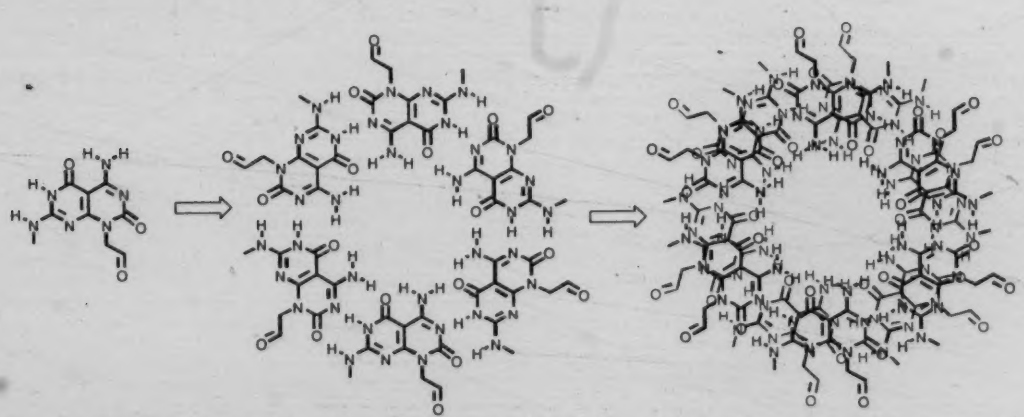

Figure 4. 11. Assembly of the rosette and its stacking at 15° turn relative to the other rosette.

It should be noted that there are two possible ways (Figure 4.12) to form helical fibers from a ribbon (platelet): via coiling (A) or twisting (B). Both types of helices were found, however helix (A) is dominant (~90% of all helices). Coiling of the helices can eventually lead to tubule formation, which was not observed in this work.

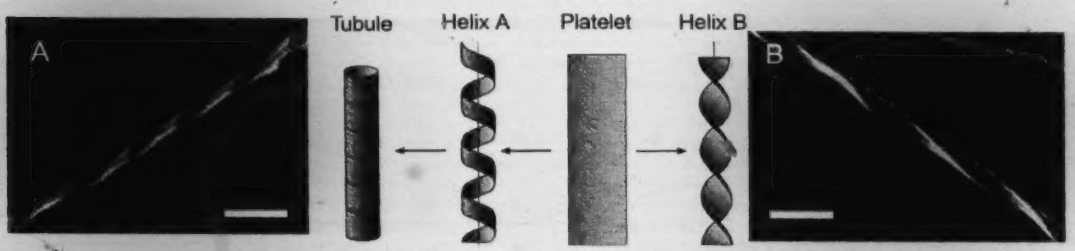

Figure 4. 12. Two types of helices observed for G^C aldehyde assemblies in water (0.25 g/L, carbon film). Scale bars are 50 nm.

It was also interesting to trace the evolution of the system after the helical fibers began to aggregate. It was noticed that parallel agglomeration of two helices leads to the helix formation with the same chirality (Figure 4.13A), while antiparallel aggregation of two helices leads to a braid-like structure (Figure 4.13B). The same was found to be true for the parallel (Figure 4.13C, D) and antiparallel (Figure 4.13E, F) agglomeration of more than two helices. Antiparallel aggregation here leads to a superribbon made of several helices. Interestingly these "superribbons" do not twist into "superhelices".

When a solution of helical bundles is allowed to age for over two weeks a white precipitate forms. SEM of this suspension showed the presence of large (up to 40 μm) platelets along with helical bundles (Figure 4.14). In fact some helical bundles appeared to be an integral part of the platelets as they seemed to protrude from them. TEM imaging of unstained and stained samples of the platelets did not allow resolving individual nanotubes in their structure. This could be due a very dense packing of nanotubes in the

platelets. The crystallinity of the platelets was confirmed by performing SAED on individual platelets (Figure 4.14G). The fact that the SAED pattern does not show ring but rather a spot structure indicates that the platelets are single crystals. Powder XRD on the platelets (Figure 4.15) also showed that they are crystalline. Comparison of the powder XRD patterns for G^C aldehyde before and after self-assembly revealed significant differences, which reflects substantial reorganization during self-assembly. The platelets obtained after self-assembly appear to be more crystalline than the bulk G^C aldehyde obtained after final deprotection.

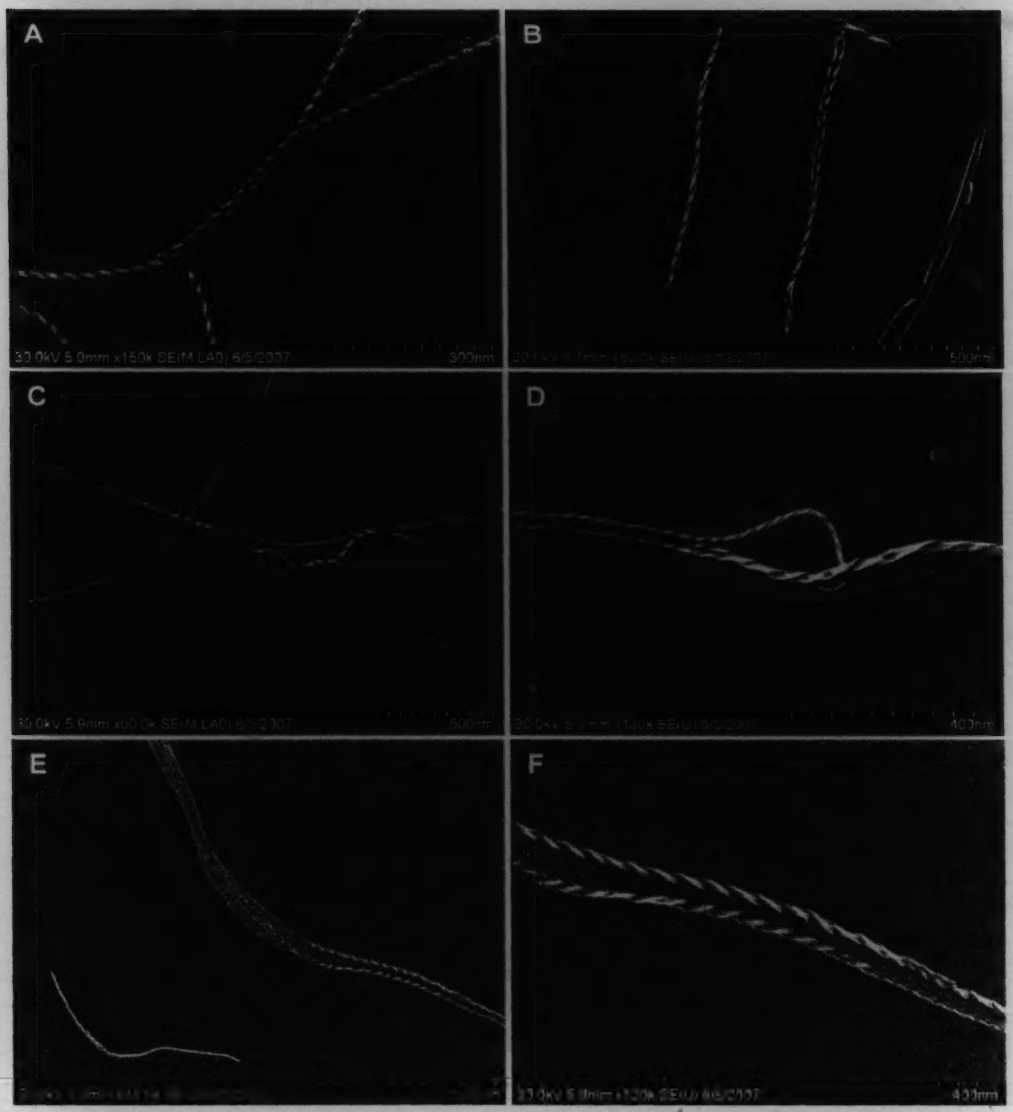

Figure 4. 13. SEM images of various aggregates formed from helical bundles (0.25 g/L, carbon film).

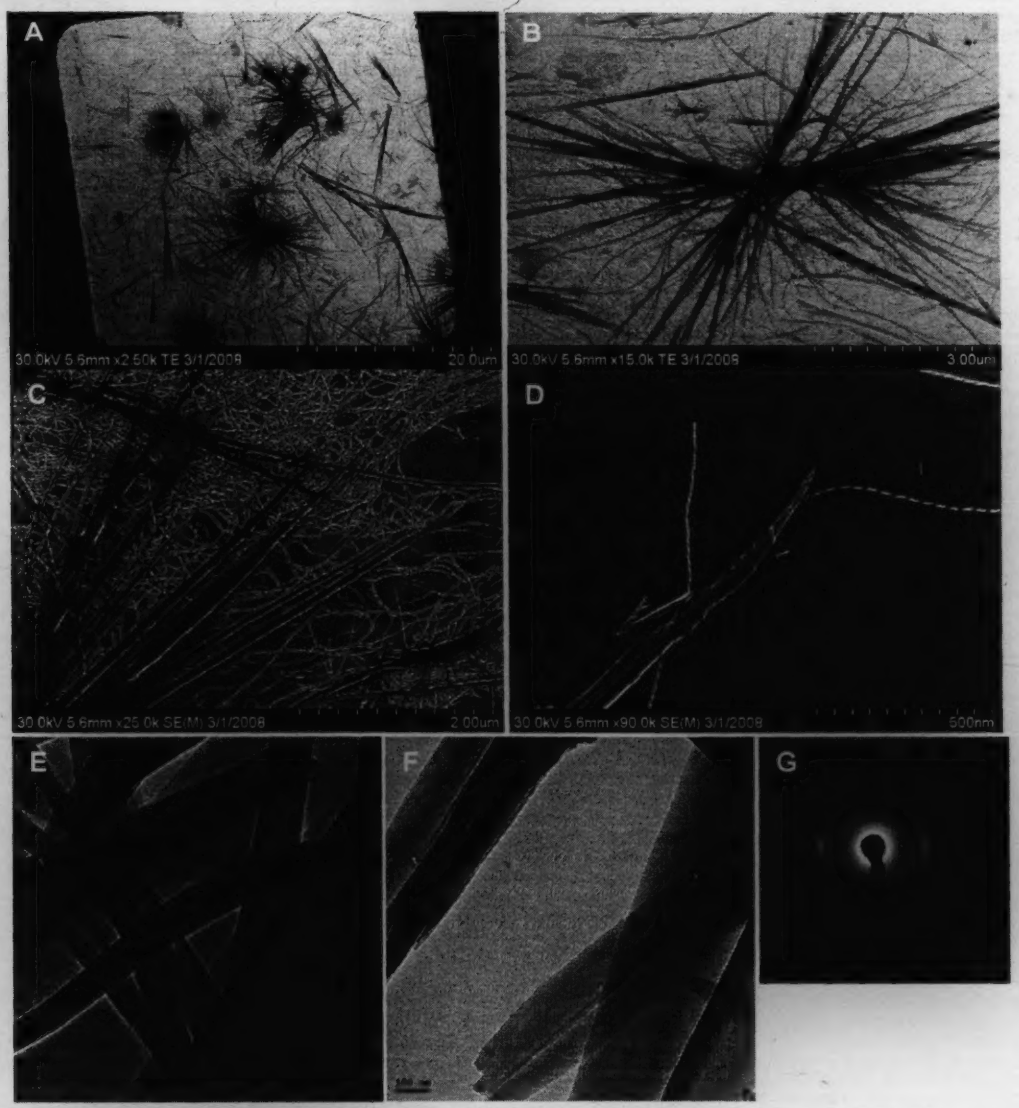

Figure 4. 14. SEM (A–D), TEM (E, F) images of platelets formed from G^C aldehyde (0.25 g/L, carbon film, two weeks) and SAED of individual platelet (G).

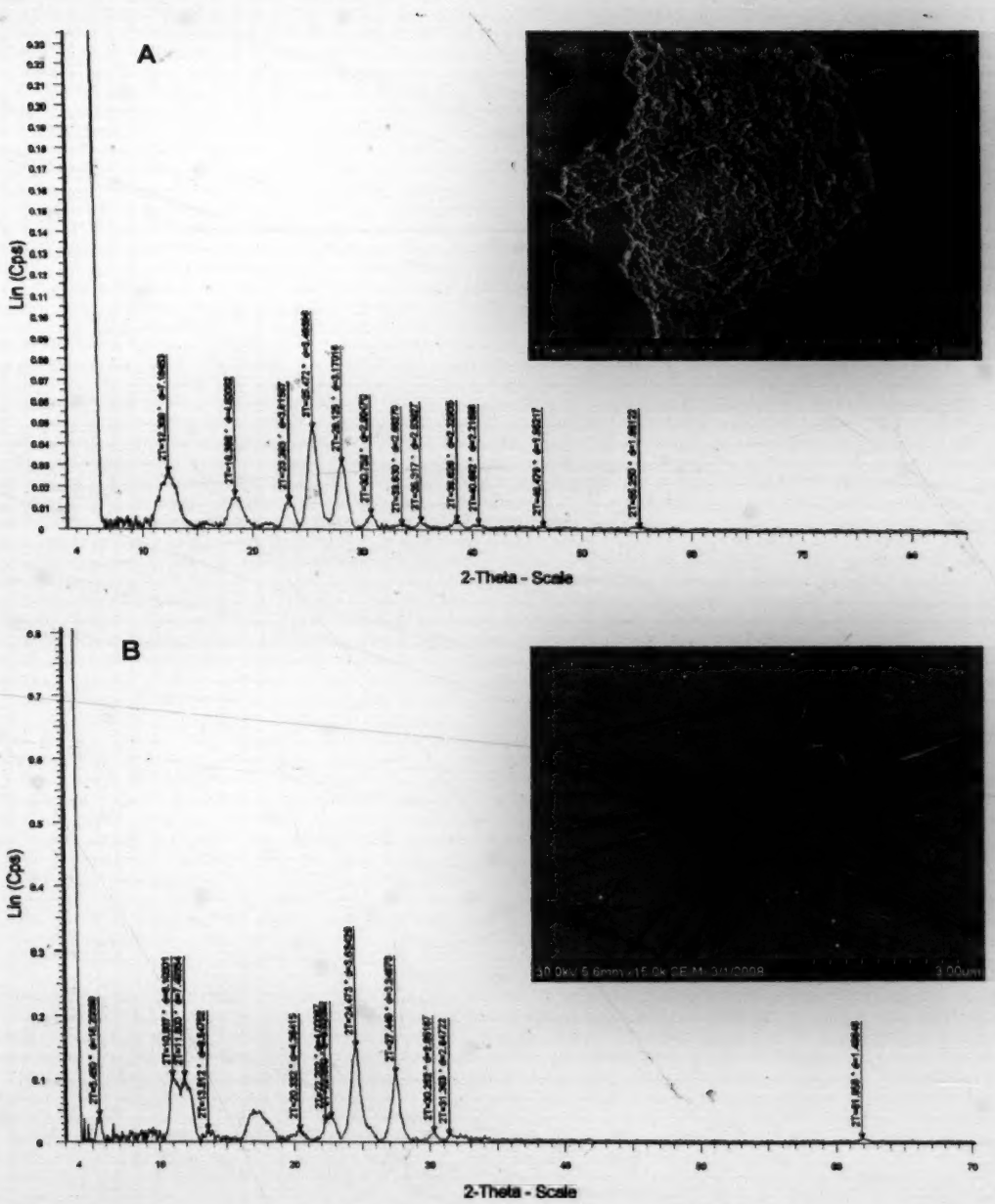

Figure 4. 15. Powder XRD and corresponding SEM images of G^C aldehyde before (A) and after (B) self-assembly.

These observations suggest that RNTs can one day yield single crystals suitable for single crystal X-ray analysis. It should be noted that crystals with sizes up to 1 mm (Figure 4.16) were grown from G^C allyl compound **2-2** (Chapter 3). It is not clear however if these tubes are made of nanotubes since they were grown in concentrated HCl. Obtaining high quality powder XRD pattern using synchrotron radiation along with modeling studies and powder XRD prediction should allow for additional insight into the atomic structure of G^C assemblies.

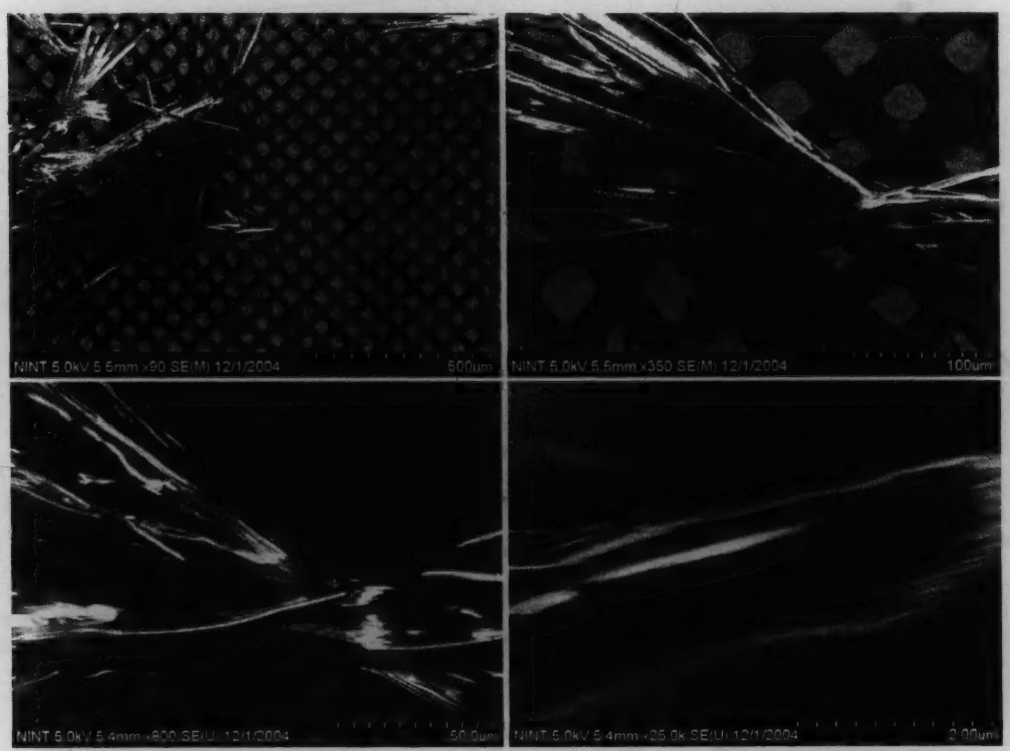

Figure 4. 16. Crystals grown from 2-2 in concentrated aqueous HCl.

4.4. Electroless silver deposition on RNTs helical bundles

The reaction of silver nitrate with helical bundles was studied in a systematic fashion. It was necessary to select the parameters that most likely have substantial impact on the morphology of the Ag/RNTs composites: concentrations of G^C module, concentration of silver nitrate, premixing times (time that organic tubes are allowed to equilibrate after preparation of the solution before mixing with silver nitrate), temperature, time of heating and additives (e.g. surfactants). Each aldehyde group provides two electrons to reduce two silver cations to the metallic state. The matrix shown in Table 4.1. was designed: RNTs concentrations are in the top row (0.01 – 0.25 g/L, all samples are assembled at 0.25 g/L for 2 days and then diluted to the indicated concentration). The aldehyde/$AgNO_3$ ratios are in the first column (1:2 – 1:100). The numbers in the cells are just the names given to the samples.

Table 4. 1. Concentration of the G^C aldehyde (columns) and ratios of aldehyde/$AgNO_3$ used for silver deposition studies.

	0.25	***0.1***	***0.05***	***0.01***
1:2	M11	M12	M13	M14
1:8	M21	M22	M23	M24
1:50	M31	M32	M33	M34
1:100	M41	M42	M43	M44

To keep reaction volumes constant, 16 silver nitrate solutions with different concentrations were used. The solutions were sonicated for one minute, heated in a water bath at 80°C for 2 hours, and then allowed to age at room temperature for one week. Representative images from these of the experiments (Table 4.1) are shown in Figures 4.17 – 4.19. M(k,l) denotes which conditions listed in the matrix were used.

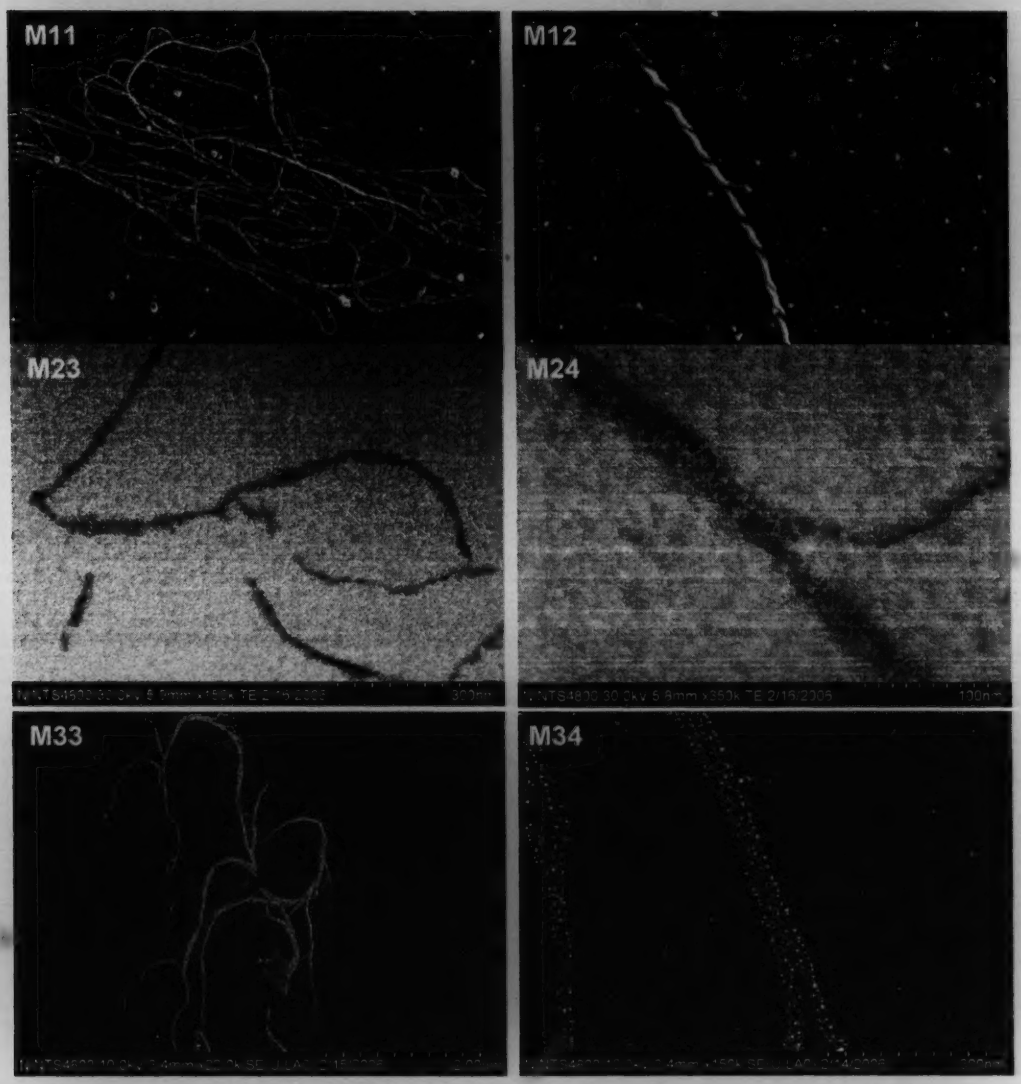

Figure 4. 17. Representative SEM images of nanotube bundles coated with silver.

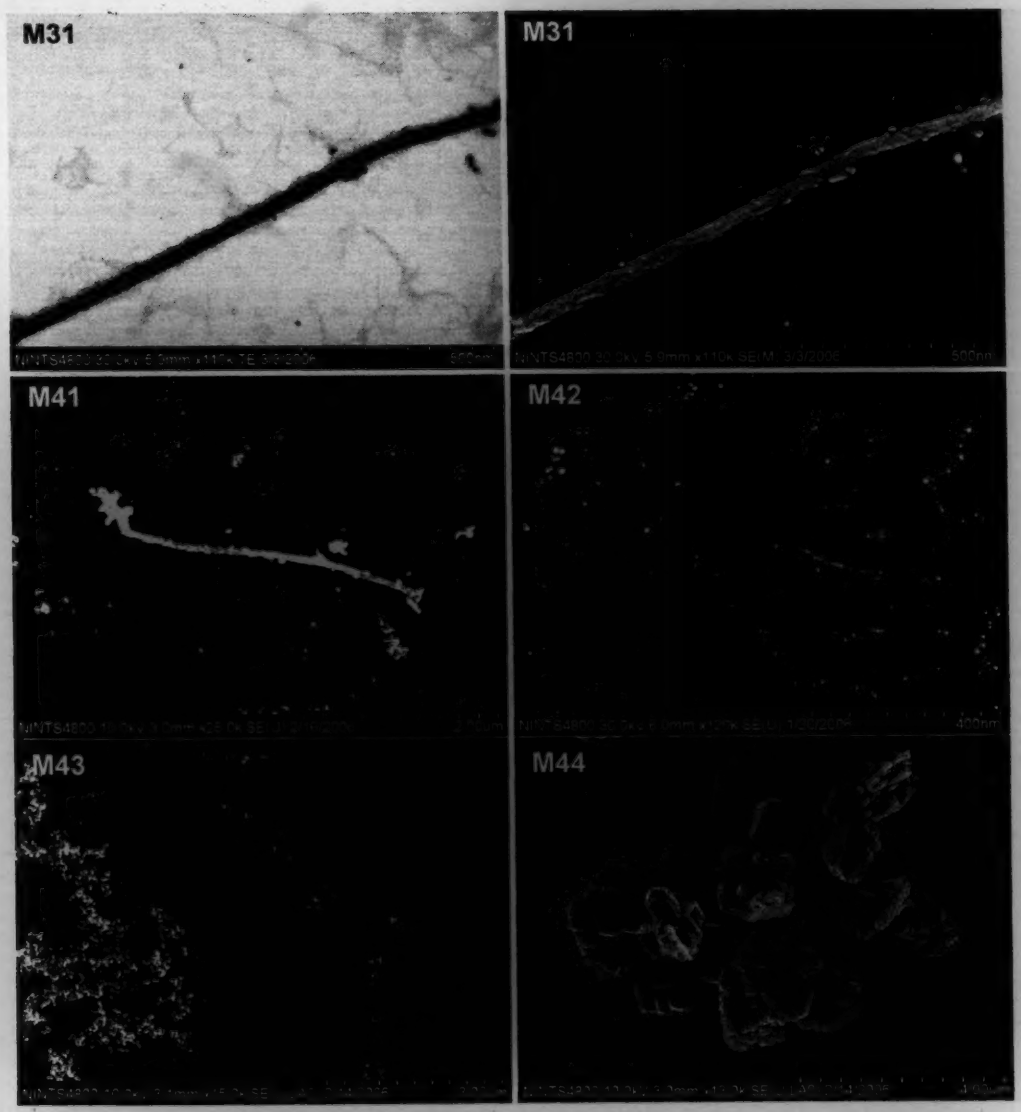

Figure 4. 18. Representative SEM images of nanotube bundles coated with silver.

It is apparent from the SEM images that only at low aldehyde/silver ratios is the helicity of the bundles preserved. However, it was not possible to see how well the bundles were coated under those conditions, and therefore TEM was used for imaging (Figure 4.20).

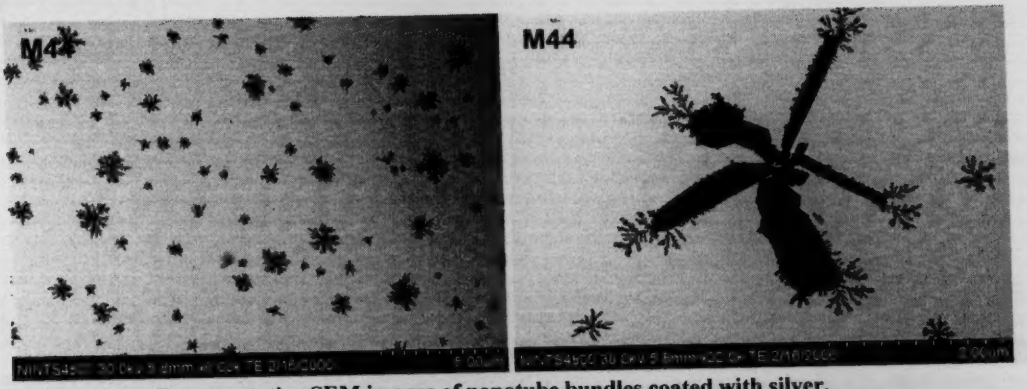

Figure 4. 19. Representative SEM images of nanotube bundles coated with silver.

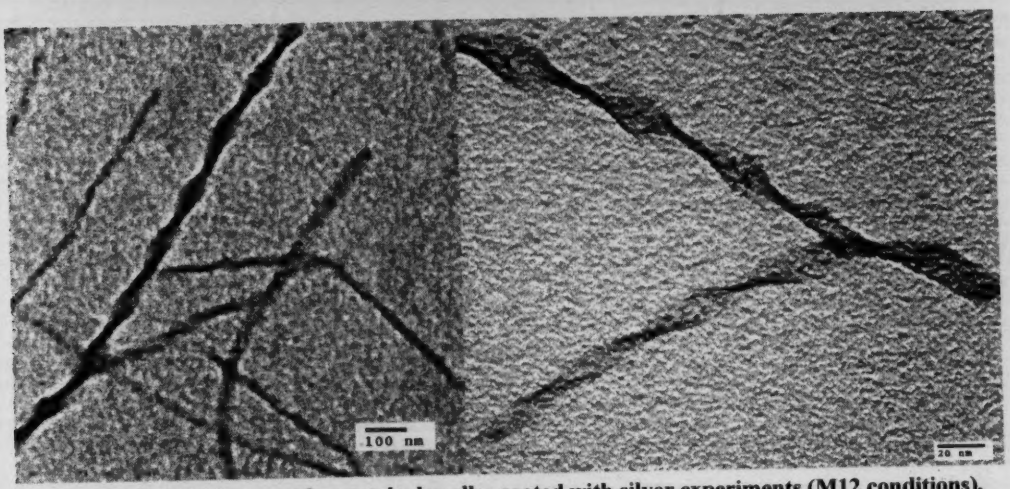

Figure 4. 20. TEM images of nanotube bundles coated with silver experiments (M12 conditions).

Very small (3.6 ± 0.8 nm) nanoparticles can be seen coating the helical bundles (Figure 4.20). The interparticle distance was several nanometers, so there was no continuous plating of the bundles. When the Ag/aldehyde ratio was increased, the size of the nanoparticles increased but not their density on the bundles. Besides, the bundles were no longer helical. At very high Ag/aldehyde ratios, silver metal nanoclusters of fractal nature were observed with no trace of RNT bundles. Longer than one week reaction times have also resulted in larger silver particles (Figure 4.19).

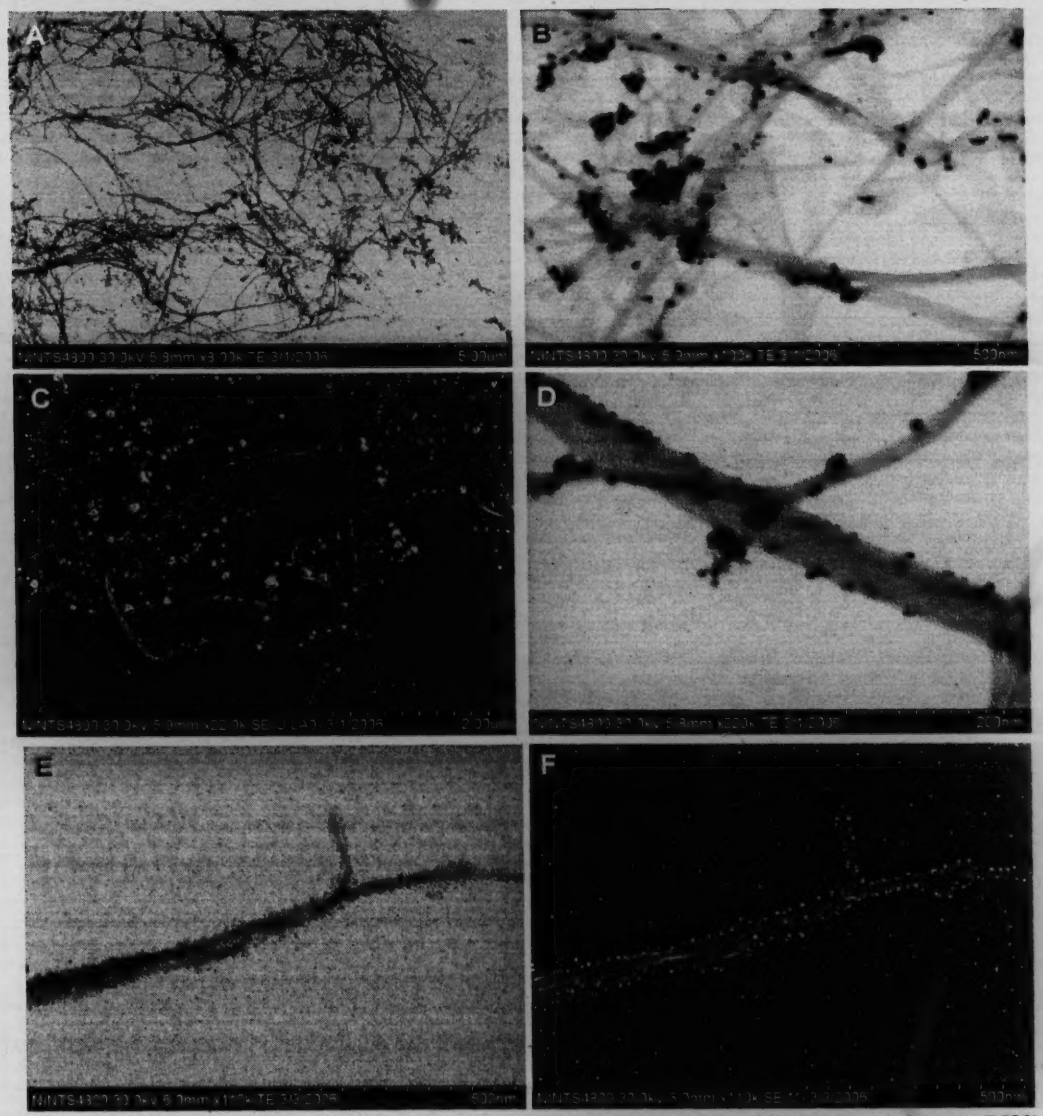

Figure 4. 21. Representative SEM images of nanotube bundles coating with silver experiments (M33) using three weeks aging time (A, B), four weeks aging time (C, D), using TBAF (E, F)

Attempts to use tetrabutylammonium fluoride[164] to control the size and polydispersity of Ag nanoparticles did yield smaller nanoparticles with higher size uniformity. However, coating of the bundles was still not continuous and large amounts of free nanoparticles were observed.

Bundles obtained in conditions M12 (Table 4.1) were studied by EDX, XPS (Figure 4.23), and SAED (Figure 4.22 and Table 4.2) in addition to SEM (Figure 4.17) and TEM (Figure 4.20).

Figure 4. 22. SAED pattern obtained for silver coated RNTs bundles (M12).

Table 4. 2. Selected area electron diffraction data assignment for silver coated RNTs. Literature data are for silver metal with f.c.c. crystal structure and lattice parameter a0 = 4.0862 Å.

Literature[161]		Experimental		hkl assigned
d spacing (Å)	ratio	d spacing (Å)	ratio	
2.359	1.00	2.31	1.00	111
2.044	1.15	2.02	1.14	002
1.445	1.63	1.42	1.62	022
1.231	1.91	1.22	1.89	113
0.914	2.58	0.90	2.56	024
0.834	2.83	0.81	2.85	224
0.691	3.41	0.68	3.40	135

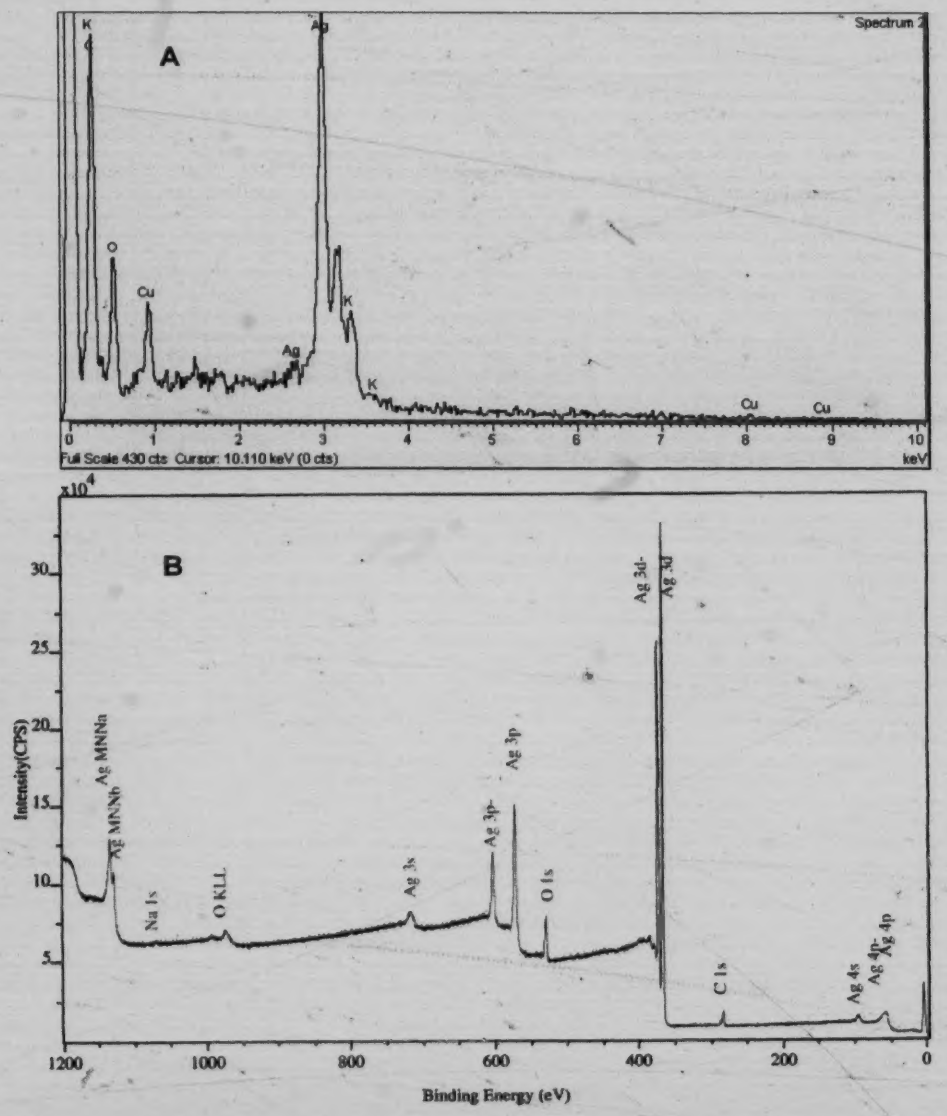

Figure 4. 23. EDX (A) and XPS (B) of silver coated RNTs obtained under conditions M12. Copper peak in EDX comes from the TEM grid that was used as a substrate. Potassium comes from contamination present in the instrument.

Large (up to 10 μm) crystals were observed in control experiments when silver nitrate solutions were subjected to the above procedure in the absence of RNTs.

It is worth mentioning that the area selected for SAED was about 0.8 μm^2, since smaller objective apertures or/and higher magnifications did not allow collecting enough signal to see distinct circular diffraction patterns. Relatively high area of diffraction however may include particles that are not attached to the nanotubes. Spot SAED pattern indicates that particles coating the bundles are single crystalline. EDX analysis was done on Hitachi 4800 equipped with EDX detector. The area analyzed was ~ 2 μm^2. XPS instrument probe diameter is 30 μm, so in this case the representative signal from a large area of the sample was collected. Detailed analysis of the XPS data indicates that most of the sample (>90%) consists of Ag(0), the remaining silver is Ag(+1) and Ag(+2). The presence of Ag(+1) and Ag(+2), likely in the form of Ag_2O and AgO, can be expected due to surface oxidation of silver nanoparticles by atmospheric oxygen.

Even though the coverage of the bundles with silver is far from continuous, it is still more uniform than previously reported systems (Figure 4.24).

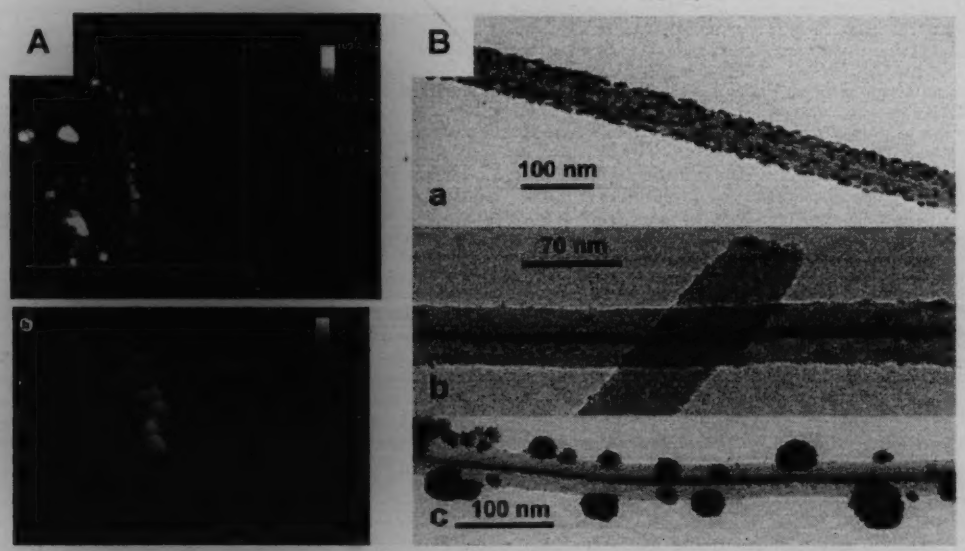

Figure 4. 24. Nanoparticles distribution along silver coated DNA (A),[85] and platinum coated porphyrin nanotubes (B).[83] Adapted with permission from refs 164 and 165. Copyright 1994 Macmillan Publishers Ltd and 2004 American Chemical Society.

The more even distribution of silver on the RNT walls most likely arises from the improved strategy of plating developed here. The literature strategies involve two steps and two reagents with metal ions adhering to the surface of a nanostructure followed by addition of a reducing agent.[83, 85] It should be noted that idea of using an aldehyde group belongs to Braun et al.[85] However they had to use an external reducing agent after initial seeding of Ag nanoparticles on DNA template. Our methodology does not require the addition of an external reducing agent, since the templating nanostructure itself (RNTs) acts as a reducing agent. That makes for even distribution of the silver metal along the nanostructure, along with the fact that aldehyde groups are positioned very close to each other (30 groups per period of 3Å between rosettes stacks in a five tube bundle). During the reaction with silver salt, numerous closely positioned nucleation sites create a stable shell in which the RNTs are encapsulated. This is in contrast with methods described in literature whereby widely separated nucleation sites are fed with an excess of metal ions and reducing agent, thereby promoting growth of an array of larger metal clusters.

Interestingly when high concentrations of the aldehyde and silver were used (M41, Table 4.1), thick (30 – 300 nm) and up to 50 μm long silver nanowires were found in the solution cast on a TEM grid after two months of aging (Figure 4.25). EDX of the nanowires showed that they are made mostly of silver. The metal coating appears to be continuous: no single nanoparticles were found by S(T)EM imaging. Although the mechanism of the nanowire formation is unclear, it appears from some HRSEM images that the wires are made of rolled up sheets. The sheets are most likely RNTs monolayers plated with silver. The presence of large amounts of amorphous material suggests that most of the G^C aldehyde served as a reducing agent and did not assemble.

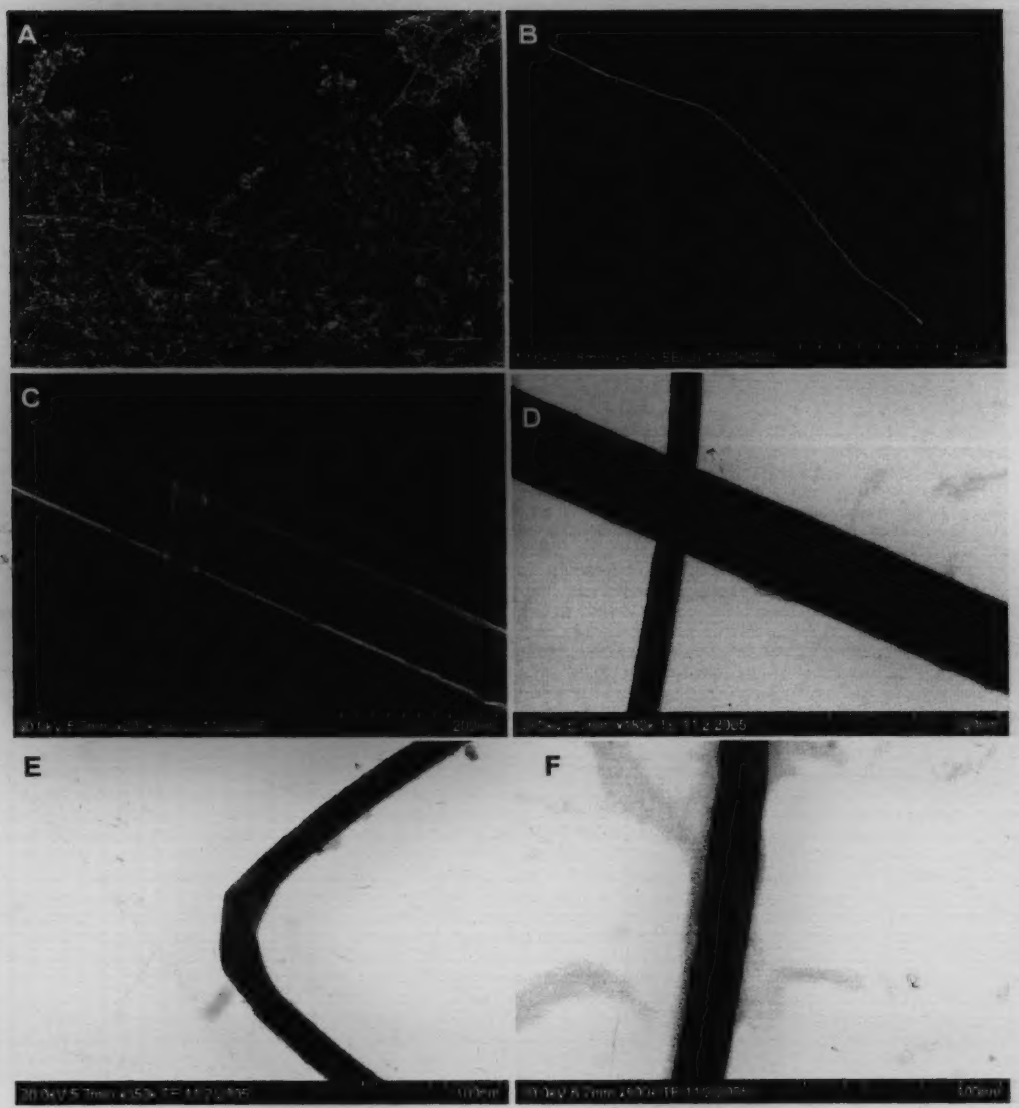

Figure 4. 25. Silver nanowires obtained at M41 conditions after two months.

4.5. Conductivity measurements

Attempts to measure conductivity of helical bundles and the corresponding silver-coated material were made on two types of electronic circuits. The first was an array of interdigitated electrodes coated with helical RNTs bundles and the second was an array of individual electrodes coated with silver nanowires.

The array of interdigitated gold electrodes was fabricated using conventional photolithography on silicon substrates.[165] The smallest gap between electrodes that was achieved by such fabrication was 2.5 μm. A solution of nanotubes (0.1 g/L) was spin cast on the electrode array. Very little contrast was observed (Figure 4.26), since organic nanotubes have much lower electron scattering ability compared to gold or silicon. Due to the large gap between electrodes, no single helices were found to bridge the gap between them. Therefore, this design was unsuitable for the conductivity measurements.

An array of individual chromium/titanium electrodes on silicon was then fabricated by an optimized photolithography procedure.[166] Thick silver nanowires were drop cast on the device. Very much improved contrast in SEM allowed for facile imaging of such devices. In order to find an individual nanowire lying across electrodes ~1500 devices were imaged using SEM. Four devices that have single silver nanowire linking two adjacent electrodes were found (Figure 4.27).

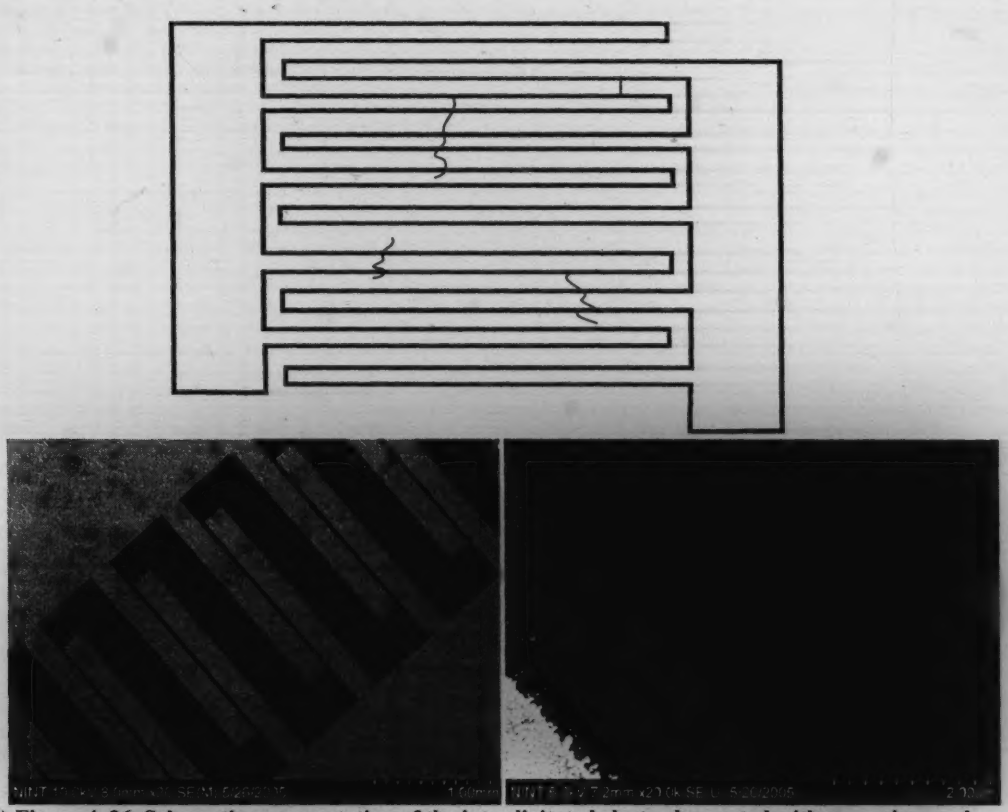

Figure 4. 26. Schematic representation of the interdigitated electrodes coated with nanowires and SEM images of actual device fabricated.

The conductivity of four junctions found was measured using NanoFab probe station and Keithley 2400 picoampermeter. Only one (Figure 4.27D) of the devices was conductive. The resistance of the thickest wire was of 54 Ohm which was 8% of the value expected for continuous silver wire 90 nm in diameter and 2.7 μm in length (measured from SEM, Figure 4.27D). This is most likely due to the fact that the nanowire is made of both metallic silver and organic material. In addition, the contacts between the nanowire and the chromium electrodes, very likely have a substantial resistance.

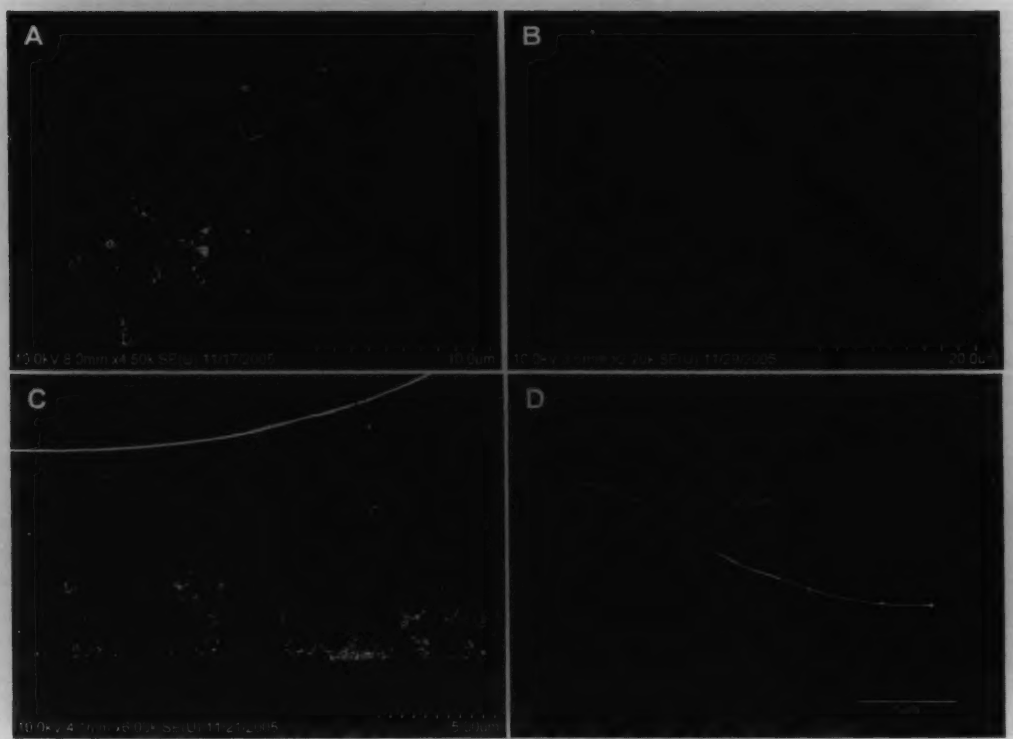

Figure 4. 27. SEM images of four devices based on individual electrodes design.

4.6. Optical enhancing properties of silver coated RNTs bundles

Silver nanoparticles are known to enhance the Raman signal of molecules absorbed on their surface due to their plasmon resonance.[167] The potential of the silver nanoparticles arrays assembled on RNTs for surface enhanced Raman spectroscopy (SERS) was explored here.

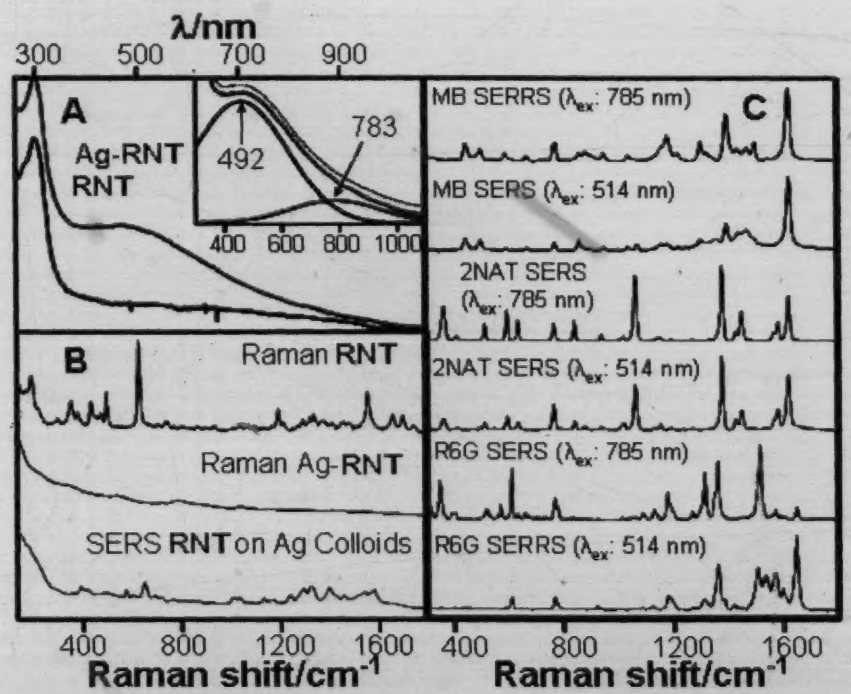

Figure 4. 28. (A) Electronic spectroscopy of RNTs and Ag-RNT (RNTs coated with silver). Inset shows the deconvolution result for longitudinal and transversal plasmons. (B) Raman and SERS (obtained on silver colloids) spectra of HRN and the SERS spectrum of the silver coated RNTs (λ_{ex}: 785 nm). (C) SERS and SERRS spectra of methylene blue (MB), 2-naphthalenethiol (2NAT) and rhodamine 6G (R6G) (10^{-7} M) on Ag-RNTs. (3 accumulations with integration times of 10 s)

Silver nanoparticles (Figure 4.17) synthesized in experiment M24 (Table 4.1) were chosen since they gave the most uniform coating of the nanotubes with nanoparticles. Electronic spectroscopy (Fig 4.28A) also confirmed the metallic nature of the silver coating. Ag-RNT (silver coated RNT) bundles presented a localized resonance plasmon around 470 nm. Deconvolution of the plasmon absorption (inset Fig 4.28A), showed the

presence of two bands, characteristic of nanowires, that may be attributed to both longitudinal (783 nm) and transversal (492 nm) plasmonic excitations.[168] Both plasmons are red-shifted compared with others described in the literature.[169] The longitudinal plasmon shift is likely due to the coupling of the plasmons of the nanoparticles along the RNT bundles, which is also supported by the intensity ratio of transversal to longitudinal plasmonic modes (inset Fig 4.28A). On the other hand, transversal mode shift is likely due to two factors: (a) the phase retardation effect because the different core:shell (Ag:RNT) dielectric constants;[170] and, (b) the aggregation effect on the wires because of the formation of bundles.[171]

Fig 4.28B shows Raman and SERS (obtained on silver colloids) spectra of RNTs and the SERS spectrum of the composite nanotube bundles. Raman of RNTs is mainly characterized by the in-plane stretching and deformation modes, especially by the ring stretching (1552 cm^{-1}) and ring breathing (625 cm^{-1}) vibrations. SERS spectrum with silver colloids is characterized by a strong enhancement in the ring breathing mode, shifted to 648 cm^{-1}, and N-C stretchings in the ring (1578, 1395 and 1320 cm^{-1}). It is also remarkable that the band at 1655 cm^{-1}, which may be related to the aliphatic carbonyl stretching mode, is enhanced, thus revealing some close interaction between the functional group and the silver surface. Notably, the spectrum of RNTs disappears after coating with silver. This phenomenon has been previously reported in metal-coated organic nanotubes, and it has been explained based on the strong confinement of the organic material by the hard metal shell, inhibiting the vibrational modes of the core material.[172] In this regard, the composite material Ag-RNTs provides a suitable and clean substrate for SERS studies of other analytes. To test the enhanced Raman activity, 10 μL

of diluted solutions of methylene blue (MB), 2-naphthalenethiol (2NAT) and rhodamine 6G (R6G) were added to 1 mL of aqueous colloidal suspension of Ag-RNTs (0.1 g/L) reaching a final concentration of 10^{-7} M for MB and R6G and 10^{-6} M for 2NAT. Then, known volumes (20 μL) of the Ag-RNT suspensions were cast onto 10 mm^2 (10^7 μm^2) areas of a glass slide and air-dried. Sections of the surface covered by the solution (~1 μm^2, ~2×10^4 and ~2×10^5 molecules/μm^2 for R6G and MB, and 2NAT respectively) were excited with 514 and 785 nm laser lines to gather the inelastic scattering in backscattering collection geometry. Surface enhanced spectra of the analytes are shown in Fig 4.28C. SERS vibrational mode assignments of these molecules can be found elsewhere.[173] R6G and MB, both with absorption profiles in the visible, show SERRS phenomena with 514 and 785 nm, respectively. 2NAT, as a representative of a non absorbing molecule in the visible spectral region shows only SERS since none of the excitation lines are in resonance with the observed electronic transitions of the molecule.

SERS and SERRS spectra of the three analytes show excellent signal to noise ratio. However, contrary to Moskovits' group recent report, where hot spots are produced by exciting the longitudinal plasmon of silver wire bundles,[174] the excitation of the longitudinal plasmon is very unlikely considering the non-continuous nature of the Ag-RNTs bundles. Moreover, bearing in mind the shape and size of the nanobundles, local field perpendicular to the long axes of the tube bundles is more probable to be responsible for the large enhancement of the Raman signal. This suggests the formation of high electromagnetic fields due to the coupling of the transversal plasmons of different nanoparticle arrays along the bundles. Thus silver coated RNT bundles provide an excellent and clean substrate for trace analysis by means of SERS.

4.7. Conclusions

A G^C molecule with an aldehyde functional group capable of reducing silver ions was designed and synthesized. Its assembly in water yielded unexpected helical RNT bundles. The assembly conditions were optimized to maximize the yield of helical bundles versus nonhelical. The structure of the helical bundles was studied in detail by SEM, TEM, and AFM techniques.

Plating of helical nanotube bundles with metal using silver nitrate was studied at various RNT concentration and RNT/Ag ratios. As RNT/Ag ratio increases, three major metal-RNT composite morphologies were obtained: a) helical RNT bundles sparsely coated with silver nanoparticles, b) non-helical RNT bundles with higher but still not continuous arrays of silver nanoparticles and c) thick (up to 300 nm) composites featuring a continuous array of metallic silver around a RNT bundle core. In addition to SEM, TEM, and AFM, the RNT/Ag composites were characterized by EDX, XPS and SAED which allowed for the metal component to be analyzed in detail. An improved metal coating strategy that combines a template and a reducing agent in one functional group expressed on the outside walls of nanotubes was developed here. This allowed for a more continuous metal coating of organic nanostructures compared to examples reported in the literature.

A nanocircuit featuring thick nanowires lying across two metal electrodes was fabricated using photolithography and random deposition techniques. The resistance of a single RNT/Ag nanowire (lengh = 2.7 μm, diameter = 90 nm) was measured to be 54 Ohm which is high for such a composite material.

SERS of nanowires was investigated. RNT/Ag composites were found to be an excellent substrate SERS detection providing up to 10^5 enhancement of Raman signal for a set of standard analytes.

Future directions may include organization of semiconductor nanoparticles using e.g. thiol functionalized nanotubes. Better integration of the nanotubes into conductive circuits should be developed. This could be achieved by using electric field, self-propelled drop based nano/micro fluidic systems, or nanomanipulation. Also it would be interesting to perform metal plating on various nanotube morphologies generated as described in Chapter 3. For that, an accessible formyl group should be integrated into the alkyl side chain of the G^C motif or obtained by simply oxidizing the allyl groups of compounds **1c-f** (Chapter 3).

4.8. Experimental part

Instruments

Chemicals were obtained from Aldrich, Fluka and used as received, unless otherwise specified. Column chromatography and TLC was performed with Merck silica gel 60 (70 -230 mesh). ^{1}H NMR and ^{13}C NMR spectra were recorded on a Varian Inova 300, 400, 600 with use of solvent proton or carbon signal as an internal standard.

Mass spectrometric analysis was performed by positive mode electrospray ionization on either a Micromass ZabSpec Hybride Sector-TOF or a PerSeptive Biosystems Mariner Biospectrometry Workstation. A suitable liquid carrier solution was infused into the electrospray source by means of syringe pump at a flow rate of 15 μL/minute. A small amount of the sample, enough to produce a concentration in the low nanogram/μL range, was dissolved in the same solution and introduced via a 1 or 2 μL-loop-injector. Prepurified nitrogen was used as a spray pneumatic aid and bath gas.

Samples for transmission electron microscopy (TEM) and scanning electron microscopy (SEM) were prepared by placing a carbon-coated 400-mesh copper grid on a 1 mg/mL- droplet of RNs solution for 25 s. The sample was stained by placing the grid on a droplet of 1% water solution of uranyl acetate for 20 s. The grid was then blotted and dried under air. TEM images were obtained with a JEOL 2010 microscope working at 200 kV. SEM images were obtained using Hitachi S-4800 scanning electron microscope. XPS analysis was done using Axis 165 X-ray Photoelectron Spectrometer.

Samples for atomic force microscopy (AFM) were prepared in a Class 10000 Clean Room by casting a 25 μL drop on 10×10 mm^2 freshly peeled Mica grade V-4 (SPI supplies) substrates on a Cookson G3-8 Desk-Top Precision Spin Coating System. All AFM measurements were performed using a Dimensions 3100 Nanoman (E scanner,

Nanoscope VI, Digital Instruments, Veeco Instruments) in tapping mode (TM-AFM). All samples were scanned at 2Hz per line. We used silicon cantilevers (NSC 15, MikroMasch USA, Inc.) with spring constants of 40 N/m.

Electrodes arrays were fabricated at Nanofab facilities at the University of Alberta using standard optical lithography equipment.

Conductivity was performed using Wentworth probe station and Keithley 2400 picoampermeter in class 1000 clean room of University of Alberta Nanofab.

Localized surface plasmon resonances (LSPR) of Ag-HRN and absorption bands of HRN, rhodamine 6G (R6G), 2-naphthalenethiol (2NAT) and methylene blue (MB) were recorded in transmission mode in a Waters UV-visible spectrophotometer.

All the vibrational experiments (Raman and surface-enhanced Raman scattering, SERS) were carried out with 514 (argon ion) and 780 nm (diode) excitation laser lines. The inelastic scattered radiation was collected with a Renishaw Invia system equipped with a CCD detector and an optical microscope. Spectra were collected in Renishaw continuous mode with accumulation times of 10 seconds. All measurements were made in a backscattering geometry using a 50x microscope objective with a NA value of 0.75, providing scattering areas of ~1 μm^2. Power at the sample was varied between 5.4 mW and 1 μW.

Raman spectra of the analytes were directly recorded from the bulk material. Samples for SERS were prepared adding 10 μL of diluted solutions of R6G, 2NAT and MB to 1 mL of Ag-HRN colloidal aqueous (0.1 g/L) suspension. After 12 hours (allowing for the chemisorption reaction to be completed) 20 μL of these colloidal solutions were then cast onto 10 mm^2 (107 μm^2) areas of a glass slide (7059 Corning) and air-dried. The surfaces

were then studied with both laser lines (514 and 780 nm). To correct for any variation of the SERS intensity not due to the enhancement by the substrate, the 520 cm^{-1} phonon mode of silicon was used as an intensity standard.

Fluorescence emission spectra of the R6G and MB diluted solutions was recorded using the Renishaw Invia system and exciting the dyes with 514 and 780 nm, respectively.

Synthesis

Compound **4-1** was synthesized according to published procedure from barbituric acid[78].

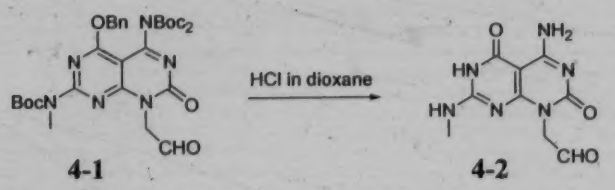

4-1 **4-2**

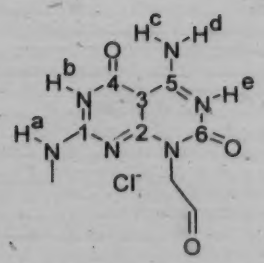

Synthesis of compound **4-2** (G^C aldehyde).

To a solution of compound **4-1** (0.11 g, 0.17 mmol) in 4 mL of anhydrous dioxane 4M HCl solution in dioxane (2 mL) was added and the mixture was refluxed for 5 h. The precipitate formed was filtered, washed with anhydrous dioxane (5 × 10 mL), and dried on a filter. Compound **A** was obtained as a white solid of HCl salt ($C_9H_{10}N_6O_3$·HCl 0.051 g, 96%), which was pure as shown by HRMS and NMR.

Positive high resolution ESI–MS: Expected mass for (M+H)/z, 251.0887. Observed 251.0889.

^{1}H NMR (400 MHz, DMSO, 300K) δ (ppm): 9.55 (CHO, s, 1H), 12.5 (Hb+He, br.s., 2H) 9.78 (Hc, s, 1H), 9.19 (Hd, s, 1H), 8.78 (Ha, s, 1H), 4.88 (CH_2, s, 2H), 2.85 (CH_3, d, J = 4 Hz, 1H)

^{1}H NMR (400 MHz, H_2O, 300K) δ (ppm): 9.61 (CHO, s, 0.05H), 5.46 ($CH(OH)_2$, t, J = 5.6 Hz, 0.95H), 4.29 (CH_2, d, J = 5.2, 0.95H), 3.05 (CH_3, s, 2.85H), 2.99 (CH_3 (of aldehyde form), s, 0.15H)

^{13}C NMR (100 MHz, DMSO, 300K) δ (ppm): 193.54 (CHO), 165.74 (C_6), 160.91 (C_5), 155.30 (C_4), 152.28 (C_1), 149.00 (C_2), 83.96 (C_3), 70.29 (CH_2), 34.88 (CH_3).

References

1. Lehn, J.-M., *Supramolecular Chemistry: Concepts and Perspectives* VCH: Weinheim, Germany, 1995.

2. Lehn, J.-M., Toward complex matter: Supramolecular chemistry and self-organization. *Proceedings of the National Academy of Sciences of the United States of America* **2002,** 99, (8), 4763-4768.

3. Lehn, J.-M., Toward self-organization and complex matter. *Science (Washington, DC, United States)* **2002,** 295, (5564), 2400-2403.

4. Johnson, D. L.; Polikandritou-Lambros, M.; Martonen, T. B., Drug encapsulation and aerodynamic behavior of a lipid microtubule aerosol. *Drug Delivery* **1996,** 3, (1), 9-15.

5. Chernozatonskii, L. A.; Gulyaev, Y. V.; Kosakovskaja, Z. J.; Sinitsyn, N. I.; Torgashov, G. V.; Zakharchenko, Y. F.; Fedorov, E. A.; Val'chuk, V. P., Electron field emission from nanofilament carbon films. *Chemical Physics Letters* **1995,** 233, (1-2), 63-68.

6. Hill, J. P.; Jin, W.; Kosaka, A.; Fukushima, T.; Ichihara, H.; Shimomura, T.; Ito, K.; Hashizume, T.; Ishii, N.; Aida, T., Self-assembled hexa-peri-hexabenzocoronene graphitic nanotube. *Science (Washington, DC, United States)* **2004,** 304, (5676), 1481-1483.

7. Shimizu, T.; Masuda, M.; Minamikawa, H., Supramolecular nanotube architectures based on amphiphilic molecules. *Chemical Reviews* **2005,** 105, (4), 1401-1443.

8. Borgnia, M.; Nielsen, S.; Engel, A.; Agre, P., CELLULAR AND MOLECULAR BIOLOGY OF THE AQUAPORIN WATER CHANNELS. *Annual Review of Biochemistry* **1999,** 68, (1), 425.

9. Iijima, S., Helical microtubules of graphitic carbon. *Nature (London, United Kingdom)* **1991,** 354, (6348), 56-8.

10. Hoger, S.; Morrison, D. L.; Enkelmann, V., Solvent Triggering between Conformational States in Amphiphilic Shape-Persistent Macrocycles. *Journal of the American Chemical Society* **2002,** 124, (23), 6734-6736.

11. Rothemund, P. W. K.; Ekani-Nkodo, A.; Papadakis, N.; Kumar, A.; Fygenson, D. K.; Winfree, E., Design and Characterization of Programmable DNA Nanotubes. *Journal of the American Chemical Society* **2004,** 126, (50), 16344-16352.

12. Curatolo, W., Glycolipid function. *Biochimica et Biophysica Acta (BBA) - Reviews on Biomembranes* **1987,** 906, (2), 137-160.

13. Toyoki, K., Synthetic Bilayer Membranes: Molecular Design, Self-Organization, and Application. *Angewandte Chemie International Edition in English* **1992,** 31, (6), 709-726.

14. Fuhrhop, J. H.; Helfrich, W., Fluid and Solid Fibers Made of Lipid Molecular Bilayers. *Chemical Reviews* **1993,** 93, (4), 1565-1582.

15. Yager, P.; Schoen, P. E., Formation of tubules by a polymerizable surfactant. *Molecular Crystals and Liquid Crystals* **1984,** 106, (3-4), 371-81.

16. Fuhrhop, J. H.; Wang, T., Bolaamphiphiles. *Chem. Rev.* **2004,** 104, (6), 2901-2938.

17. Ambrosi, M.; Fratini, E.; Alfredsson, V.; Ninham, B. W.; Giorgi, R.; LoNostro, P.; Baglioni, P., Nanotubes from a Vitamin C-Based Bolaamphiphile. *J. Am. Chem. Soc.* **2006,** 128, (22), 7209-7214.

18. Zhan, C.; Gao, P.; Liu, M., Self-assembled helical spherical-nanotubes from an l-glutamic acid based bolaamphiphilic low molecular mass organogelator. *Chemical Communications* **2005,** (4), 462-464.

19. Boettcher, C.; Schade, B.; Fuhrhop, J. H., Comparative Cryo-Electron Microscopy of Noncovalent N-Dodecanoyl- (D- AND L-) serine Assemblies in Vitreous Toluene and Water. *Langmuir* **2001,** 17, (3), 873-877.

20. Jenekhe, S. A.; Chen, X. L., Self-Assembled Aggregates of Rod-Coil Block Copolymers and Their Solubilization and Encapsulation of Fullerenes. *Science* **1998,** 279, (5358), 1903-1907.

21. Massey, J.; Power, K. N.; Manners, I.; Winnik, M. A., Self-Assembly of a Novel Organometallic-Inorganic Block Copolymer in Solution and the Solid State: Nonintrusive Observation of Novel WormLike Poly(ferrocenyldimethylsilane)-b-Poly(dimethylsiloxane) Micelles. *J. Am. Chem. Soc.* **1998,** 120, (37), 9533-9540.

22. Grumelard, J.; Taubert, A.; Meier, W., Soft nanotubes from amphiphilic ABA triblock macromonomers. *Chemical Communications* **2004,** (13), 1462-1463.

23. Shen, H.; Eisenberg, A., Block Length Dependence of Morphological Phase Diagrams of the Ternary System of PS-b-PAA/Dioxane/H2O. *Macromolecules* **2000,** 33, (7), 2561-2572.

24. Yu, K.; Eisenberg, A., Bilayer Morphologies of Self-Assembled Crew-Cut Aggregates of Amphiphilic PS-b-PEO Diblock Copolymers in Solution. *Macromolecules* **1998,** 31, (11), 3509-3518.

25. Gao, X. Y.; Matsui, H., Peptide-based nanotubes and their applications in bionanotechnology. *Advanced Materials* **2005,** 17, (17), 2037-2050.

26. Martin, C. R.; Kohli, P., The emerging field of nanotube biotechnology. *Nature Reviews Drug Discovery* **2003,** 2, (1), 29-37.

27. Zhou, Y.; Shimizu, T., Lipid Nanotubes: A Unique Template To Create Diverse One-Dimensional Nanostructures. *Chem. Mater.* **2008,** 20, (3), 625-633.

28. Desantis, P.; Morosett.S; Rizzo, R., Conformational-Analysis of Regular Enantiomeric Sequences. *Macromolecules* **1974,** 7, (1), 52-58.

29. Nelson, J. C.; Saven, J. G.; Moore, J. S.; Wolynes, P. G., Solvophobically driven folding of nonbiological oligomers. *Science* **1997,** 277, (5333), 1793-1796.

30. Hill, D. J.; Mio, M. J.; Prince, R. B.; Hughes, T. S.; Moore, J. S., A Field Guide to Foldamers. *Chem. Rev.* **2001,** 101, (12), 3893-4012.

31. Cuccia, L. A.; Lehn, J. M.; Homo, J. C.; Schmutz, M., Encoded helical self-organization and self-assembly into helical fibers of an oligoheterocyclic pyridine-pyridazine molecular strand. *Angewandte Chemie-International Edition* **2000,** 39, (1), 233-+.

32. Ghadiri, M. R.; Granja, J. R.; Milligan, R. A.; McRee, D. E.; Khazanovich, N., Self-assembling organic nanotubes based on a cyclic peptide architecture. *Nature (London, United Kingdom)* **1993,** 366, (6453), 324-7.

33. Sanchez-Ouesada, J.; Isler, M. P.; Ghadiri, M. R., Modulating ion channel properties of transmembrane peptide nanotubes through heteromeric supramolecular assemblies. *Journal of the American Chemical Society* **2002,** 124, (34), 10004-10005.

34. Harada, A.; Li, J.; Kamachi, M., Synthesis of a tubular polymer from threaded cyclodextrins. *Nature* **1993,** 364, (6437), 516-518.

35. Zhang, J. S.; Moore, J. S., Nanoarchitectures .3. Aggregation of Hexa(Phenylacetylene) Macrocycles in Solution - a Model System for Studying Pi-Pi Interactions .2. *Journal of the American Chemical Society* **1992,** 114, (24), 9701-9702.

36. Hunter, C. A.; Sanders, J. K. M., The Nature of Pi-Pi Interactions. *Journal of the American Chemical Society* **1990,** 112, (14), 5525-5534.

37. Rosselli, S.; Ramminger, A. D.; Wagner, T.; Silier, B.; Wiegand, S.; Haussler, W.; Lieser, G.; Scheumann, V.; Hoger, S., Coil-ring-coil block copolymers as building blocks for supramolecular hollow cylindrical brushes. *Angewandte Chemie-International Edition* **2001,** 40, (17), 3138-3141.

38. Schappacher, M.; Deffieux, A., Synthesis of Macrocyclic Copolymer Brushes and Their Self-Assembly into Supramolecular Tubes. *Science* **2008,** 319, (5869), 1512-1515.

39. Mathias, J. P.; Seto, C. T.; Simanek, E. E.; Whitesides, G. M., Self-Assembly through Hydrogen-Bonding - Preparation and Characterization of 3 New Types of Supramolecular Aggregates Based on Parallel Cyclic Ca3.M3 Rosettes. *Journal of the American Chemical Society* **1994,** 116, (5), 1725-1736.

40. Gellert, M.; Lipsett, M. N.; Davies, D. R., Helix Formation by Guanylic Acid. *Proceedings of the National Academy of Sciences of the United States of America* **1962,** 48, (12), 2013-&.

41. Burge, S.; Parkinson, G. N.; Hazel, P.; Todd, A. K.; Neidle, S., Quadruplex DNA: sequence, topology and structure. *Nucleic Acids Research* **2006,** 34, (19), 5402-5415.

42. Davis, J. T., G-quartets 40 years later: From 5 '-GMP to molecular biology and supramolecular chemistry. *Angewandte Chemie-International Edition* **2004,** 43, (6), 668-698.

43. Kang, C.; Zhang, X. H.; Ratliff, R.; Moyzis, R.; Rich, A., Crystal-Structure of 4-Stranded Oxytricha Telomeric DNA. *Nature* **1992,** 356, (6365), 126-131.

44. Wong, A.; Fettinger, J. C.; Forman, S. L.; Davis, J. T.; Wu, G., The sodium ions inside a lipophilic G-quadruplex channel as probed by solid-state Na-23 NMR. *Journal of the American Chemical Society* **2002,** 124, (5), 742-743.

45. Kanie, K.; Yasuda, T.; Nishii, M.; Ujiie, S.; Kato, T., Hydrogen-bonded lyotropic liquid crystals of folic acids: Responses to environment by exhibiting different complex patterns. *Chemistry Letters* **2001**, (6), 480-481.

46. Sessler, J. L.; Sathiosatham, M.; Doerr, K.; Lynch, V.; Abboud, K. A., A G-quartet formed in the absence of a templating metal cation: A new 8-(N,N-dimethylaniline)guanosine derivative. *Angewandte Chemie-International Edition* **2000,** 39, (7), 1300-1304.

47. Yagai, S.; Nakajima, T.; Karatsu, T.; Saitow, K.; Kitamura, A., Phototriggered self-assembly of hydrogen-bonded rosette. *Journal of the American Chemical Society* **2004,** 126, (37), 11500-11508.

48. Seto, C. T.; Whitesides, G. M., Self-Assembly Based on the Cyanuric Acid Melamine Lattice. *Journal of the American Chemical Society* **1990,** 112, (17), 6409-6411.

49. Marsh, A.; Nolen, E. G.; Gardinier, K. M.; Lehn, J. M., Janus Molecules - Synthesis of Double-Headed Heterocycles Containing 2 Identical Hydrogen-Bonding Arrays. *Tetrahedron Letters* **1994,** 35, (3), 397-400.

50. Marsh, A.; Silvestri, M.; Lehn, J. M., Self-complementary hydrogen bonding heterocycles designed for the enforced self-assembly into supramolecular macrocycles. *Chemical Communications* **1996**, (13), 1527-1528.

51. Mascal, M.; Hext, N. M.; Warmuth, R.; Moore, M. H.; Turkenburg, J. P., Programming a hydrogen-bonding code for the specific generation of a supermacrocycle. *Angewandte Chemie-International Edition in English* **1996,** 35, (19), 2204-2206.

52. Kolotuchin, S. V.; Zimmerman, S. C., Self-assembly mediated by the donor-donor-acceptor center dot acceptor-acceptor-donor (DDA center dot AAD) hydrogen-bonding motif: Formation of a robust hexameric aggregate. *Journal of the American Chemical Society* **1998,** 120, (35), 9092-9093.

53. Zimmerman, S. C.; Duerr, B. F., Controlled Molecular Aggregation .1. Cyclic Trimerization Via Hydrogen-Bonding. *Journal of Organic Chemistry* **1992,** 57, (8), 2215-2217.

54. Kimizuka, N.; Fujikawa, S.; Kuwahara, H.; Kunitake, T.; Marsh, A.; Lehn, J. M., Mesoscopic Supramolecular Assembly of a Janus Molecule and a Melamine Derivative Via Complementary Hydrogen-Bonds. *Journal of the Chemical Society-Chemical Communications* **1995**, (20), 2103-2104.

55. Kimizuka, N.; Kawasaki, T.; Hirata, K.; Kunitake, T., Tube-Like Nanostructures Composed of Networks of Complementary Hydrogen-Bonds. *Journal of the American Chemical Society* **1995,** 117, (23), 6360-6361.

56. Forman, S. L.; Fettinger, J. C.; Pieraccini, S.; Gottarelli, G.; Davis, J. T., Toward Artificial Ion Channels: A Lipophilic G-Quadruplex. *J. Am. Chem. Soc.* **2000,** 122, (17), 4060-4067.

57. Whitesides, G. M.; Simanek, E. E.; Mathias, J. P.; Seto, C. T.; Chin, D. N.; Mammen, M.; Gordon, D. M., Noncovalent Synthesis - Using Physical-Organic Chemistry to Make Aggregates. *Accounts of Chemical Research* **1995,** 28, (1), 37-44.

58. Mammen, M.; Simanek, E. E.; Whitesides, G. M., Predicting the relative stabilities of multiparticle hydrogen-bonded aggregates based on the number of hydrogen bonds and the number of particles and measuring these stabilities with titrations using dimethyl sulfoxide. *Journal of the American Chemical Society* **1996,** 118, (50), 12614-12623.

59. Klok, H. A.; Jolliffe, K. A.; Schauer, C. L.; Prins, L. J.; Spatz, J. P.; Moller, M.; Timmerman, P.; Reinhoudt, D. N., Self-assembly of rodlike hydrogen-bonded nanostructures. *Journal of the American Chemical Society* **1999,** 121, (30), 7154-7155.

60. Rzepecki, P.; Hochdorffer, K.; Schaller, T.; Zienau, J.; Harms, K.; Ochsenfeld, C.; Xie, X.; Schrader, T., Hierarchical self-assembly of aminopyrazole peptides into nanorosettes in water. *Journal of the American Chemical Society* **2008,** 130, 586-591.

61. Smith, J. A. S.; Wehrle, B.; Aguilarparrilla, F.; Limbach, H. H.; Focesfoces, M. D.; Cano, F. H.; Elguero, J.; Baldy, A.; Pierrot, M.; Khurshid, M. M. T.; Larcombemcdouall, J. B., Intermolecular Triple Proton and Deuteron Transfer in Crystalline 3,5-Dimethylpyrazole Studied by Nmr, Nqr, and X-Ray-Methods. *Journal of the American Chemical Society* **1989,** 111, (19), 7304-7312.

62. Fenniri, H.; Deng, B. L.; Ribbe, A. E., Helical rosette nanotubes with tunable chiroptical properties. *Journal of the American Chemical Society* **2002,** 124, (37), 11064-11072.

63. Fenniri, H.; Packiarajan, M.; Vidale, K. L.; Sherman, D. M.; Hallenga, K.; Wood, K. V.; Stowell, J. G., Helical rosette nanotubes: Design, self-assembly, and characterization. *Journal of the American Chemical Society* **2001,** 123, (16), 3854-3855.

64. Moralez, J. G.; Raez, J.; Yamazaki, T.; Motkuri, R. K.; Kovalenko, A.; Fenniri, H., Helical rosette nanotubes with tunable stability and hierarchy. *Journal of the American Chemical Society* **2005,** 127, 8307-8309.

65. Chun, A. L.; Moralez, J. G.; Fenniri, H.; Webster, T. J., Helical rosette nanotubes: a more effective orthopaedic implant material. *Nanotechnology* **2004,** 15, (4), S234-S239.

66. Raez, J.; Moralez, J. G.; Fenniri, H., Long-range flow-induced alignment of self-assembled rosette nanotubes on Si/SiOx and poly(methyl methacrylate)-coated Si/SiOx. *Journal of the American Chemical Society* **2004,** 126, (50), 16298-16299.

67. Johnson, R. S.; Yamazaki, T.; Kovalenko, A.; Fenniri, H., Molecular basis for water-promoted supramolecular chirality inversion in helical Rosette nanotubes. *Journal of the American Chemical Society* **2007,** 129, (17), 5735-5743.

68. Seeman, N. C., Biochemistry and Structural DNA Nanotechnology: An Evolving Symbiotic Relationship. *Biochemistry* **2003,** 42, (24), 7259-7269.

69. Winfree, E.; Liu, F. R.; Wenzler, L. A.; Seeman, N. C., Design and self-assembly of two-dimensional DNA crystals. *Nature* **1998,** 394, (6693), 539-544.

70. O'Neill, P.; Rothemund, P. W. K.; Kumar, A.; Fygenson, D. K., Sturdier DNA nanotubes via ligation. *Nano Letters* **2006,** 6, (7), 1379-1383.

71. Liu, D.; Park, S. H.; Reif, J. H.; LaBean, T. H., DNA nanotubes self-assembled from triple-crossover tiles as templates for conductive nanowires. *Proceedings of the National Academy of Sciences of the United States of America* **2004,** 101, (3), 717-722.

72. Zheng, Y. X.; Wong, M. L.; Alberts, B.; Mitchison, T., Nucleation of Microtubule Assembly by a Gamma-Tubulin-Containing Ring Complex. *Nature* **1995,** 378, (6557), 578-583.

73. Sakai, N.; Mareda, J.; Matile, S., Rigid-rod molecules in biomembrane models: From hydrogen-bonded chains to synthetic multifunctional pores. *Accounts of Chemical Research* **2005,** 38, (2), 79-87.

74. Aoyagi, M.; Biradha, K.; Fujita, M., Quantitative formation of coordination nanotubes templated by rodlike guests. *Journal of the American Chemical Society* **1999,** 121, (32), 7457-7458.

75. John, G.; Mason, M.; Ajayan, P. M.; Dordick, J. S., Lipid-Based Nanotubes as Functional Architectures with Embedded Fluorescence and Recognition Capabilities. *Journal of the American Chemical Society* **2004,** 126, (46), 15012-15013.

76. G. John, M. Mong., Nanotube Formation from Renewable Resources via Coiled Nanofibers. *Advanced Materials* **2001,** 13, (10), 715-718.

77. Menger, F. M.; Peresypkin, A. V., A combinatorially-derived structural phase diagram for 42 zwitterionic geminis. *Journal of the American Chemical Society* **2001,** 123, (23), 5614-5615.

78. Fenniri, H.; Deng, B. L.; Ribbe, A. E.; Hallenga, K.; Jacob, J.; Thiyagarajan, P., Entropically driven self-assembly of multichannel rosette nanotubes. *Proceedings of the National Academy of Sciences of the United States of America* **2002,** 99, 6487-6492.

79. Cho, C. P.; Perng, T. P., One-dimensional organic and organometallic nanostructured materials. *Journal of Nanoscience and Nanotechnology* **2008,** 8, 69-87.

80. Elias, B.; Shao, F. W.; Barton, J. K., Charge migration along the DNA duplex: Hole versus electron transport. *Journal of the American Chemical Society* **2008,** 130, 1152-+.

81. Guo, X.; Gorodetsky, A. A.; Hone, J.; Barton, J. K.; Nuckolls, C., Conductivity of a single DNA duplex bridging a carbon nanotube gap. *Nat Nano* **2008,** 3, (3), 163-167.

82. Zhou, W. D.; Li, Y. L.; Zhu, D. B., Progress in polydiacetylene nanowires by self-assembly and self-polymerization. *Chemistry-an Asian Journal* **2007,** 2, (2), 222-229.

83. Wang, Z. C.; Medforth, C. J.; Shelnutt, J. A., Self-metallization of photocatalytic porphyrin nanotubes. *Journal of the American Chemical Society* **2004,** 126, (51), 16720-16721.

84. Dujardin, E.; Peet, C.; Stubbs, G.; Culver, J. N.; Mann, S., Organization of metallic nanoparticles using tobacco mosaic virus templates. *Nano Letters* **2003,** 3, (3), 413-417.

85. Braun, E.; Eichen, Y.; Sivan, U.; Ben-Yoseph, G., DNA-templated assembly and electrode attachment of a conducting silver wire. *Nature* **1998,** 391, (6669), 775-778.

86. Pons, M.; Millet, O., Dynamic NMR studies of supramolecular complexes. *Progress in Nuclear Magnetic Resonance Spectroscopy* **2001,** 38, (4), 267-324.

87. Brown, S. P.; Spiess, H. W., Advanced solid-state NMR methods for the elucidation of structure and dynamics of molecular, macromolecular, and supramolecular systems. *Chemical Reviews* **2001,** 101, (12), 4125-4155.

88. Chierotti, M. R.; Gobetto, R., Solid-state NMR studies of weak interactions in supramolecular systems. *Chemical Communications* **2008,** (14), 1621-1634.

89. Mascal, M.; Hext, N. M.; Warmuth, R.; Arnall-Culliford, J. R.; Moore, M. H.; Turkenburg, J. P., The G-C DNA base hybrid: Synthesis, self-organization and structural analysis. *Journal of Organic Chemistry* **1999,** 64, (23), 8479-8484.

90. Colominas, C.; Luque, F. J.; Orozco, M., Tautomerism and protonation of guanine and cytosine. Implications in the formation of hydrogen-bonded complexes. *Journal of the American Chemical Society* **1996,** 118, (29), 6811-6821.

91. Cohen, Y.; Avram, L.; Frish, L., Diffusion NMR spectroscopy in supramolecular and combinatorial chemistry: An old parameter - New insights. *Angewandte Chemie-International Edition* **2005,** 44, (4), 520-554.

92. Brown, S. P.; Perez-Torralba, M.; Sanz, D.; Claramunt, R. M.; Emsley, L., The Direct Detection of a Hydrogen Bond in the Solid State by NMR through the Observation of a Hydrogen-Bond Mediated 15N-15N J Coupling. *J. Am. Chem. Soc.* **2002,** 124, (7), 1152-1153.

93. Pham, T. N.; Masiero, S.; Gottarelli, G.; Brown, S. P., Identification by 15N Refocused INADEQUATE MAS NMR of Intermolecular Hydrogen Bonding that Directs the Self-Assembly of Modified DNA Bases. *J. Am. Chem. Soc.* **2005,** 127, (46), 16018-16019.

94. Pham, T. N.; Griffin, J. M.; Masiero, S.; Lena, S.; Gottarelli, G.; Hodgkinson, P.; Fillip, C.; Brown, S. P., Quantifying hydrogen-bonding strength: the measurement of (2h)J(NN) couplings in self-assembled guanosines by solid-state N-15 spin-echo MAS NMR. *Physical Chemistry Chemical Physics* **2007,** 9, (26), 3416-3423.

95. Ziessel, R.; Pickaert, G.; Camerel, F.; Donnio, B.; Guillon, D.; Cesario, M.; Prange, T., Tuning organogels and mesophases with phenanthroline Ligands and their copper complexes by inter- to intramolecular hydrogen bonds. *Journal of the American Chemical Society* **2004,** 126, (39), 12403-12413.

96. Colomer, J. F.; Henrard, L.; Flahaut, E.; Van Tendeloo, G.; Lucas, A. A.; Lambin, P., Rings of double-walled carbon nanotube bundles. *Nano Letters* **2003,** 3, (5), 685-689.

97. Levitt, M. H., Symmetry in the design of NMR multiple-pulse sequences. *Journal of Chemical Physics* **2008,** 128, (5).

98. Hodgkinson, P., Heteronuclear decoupling in the NMR of solids. *Progress in Nuclear Magnetic Resonance Spectroscopy* **2005,** 46, (4), 197-222.

99. Sorensen, M. D.; Meissner, A.; Sorensen, O. W., Spin-state-selective coherence transfer via intermediate states of two-spin coherence in IS spin systems: Application to E.COSY-type measurement of J coupling constants. *Journal of Biomolecular Nmr* **1997,** 10, (2), 181-186.

100. Ho, R. M.; Chen, C. K.; Chiang, Y. W.; Ko, B. T.; Lin, C. C., Tubular nanostructures from degradable core-shell cylinder microstructures in chiral diblock copolymers. *Advanced Materials* **2006,** 18, (18), 2355-+.

101. Terrones, M.; Grobert, N.; Olivares, J.; Zhang, J. P.; Terrones, H.; Kordatos, K.; Hsu, W. K.; Hare, J. P.; Townsend, P. D.; Prassides, K.; Cheetham, A. K.; Kroto, H. W.; Walton, D. R. M., Controlled production of aligned-nanotube bundles. *Nature* **1997,** 388, (6637), 52-55.

102. Gao, J. B.; Yu, A. P.; Itkis, M. E.; Bekyarova, E.; Zhao, B.; Niyogi, S.; Haddon, R. C., Large-scale fabrication of aligned single-walled carbon nanotube array and hierarchical single-walled carbon nanotube assembly. *Journal of the American Chemical Society* **2004,** 126, (51), 16698-16699.

103. Remskar, M.; Mrzel, A., Inorganic nanotubes: self-assembly and geometrical stabilisation of new compounds. *Vacuum* **2003,** 71, (1-2), 177-183.

104. Yada, M.; Taniguchi, C.; Torikai, T.; Watari, T.; Furuta, S.; Katsuki, H., Hierarchical two- and three-dimensional microstructures composed of rare-earth compound nanotubes. *Advanced Materials* **2004,** 16, (16), 1448-+.

105. Adachi, M.; Harada, T.; Harada, M., Formation of huge length silica nanotubes by a templating mechanism in the laurylamine/tetraethoxysilane system. *Langmuir* **1999,** 15, (21), 7097-7100.

106. Matsui, H.; Douberly, G. E., Organization of peptide nanotubes into macroscopic bundles. *Langmuir* **2001,** 17, (25), 7918-7922.

107. Yan, Y. H.; Chan-Park, M. B.; Zhang, Q., Advances in carbon-nanotube assembly. *Small* **2007,** 3, (1), 24-42.

108. Ajayan, P. M., Nanotubes from carbon. *Chemical Reviews* **1999,** 99, 1787-1799.

109. Zeng, X. B.; Ungar, G.; Liu, Y. S.; Percec, V.; Dulcey, S. E.; Hobbs, J. K., Supramolecular dendritic liquid quasicrystals. *Nature* **2004,** 428, (6979), 157-160.

110. Tikhomirov, G.; Oderinde, M.; Makeiff, D.; Mansouri, A.; Lu, W.; Heirtzler, F.; Kwok, D. Y.; Fenniri, H., Synthesis of Hydrophobic Derivatives of the G^C Base for Rosette Nanotube Self-Assembly in Apolar Media. *J. Org. Chem.* **2008,** 73, (11), 4248-4251.

111. Knez, M.; Sumser, M. P.; Bittner, A. M.; Wege, C.; Jeske, H.; Hoffmann, D. M. P.; Kuhnke, K.; Kern, K., Binding the tobacco mosaic virus to inorganic surfaces. *Langmuir* **2004,** 20, (2), 441-447.

112. Moralez, J. G.; Raez, J.; Yamazaki, T.; Motkuri, R. K.; Kovalenko, A.; Fenniri, H., Helical rosette nanotubes with tunable stability and hierarchy. *Journal of the American Chemical Society* **2005,** 127, (23), 8307-8309.

113. Wang, Y.; Ma, C. L.; Sun, X. L.; Li, H., Preparation and photoluminescence properties of organic-inorganic nanocomposite with a mesolamellar nickel oxide. *Microporous and Mesoporous Materials* **2004,** 71, (1-3), 99-102.

114. Okamoto, K.; Kapoor, M. P.; Inagaki, S., Organosilicate-surfactant lamellar mesophase with molecular-scale periodicity in the silicate layers. *Chemical Communications* **2005**, (11), 1423-1425.

115. So, P. T. C.; Gruner, S. M.; Erramilli, S., Pressure-Induced Topological Phase-Transitions in Membranes. *Physical Review Letters* **1993,** 70, (22), 3455-3458.

116. Tikhomirov, G.; Yamazaki, T.; Kovalenko, A.; Fenniri, H., Hierarchical Self-Assembly of Organic Prolate Nanospheroids from Hydrophobic Rosette Nanotubes. *Langmuir* **2008,** 24, (9), 4447-4450.

117. Grigor'ev, D. P., *Ontogeny of Minerals*. Israel Program for Scientific Translations: Jerusalem, 1965.

118. Punin, Y. O., Crystal Splitting. In *Zap. Vses. Mineral. Ova.*, Vol. 110, pp 666-686.

119. Hu, Y. H.; Chen, K. Z., Crystal splitting in the growth of beta-FeO(OH). *Journal of Crystal Growth* **2007,** 308, (1), 185-188.

120. Kelly, A. T.; Rusakova, I.; Ould-Ely, T.; Hofmann, C.; Luttge, A.; Whitmire, K. H., Iron phosphide nanostructures produced from a single-source organometallic precursor: Nanorods, bundles, crosses, and spherulites. *Nano Letters* **2007,** 7, (9), 2920-2925.

121. Tang, J.; Alivisatos, A. P., Crystal splitting in the growth of Bi2S3. *Nano Letters* **2006,** 6, (12), 2701-2706.

122. Schenning, A.; Benneker, F. B. G.; Geurts, H. P. M.; Liu, X. Y.; Nolte, R. J. M., Porphyrin wheels. *Journal of the American Chemical Society* **1996,** 118, (36), 8549-8552.

123. Doan, S. C.; Shanmugham, S.; Aston, D. E.; McHale, J. L., Counterion Dependent Dye Aggregates: Nanorods and Nanorings of Tetra(p-carboxyphenyl)porphyrin. *J. Am. Chem. Soc.* **2005,** 127, (16), 5885-5892.

124. Biemans, H. A. M.; Rowan, A. E.; Verhoeven, A.; Vanoppen, P.; Latterini, L.; Foekema, J.; Schenning, A.; Meijer, E. W.; de Schryver, F. C.; Nolte, R. J. M., Hexakis porphyrinato benzenes. A new class of porphyrin arrays. *Journal of the American Chemical Society* **1998,** 120, (43), 11054-11060.

125. Jeukens, C.; Lensen, M. C.; Wijnen, F. J. P.; Elemans, J.; Christianen, P. C. M.; Rowan, A. E.; Gerritsen, J. W.; Nolte, R. J. M.; Maan, J. C., Polarized absorption and emission of ordered self-assembled porphyrin rings. *Nano Letters* **2004,** 4, (8), 1401-1406.

126. Lensen, M. C.; Takazawa, K.; Elemans, J.; Jeukens, C.; Christianen, P. C. M.; Maan, J. C.; Rowan, A. E.; Nolte, R. I. M., Aided self-assembly of porphyrin nanoaggregates into ring-shaped architectures. *Chemistry-a European Journal* **2004,** 10, (4), 831-839.

127. Ohara, P. C.; Heath, J. R.; Gelbart, W. M., Self-assembly of submicrometer rings of particles from solutions of nanoparticles. *Angewandte Chemie-International Edition in English* **1997,** 36, (10), 1078-&.

128. Tripp, S. L.; Pusztay, S. V.; Ribbe, A. E.; Wei, A., Self-assembly of cobalt nanoparticle rings. *Journal of the American Chemical Society* **2002,** 124, (27), 7914-7915.

129. Nie, Z. H.; Fava, D.; Kumacheva, E.; Zou, S.; Walker, G. C.; Rubinstein, M., Self-assembly of metal-polymer analogues of amphiphilic triblock copolymers. *Nature Materials* **2007,** 6, 609-614.

130. Kim, J. K.; Lee, E.; Huang, Z. G.; Lee, M., Nanorings from the self-assembly of amphiphilic molecular dumbbells. *Journal of the American Chemical Society* **2006,** 128, (43), 14022-14023.

131. Wang, H.; DiGate, R. J.; Seeman, N. C., An RNA topoisomerase. *Proceedings of the National Academy of Sciences of the United States of America* **1996,** 93, (18), 9477-9482.

132. Pochan, D. J.; Chen, Z. Y.; Cui, H. G.; Hales, K.; Qi, K.; Wooley, K. L., Toroidal triblock copolymer assemblies. *Science* **2004,** 306, (5693), 94-97.

133. Carlson, J. C. T.; Jena, S. S.; Flenniken, M.; Chou, T. F.; Siegel, R. A.; Wagner, C. R., Chemically controlled self-assembly of protein nanorings. *Journal of the American Chemical Society* **2006,** 128, (23), 7630-7638.

134. Daube, S. S.; Arad, T.; Bar-Ziv, R., Cell-free co-synthesis of protein nanoassemblies: Tubes, rings, and doughnuts. *Nano Letters* **2007,** 7, (3), 638-641.

135. Bottcher, C.; Endisch, C.; Fuhrhop, J. H.; Catterall, C.; Eaton, M., High-yield preparation of oligomeric C-type DNA toroids and their characterization by cryoelectron microscopy. *Journal of the American Chemical Society* **1998,** 120, (1), 12-17.

136. Hud, N. V.; Downing, K. H., Cryoelectron microscopy of lambda phage DNA condensates in vitreous ice: The fine structure of DNA toroids. *Proceedings of the National Academy of Sciences of the United States of America* **2001,** 98, (26), 14925-14930.

137. Cooper, A., Precipitation of Toroidal Collagen Fibrils. *Biochemical Journal* **1969,** 112, (4), 515-&.

138. Rasched, G.; Ackermann, D.; Schmidt, T. L.; Broekmann, P.; Heckel, A.; Famulok, M., DNA minicircles with gaps for versatile functionalization. *Angewandte Chemie-International Edition* **2008,** 47, (5), 967-970.

139. Mayer, G.; Ackermann, D.; Kuhn, N.; Famulok, M., Construction of DNA architectures with RNA hairpins. *Angewandte Chemie-International Edition* **2008,** 47, (5), 971-973.

140. Liu, J.; Dai, H. J.; Hafner, J. H.; Colbert, D. T.; Smalley, R. E.; Tans, S. J.; Dekker, C., Fullerene 'crop circles'. *Nature* **1997,** 385, (6619), 780-781.

141. Sano, M.; Kamino, A.; Okamura, J.; Shinkai, S., Ring closure of carbon nanotubes. *Science* **2001,** 293, (5533), 1299-1301.

142. Martel, R.; Shea, H. R.; Avouris, P., Rings of single-walled carbon nanotubes. *Nature* **1999,** 398, (6725), 299-299.

143. Guo, A.; Fu, Y. Y.; Guan, L. H.; Zhang, Z.; Wu, W.; Chen, J.; Shi, Z. J.; Gu, Z. N.; Huang, R.; Zhang, X., Spontaneously formed closed rings of single-wall carbon nanotube bundles and their physical mechanism. *Journal of Physical Chemistry C* **2007,** 111, (9), 3555-3559.

144. Vossmeyer, T.; Chung, S. W.; Gelbart, W. M.; Heath, J. R., Surprising superstructures: Rings. *Advanced Materials* **1998,** 10, (4), 351-353.

145. Charvolin, J.; Sadoc, J. F., A geometrical template for toroidal aggregates of chiral macromolecules. *European Physical Journal E* **2008,** 25, (3), 335-341.

146. Greef, T. F. A.; Meijer, E. W., Materials science - Supramolecular polymers. *Nature* **2008,** 453, (7192), 171-173.

147. Lee, S. W.; Kwok, D. Y.; Laibinis, P. E., Chemical influences on adsorption-mediated self-propelled drop movement. *Physical Review E* **2002,** 65, (5).

148. Pullerits, T.; Sundstrom, V., Photosynthetic light-harvesting pigment-protein complexes: Toward understanding how and why. *Accounts of Chemical Research* **1996,** 29, (8), 381-389.

149. De Luca, L.; Giacomelli, G.; Porcheddu, A., Beckmann rearrangement of oximes under very mild conditions. *Journal of Organic Chemistry* **2002,** 67, (17), 6272-6274.

150. Samitsu, S.; Shimomura, T.; Ito, K.; Fujimori, M.; Heike, S.; Hashizume, T., Conductivity measurements of individual poly(3,4-ethylenedioxythiophene)/poly(styrenesulfonate) nanowires on nanoelectrodes using manipulation with an atomic force microscope. *Applied Physics Letters* **2005,** 86, (23).

151. Nuraje, N.; Su, K.; Yang, N. L.; Matsui, H., Liquid/liquid interfacial polymerization to grow single crystalline nanoneedles of various conducting polymers. *Acs Nano* **2008,** 2, (3), 502-506.

152. Chae, S. K.; Park, H.; Yoon, J.; Lee, C. H.; Ahn, D. J.; Kim, J. M., Polydiacetylene supramolecules in electrospun microfibers: Fabrication, micropatterning, and sensor applications. *Advanced Materials* **2007,** 19, (4), 521-+.

153. Spanggaard, H.; Krebs, F. C., A brief history of the development of organic and polymeric photovoltaics. *Solar Energy Materials and Solar Cells* **2004,** 83, (2-3), 125-146.

154. Tivanski, A. V.; Walker, G. C., Ferrocenylundecanethiol self-assembled monolayer charging correlates with negative differential resistance measured by conducting probe atomic force microscopy. *Journal of the American Chemical Society* **2005,** 127, (20), 7647-7653.

155. Ramachandran, G. K.; Tomfohr, J. K.; Li, J.; Sankey, O. F.; Zarate, X.; Primak, A.; Terazono, Y.; Moore, T. A.; Moore, A. L.; Gust, D.; Nagahara, L. A.; Lindsay, S. M., Electron transport properties of a carotene molecule in a metal-(single molecule)-metal junction. *Journal of Physical Chemistry B* **2003,** 107, 6162-6169.

156. Hurley, P. T.; Ribbe, A. E.; Buriak, J. M., Nanopatterning of alkynes on hydrogen-terminated silicon surfaces by scanning probe-induced cathodic electrografting. *Journal of the American Chemical Society* **2003,** 125, (37), 11334-11339.

157. Yang, W. S.; Chai, X. D.; Chi, L. F.; Liu, X. D.; Cao, Y. W.; Lu, R.; Jiang, Y. S.; Tang, X. Y.; Fuchs, H.; Li, T. J., From achiral molecular components to chiral supermolecules and supercoil self-assembly. *Chemistry-a European Journal* **1999,** 5, (4), 1144-1149.

158. He, X. R.; Li, Q. K.; Li, Y. L.; Wang, N.; Song, Y. B.; Liu, X. F.; Yuan, M. J.; Xu, W.; Liu, H. B.; Wang, S.; Shuai, Z. G.; Zhu, D. B., Spontaneously aggregated chiral nanostructures from achiral tripod-terpyridine. *Journal of Physical Chemistry B* **2007,** 111, (28), 8063-8068.

159. Bao, C. Y.; Lu, R.; Jin, M.; Xue, P. C.; Tan, C. H.; Xu, T. H.; Liu, G. F.; Zhao, Y. Y., Helical stacking tuned by alkoxy side chains in pi-conjugated triphenylbenzene discotic derivatives. *Chemistry-a European Journal* **2006,** 12, (12), 3287-3294.

160. Jeong, K. U.; Knapp, B. S.; Ge, J. J.; Jin, S.; Graham, M. J.; Harris, F. W.; Cheng, S. Z. D., Origin of self-assembled helical supramolecular structures in achiral C6 biphenyl carboxylic acid compounds. *Chemistry of Materials* **2006,** 18, (3), 680-690.

161. Brizard, A.; Oda, R.; Huc, I., Chirality effects in self-assembled fibrillar networks. In *Low Molecular Mass Gelators: Design, Self-Assembly, Function*, 2005; Vol. 256, pp 167-218.

162. Rowan, A. E.; Nolte, R. J. M., Helical molecular programming. *Angewandte Chemie-International Edition* **1998,** 37, (1-2), 63-68.

163. vanEsch, J.; DeFeyter, S.; Kellogg, R. M.; DeSchryver, F.; Feringa, B. L., Self-assembly of bisurea compounds in organic solvents and on solid substrates. *Chemistry-a European Journal* **1997,** 3, (8), 1238-1243.

164. Murphy, C. J.; San, T. K.; Gole, A. M.; Orendorff, C. J.; Gao, J. X.; Gou, L.; Hunyadi, S. E.; Li, T., Anisotropic metal nanoparticles: Synthesis, assembly, and optical applications. *Journal of Physical Chemistry B* **2005,** 109, (29), 13857-13870.

165. Xia, Y. N.; Whitesides, G. M., Soft lithography. *Angewandte Chemie-International Edition* **1998,** 37, (5), 551-575.

166. Lichtenberg, J.; de Rooij, N. F.; Verpoorte, E., A microchip electrophoresis system with integrated in-plane electrodes for contactless conductivity detection. *Electrophoresis* **2002,** 23, (21), 3769-3780.

167. Kneipp, K.; Kneipp, H.; Kneipp, J., Surface-enhanced Raman scattering in local optical fields of silver and gold nanoaggregatess - From single-molecule Raman spectroscopy to ultrasensitive probing in live cells. *Accounts of Chemical Research* **2006,** 39, (7), 443-450.

168. Link, S.; Mohamed, M. B.; El-Sayed, M. A., Simulation of the optical absorption spectra of gold nanorods as a function of their aspect ratio and the effect of the medium dielectric constant. *Journal of Physical Chemistry B* **1999,** 103, (16), 3073-3077.

169. Govindaraj, A.; Satishkumar, B. C.; Nath, M.; Rao, C. N. R., Metal nanowires and intercalated metal layers in single-walled carbon nanotube bundles. *Chemistry of Materials* **2000,** 12, (1), 202-205.

170. Alvarez-Puebla, R. A.; Ross, D. J.; Nazri, G. A.; Aroca, R. F., Surface-enhanced Raman scattering on nanoshells with tunable surface plasmon resonance. *Langmuir* **2005,** 21, 10504-10508.

171. Tao, A. R.; Yang, P. D., Polarized surface-enhanced Raman spectroscopy on coupled metallic nanowires. *Journal of Physical Chemistry B* **2005,** 109, 15687-15690.

172. Li, L.; Shi, J. L.; Zhang, L. X.; Xiong, L. M.; Yan, J. N., A novel and simple in-situ reduction route for the synthesis of an ultra-thin metal nanocoating in the channels of mesoporous silica materials. *Advanced Materials* **2004,** 16, (13), 1079-+.

173. Naujok, R. R.; Duevel, R. V.; Corn, R. M., Fluorescence and Fourier-Transform Surface-Enhanced Raman-Scattering Measurements of Methylene-Blue Adsorbed onto a Sulfur-Modified Gold Electrode. *Langmuir* **1993,** 9, (7), 1771-1774.

174. Lee, S. J.; Morrill, A. R.; Moskovits, M., Hot spots in silver nanowire bundles for surface-enhanced Raman spectroscopy. *Journal of the American Chemical Society* **2006,** 128, (7), 2200-2201.

APPENDIX

The quantitative analysis of *solvent nature – nanostructure morphology* dependence

Some *qualitative* correlation between the solvent nature and the nanostructure morphology can be noticed for the nanoscale architectures of **1a-f** assembled in the various solvents. Figure 2.5 (page 111) suggests that the nanostructure morphology is more dependent on the solvent nature than the structure of the compound. It is likely due to the structural similarity of the G^C derivatives studied. In general, the nanostructure size increases as solvent polarity increases. In order to use the observed correlations for the design of new morphologies in a more precise fashion, it is desirable to find *quantitative* solvent nature – nanostructure morphology correlations. To quantify these correlations, two sets of parameters are necessary: one that describes solvent (*solvent parameters*) and the other that describes nanostructures assembled in the respective solvent (*nanostructure parameters*). Since the nanostructure's morphology depends on the solvent, the nanostructure parameter will be used as the function of the solvent parameter.

Numerous *solvent parameters* can be used to explain solvent effect on compounds' reactivity, solubility, and other properties. Such parameters are based on the solvent's

different physicochemical quantities, e.g. rate constants, solvatochromic shifts in ultraviolet/visible spectra, solvent-induced shifts in infrared frequencies. Some solvent parameters are purely empirical in nature, i.e. they are based directly on some experimental measurement. Other solvent parameters are based on analyzing experimental results. Such parameters are considered to quantify some particular aspect of solvent capability for interaction with solutes. Several solvent parameters (dielectric constant, logP) and physical properties (boiling point, viscosity) can be useful to quantify the aggregates morphology observed in this work.

Parameters that effectively describe a solvent's ability to modulate the van der Waals interactions can be good descriptors for correlation studies. *Polarity* of the solvents can be a good parameter for this purpose. When applied to solvents, this rather ill-defined term covers their overall solvation capability, which in turn depends on the action of all possible, nonspecific and specific, intermolecular interactions between solute ions or molecules and solvent molecules, excluding such interactions leading to definite chemical alterations of the ions or molecules of the solute. Occasionally, the term "solvent polarity" is restricted to nonspecific solute/solvent interactions only (i.e. to van der Waals forces)[1]. Nevertheless, there are several quantitative parameters that are related to the polarity. Some of these parameters (dielectric constant, Dimroth–Reichardt E_T

parameter, and partition coefficient[1-3]) used to trace wanted correlations are defined below.

a) Dielectric constant ε (or relative static permittivity) is a measure of the extent to which a solvent concentrates electrostatic lines of flux. It is the ratio of the amount of stored electrical energy when a potential is applied, relative to the permittivity of a vacuum.

b) Dimroth–Reichardt E_T parameter is a measure of the ionizing power (loosely polarity) of a solvent, based on the maximum wavenumber of the longest wavelength electronic absorption band of a standard compound in a given solvent. E_T, is given by:

$E_T = 2.859 \times 10^{-3\nu} = 2.859 \times 10^4 \lambda^{-1}$

where E_T is in kcal mol^{-1}, ν is in cm^{-1} and λ is in nm.

c) Partition coefficient is the ratio of concentrations of a compound in the two phases of a mixture of two immiscible solvents at equilibrium.[3] A logarithm of the partition coefficient logP between octanol and water is commonly used in qualitative structure – activity relationship (QSAR) for e.g. drug design.

$$log\ P_{oct/wat} = log\left(\frac{[solute]_{octanol}}{[solute]^{un-ionized}_{water}}\right)$$

Several other solvent parameters can be used: Flory – Huggins, Grunwald–Winstein, Kamlet–Taft, and Koppel–Palm parameters, solvophobicity, Z-value, solvent donor number, and many others. However, many of these parameters are related to the parameters chosen above and some of them describe the properties of the solvents that are not relevant for this case (acid-base properties or lone pair donor abilities).

A parameter that quantifies a particular nanostructure (*nanostructure parameter*) is required. The size of the aggregates depends mostly on a solvent. The volume of the nanostructure can be used as a quantitative parameter. However, as was discussed above, most of the nanostructures have anisotropy, because they are assembled from anisotropic modules (rosettes, tubes). Two of the three dimensions depend on the van der Waals interactions between alkyl chains, while the third dimension depends on the π-π stacking. The volume depends on these two quite different forces and consequently is not very suitable as a nanostructure parameter. We can consider only one dimension of a nanostructure like length, width, or height. In most of the morphologies in this work, the longest dimension is along the tube length which depends on stacking interactions. A very high polydispersity (many RNTs with different lengths) was observed for this dimension, while the other two dimensions that are dependant on van der Waals interactions (acting along the perpendicular to the nanotube axes) were found to be more

monodisperse. A good parameter combining the latter two dimensions would be the surface area (S) of the nanostructure cross-section perpendicular to the tubes axis or S divided by the cross-section of a single nanotube (S/s). Three chosen parameters (dielectric constant, Dimroth–Reichardt E_T parameter, and logP), along with boiling point and viscosity are given in Table 5.1. The dependence of the cross-section surface area *S* divided by the surface area of a single tube result *s* (calculated from averaged measurements in SEM images for compound **1a** at 0.25 g/L) on the selected parameters is shown in the Figure 5.1.

Table 5.1. Parameters used for qualitative correlations.

solvent	S, nm^2	S/s	ε	E_T	logP	BP, °C	η, cP
Hexane	16.6	1.00	2.02	31.1	3.9	69	0.29
chloroform	49009	2950	4.81	39.1	2	61	0.54
decanol	2000	120	8.1	47.7	4	231	9.3
heptanol	270	16.2	6.7	48.8	2.4	176	4.5
butanol	166	9.99	17.8	50.2	0.65	118	3
nitromethane	15000	903	39.4	46.3	-0.24	102	0.61
DMF	7853	473	38.3	43.8	-1	153	0.92
DMSO	17671	1060	47.2	45.1	-1.3	189	2.1

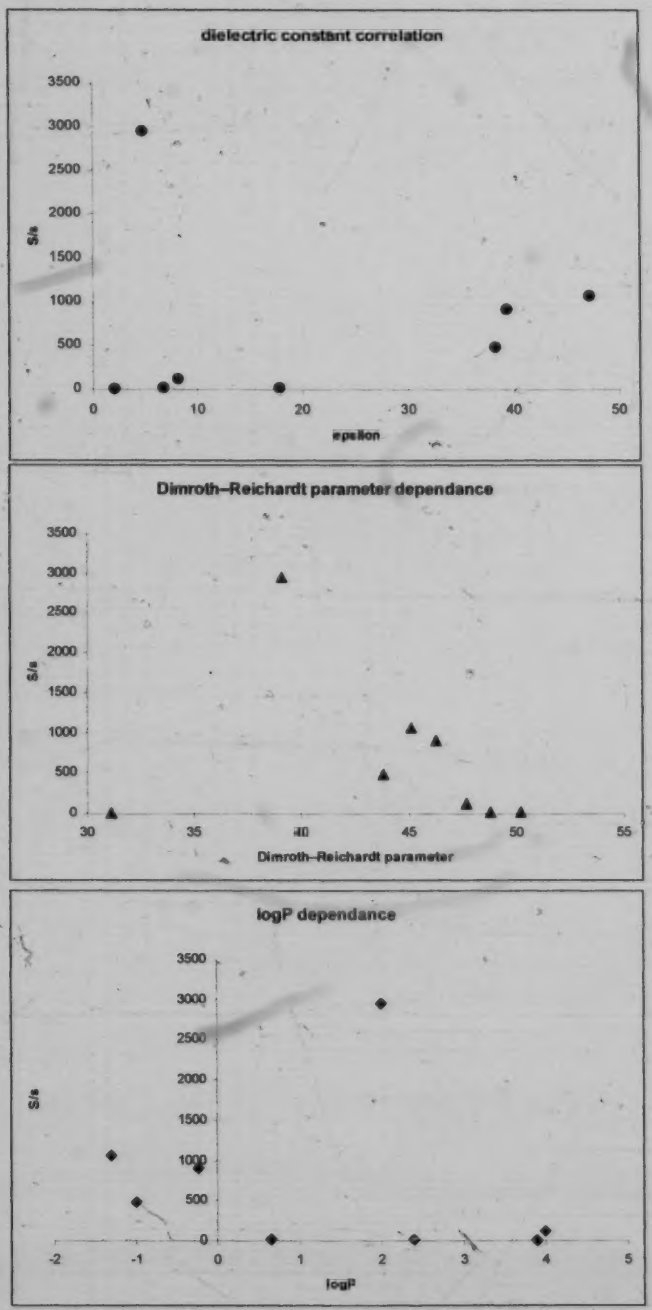

Figure 5. 1. Dependence of the nanostructure cross-section surface area divided by the surface area of a single tube result (S/s) calculated and averaged from SEM images for compound 1a at 0.25 g/L

Figure 5.1 suggests that the dependence of the nanostructure cross-section area on the solvent parameters is mostly non-linear. The size of the structures in DMF (S/s = 473), nitromethane (S/s = 903), and DMSO (S/s = 1060) follows the solvents' dielectric constant order (38.3, 39.4, 47.2 respectively). However, in alcohol series, the order is the opposite: the most polar butanol yields the thinnest RNTs bundles (Table 5.1). Using nonlinear coordinates (reverse values, squares or their linear and nonlinear constructs) will not reverse the order but will only change the individual parameters' contributions. Even though the general trend (increase in the size of nanostructures) can be noticed going from single nanotubes in nonpolar hexane to very thick bundles in very polar DMSO, some "deviations" can be noticed. For example, unexpectedly large nanostructures (larger than for any of the more polar alcohols) are formed in chloroform. These observations indicate that there are more than one factor affecting the self-assembly. Even though the experiments were done at the same concentration, keeping the ageing time constant, the assembly was performed at the solvents boiling points that are different. The viscosity of the solvent also varies significantly (Table 5.1). It is possible that "unusually" large and highly ordered nanostructures formed in chloroform are the result of more *thermodynamically* controlled process compared to more polar solvents where assembly is more *kinetically* controlled. An analogy can be

made to the crystallization process that gives larger crystals in an equilibrium versus small crystals during non-equilibrium growth. This can explain the reverse order in chloroform, decanol, heptanol, butanol series. It is likely that the assembly is more thermodynamically controlled in lower viscosity and high boiling point nitromethane, DMF and DMSO where the "normal" order is restored. The exact shape of an aggregate is difficult to correlate to a solvent parameter. Surface to volume ratio would be a good parameter for this comparison, as it depend on the shape; however it can work only for the structures close in size (e.g. bow-ties and nanospheroids in chloroform), which is not the generally the case. Even though parameters suggested here describe the *solvent nature – nanostructure morphology* correlations only to a limited extent, the discussion presented above is an important step towards understanding the factors governing this complex hierarchical process.

References

1. Dutkiewicz, M.; Dutkiewicz, E., The Relation between the Nonlinear Dielectric Effect and Solvent Polarity. *Journal of Solution Chemistry* **1993,** 22, (9), 787-795.

2. Reichardt, C., *Solvents and solvent effects in organic chemistry* Weinheim : Wiley-VCH, : 2003.

3. Leo, A.; Hansch, C.; Elkins, D., Partition Coefficients and Their Uses. *Chemical Reviews* **1971,** 71, (6), 525-561.